Laser written integrated photonics for quantum information science

By

Thomas Meany

A thesis submitted to Macquarie University
for the degree of
Doctor of Philosophy
Department of Physics and Astronomy
August 2014

MACQUARIE UNIVERSITY
FACULTY OF SCIENCE

Typeset in $\LaTeX\,2_\varepsilon$.

Except where acknowledged in the customary manner (See statement of candidate), the material presented in this thesis is, to the best of my knowledge, original and has not been submitted in whole or part for a degree in any university.

Statement of candidate

This thesis work was performed in collaboration with others. The input of other collaborators is gratefully acknowledged and detailed section by section below.

In chapter 4, the laser systems, microscopy equipment, sample preparation equipment and classical characterisation facilities were in place before the commencement of my thesis work. These facilities were primarily developed and maintained by Peter Dekker, Simon Gross, Graham Marshall, and Martin Ams. Simon Gross, Christopher Miese and Alex Fuerbach were the primary designers of the Femtosource laser writing system and training in using that system was provided by Simon Gross. Access to the OptoFab facilities, infrastructure prodived by the Australian National Nano-fabrication facility is acknowledged. Facilites included: femtosecond laser, characterisation equipment and laser inscription facilities.

In chapter 5, Fig. 5.14 and 5.15 show data which was collected and plotted by Simon Gross. The samples which contained nano-gratings were fabricated by Sören Richter during a collaborative visit to Macquarie University using the Femtosource laser system. However, all further characterisation, data and interpretation are my own work.

In chapter 6, the maximum likelihood estimation was performed by Michael Delanty and using that data to predict non-classical behaviour was the work of Michael Delanty.

In chapter 7, the characterisation of the Knill circuit was completed in University of Queensland in the group of Andrew White. The coherent state characterisation was completed in collaboration with Devon Biggerstaff and input from Alessandro Fedrizzi, Matthew Broome and Andrew White.

In chapter 8, the work was completed as an international exchange between Macquarie University, University of Sydney and the University of Nice. The PPLN waveguide chip was designed, fabricated and characterised entirely by members of the university of Nice, Lutfi Ngah, Olivier Alibart, and Sébastien Tanzilli. Olivier Alibart and Lutfi Ngah travelled to Macquarie University and during that time assisted in the setup of the experimental apparatus most of which was borrowed from Nice and the University of Sydney. Switches, used during the experiment were designed and packaged by Matthew Collins. The process of characterising the coincidence-to-accidental ratio of the sources, interfacing components and multiplexing the source outputs was done individually and completed in Macquarie University.

All men dream: but not equally. Those who dream by night in the dusty recesses of their Minds wake in the day to find that it was vanity: but the dreamers of the day are dangerous men, for they may act their dream with open eyes, to make it possible. This I did..[1]

T.E. Lawerence

Go raibh míle maith agat

Mum, dad and Fiach you taught me how to dream in the daytime. Mum, you are probably the only person I know who encourages my wild ideas, often to a conclusion. This thesis is one of them. Fiach your wisdom is so far beyond your years that it seems as though you never stop growing and I look up to you more every day. Diane, Aisling and Len *"de Gadfadda"* I've learned so much from you and always been inspired. Especially when it come to acting the maggot. I have been blessed to be surrounded by wonderful warm family and friends that I could fill another ten theses thanking, so I just say aboy da kid. Griff I have to give you special mention since you were mad enough to come to this strange island as well and we had some great times. Катя, Большое спасибо! Я люблю тебя навсегда.Вы красивая дух

This thesis would not have been possible without my fantastic supervisors Mick Withford and Mike steel. You guys are amazing. Your patience, your support, your advice, I just cant properly express how much it has meant to me to join your group and learn so much. Macquarie University and the physics, photonics and Qscitech departments have been so kind to me and Judith Dawes and Dave Coutts deserve special mention for making this environment one in which I have been so happy. My fellow group members are all unique and exceptional people, everyone has helped me so much and in writing this I smile again, just as I have done, every day I spent with you. Jocelyn (my thesis buddy!), Yuwen, Iza, Zach, Glen, Blake, Nick, Chris, Alex, Marty, Nem, Luke, and BJ you guys are so great to work with! However, special mention must go to two people, Graham Marshall and Simon Gross. Graham, you are someone I greatly admire for your knowledge and skill. It was fantastic learning from you! Simon, you have taught me so much and your work ethic, drive, knowledge and love of science is absolutely inspirational. Peter Deker has been the lab manager during my thesis and he is a man equally at home in a laser lab as he is in a workshop or building site. His humour and pragmatism have been such a pleasure for these past years. During my studies I have had the joy of working outside my university with other fantastic people. In the University of Queensland I spent a month learning from Devon(s!), Mike, Martin, Alessandro, Marcello, Matt, Till and Andrew. You guys are so much fun and so knowledgeable. I learned so much during my visit, thank you. I visited the University of Nice and had another superb time. The guys Seb, Lutfi, Florien, Armandine and Bernard were such a hilarious crew and it was a pleasure to join you. I learned so much. Special mention must go to Olivier Alibart who is a scientist *extraordinaire*! Your vast knowledge and advice has been a huge help and I had a blast working with you. The group of University of Sydney, Alex, Chunle, Matt and Ben are wonderful. I continue to be inspired by Matt Collins' knowledge and skill, you're an inspiration mate.

During my time in Macquarie University I had the great joy of working for Katherine Stewart teaching science. It taught me about the beautiful Australian bush as well as the skills needed in a classroom. Nada you are just awe inspiring. Your skills of organisation and your passion for teaching are incredible. Linda and Jenny it was a pleasure to work and learn with you, even on late night exam marking! Thank you so much, I will miss you.

This thesis did not only encompass science, often I pestered and annoyed many more people beyond my own field. I give a special thanks to Shelly who was kind enough to tolerate my consistent tardiness and inconvenient requests. In Macquarie Carol, Lisa, Anita, Agnes, Laura and Jane, you have been so patient with my inability to fill out virtually any document correctly! Thank you so much. All your efforts are so greatly appreciated, even if there is the occasional grumble!

Before I came to study in Australia I had wonderful teachers and one of them is Gilles Cheriaux. He took me into his group and taught me about laser physics, Thank you. In NUIG I had the pleasure of learning from Gerard O'Connor who first taught me about quantum mechanics and lasers. Ger you have been a great advisor and your support has been a huge influence. Sasha Goncharov, you were a brilliant thesis supervisor and I still use the optical techniques I learned from you! Tom Glynn, Andy Shearer, and of course Frank Imbush truly inspired me, you are fantastic teachers.

Mike Steel, I owe you a special thanks for all your help especially with this thesis:

"il miglior fabbro"

Abstract

This thesis details the study of quantum information science (QIS) using integrated photonics. Integrated photonic devices are fabricated in glass using the femtosecond laser direct write (FLDW) technique. This method uses a focused high power laser to produce a localised refractive index change in a glass substrate which can be used to form waveguides. A rigorous parameter study of laser inscription and glass structure is performed to isolate regions where low loss waveguides can be formed. Unique, three-dimensional, circuit designs are created which are then characterised to determine symmetry and to ascertain their performance for QIS.

The circuit designs include 3D multiports which permit the unitary transformation of a set of optical modes. Single photons are injected into this device to determine it's performance and compare it to bulk optic, fibre optic and lithographically fabricated examples. The 3D multiports show high fidelity operation and a comparable performance to other circuit design platforms. Building on this work which shows the high quality of laser inscribed devices, an inherently quantum circuit is designed. It has the function of operating as a basic two-qubit circuit element which applies a phase shift to a qubit in a target mode, conditional on the state of a control qubit. This circuit is heralded, meaning that it operates in the presence of two additional ancilla modes which trigger the success of the probabilistic gate. The design of this circuit required detailed analysis of the reproducibility of laser written circuits in the presence of performance tolerance to fabrication imperfections.

The devices described previously were characterised, non-classically, using a bulk source of photon pairs. This limits the application of the devices beyond demonstrations or prototypes, hence it is desirable to also integrate these devices with on-chip sources of single photons. Such a source of single photons is available in the form of a quasi phase-matched nonlinear crystal which emits heralded single photons. An experiment was undertaken to design a hybrid circuit, composed of both linear and nonlinear elements to produce heralded single photons, to produce multiple sources of heralded single photons. This was completed and experiments exploiting high speed switching to combine individual sources and an experiment to manipulate photon pair states is completed.

This work builds on the knowledge of FLDW structures for on chip routing and manipulation of light. Demonstrations of integrated circuits and hybrid integrated devices shows the potential for high quality and compact monolithic on-chip quantum circuits.

We have tested and tasted too much, lover- Through a chink too wide there comes in no wonder. [2]

Patrick Kavanagh

Thesis outline

In this thesis waveguide circuits for quantum information applications are fabricated using a laser inscription process. Hence, this thesis will focus on two core areas: femtosecond laser waveguide writing and quantum information science. This thesis will be divided into seven chapters. The first two chapters act as an introduction to the core experimental material contained in chapters 3-6. A detailed summary and outlook is contained at the end of each experimental chapter with ideas and opportunities for the next steps that could be taken. At the end of this thesis a conclusion and outlook on future perspectives is contained in chapter 7. For the interested reader appendix A contains a summary of the theory of waveguide operation and appendix B provides a thorough outline of the experimental apparatus used to perform the experimental work contained in this thesis.

Chapters 1 provides an introduction to quantum information science. This chapter initially outlines the principle of two-photon interference from a historical perspective. This is an important concept since it is a physical behaviour which can only be described using quantum mechanics and underlies the functioning of quantum logic circuits. This is relevant for chapter 4 in particular where two photon characterisations are performed on optical multiports. The concept of linear optical quantum computing (LOQC) is developed starting initially from a brief description of entanglement and its applications. An explanation of the challenges of this scheme and the advantages of waveguide circuits for its implementation is provided and is relevant for chapter 5 which details the design of a quantum controlled-phase circuit. Finally a brief outline of the production of pairs of photons using nonlinear processes which is used in chapter 6 for the design of a multiplexed single photon source.

Chapter 2 contains a background to the fabrication of waveguides in glass using an ultrafast laser. The chapter is broken into two parts the first of which details the underlying material processes which occur resulting in refractive index change. The second section outlines practical fabrication approaches used in the production of waveguides. This material is then used in chapter 3 for the production of low loss waveguides for single mode operation at 800 nm. The goal of this chapter was to find a regime where low loss waveguide fabrication could be achieved at high speed. This is important since one of the strengths of the laser inscription technique lies in the fact that it can be used as a rapid prototyping process. Prior studies had shown that this could be achieved at the telecommunications wavelength of 1550 nm but a rigorous study was lacking at the wavelength of 800 nm. Furthermore the origin of this loss was found to be due to trace iron ions within glass samples and an alternative glass was found displaying much lower levels of trace impurities showing it is more amenable to quantum information science applications. Though this study appears at the start of the thesis it should be noted that this was an ongoing study over the course of the thesis. Hence, findings here were not incorporated into every subsequent section.

Chapters 4 describes the design, fabrication and characterisation of a three and four arm multiport beamsplitter. The rigorous characterisation of such circuits using non classical light had never been completed prior to the authors experiments. The reults of this section, most notably the relative phases and reflectivities of the beamplitters, meant a more complex quantum circuit could be fabricated. The design and implementation of a controlled-phase gate are detailed in chapter 5. Parametric studies of the reproducability of component beamsplitters and a classical characterisation of the device is described. However, further studies of the circuit were prevented due to the lack of available low noise single photon sources.

The need for high efficiency low noise sources of single photons motivated the studies undertaken in chapter 6. A hybrid source of 4 heralded photons is produced using waveguides formed in a nonlinear crystal and laser inscribed waveguides. This method had never been used before and it took advantage of the high photon production efficiency of a nonlinear media and the low propagation loss and ease of routing available in glass circuits. The properties of the photons production statistics is then manipulated using a fast switching technique to produce a signal to noise ratio which is otherwise unattainable. This work shows the first steps towards a reconfigurable source-circuit hybrid an important alternative method to achieving a quantum computer in future.

In the final chapter of this work is a summary of the achievements and their context in the broader literature. Prospects and directions for future work are outlined with ideas which have evolved from experiments contained here. For those wishing to recreate this work an experimental methods section is contained in appendix B.

Contents

..we have involved ourselves in a colossal muddle, having blundered in the control of a delicate machine, the working of which we do not understand [3]

John Maynard Keynes

1

Background to quantum information science

Central to the research into quantum information science (QIS) is the possibility of a quantum computer being produced which would have the capability to factor large integers more efficiently than classical means [4]. The difficulty of factoring large composites is the basis of the public key cryptosystem RSA. This has given a diverse array of research fields the funding to pursue not just applications of quantum systems but the underlying physical phenomena also. The result has been a huge boost to the understanding of fundamental physics. Whether or not a quantum computer is ever realised, it is a tremendously exciting time for the understanding of matter at its smallest scale. Photonics has been integral to a vast range of developments in fundamental quantum mechanics. Owing to the diverse array of fields studying QIS the discussion here will focus mainly on the area of quantum optics and the advances in optics which have been so crucial to the understanding and application of quantum mechanical phenomena.

This chapter introduces background material relevant to the quantum information components of this thesis, it takes a historical bent in order to introduce the reader to the relevant details and also to highlight significant discoveries. The chapter is broken into 6 sections. Section 1 outlines an early experiment using pairs of photons to study the non-classical behaviour of light and the methods used to do so which are relevant to the experimental methods of this thesis. Section 2 will describe the basic theory of quantum information science and show how the early discoveries of quantum phenomena can be exploited in quantum technologies such as quantum computing, communication and sensing. Section 3 will explain the reasons for choosing an optical approach to quantum information science and the challenges which must be overcome in using photons as qubits. Section 4 will detail the move from tabletop experimental demonstrations to on-chip circuits which enable more complex and scalable optical quantum devices. Finally, the last section contains a theoretical background to the nonlinear production of photons which is necessary for understanding the challenges of increasing the complexity of quantum optical circuits.

1.1 Hong Ou Mandel and the length of the photon wavepacket

A paper by Hong, Ou and Mandel (HOM) in 1987 [5] entitled: 'Measurement of subpicosecond time intervals between two photons by interference' is a significant development in quantum optics. The purpose of the work was to build on previous work in the area of spontaneous parametric down conversion (SPDC) sources and use it to measure the time between two photons by quantum interference and in essence the length of the photon wavepacket. Work in this area had been active and Burnham *et al.* reported producing down converted photons from an ADP crystal in 1970 [6] and Abram *et al.* had performed photon correlation measurements in 1986 [7]. The process of SPDC involves the production of two photons (referred to as the signal and idler) with frequencies ω_s and ω_i from a single parent photon of frequency ω_p This occurs inside a nonlinear crystal which satisfies the phase matching conditions requiring the conservation of energy and momentum:

$$\omega_p = \omega_s + \omega_i, \tag{1.1}$$

$$\vec{k}_p = \vec{k}_s + \vec{k}_i, \tag{1.2}$$

where $\vec{k}_p$, $\vec{k}_s$ and $\vec{k}_i$ are the pump signal and idler wave vectors, respectively. Thus, by appropriate selection of crystal optical axes, a pair of entirely degenerate photons which are identical in spatial mode, polarisation and frequency can be produced [8].

The experiment of Hong, Ou and Mandel consisted of a way to overlap a pair of down converted photons produced by a nonlinear crystal on a 50:50 beamsplitter and temporally delay the arrival of one photon with the other. The output from the beamsplitters is then measured using single photon detectors and coincidence measurements between the two detectors performed. When there is no way of knowing which path the photons took, which in this case would mean that the two photons arrive at the beamsplitter at precisely the same time, both photons exit one port of the beamsplitter. Thus no photon coincidences are recorded. However when the photons strike the beamsplitter at times outside the coherence length of the photon wavepacket the photons are distinguishable and thus exit both ports of the beamsplitter with equal probability, this then results in coincidences. Typically a plot of photon coincidence counts vs. temporal delay is recorded and the dip in coincidences is referred to as a HOM dip as seen in Fig. 4.4

By considering a beamsplitter, with equal transmission and reflection coefficients, we can understand that it performs a unitary operation on a set of optical modes [9]. We can define a mode creation operator which is denoted by $a_i^\dagger|n_i\rangle = \sqrt{n+1}|(n+1)_i\rangle$, where n denotes photon number in a given mode i. The initial state is the vacuum state $|0\rangle$ which contains no photons. The beamsplitter transforms input mode creation operators ($a_1^\dagger$ and $a_2^\dagger$) to output mode operators ($b_1^\dagger$ and $b_2^\dagger$),

$$\begin{aligned} a_1^\dagger &\rightarrow \tfrac{1}{\sqrt{2}}\left(b_1^\dagger + b_2^\dagger\right) \\ a_2^\dagger &\rightarrow \tfrac{1}{\sqrt{2}}\left(b_1^\dagger - b_2^\dagger\right). \end{aligned} \tag{1.3}$$

Therefore if we chose as an input state $|1_1 1_2\rangle$, we obtain the following output [10],

$$|1_1 1_2\rangle = a_1^\dagger a_2^\dagger |0_1 0_2\rangle \rightarrow \frac{1}{2}\left(b_1^\dagger + b_2^\dagger\right)\left(b_1^\dagger - b_2^\dagger\right)|0_1 0_2\rangle = \frac{1}{\sqrt{2}}\left(|2_1 0_2\rangle - |0_1 2_2\rangle\right). \tag{1.4}$$

This equation shows the output state is entangled since this is no longer separable. This state is often generalised to $|N0\rangle - |0N\rangle$ where N corresponds to photon number occupied by one mode and zero denotes vacuum (or no photons present) in the other mode. This two-photon interference is caused by the beamsplitter introducing an indistinguishability between the possible paths of the photons [11]. This is in no way due to any first order interference occurring due to overlapping the photons at the beamsplitter, since these are incoherent particles (see section 1.1). This fact has been shown in an experiment by Pittman *et al.* where which-path interference can be observed for particles which *do not* overlap in anyway at the beamsplitter [12].

This two-photon interference effect is crucial for introducing an effective particle interaction when using linear optics to produce two-qubit gates as will be described in the next section.

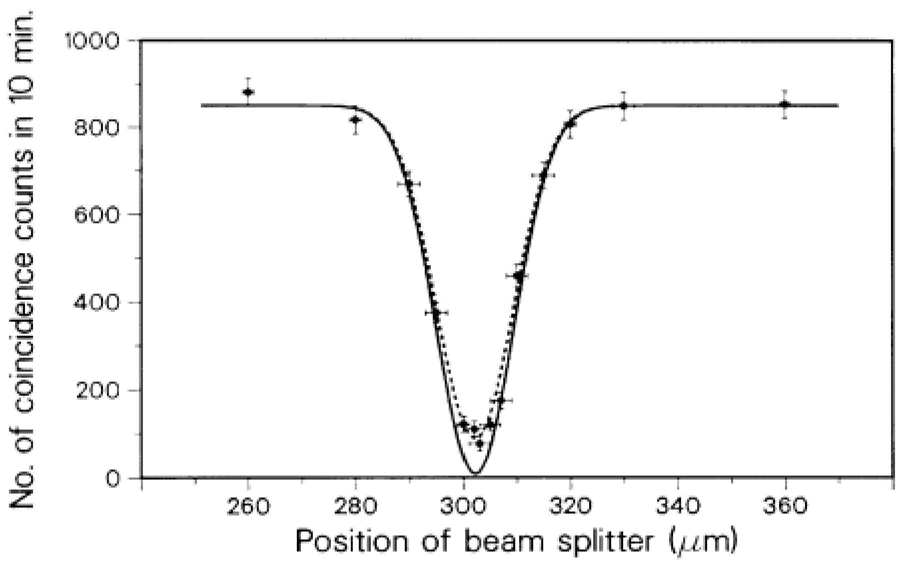

Figure 1.1: The origional HOM dip recorded by Hong On and Mandel in their 1987 paper, the width of the dip corresponds to the coherence length of the source and the depth of the dip depends on the *distinguishability* of the photons [5]

1.2 Quantum information science essentials

1.2.1 The quantum bit

The quantum bit, or *qubit*, is the quantum analogue of the classical bit. However, rather than the fixed values of the classical bit of "0" and "1" the qubit can exist in a superposition of these states. The state of a single qubit can be be described by:

$$|\psi\rangle = \alpha|\mathbf{0}\rangle + \beta|\mathbf{1}\rangle, \tag{1.5}$$

where $|\mathbf{0}\rangle$ is a ket with a logical state denoted by bold numbering, α and β are complex coefficients and $|\alpha|^2 + |\beta|^2 = 1$. A general n-qubit quantum system, represented by a 2^n bitstring, can be defined as:

$$|\psi\rangle = \sum_{i=0}^{2^{n-1}} c_i|x_i\rangle, \tag{1.6}$$

where the complex coefficients are normalised by

$$\sum_{i=0}^{2^{n-1}} |c_i|^2 = 1. \tag{1.7}$$

Each qubit doubles the number of states which can be represented and this is core to the exponential scaling of computing power with only polynomial increase in required resources offered by quantum computing.

1.2.2 Evolution of the state

A quantum state $|\psi\rangle$ can undergo unitary evolution,

$$U|\psi\rangle = |\psi^{'}\rangle = \sum_{i=0}^{2^{n-1}} c_i^{'}|x_i\rangle, \tag{1.8}$$

where the squares of the complex coefficient of the new state vector still sum to one,

$$\sum_{i=0}^{2^{n-1}} |c_i^{'}|^2 = 1. \tag{1.9}$$

Furthermore applying U^{-1} to $|\psi^{'}\rangle$ will return the initial state. Although at first this does not seem significant it is in fact another critical feature of quantum information processing. The unitarity of the process has implications for the process of measurement and also prevents the deterministic amplification of an arbitrary state, resulting in the no-cloning theorem [13]. Unlike in classical computing or communication, where n input bits in a logic circuit return a single output bit which can be copied multiple times, every n qubits entered into a quantum logic circuit will return n output qubits and the output state of this system cannot be copied and stored. This can be understood if we try to define the copying unitary as follows,

$$U_{\text{copy}}|\mathbf{0}_1\rangle|\mathbf{0}_2\rangle = |\mathbf{0}_1\rangle|0_2\rangle, U_{\text{copy}}|\mathbf{1}_1\rangle|\mathbf{0}_2\rangle = |\mathbf{1}_1\rangle|\mathbf{1}_2\rangle, \tag{1.10}$$

where here the subscripts simply refer to different qubits. This unitary copies the state of qubit 1 onto qubit 2, initially in state $|\mathbf{0}_2\rangle$. However a problem arises if we try to copy a general qubit in a superposition state, $|\psi_1\rangle = \alpha|\mathbf{0}\rangle + \beta|\mathbf{1}\rangle$,

$$U_{\text{copy}}|\psi_1\rangle|\mathbf{0}_2\rangle = \alpha|\mathbf{0}_1\mathbf{1}_2\rangle + \beta|\mathbf{1}_1\mathbf{1}_2\rangle \neq |\psi_1\rangle|\psi_2\rangle. \tag{1.11}$$

This shows that it is not possible in principle to perfectly reproduce an unknown quantum state.

The unitarity of quantum processes is also fundamental to the concept of quantum parallelism, one of the core properties offered by quantum computers over classical computers. Quantum processors could in principle calculate simultaneously a function, $f(x)$ for all possible values of x. Of course extracting this information requires measurement, therefore collapsing the state of a qubit into some eigenvector of the measurement operator and returning a number which is its eigenvalue. Hence since the quantum state cannot be observed without being projected into a state. Thus the qubit superposition state can no longer be recreated and retransmitted, meaning the methods of computation and information extraction become significantly different resulting in specific quantum algorithms [14].

1.2.3 Basics of quantum logic gates

The similarities with classical computing can be extended to consider a universal set of unitary operations. In classical information processing, any Boolean operation can be performed using a set of NAND gates. In quantum information the set of one qubit and two qubit gates which are required to produce any composite $2^n \times 2^n$ unitary are the Hadamard, the phase gate and the controlled-NOT gate [15]. The Hadamard gate is represented by,

$$H = \frac{1}{\sqrt{2}} \begin{bmatrix} 1 & 1 \\ 1 & -1 \end{bmatrix}, \tag{1.12}$$

which performs the following operation on a qubit,

$$\begin{aligned} H|\mathbf{0}\rangle &= \tfrac{1}{\sqrt{2}} \begin{bmatrix} 1 & 1 \\ 1 & -1 \end{bmatrix} \begin{bmatrix} 1 \\ 0 \end{bmatrix} = \tfrac{1}{\sqrt{2}}(|\mathbf{0}\rangle + |\mathbf{1}\rangle), \\ H|\mathbf{1}\rangle &= \tfrac{1}{\sqrt{2}} \begin{bmatrix} 1 & 1 \\ 1 & -1 \end{bmatrix} \begin{bmatrix} 0 \\ 1 \end{bmatrix} = \tfrac{1}{\sqrt{2}}(|\mathbf{0}\rangle - |\mathbf{1}\rangle). \end{aligned} \tag{1.13}$$

The computational basis is transformed into an equal superposition of $|\mathbf{0}\rangle$ and $|\mathbf{1}\rangle$. The action of the phase gate,

$$\phi = \begin{bmatrix} 1 & 0 \\ 0 & e^{i\phi} \end{bmatrix}, \tag{1.14}$$

performs the operation $\phi|\psi\rangle = \alpha|\mathbf{0}\rangle + e^{i\phi}\beta|\mathbf{1}\rangle$, to an input state $|\psi\rangle$. Finally the two-qubit gate interacts a pair of qubits. The controlled-NOT gate performs the following operation:

$$U_{CNOT}|\psi\rangle = \begin{bmatrix} 1 & 0 & 0 & 0 \\ 0 & 1 & 0 & 0 \\ 0 & 0 & 0 & 1 \\ 0 & 0 & 1 & 0 \end{bmatrix} \begin{bmatrix} c_0 \\ c_1 \\ c_2 \\ c_3 \end{bmatrix} = \begin{bmatrix} c_0 \\ c_1 \\ c_3 \\ c_2 \end{bmatrix} \tag{1.15}$$

this operation flips the final two elements of the two-qubit state vector. This could be compared to the classical *XOR* gate where a target register is flipped conditional on the state of a control register. Such a gate combined with a Hadamard gate can be used to produce a maximally entangled state. A two qubit input state $|\psi\rangle = |\mathbf{00}\rangle$ is initially transformed by a Hadamard operation on a single qubit resulting in the state $\frac{1}{\sqrt{2}}(|\mathbf{0}\rangle + |\mathbf{1}\rangle)|\mathbf{0}\rangle$ which when operated on by the CNOT results in the state,

$$|\Phi^+\rangle = \frac{1}{\sqrt{2}}(|\mathbf{00}\rangle + |\mathbf{11}\rangle). \tag{1.16}$$

This state is entangled since by measuring either component of the two qubit state, collapses the state of the other qubit. Another way to describe this state is to say that this state is not separable. In addition, the following two qubit states which in combination with equation 1.16 form a set of maximally entangled states referred to as the Bell states are:

$$\begin{aligned} |\Phi^-\rangle &= \tfrac{1}{\sqrt{2}}(|\mathbf{00}\rangle - |\mathbf{11}\rangle), \\ |\Psi^+\rangle &= \tfrac{1}{\sqrt{2}}(|\mathbf{01}\rangle + |\mathbf{10}\rangle), \\ |\Psi^-\rangle &= \tfrac{1}{\sqrt{2}}(|\mathbf{01}\rangle - |\mathbf{10}\rangle). \end{aligned} \tag{1.17}$$

This bipartite behaviour is integral to quantum information processing and permits for instance the process of quantum teleportation [16].

1.2.4 Application of entanglement - teleportation

If we take a qubit $|\psi_1\rangle = \alpha|\mathbf{0}_1\rangle + \beta|\mathbf{1}_1\rangle$ and interact it with a singlet state $|\Phi^-_{23}\rangle = (|\mathbf{0}_2\mathbf{1}_3\rangle - |\mathbf{1}_2\mathbf{0}_3\rangle)/\sqrt{2}$, distributed between two parties (normally referred to as Alice and Bob) we obtain:

$$|\psi_1\rangle|\Phi^-_{23}\rangle = \frac{1}{\sqrt{2}}\left(\alpha(|\mathbf{0}_1\mathbf{0}_2\mathbf{1}_3\rangle - |\mathbf{0}_1\mathbf{1}_2\mathbf{0}_3\rangle) + \beta(|\mathbf{1}_1\mathbf{0}_2\mathbf{1}_3\rangle - |\mathbf{1}_1\mathbf{1}_2\mathbf{0}_3\rangle)\right). \tag{1.18}$$

In a communication sense we could imagine that the singlet state $|\Phi_{23}\rangle$ is shared between Alice and Bob and the desire of Alice is to transmit the state of $|\psi_1\rangle$ to Bob and this is summarised conceptually in Fig. 1.2. This can be performed by now rearranging equation 1.18 in the form of the Bell states defined in equations 1.16 and 1.17,

$$\begin{aligned} |\psi_{123}\rangle = |\psi_1\rangle|\Phi^-_{23}\rangle = \tfrac{1}{\sqrt{2}}\Big[\alpha\left(\tfrac{|\Psi^+_{12}\rangle + \Psi^-_{12}\rangle}{\sqrt{2}}|\mathbf{1}_3\rangle - \tfrac{|\Phi^+_{12}\rangle + \Phi^-_{12}\rangle}{\sqrt{2}}|\mathbf{0}_3\rangle\right) + \\ \beta\left(\tfrac{|\Phi^+_{12}\rangle - \Phi^-_{12}\rangle}{\sqrt{2}}|\mathbf{1}_3\rangle - \tfrac{|\Psi^+_{12}\rangle - \Psi^-_{12}\rangle}{\sqrt{2}}|\mathbf{0}_3\rangle\right)\Big]. \end{aligned} \tag{1.19}$$

This can be further rearranged to form,

$$|\psi_{123}\rangle = \tfrac{1}{2}\left[|\Psi^{+}_{12}\rangle(\alpha|\mathbf{1}_3\rangle - \beta|\mathbf{0}_3\rangle) + |\Psi^{-}_{12}\rangle(\alpha|\mathbf{1}_3\rangle + \beta|\mathbf{0}_3\rangle) + \right. \\ \left. |\Phi^{+}_{12}\rangle(-\alpha|\mathbf{0}_3\rangle + \beta|\mathbf{1}_3\rangle) + |\Phi^{-}_{12}\rangle(-\alpha|\mathbf{0}_3\rangle - \beta|\mathbf{1}_3\rangle)\right]. \tag{1.20}$$

This equation describes a superposition of the Bell states and if a measurement is performed by Alice in the Bell state basis then any of these outcomes will have an equal probability of 1/4. This measurement then projects the state held by Bob into a state $|\phi_3\rangle$. If the measurement Alice performs retrieves a $|\Psi^+\rangle$ outcome, then Bob's state will be $-|\phi_3\rangle = -\begin{bmatrix}\alpha \\ \beta\end{bmatrix}$ which is the state $|\psi_1\rangle$ with a global phase. The other outcomes,

$$\begin{aligned} |\Psi^-\rangle &\rightarrow \begin{bmatrix} -1 & 0 \\ 0 & 1 \end{bmatrix} |\phi_3\rangle = Z|\phi_3\rangle \\ |\Phi^+\rangle &\rightarrow \begin{bmatrix} 0 & 1 \\ 1 & 0 \end{bmatrix} |\phi_3\rangle = X|\phi_3\rangle \\ |\Phi^-\rangle &\rightarrow \begin{bmatrix} 0 & -1 \\ 1 & 0 \end{bmatrix} |\phi_3\rangle = iY|\phi_3\rangle \end{aligned} \tag{1.21}$$

will result in the initial $|\psi_1\rangle$ state with single qubit rotations. These rotations correspond to the Pauli matrices, X (the bit flip), Y (the bit flip combined with a phase flip) and Z (the phase flip). The key element of this portion of the protocol is that once Alice performs the measurement the result is a classical piece of information which is a number labelling the state in which the superposition collapsed. This information can be sent to Bob classically, who will then know which qubit rotation must be performed on the state $|\phi_3\rangle$ to return $|\psi_1\rangle$. The measurement performed by Alice results in two particles with states $|\Psi^{\pm}\rangle$ or $|\Phi^{\pm}\rangle$ and no knowledge of the state $|\phi_1\rangle$ which has been teleported to Bob. Thus the no-cloning theorem is satisfied because Alice does not clone the state $|\phi_1\rangle$ but rather destroys it by measurement. The no-signalling theorem is fulfilled because although the teleportation occurs seemingly instantaneously, the message received by Bob is meaningless without the classical information (which cannot travel faster than the speed of light) transmitted by Alice to Bob which contains the information of the qubit rotation to perform in order to retrieve $|\phi_1\rangle$ from $|\phi_3\rangle$.

This is a fascinating and practical component of quantum information science and is fundamental to both quantum cryptography and in fact computation as will be shown in the next section. Teleportation can act as a circuit primitive as was shown by Gottesman and Chuang [17]. The previous section showed how a single qubit and two qubit gate, the Hadamard and CNOT, could be used to produce the maximally entangled Bell states. However, the teleportation protocol can also be used to produce the operation of the Hadamard and CNOT.

1.3 Optical quantum information processing

The previous section outlined the general operation required for quantum information processing and although this chapter focuses on quantum computation, its clear that the processes of communication, computation and sensing are interlinked. DiVincenzo

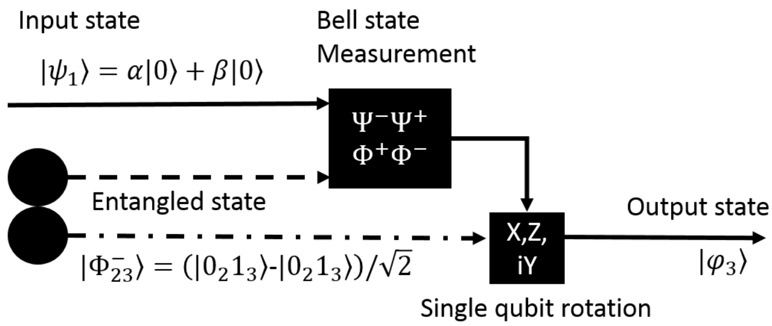

FIGURE 1.2: The conceptual operation of teleportation summarising equation 1.18. An input state $|\psi_1\rangle$ is telported to bob by the use of a shared entanglement resource. A measurement is performed by Alice in the Bell state basis on one half of an entangled state $|\Phi^+_{23}\rangle$ and the state she wishes to teleport $|\psi_1\rangle$. The outcome of this measurement is then used to apply the correct single qubit rotation to the teleported state $|\phi_3\rangle$ required to return the initial state [16].

determined the suitability of a particular architecture quantum computing using a set of criterion [15], the most important of which are a set of two-qubit gates. Finding a system which fulfils the DiVincenzo criteria for scalable quantum computing leads us to the question of utilising optics for this purpose [15, 18]. The lack of system decoherence to the environment makes optics highly desirable as a means to store qubits and since classical communication channels are based on optics this becomes another motivator for the exploration of an optical means for performing quantum computing or communication.

1.3.1 An optically encoded qubit

Using photons as the particle upon which to encode a qubit gives a wide range of encoding options. Photons have the advantage of extremely low decoherence but equivalently they do not easily interact with one another. Qubits can be encoded in time-bins (photon arrival times) and this is a desirable protocol, for instance if one wishes to distribute multiple qubits across a single spatial mode [19]. As in classical communication channels photon frequency can be used to encode information [20]. Qubits and in fact "qudits", generalisations of encoding in more than two distinct levels (such as $|\mathbf{0}\rangle$ and $|\mathbf{1}\rangle$) but rather d distinct levels, can be enabled by encoding in transverse spatial modes of the photon [21]. Such an encoding scheme is highly desirable as classical mode multiplexing techniques in optical fibre are becoming a key technology capable of overcoming current classical communication bandwidth constraints [22]. Demonstrations of such encoding schemes show exceptional promise for quantum communication. Carpenter *et al.* have demonstrated both quantum and classical channels encoded in different modes of the same fibre [23], while Goyal and Konrad have proposed a teleportation protocol for qudits [24]. Although these methods show great promise, the bulk of work performed to date exploits either a polarisation encoding or a path encoding scheme. However, it must be noted that regardless of the particular method used to encode the information onto the particle all of these encoding methods are equivalent, and conversion from one scheme to another is possible.

To demonstrate this, first consider a qubit encoded in the polarisation of a photon. The horizontal polarisation corresponds to $|\mathbf{0}\rangle$, $|\mathbf{0}\rangle \rightarrow |H\rangle$, while the vertical polarisation corresponds to $|\mathbf{1}\rangle$, $|\mathbf{1}\rangle \rightarrow |V\rangle$. Single qubits are now described by $|\psi\rangle = \alpha|H\rangle + \beta|V\rangle$, with $|\alpha|^2 + |\beta|^2 = 1$, single qubit gates now correspond to waveplate rotations, with a hadamard gate now represented by a half waveplate at an angle of 45 degrees. We could convert this encoding system to spatial mode encoding by simply using a polarising beamsplitter, which would separate the $|H\rangle$ and $|V\rangle$ components into distinct spatial modes where the presence of a photon in one mode corresponds to a $|\mathbf{0}\rangle$ and the presence of a photon in the other mode corresponds to a $|\mathbf{1}\rangle$. In fact, by using an unbalanced Mach Zehnder interferometer it is possible to convert polarisation or spatial encoding to time-bin encoding (and vice-versa) [25, 26]. Time bin encoding photons involves encoding the logical states in the arrival time of one photon with respect to another. Furthermore, transverse spatial mode encoding is possible using a scheme such as that described by Carpenter *et al.* which uses a spatial light modulator to implement complex phase distributions on an incoming light field [27].

1.3.2 Linear optical quantum computing

An initial proposal for quantum information processing (QIP) utilising photons came from G. Milburn in 1989 in a proposal to implement a Fredkin gate [28]. This is a universal logic gate consisting of 3 bits, which swaps the final two bits if the first bit is set [29]. Unfortunately, the requirement of a nonlinear coupling between optical modes which contain only a few photons makes this proposal unfeasible. Two qubit gates are a key requirement in the Di Vincenzo crieria for scalable quantum computing and the lack of a photon-photon mediated interaction meant that optics would be eliminated as a possible means of forging a quantum computer.

Gottesman and Chuang devised a protocol for forming a two qubit gate by using teleportation and exploits multiple entangled states, such as GHZ states, to perform computations [17]. Experimental efforts sought to exploit the ease of manipulation of the polarization degree of freedom of photons as qubits to demonstrate grovers search algorithm [30–32]. However, these schemes required an exponential increase in resources with circuit size therefore limiting the range of demonstrations. However, in 2001, a landmark paper by Knill, Laflamme and Milburn [33] (KLM) outlined a means to perform efficient quantum computing using only linear optical elements. This built on the concept of only requiring single qubit operations to form a circuit when they are combined with projective measurement. In this proposal the nonlinear phase shift, or nonlinear sign (NS_x), required for a two-qubit operation was achieved through a measurement induced nonlinearity where projective measurement, combined with the two photon interference, described in section 1.1, result in a probabilistic but heralded gate operation. The NS_x described in their paper is shown in Fig. 1.3 and the operation of this sign shift gate is to produce a sign change on one mode, $\alpha_0|0\rangle + \alpha_1|1\rangle + \alpha_2|2\rangle \rightarrow$

$\alpha_0|0\rangle + \alpha_1|1\rangle - \alpha_2|2\rangle$. The operation is achieved by using two ancilla modes, one of which contains a single photon. The combination of beamsplitters can be used to form a unitary operation, in this case,

$$U = \begin{pmatrix} 1-\sqrt{2} & \frac{1}{\sqrt[4]{2}} & \sqrt{\left(\frac{3}{\sqrt{2}}-2\right)} \\ \frac{1}{\sqrt[4]{2}} & \frac{1}{2} & \frac{1}{2}-\frac{1}{\sqrt{2}} \\ \sqrt{\left(\frac{3}{\sqrt{2}}-2\right)} & \frac{1}{2}-\frac{1}{\sqrt{2}} & \sqrt{2}-\frac{1}{2} \end{pmatrix}. \tag{1.22}$$

This unitary transforms creation operators acting on the photon number subspace,

$$\begin{aligned} \hat{a}_1^\dagger &\to (1-\sqrt{2})\hat{b}_1^\dagger + \tfrac{1}{\sqrt[4]{2}}\hat{b}_2^\dagger + \sqrt{\left(\tfrac{3}{\sqrt{2}}-2\right)}\hat{b}_3^\dagger \\ \hat{a}_2^\dagger &\to \tfrac{1}{\sqrt[4]{2}}\hat{b}_1^\dagger + \tfrac{1}{2}\hat{b}_2^\dagger + \left(\tfrac{1}{2}-\tfrac{1}{\sqrt{2}}\right)\hat{b}_3^\dagger, \end{aligned} \tag{1.23}$$

where $\hat{a}_i^\dagger$ and $\hat{b}_i^\dagger$ correspond to the creation operators acting on the input and output modes. The gate therefore transforms the input state $|2_1 1_2 0_3\rangle$,

$$\begin{aligned} \hat{a}_1^\dagger\hat{a}_1^\dagger\hat{a}_2^\dagger|0_1 0_2 0_3\rangle &\to \eta_1\hat{b}_1^{\dagger 3} + \eta_2\hat{b}_2^{\dagger 3} - \eta_3\hat{b}_3^{\dagger 3} + \eta_4\hat{b}_1^\dagger\hat{b}_2^{\dagger 2} + \eta_5\hat{b}_1^\dagger\hat{b}_3^{\dagger 2} \\ &\quad -\eta_6\hat{b}_2^\dagger\hat{b}_3^{\dagger 2} + \eta_7\hat{b}_1^{\dagger 2}\hat{b}_3^\dagger - \eta_8\hat{b}_2^{\dagger 2}\hat{b}_3^\dagger + \eta_9\hat{b}_1^\dagger\hat{b}_2^\dagger\hat{b}_3^\dagger - \eta_{10}\hat{b}_0^{\dagger 2}\hat{b}_1^\dagger|0_1 0_2 0_3\rangle \\ &= \eta_1|3_1 0_2 0_3\rangle + \eta_2|0_1 3_2 0_3\rangle - \eta_3|0_1 0_2 3_3\rangle + \eta_4|1_1 2_2 0_3\rangle + \eta_5|1_1 0_2 2_3\rangle \\ &\quad -\eta_6|0_1 1_2 2_3\rangle + \eta_7|2_1 0_2 1_3\rangle - \eta_8|0_1 2_2 1_3\rangle + \eta_9|1_1 1_2 1_3\rangle \ \overset{\textit{postselect}}{\cancel{-(\eta_{10}|2_1 1_2 0_3\rangle)}}, \end{aligned} \tag{1.24}$$

where η_i are the probabilities for a specific output state and $\sum_{i=1}^{10}|\eta_i|^2 = 1$. The post selection occurs when the state $|2_1 1_2 0_3\rangle$ is detected by measuring a single photon in mode 2 and zero photons in mode 3 which indicate that the gate has operated correctly, producing a sign shift on one mode. This occurs with a probability $|\eta_{10}|^2$ which for this gate is 1/4. Furthermore by concatenating a pair of these NS gates a conditional sign flip (CZ) can be produced with a probability of 1/16.

Implementation challenges

After the publication of this paper the challenges of actually implementing these NS gates became obvious. Practical issues which either reduce or remove the ability to herald circuit operation are due to combinations of inefficient qubit preparation, system loss, number resolving detection (the ability to distinguish between 1 or more photons) and dark counts. To elaborate, if we look at the terms in Eq. 1.24 that are eliminated when postselection occurs, the term $\eta_4|1_1 2_2 0_3\rangle$, with 2 photons in mode 2, or $\eta_2|0_1 3_2 0_3\rangle$, with 3 photons in mode 2, will produce a "count", or detection event, that without number resolving detection will not be distinguishable from the desired single photon count in mode 2 as in term $\eta_{10}|2_1 1_2 0_3\rangle$. These are obviously erroneous events and in this case would occur with a probability of $|\eta_2|^2 = 0.12$ and $|\eta_4|^2 = 0.06$. Single photon detectors also produce *dark counts*, unintended counts, which will mean that an efficiency reduction can be caused by falsely measuring photons in mode 3,

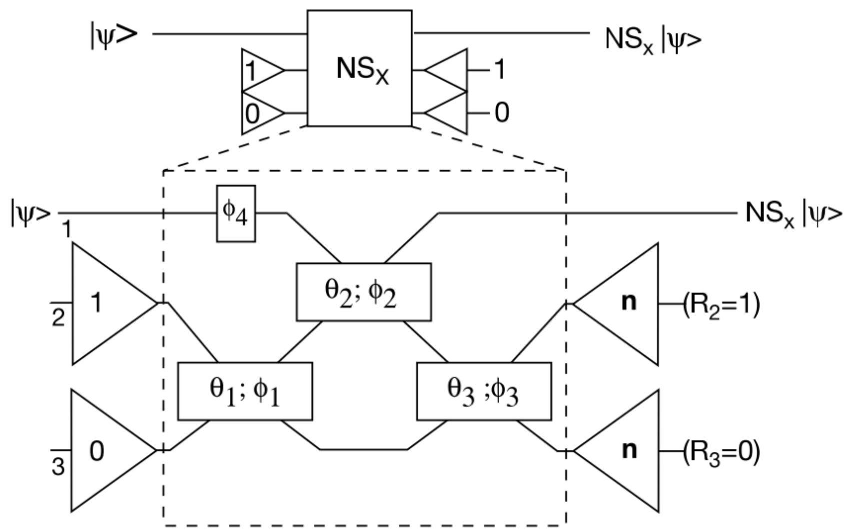

Figure 1.3: The layout of the NS_x gate where the value of x corresponds to the desired phase shift induced on the state $|\psi\rangle$ and is achieved by setting the beamsplitter angles (θ and ϕ), which define the reflectivity of the beamsplitters through $e^{i\phi}\cos(\theta)$ [33].

therefore discarding otherwise successful $\eta_{10}|2_1 1_2 0_3\rangle$ events. Even worse is if no photon is measured by a detector in mode 3 but a dark count registers in mode 2, such as for term $\eta_1|3_1 0_2 0_3\rangle$, meaning that an event, caused only by detector ineffectiveness, will be counted as successful. Furthermore, system loss occurring after the circuit, but before (or within) the detection apparatus, may cause terms with a single photon in mode 2 and mode 3 to be counted as a successful events if the photon in mode 3 is lost. Alternatively loss in mode 3 combined with a dark count in mode 2 would also result in a false result. Finally, unless photons states can be deterministically prepared, this will also result in errors due to the fact that most photon detection apparatus cannot distinguish between one or more single photons in a single photons in a given arrival time.

Since the specific scheme described by KLM was not practical with lossy systems, imperfect photon sources and detectors, a series of more realistic proposals and demonstrations followed. In the previous section it was outlined how a unitary operation could be applied to a set of optical modes in order to probabilistically produce an output state [33]. It had been shown by Reck *et al.* that any arbitrary unitary could be produced using beamsplitters (2 input/output devices) and phase shifters [34]. However, it is not trivial to determine what unitary operation, feasible with linear optic components, can produce a single output state (from the many possibilities) both effectively, considering imperfect detection, and efficiently [35–38]. Knill proposed a CZ gate, operating with ancillas and an efficiency of 2/27 and Lund *et al.* provide an overview of other methods used to produce CZ gates [36, 38]. Proposals to produce CNOT gates utilising the nonlinear sign gate evolved from the work of KLM to develop an implementable protocol [35, 37]. A demonstration of a CNOT gate utilising a pair of qubits and a single ancilla mode containing one photon was performed by Pittman *et al.* [39] and followed by a more elaborate device based on the proposal of Ralph *et al.* [37] capable of producing all four entangled Bell states (see Eq. 1.16 and Eq. 1.17) [40]. This circuit utilised a pair of calcite prisms as the means of translating polarisation state encoding into path (a Jamin-Lebedeff interferometer). The benefit of this approach is that a minor displacement of either prism effects both spatial modes simultaneously meaning that despite inherent instability of the bulk optical setup, the relative displacements can be cancelled. This process, though effective, was superseded by an elegant approach which uses *partially* polarising beamspitters (PPBS). These devices have a polarisation dependent reflectivity which means that with a single component an operation on both modes of the qubit can be performed. They were exploited by Langford *et al.* to produce a compact CZ gate [41]. However, despite the ingenious methods used to produce entangling optical gates such as the CNOT and CZ it is clear that for a significant increase in circuit complexity a different method other than bulk optical components would be required.

1.4 Integrated quantum photonics

With the groundwork theory of linear optical quantum computing (LOQC) initiated in 2001 and several bulk optic implementations developed over the next six years, the question of practicality became quite obvious. An optical table thick with beam spitters, phase shifters and mirrors does not approximate a practical quantum computer. Furthermore, the limit of complexity of bulk quantum circuits was also being approached due to the challenge of stabilising multiple nested interferometric devices. This led to a ground breaking paper by Politi *et al.* in 2008 [42], which detailed a CNOT gate using path encoded photons [43, 44] in waveguides on a silica-on-silicon chip. This device leveraged a lithographic platform matured through decades of integrated photonic device fabrication. Optical modes were confined within waveguides and bulky beamsplitters were replaced by a directional coupler (two waveguides brought closely together so their fields overlap and exchange energy). Essentially the initial step toward a miniaturised and integrated quantum device had been taken. Although the photon source and detection system remained large and bulky devices, metres of optical bench had been reduced to several millimetres, with the added benefit of near complete environmental isolation.

1.4.1 Integrated optic platforms

A variety of methods exist which can produce waveguide devices but the ultimate goal remains the same, to confine light. More detail on optical waveguide theory is contained in pppendix A and chapter 2. Multiple methods to confine light exist but the simplest is the optical waveguide which is formed by a region of higher refractive index than that of the surrounding material. This structure guides light along a higher index core by the process of total internal reflection. Exotic structures, such as plasmonic circuits or photonic crystal waveguides guide light by a different method and offer some highly desirable properties. Plasmonic waveguides offer subwavelength confinement, operating by the coupling of the photon energy to a free electron gas at the interface of a dielectric and a metal, but unfortunately exhibit high transmission loss [45, 46]. Photonic crystal waveguides offer confinement based on a photonic bandgap. This originates from a periodic modulation of the potential causing a splitting of the energy bands meaning that no propagating wave solutions can be found in the region. Photonic crystal waveguides offer the possibility to uniquely engineer waveguide dispersion characteristics, a desirable property when producing photons through nonlinear frequency conversion processes [47, 48].

Most of the integrated circuits used for quantum information science (QIS) have exploited a refractive index contrast between the waveguide and bulk to confine light by total internal reflection. The fabrication schemes of planar lightwave circuits (PLC) vary but typically include application of a photoresist to a substrate material combined with an illumination under ultraviolet (UV) light and a mask, thus imprinting a "negative" (or "positive") image of the desired circuit structure. Subsequently the substrate is etched, removing (or preserving) the exposed section, revealing the stucture of the waveguide circuit. Ridge waveguides operate by the index contrast of the material with air, which is extremely high (for GaAs and GaP $n > 3$) and mode sizes as small as 150-250 nm are possible for index contrasts of 1-3 and waveguide diameters of 300-400 nm at wavelengths of 800 nm [49, 50]. However, due to sidewall roughness contributing to significant losses, these ridge waveguides are often surrounded by a cladding material such as silica. Silicon has a refractive index of 3.4 and is transparent in the infrared (IR) making it an attractive material as a photonic interconnect. These properties make it an excellent candidate for quantum optical technologies. Silicon-on-insulator (SOI) and silicon oxynitride have been core material platforms for the design of multiple integrated circuits for quantum information science. Demonstrations of algorithms have been enabled using this technology [51, 52]. Furthermore quantum walks and multiphoton interactions have been engineered in this platform [53, 54], and reconfigurable single and two-qubit interactions [55–57]. A fully integrated photon generation and manipulation facility has been demonstrated on an SOI photonic chip [58]. The potential for circuit scaling using the SOI technology is interesting but still needs a large number of adaptations to be truly CMOS compatible [59–61]. Other technologies such as lithium niobate offer a range of useful features, such as high speed electro-optic modulation and large second order optical nonlinearities. The nonlinear properties have been exploited for integrated photon pair generation and for high speed switching of entangled photon states [62, 63]. Furthermore there has been a recent demonstration of photon generation and manipulation in a monolithic integrated circuit [64]. On-chip photon detection has been demonstrated in both circuits in GaAs [65, 66] and lithium niobate [67].

1.4.2 Femtosecond laser direct write technique

Although there has been progress in developing integrated photonic circuits for quantum information and crucial circuit elements have been produced in isolation and in monolithic demonstrations, there is still a number of challenges in integrated quantum photonics (IQP). One of the overall challenges facing the field is the availability of photon sources and detection capabilities which must be interfaced with prototype circuits. Many bulk optical photon sources operate at 800 nm and are then coupled into waveguide circuits to perform characterisations. These circuits therefore would ideally be transparent at 800 nm and have a mode size closely matched to that of a single mode fibre. This is one of the current failings of using silicon waveguide circuits. The small mode size means large input and output coupling losses which therefore increase experimental duration. Furthermore, lithographic fabrication requires a photo mask for each new circuit design. This means that if a circuit design parameters need to be tweaked very slightly, an entirely new mask must be fabricated which is labour intensive.

The femtosecond laser direct-write (FLDW) technique (described in detail in chapter 2) uses a laser to produce refractive index change in glass. This technique allows one to draw a circuit without a photo-mask and therefore rapidly adjust and prototype circuit designs. This technique was initially applied to path encoded qubits by Marshall *et al.* showing that laser written circuits could offer equally high two-photon interference visibilities as their lithographically produced counterparts [68]. Subsequently, Sansoni *et al.* demonstrated that these circuits could also be used for photons encoded in polarisation [69]. This was subsequently incorporated with a demonstration of a partially polarising directional coupler to form a CNOT gate for polarisation encoded qubits [70]. A further demonstration of integrated optical waveplates has shown the potential of producing polarisation encoded circuits [71, 72]. Experiments have exploited an alternative UV laser writing method to form circuits for quantum information and have shown phase control and on-chip photon number resolving detection [73–75]. The FLDW technique also permits a truly 3D capability and initial demonstrations have included multiport beamsplitters and quantum walk devices [76–78]. Futher investigations of the 2 dimensional arrays possible using the FLDW technique has led to investigations and simulations of single and two-photon correlations in waveguide arrays [79–84]. Furthermore a range of circuits have been fabricated in florescent glass which permit the direct visualisation of the propagation of light in such structures, an otherwise extremely challenging feature to recreate [85–87]. The convenience of the rapid prototyping of laser written waveguide arrays has also permitted the design of structures exhibiting uniform distribution and complex disorder patterns for the observation of Anderson localisation and Bloch oscillations [88–90]. Finally, interest in boson sampling has motivated a range of waveguide arrays for the exploration of mutiphoton unitary sampling [91–93].

1.5 Sources of optical qubits

Though alternative methods of photon production exist, the spontaneous process of photon pair production in a nonlinear media is the method that was utilised during this thesis. In this section an explanation of the production process and the implications this has on QIP experiments is outlined. This section is by no means exhaustive and the reader is referred to two reference texts for a more detailed discussion of the concepts outlined here, [94, 95]. Any mediums dielectric polarisation, P (dipole moment/unit volume) has, in addition to a linear response to an electric field E, a nonlinear response and this can be expanded in a power series,

$$\mathbf{P} = \epsilon_0 \left(\chi^{(1)} + \chi^{(2)}\mathbf{E} + \chi^{(3)}\mathbf{E}^2 + ...\right)\mathbf{E}. \tag{1.25}$$

This equation is a simplification since the dielectric polarisability is a tensor product but importantly shows the nonlinear response of a material depends on the nonlinear susceptibility $\chi^{(i)}$ which, for materials without a centre of inversion such as crystals, is dependent on $\chi^{(2)}$ and a function of the square of the electric field. The equations 1.1 and 1.2 define the phase matching conditions for the conservation of energy and momentum in spontaneous parametric downconversion. In fact, this also occurs over a range of frequencies determined by the bandwidth of the pump laser and the refractive index of the material, which for a birefringent crystal, depends on the optical axis of the crystal. To understand this a definition of the phase matching condition can be written as,

$$\Delta k = k_p(2\omega_0) - 2k_{s,i}(\omega_0), \tag{1.26}$$

where p, s and i refer to the pump, signal and idler fields respectively. The phase accumulated during a passage through a nonlinear material is given by,

$$\Delta\phi = \Delta k L, \tag{1.27}$$

where the value $\Delta\phi = \pi$ defines the coherence length, or the maximum length over which an nonlinear process can occur efficiently. A two photon state can written as:

$$|\psi\rangle = \frac{1}{\sqrt{2}}\int_0^\infty d\omega_1 \int_0^\infty d\omega_2 \Phi(\omega_1,\omega_2)\hat{a}^\dagger_{s,\omega_1}\hat{a}^\dagger_{i,\omega_2}|\text{vac}\rangle \tag{1.28}$$

with the creation operators satisfying $\left[\hat{a}_{n\omega}, \hat{a}^\dagger_{m\omega'}\right] = \delta_{n,m}\delta(\omega-\omega')$, the subscripts n, m are used to define different modes of the two frequencies ω, ω' (if required) and the "biphoton" wavefunction $\Phi(\omega_1,\omega_2)$ is normalised so that $\int_0^\infty d\omega_1 \int_0^\infty d\omega_2 |\Phi(\omega_1,\omega_2)|^2 = 1$. It is also significant that $\Phi(\omega_1,\omega_2)$ is not factorisable, meaning that different frequencies can share correlations. If a narrow pump bandwidth is used, as is the case for a continuous wave (CW) pump, then $\Phi(\omega_1,\omega_2)$ can be selected using narrow filters. Since photon pair production is inherently a spontaneous process, the time window over which it can occur can be reduced by using a pulsed laser with a large duty cycle. Pulsed femtosecond lasers with duty cycles on the order of 10^{-7} mean that although the nonlinear process is still spontaneous, the probability of finding a photon in a given time window is limited to the coherence length of the laser pulse. This means that for short pulse duration pump laser filters must be used to select only the central frequency band of the generated photons. In the case where filters are used the frequency correlations of the transmitted photons reduce to the CW case [94].

Making the single mode assumption an interaction Hamiltonian can be used to describe the production of a signal and idler photon (following reference [94]),

$$\hat{H}_{\text{Int}} = i\hbar\chi\hat{a}_s^\dagger\hat{a}_i^\dagger + H.c., \tag{1.29}$$

where $\hat{a}_{s,i}^\dagger$ is the creation operator and the χ term defines the pump interaction with the medium. The state undergoes unitary evolution so,

$$|\psi(t)\rangle = \hat{U}(t)|\psi(0)\rangle = e^{-\frac{it}{\hbar}\hat{H}_{\text{Int}}}|\psi(0)\rangle = e^{\eta\hat{a}_s^\dagger\hat{a}_i^\dagger - H.c.}|0\rangle \tag{1.30}$$

where $\eta = \chi t$ and this equation describes a two mode squeezed state. For the case where this is operating below threshold as a spontaneous process,

$$|\psi(t)\rangle \approx (1 - |\eta|^2/2)|0\rangle + \eta|1_s1_i\rangle + \eta^2|2_s2_i\rangle + ..., \tag{1.31}$$

meaning that, since η is very small, there is a very high probability of no interaction between the pump and the medium, yielding vacuum. However, there is a small probability of producing a pair of photons $|\eta|^2$ and a non-vanishing probability of producing multiple photon pairs. This is important because if we consider the two-photon interference which was described in section 1.1, it can be seen that significantly different behaviour occurs for two pairs of photons, $|2_12_2\rangle$, in a beamsplitter compared to a single pair, $|1_11_2\rangle$. It can be seen from the mode transformations in Eq. 1.3 that multi-pair path interference $|2_12_2\rangle$ will result in different outputs than the case of a single pair,

$$\left(\hat{a}_1^\dagger\right)^2\left(\hat{a}_2^\dagger\right)^2|0_10_2\rangle \rightarrow \left(\frac{\hat{b}_1^\dagger + \hat{b}_2^\dagger}{\sqrt{2}}\right)^2\left(\frac{\hat{b}_1^\dagger - \hat{b}_2^\dagger}{\sqrt{2}}\right)^2|0_10_2\rangle = \sqrt{\frac{3}{8}}\left(|4_10_2\rangle + |0_14_2\rangle\right) - \frac{1}{2}|2_12_2\rangle. \tag{1.32}$$

Thus the output probability of obtaining photons only in a single output mode of the beamsplitter is now no longer $|\frac{1}{\sqrt{2}}|^2 + |\frac{1}{\sqrt{2}}|^2 = 1$ but instead is $|\sqrt{\frac{3}{8}}|^2 + |\sqrt{\frac{3}{8}}|^2 = \frac{3}{4}$. Since detectors cannot distinguish between four or two photons this means that such events result in errors for quantum circuits.

1.6 Summary

This chapter has outlined the key background material required for understanding the contents of this thesis. Initially a historical account of the fundamental questions which underpin quantum optical experiments relevant to this thesis is described. Then an outline of the basic theory underpinning quantum information science is presented, regardless of the physical system used to study it. Optical quantum information science is introduced and the challenges of implementing two-qubit gates is described which is particularly relevant for the chapter 5 which details the fabrication of a heralded quantum circuit. Subsequently, the application of integrated optics to quantum information science is detailed with specific emphasis on the femtosecond laser direct write (FLDW) technique. Finally, the methods and theory of photon production is described with specific emphasis on the challenges of spontaneous parametric down-conversion (SPDC) sources. This is important background material for chapter 6 which outlines the use of SPDC sources in hybrid circuits. The next chapter will describe the fabrication of waveguide circuits using the femtosecond laser direct-write technique.

"Have you read the manual?"

Mike Steel

2 Background to integrated optics

Davis *et al.* were the first to demonstrate the modification of transparent materials using visible wavelength femtosecond lasers and produced waveguiding devices in a number of materials [96]. This was motivated by the ongoing work in UV modification of fibres/glasses for the purpose of designing passive and active components for telecommunications networks. Previously this was not explored due to the lower photon energy of the visible wavelengths. However, the availability of short pulse lasers meant the possibility of peak powers sufficient to modify materials through nonlinear processes. This process has evolved from a curiosity to a commercially viable fabrication platform. This has been demonstrated by the commercialisation of this technology by the company Translume. Furthermore, continuing interest is demonstrated by significant recent investment in companies like, Optoscribe, Nanoscribe and Femtoprint [97–99].

The fabrication process is conceptually simple. A laser focus is drawn through a glass material tracing out a localised high index light guiding core region surrounded by the bulk which acts as a cladding. This means a lightwave circuit can be fabricated with arbitrary three dimensional designs by alignment of a laser focus inside a substrate. Furthermore, this is in contrast to planar lightwave circuit manufacture exploiting, for example, flame hydrolysis and reactive ion etching fabrication methods [100]. This involves multiple steps, hence, on-the-fly adjustment or modification to fabrication parameters is not practical.

This chapter is divided into two sections, an introduction to femtosecond processing of transparent material and a description of practical fabrication processes. The first section provides a brief background of the ionisation processes which lead to absorption of laser energy in transparent materials. The exchange of this energy to the lattice and the resultant material modification is discussed in the context of glass structure. The second section outlines the fabrication constraints imposed by laser parameters such as pulse energy, pulse duration, polarisation, repetition rate and numerical aperture of the focusing objective and linear and nonlinear propagation. A background to fundamental waveguide theory is provided in appendix A and outlines waveguide theory, necessary for understanding the behaviour and properties of laser written waveguides.

2.1 Femtosecond laser direct write technique

The devices described in this thesis have all been laser inscribed using infra-red radiation in transparent materials. Thus, these materials show no linear absorption at the laser wavelength and material modification mechanisms are due to a number of nonlinear processes. The pulse duration contribution is crucial to the laser-material interaction. A brief description of the underlying material interaction and modification process is the purpose of this section. For further detailed information the reader is directed to the books [101, 102], for details on laser microfabrication and [103], for additional details on glass composition.

2.1.1 Glass composition

Glass was the material used for lightwave circuit fabrication during this thesis. The study of glass as a tool has been dated as early as 1500 BC and since the development of optical fibres in the last 50 years a range of fused silicas, with precisely defined properties have become available [104]. Understanding the underlying processes which occur when glass is modified using an ultrafast laser is challenging. This is due, at least in some way, to the fact that the specific definition of a glass is rather broad and encompasses any substance that exhibits a glass transformation behaviour [103, 105]. SiO_2, the main component of all glasses relevant to this thesis, can exist in up to 22 different states from amorphous silica to crystalline quartz. Glass transformation behaviour is illustrated in Fig. 2.1, where the transition between the volume of the material, from crystalline to amorphous, is determined by the cooling rate of the liquid melt. This is particularly insightful for laser processing of these materials since one of the processes which occurs during fabrication is heating. Hence the temperature to which the material is heated and its cooling rate will determine the subsequent density of the material. This leads to the description of a glass using the fictive temperature, T_f, model. This defines the structure of glass as that of a supercooled liquid, which has the same structure as the glass state. The fictive temperature is the temperature of the glass which has the same equilibrium state compared to that of the non-equilibrium, liquid temperature. Figure 2.1 shows the extrapolation of the lines for the glass and supercooled liquid state and the intersection points are the fictive temperature [106].

The other significant temperature values of a glass correspond to those highlighted in Fig. 2.2 which shows the viscosity versus temperature [107]. The strain (or stress) point is the temperature below which a glass can be rapidly cooled without permanently inducing stress in the material. The annealing point is the temperature above which stresses in the glass can be relieved after several minutes, the softening point is the temperature at which the glass will begin to sag under its own weight and the working point is the temperature where the glass can be deformed. The composition of glass, including small quantities of additional elements such as boron, has a significant effect

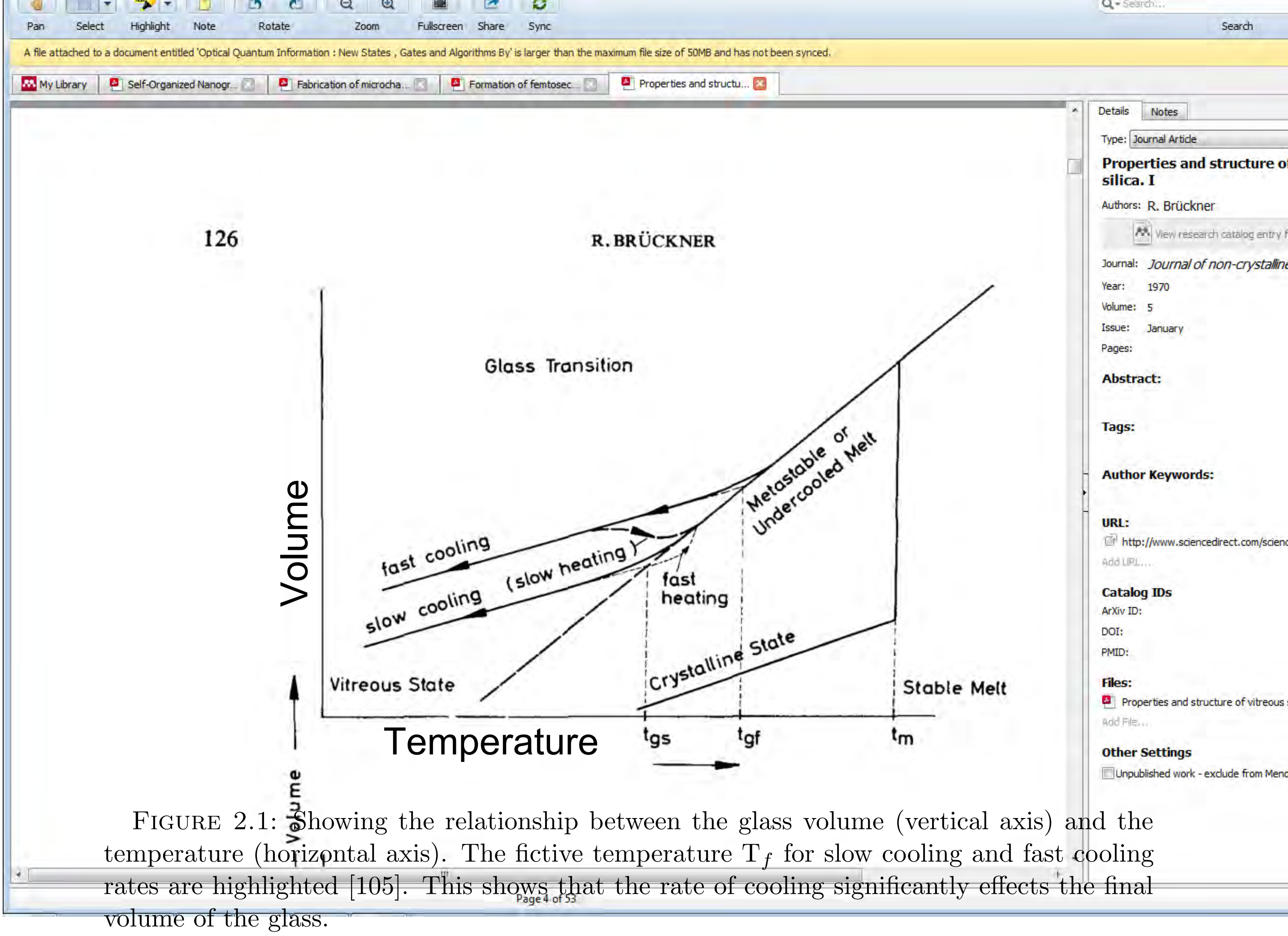

FIGURE 2.1: Showing the relationship between the glass volume (vertical axis) and the temperature (horizontal axis). The fictive temperature T_f for slow cooling and fast cooling rates are highlighted [105]. This shows that the rate of cooling significantly effects the final volume of the glass.

on the resulting glass behaviour with respect to temperature. This can be observed in Fig. 2.2, where for two different glasses, borosilicate (silica doped with boron) and fused silica, the working point temperatures values vary considerably. This fact is significant in practice because it means that, although their optical transmission properties are similar, their response to temperature differs considerably. Glass modification processes resulting from thermal processes during laser inscription of glass plays an important role in refractive index modification. This was studied by Schaffer *et al.* and the effect of cumulative heating on the size of modifications was studied [108]. This work was also explored later with a greater emphasis on waveguiding properties by Eaton *et al.* and is important in understanding the modification of borosilicate glass [109, 110]. Furthermore, the waveguides in this thesis are thermally annealed after laser processing in order to improve their guidance performance and the temperatures values in Fig. 2.2 are referred to when discussing this step [111].

Depending on the temperature of the melt at the focus of a laser and the subsequent cooling rate, the change in the glasses density can produce a refractive index change and this can therefore be both positive or negative based on the glass composition, as observed by Chan *et al.* in fused silica and phosphate glasses [112]. However, this process is not the only explanation for refractive index change since work performed by Ponader *et al.* has observed density changes, in fused silica, which are inconsistent with a fictive temperature model [113]. Hence, the next section will outline in more detail the absorption processes which occur during short (sub ps) pulse duration laser processing of glass and seek to provide further insights into the mechanism of the refractive index change.

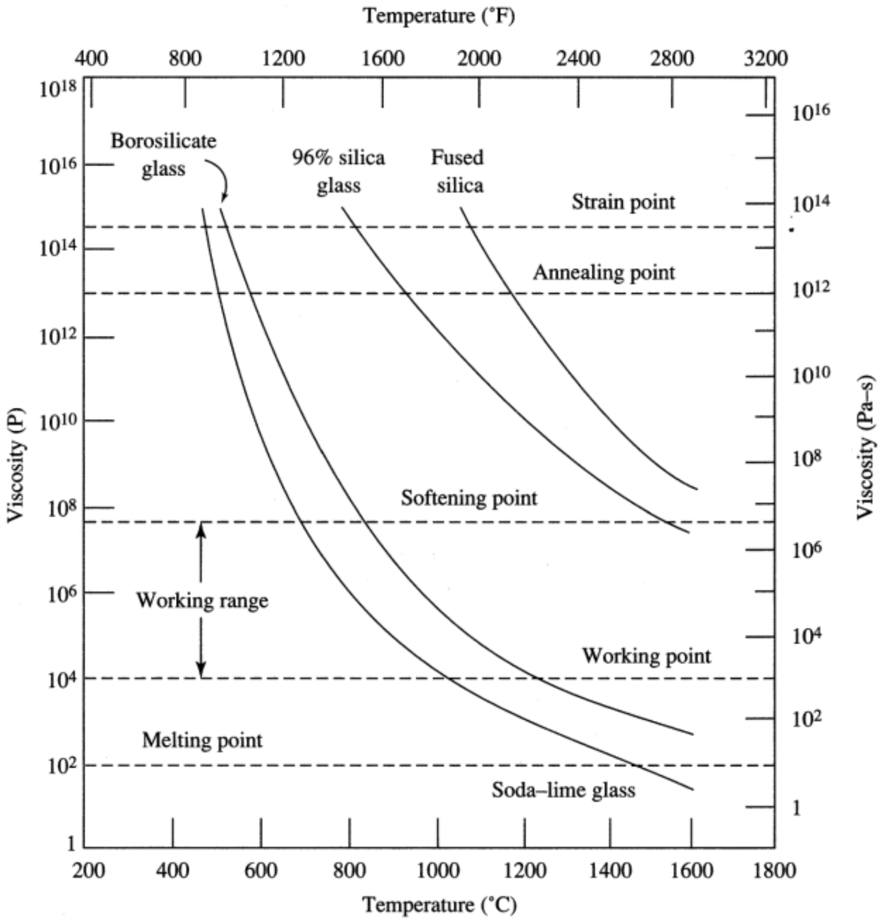

FIGURE 2.2: Showing the relationship between the glass viscosity and temperature. The significant viscosities, for different glass types, are highlighted [107].

2.1.2 Laser material interaction

Laser material modification and pulse duration are intrinsically linked through energy transfer time scales from the incident laser pulse to the material [114]. When a laser pulse strikes a material, energy is transferred from electrons to the lattice in a time scale of picoseconds. Following this, shock waves can propagate from the focal plasma in the range of nanoseconds and finally thermal diffusion occurs in microseconds [115]. Hence short pulse lasers (sub-ps) have a localised energy transfer process which occurs before the energy is transferred, through thermal diffusion, to the rest of the material. This is the basis of the small feature size attainable through ultrafast laser processing. The other crucial fundamental process occurring in transparent material, again due to the high peak powers attainable using short pulse lasers, is nonlinear absorption [116]. In transparent materials the absorption of laser energy occurs through nonlinear ionization processes where multi-photon, tunnelling and avalanche ionization can occur. These absorption processes are dependent on the intensity of the incident laser.

Multi-photon and tunnelling ionization mechanisms constitute the photo-ionisation processes responsible for energy absorption. This is the direct interaction between an optical field and dielectric which promotes bound electrons from the valence band to the conduction band. These processes can occur in isolation or in combination and the degree to which a process dominates can be described by the Keldysh Parameter [117],

$$\gamma = \frac{\omega}{e}\left(\frac{mcn\epsilon_0 E_g}{I}\right)^{\frac{1}{2}}, \tag{2.1}$$

where ω is the laser frequency, I is the laser intensity at the focus, n is the refractive index of the material, E_g is the bandgap of the material, ϵ_0 is the permittivity of free space, m and e are the reduced mass and charge of the electron. The relationship between γ and photo-ionisation processes is obtained from Eq. 2.1 where $\gamma \propto I^{-\frac{1}{2}}$. This relationship is depicted diagrammatically in Fig. 2.3 (taken from [118]) which shows that for $\gamma < 1$ (high intensities) tunnelling ionisation occurs, while for $\gamma > 1.5$ (low intensity) multi-photon ionisation dominates and between these values there is an intermediate regime where both processes contribute to ionisation. Multi-photon absorption involves N photons, of energy $h\eta$, being absorbed simultaneously and in the process overcome the energy gap E_g of the material [119]. Tunnelling can occur when the high electric field of the incident laser reduces the Coulomb potential energy barrier.

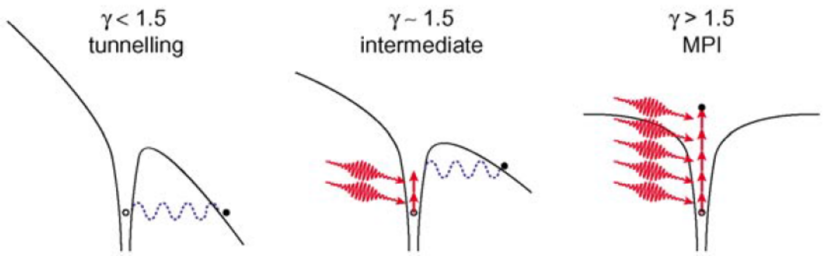

Figure 2.3: Showing the relationship between the Keldysh Parameter, γ and ionisation mechanisms [118].

At high peak powers free electrons, generated through photon-ionisation processes, act as a seed for avalanche ionization. Avalanche ionization occurs when free carriers continue to absorb energy from the incident field and transfer this energy to other electrons through collisions [120]. This process is dependent on the density of free carriers and therefore increases exponentially as an avalanche. Hence this process is a significant contributor to glass modification processes. The free carrier population, N induced by avalanche ionisation is

$$N(t) = N_0 e^{\frac{t}{\tau}}, \tag{2.2}$$

where N_0 is the initial density, and τ is the time cascade constant [120]. This equation shows the significance of photo-ionisation rates in the production of an initial density of carriers while the time dependence of the equation and the cascade time constant mean that the pulse duration of the incident laser becomes critical. At long pulse durations the free electron plasma begins to interact with the incoming beam.

2.1.3 Relaxation and modification

Once absorbed, the energy from the incident laser is then transferred to the lattice. This process, described briefly in the previous section, has been studied since shortly after the development of the laser and is quite well understood. However, the relaxation process, where the intense energy transferred to the lattice producing a material modification, is less well understood. Since the initial paper by Davis *et al.* in 1996 there have been a number of proposals which describe the fundamental processes which occur [96]. There are three mechanisms proposed which contribute individually or cumulatively to the refractive index modification process. These include: colour centre formation, thermal processes of heating followed by re-solidification with increased density, and photostructural modification involving restructuring of chemical bonds in the material [116]. Chemical bond restructuring was initially proposed by Davis *et al.*-electron spin resonance measurements showed evidence of peroxy radicals and non-bridging oxygen hole centres in laser modified regions [96]. Furthermore, work by Juodkazis *et al.* has shown a strong correlation between deposited energy and the resultant expanded volume resulting in voids at high deposited energy and enormous megabar pressures [121, 122]. This process is also strongly dependent on incident polarisation [123]. This chemical change can be accompanied by colour centre formation [124–126]. However, colour centre formation is unlikely to be the sole origin of the index change since it has been shown that the refractive index change persists even after annealing of the centres [127]. Furthermore, Dekker *et al.* quantified the colour centre contribution to the induced index change, of approximately 15%, using a Bragg grating response [128]. The change in glass density as a result of rapid cooling rates is well understood in glass manufacture processes [105]. The argument for densification in laser written glasses is supported by strong evidence from Raman spectroscopy. An increase in 3 and 4 member rings in silica structure after laser exposure has been observed [129, 130]. This process can also cause a decrease in refractive index, depending on the initial glass composition, as was observed by Chan *et al.* in phosphate glass [112]. However Little *et al.* observed that, in BK7 borosilicate glass, thermal processes also contributed to the origin of the modifications where, for a low repetition rate (1 kHz) laser, chemically induced modification was the dominating mechanism and for high repetition rates (5.1 MHz) densification was the dominant process [126]. Furthermore, these processes are dependent on a large number of competing parameters which contribute cumulatively or individually to material modification including but not limited to: glass composition, pulse duration, polarisation, repetition rate, wavelength and exposure conditions. Hence it is reasonable to assume that some or all of these effects contribute to material modification to varying degrees.

Regardless of the underlying mechanism, the resultant modifications can be broadly grouped into three categories, smooth isotropic refractive index change, birefringent formations and voids [131]. A summary of these mechanisms is shown in Fig. 2.4. At high intensities micro-explosions can form voids in the glass. These are regions of low density (the void) which are then surrounded by the expelled material which produces a denser shell as small as 200 nm in diameter [132]. The formation of self organised bubbles in glass has also been studied where a cumulative heating process produces

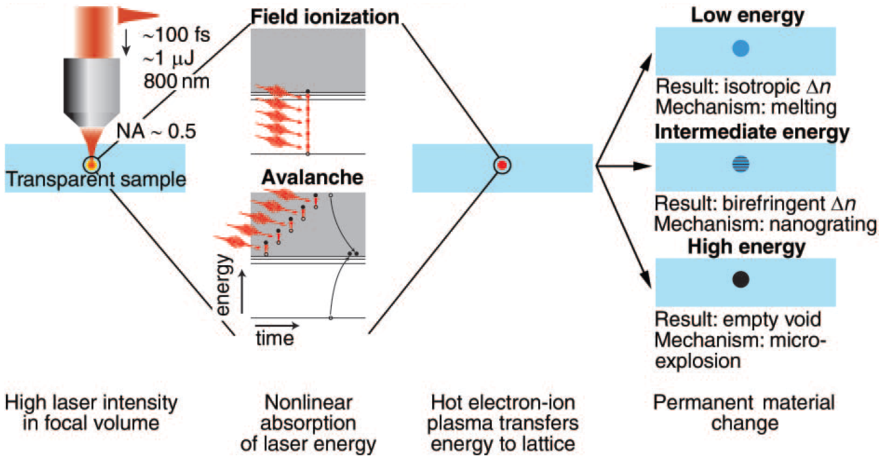

Figure 2.4: The laser processing of a glass sample and the resultant modifications; at high intensities void formation occurs, at low intensities smooth refractive index change occurs and at intermediate intensities nanoformations occur [131].

periodically spaced modulations [133]. Voids and related structures can be used for the three dimensional storage of data [134]. These structures can also be used to produce stress induced guidance in materials which do not experience positive smooth refractive index change.

At an intermediate intensity, periodic nanoformations can be observed which exhibit a large birefringence [135, 136]. These sub-wavelength structures were first imaged by Shimotsuma *et al.* [137]. These structures are periodic planes which exhibit a spacing, Λ, below the wavelength, λ of the incident laser. It has been observed that $\Lambda = \lambda/2n$ and the direction of the planes in orthogonal to the polarisation of the writing laser [138]. An image, taken from [138] (see Fig. 2.5), clearly shows the nanoplanes for orthogonal polarisations and for circular polarisation. These nanoplanes consist of periodically modulating regions of increased oxygen concentration [138]. However there is debate over the precise formation mechanism and Shimotsuma *et al.* proposed an interference of the incident laser field with the induced plasma wave [137]. However, the plasma lifetime of 150 fs is too short to interfere with the subsequent pulse. Current explanations of these processes describe a dielectric breakdown leading to nanoplasma formation which develop to form planes and then align with the polarisation of the incident laser field [138–140]. This is also supported by the formation of chiral structures within fused silica which follow the handedness of the circularly polarised laser [141]. The nanoplasma interference model is also supported by observations of a “Quill effect”, or non-reciprocal writing, where nanoplane formation is dependent on the orientation wavefront of the incoming laser beam in addition to other parameters [142]. However, these nanoplane structures are also referred to as nanocracks and nanovoids since the actual structure is not fully understood. Lancry *et al.* have noted that in fact nanovoid formation is present in laser modified zones [143]. As this is an intermediate pulse energy regime, between examinable void formation and smooth isotropic refractive index change, there is justification for assuming that the formation of nanoscale cracks or voids does occur. However, recent results have shown that the stress surrounding these features plays a dominant role in the ultimate etch rate [144]. This is supported by observable features like increased etch rates when the planes are aligned parallel to the waveguide [138]. Hence, groups have studied the development of these nanoformations using focused ion beam lithography to observe the formation of void-like structures without resorting to chemical etching [145], while other groups have exploited the cleavage planes induced by these nanoformations to avoid etching procedures [143]. Using these techniques Lancry *et al.* have shown that the nanostructures, formed by decomposition of the SiO_2 oxide, are composed of nanoporous glass with a substantially lower index of $\Delta n = -0.2$ [143, 146]. Despite the remaining uncertainties, the form birefringence and self organised subwavelength period of these structures makes them highly desirable for a range of applications [147, 148]. Building on previous work by Glezer *et al.* which uses laser inscribed nanovoids for 3D data storage [134], nanograting waveguides have been used for 5D data storage [149, 150]. The orientation of the birefringent axis and the strength of the retardance, both of which are independently controllable, provide the additional degrees of freedom. Furthermore, these structures formed within waveguides can be used for polarisation control both for bulk optic components and in integrated circuits [151–154].

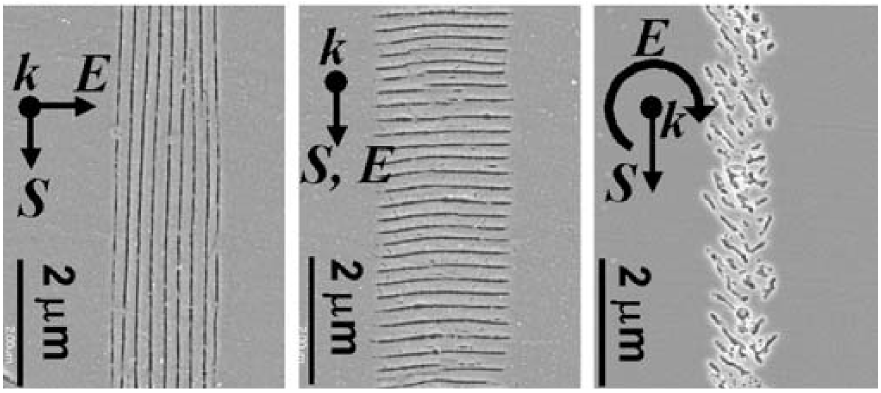

FIGURE 2.5: A scanning electron micrograph which shows nano planes formed in a glass after irradiation by laser pulses. The planes align to the polarisation direction of the incident beam and it can be seen that when circular polarisation is used the plane directions become scrambled [138].

For low pulse energies, where the resulting modification is a smooth change in refractive index, applications include waveguide formation and ultimately integrated circuit design. Both positive and negative refractive index change can be exploited to form waveguides. Waveguides can be formed using a "depressed" structure where low index modifications surround a virgin core as has been achieved using ZBLAN glass [155]. This procedure has the advantage of leaving the properties of the core guiding region completely unchanged from the bulk material. The core size can be chosen independently of the laser modification size and the size of the depressed region can be changed to optimise mode-dependent radiative loss from the structure [156, 157]. This has permitted elegant demonstrations of high slope efficiency waveguide lasers and buried Bragg grating designs [158–160]. However one drawback of this depressed method is the difficulty of producing smooth low-loss directional coupler junctions to enable evanescent coupling and form circuits [161]. Positive index change can be used to form waveguides as the laser is translated through a glass producing a high index core while the surrounding bulk acts as the cladding.

This section has detailed the underlying material changes which occur during the laser processing of glass substrates. A brief description of glass transformation behaviour was outlined followed by a basic explanation of the nonlinear absorption which occurs at the laser focus. The causes of the resultant refractive index change are outlined and an explanation of the resultant behaviour of the modified material is discussed. This assists in understanding the relevant processing parameters for the formation of positive index change is the subject of the next section.

2.2 Practical considerations

This section includes a brief description of the techniques exploited to form smooth isotropic refractive index change in glass substrates. A major contributor to waveguide formation process is the repetition rate of the incident laser which dictates the focusing conditions and ultimately determines the waveguide properties.

2.2.1 Repetition rate

Investigations into refractive index change in materials led to the discovery of two different modification regimes [109, 110]. A regime where pulse arrive successively before the thermal diffusion time of the material of $\sim 1\ \mu$s corresponding to laser repetition rates above 1 MHz, is known as the cumulative heating regime. This leads to a large heat buildup at the focus. The other regime is known as the athermal heating regime where the pulse separation is above the thermal diffusion time of the material leading to successive heating and cooling [110]. The cumulative heating process is itself a function of the laser intensity and translation speed and a threshold effect. This can be seen in Fig. 2.6, where the change from thermal to heat accumulation can be seen over a very small change in pulse energy changes both the size and modification profile of the waveguides. Furthermore, the sign of the refractive index change can be completely dependent on repetition rate [162, 163]. In the previous section it was shown in Fig. 2.2 that borosilicate glass has significantly different thermal properties to those of fused silica glass and this is one of the primary reasons for the choice of borosilicates for use with high repetition rate lasers in the cumulative heating regime.

2.2.2 Ultrafast laser fabrication techniques

In order to form a modification inside a transparent material light must be brought to a focus and the means to do so has a significant effect on waveguide morphology. This process is essentially the inverse of microscopy so many groups have exploited

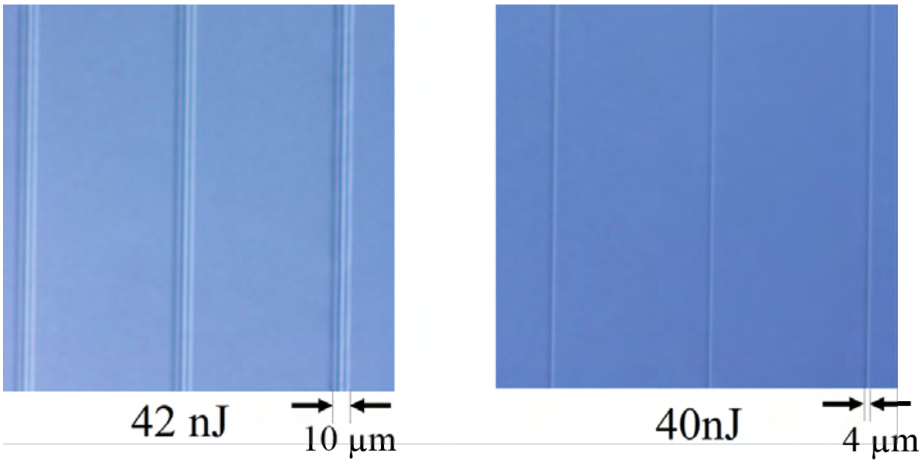

FIGURE 2.6: This image displays an optical micrograph of the top of a glass sample in which optical waveguides have been inscribed. The objective used was a 100× Zeiss oil immersion lens and the translation speeds (from left to write) were 1600, 1800, 2000 mm/min, using a single pass with a 5 MHz laser. All other parameters remained unchanged. Transition from thermal diffusion to heat accumulation as a result of different pulse energies of 40 nJ (left) and 42 nJ (right).

highly developed methods for image formation to produce waveguiding devices [164–167]. When bringing light to a focus within a high index medium, the most significant aberration is spherical aberration and changes the waveguide diameter as a function of depth within in the dielectric. This is the reason that 170 μm was a depth frequently used when writing waveguides since most objectives, designed primarily for imaging samples under a coverslip of 170 μm thickness, have correction collars to account for this. Oil immersion objectives can almost completely (depending on the refractive index of the substrate) eliminate this aberration. The numerical aperture (NA) of an objective determines the beam radius produced by a Gaussian beam,

$$w(z) = w_0\sqrt{1 + \left(\frac{z}{z_0}\right)^2} \tag{2.3}$$

where the radius is a function of z, the position from the minimum radius w_0 and the Rayleigh range z_0, the distance over which the radius increases by a factor of two. The minimum beam radius and Rayleigh range then depend on the NA,

$$w_0 = \frac{M^2\lambda}{\pi \mathrm{NA}}, z_0 = \frac{M^2 n\lambda}{\pi \mathrm{NA}^2} \tag{2.4}$$

where λ is the wavelength of light, n the refractive index and M^2 is a the beam quality factor (minimum of 1 for a Gaussian beam). These equations show that the beam radius decreases with NA^{-1} while the Rayleigh range decreases with NA^{-2}. Hence increasing the NA of an objective can increase the symmetry of waveguides.

However, in laser processing, where high intensities are achieved at the focus, linear effects are not the only cause of distorted waveguide morphologies, the nonlinear response of the material becomes significant. Since glass is an isotropic material with a centre of inversion, nonlinear propagation effects are dependent on the third order nonlinearity $\chi^{(3)}$ [168]. The result is an intensity dependent refractive index change,

$$n = n_0 + n_2 I, \tag{2.5}$$

where n_0 is the linear refractive index and $n_2 \propto \frac{2}{3}\chi^{(3)}/n_0^2$ in the nonlinear contribution to the resulting refractive index and dependent on the intensity I. The resultant index in the presence of an electric field is dependent on the intensity. Hence a Gaussian beam results in a positive lens (for positive n_2) and this process results in self-focusing. This is an undesirable effect for laser writing waveguides since this can result in filamentation and highly elliptical modifications.

During this thesis work two processes were exploited to counteract the ellipticity induced by the focusing geometry. Both approaches were tailored to the modification regime used for fabrication. The first used the athermal processing regime where the size of the modifications are linked directly to the waist of the beam. Furthermore the ellipticity is related to the Rayleigh range of the objective. Hence, though the asymmetry could be reduced by using a high NA objective the waveguide size would be small, on the scale of microns. Ams *et al.* showed it was possible to produce waveguides with a cylindrical geometry using an astigmatic beamshaping technique by expanding the beam in one direction (the direction corresponding to the cross section of the waveguide) with respect to the other using a slit [169]. This means that an NA ~ 0.5 can be used to produce symmetric structures of $\sim 3 - 5$ μm necessary for waveguide operation. Unfortunately this technique only works for a single depth due to spherical aberration and is not ideal for 3D structure formation unless adaptive slit methods are used to compensate for depth changes [170]. The slit approach also dumps the majority of the laser power. A more elegant approach is to use the astigmatic beamshaping technique exploited by Cerullo *et al.* which expands the beam in one direction using a cylindrical lens, therefore conserving all of the laser power [171, 172]. Another approach is to avoid beam shaping and simply concatenate multiple highly elliptical waveguides in close proximity thereby forming a symmetric square region of refractive index change [173, 174]. In fact this technique is highly versatile and has been exploited to produce 3D waveguide circuits in highly nonlinear glass, such as chalcogenide, which has a refractive index of $n > 2$ [175]. Beam shaping techniques have used adaptive methods such as deformable mirrors, spatial light modulators and modulating beam profiles with feedback [164, 176, 177]. Spatio-temporal focusing uses a beam that is spectrally dispersed prior to illumination on the objective and then brought to a focus within the sample. This is an approach that means low NA objectives with large working distances can be used [178, 179].

The thermal processing regime allows decoupling of modification size from the incident beam waist. Thus waveguides can be formed using high NA oil immersion objectives which produce small, highly symmetric features, while compensating for the spherical aberration. However, due to the high NA only a limited working distance of 400 μm is obtainable but within this distance highly symmetric waveguides can be obtained.

2.3 Summary

This chapter has summarised the essential information required for the understanding of the laser fabrications aspects of this thesis. The absorption of laser radiation by a glass and the resulting modification was discussed in section 2.1. This is important in the understanding the underlying mechanisms which occur during the fabrication of optical waveguides and is an important aspect to consider for chapter 3. This chapter seeks to find a regime for the fabrication of low-loss single mode waveguides for use at 800 nm material and structural changes play a role in delineating specific factors which contribute to loss. In section 2.2 practical fabrication details were outlined with an emphasis on the repetition rate of the laser since it is most relevant to parameter studies contained in chapter 3. The reason for the choice of fabrication techniques such as high repetition rate and high numerical aperture oil immersion objectives and the type of modifications they produce when compared to low repetition rate systems has also been discusses. This is an important feature that has been used for the fabrication of waveguides at high repetition rates in chapter 3. For further details on the specifics of each laser system used the reader is directed to appendix B.

Give it a red hot go, mate.

Peter Dekker

3 Towards low loss waveguides

Loss is an important parameter in any circuit design. However, for quantum information science (QIS) applications, loss is a critical factor. A fundamental principle in QIS, the no-cloning theorem, precludes the amplification of quantum data. This feature motivates interest in quantum cryptography, but it also means transmission loss is a vital parameter in circuit design. The increasing complexity of the quantum optical devices under investigation places tighter constraints on the transmission properties of the underlying waveguides and components. System losses have a dramatic effect on experimental duration, especially as the number of qubits used during analysis increases. They also tend to drive non-classical states back towards classical states with Poisson photon statistics. In addition, limitations imposed by the switching times of the fast electronics involved in heralded single photon detection and counting systems (typically several tens of ns), often necessitate the use of optical delay lines that are metres in length. If such delays were incorporated on-chip and total system losses must remain less than a few dB then propagation losses of 0.1 dB/cm or better are required. Despite the large amount of work performed in both fused silica and borosilicate glass to discover a parameter space where high throughput single mode waveguides can be formed at 1550 nm, there remains a lack of a rigorous study at the wavelength of 800 nm. This is the operation wavelength the SPDC source used for experiments in this thesis, as well as high efficiency ($\sim 60\%$) detectors. Therefore low loss single mode waveguides are essential for later experimental work.

Section 3.1 of this chapter briefly outlines constraints on circuit size imposed by the refractive index and dimensions of laser inscribed waveguides. In section 3.2 parametric studies which isolate waveguide designs used in later work are discussed. Characterisations are performed of the mode size produced by waveguide writing parameters in glass substrates including fused silica and borosilicate. A parameter space in fused silica is found where waveguides can be formed. However, in borosilicate glass a fabrication regime is isolated which is >2 orders of magnitude faster to fabricate than in fused silica. An in depth study of the waveguides formed in these borosilicate substrates is performed with specific emphasis on low-loss transmission. This work is the building block of more advanced circuit designs used in later chapters. Finally, a brief study of sub-micron periodic structures in Eagle-2000 glass is outlined.

3.1 Bend loss: constraints on circuit size

Waveguide circuits are composed of evanescently coupled waveguides which are interrogated at the input and outputs of the circuit by commercially available V-groove arrays. This means that waveguide circuits typically include waveguide bends and these have a significant effect on overall circuit transmission. The loss from a bend, γ, is a function of waveguide radius, ρ, waveguide refractive index contrast, Δn, and the radius of curvature of the waveguide [180], R_c. For a Gaussian refractive index distribution

$$\gamma = \frac{\pi^{\frac{1}{2}}}{2\rho}\left(\frac{\rho}{R_c}\right)^{\frac{1}{2}}\frac{V^4}{(V+1)^2(V-1)^{\frac{1}{2}}}e^{\left(-\frac{4}{3}\frac{R_c}{\rho}\frac{(V-1)^3}{V^2}\Delta n\right)}, \tag{3.1}$$

where $V = k\rho n_{co}\left((2\Delta n)^{\frac{1}{2}}\right)$, $\Delta n = \frac{1}{2}\left(1-\left(\frac{n_{cl}}{n_{co}}\right)^2\right)$, $k = \frac{2\pi}{\lambda}$, λ is the wavelength of light, n_{co} is the refractive index of the core and n_{cl} is the refractive index of the cladding. Recall from chapter 2 that V, the normalised frequency, defines the single mode cut off of a waveguide (V=2.405) and typical laser inscribed refractive index contrasts range from $\Delta = 10^{-3} - 10^{-2}$. Its clear from Eq. 3.1 that the loss increases exponentially with the local radius of curvature. For a simple device, such as a directional coupler, waveguides transition from an initial spacing of a V-groove array, 127 μm or 250 μm, into an interaction region spacing of $\sim$ 10 μm. This can be achieved through the use of functions which minimise the maximum radius of curvature of the function by distributing it over the largest extent of the bend.

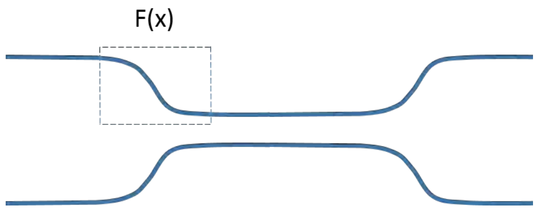

FIGURE 3.1: Diagram of a directional coupler. This is the integrated optical analogue of the beamsplitter and takes an input and splits it across two modes. In this image the curved region corresponding to a raised Sine is highlighted.

Figure 3.2 shows the effect of both waveguide diameter and refractive index contrast on the attenuation resulting from different radii of curvature for the wavelength of 800 nm. These graphs show that for the range of diameters and refractive index contrasts that we observe in laser written waveguides, there is a significant region where

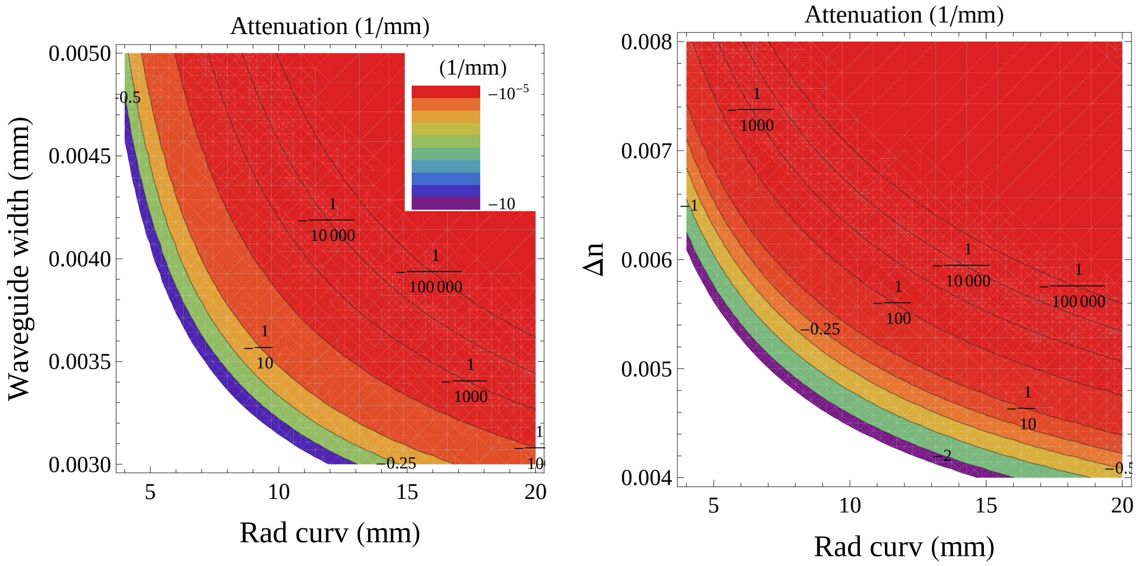

(a) (b)

FIGURE 3.2: The attenuation (mm^{-1}) for radii of curvature of bends (a) for varying waveguide diameter and a fixed waveguide refractive index contrast of 4×10^{-3} (b) for varying refractive index contrast and a fixed waveguide diameter of 2.9 μm.

low loss bends can be observed for radii of curvature $R_c > 10$ mm. Though this information is valuable in mapping out a parameter space it is important to contextualise it with an example. Figure 3.3 shows the critical parameters in designing a bend in a circuit. The function is based on a directional coupler fold in region, an "s-bend" as shown in Fig. 3.1 and the function is described by a raised sine, $f(z) = z - \mathrm{Sin}(2\pi z)/2\pi$, which gives a smooth transition from an input to an output over the length of the function z. Although this function creates a smaller radius of curvature than other functions, such as those exploiting a cosine or polynomial, it produces the most gradual rate of change of the bend. Therefore it has been shown to minimise refractive index mismatch caused by sudden changes in the effective index of the waveguide induced by the bend [181, 182]. The function can be seen in Fig. 3.3 (a) and the local radii of curvature, at each position along that function, can be seen in Fig. 3.3 (b), where the minimum radii of curvature is >10 mm. The overall transmission through this function is above 90% (See Fig. 3.3 (d)).

3.2 Parametric studies to isolate waveguide designs

Investigations of waveguide properties centred around the features of the two laser systems used for fabrication (for more details see chapter B). One laser system, the Hurricane, with a low repetition rate (1 kHz) has an optimum processing window for the fabrication of fused silica waveguides. Another, the Femtosource XL500, a high

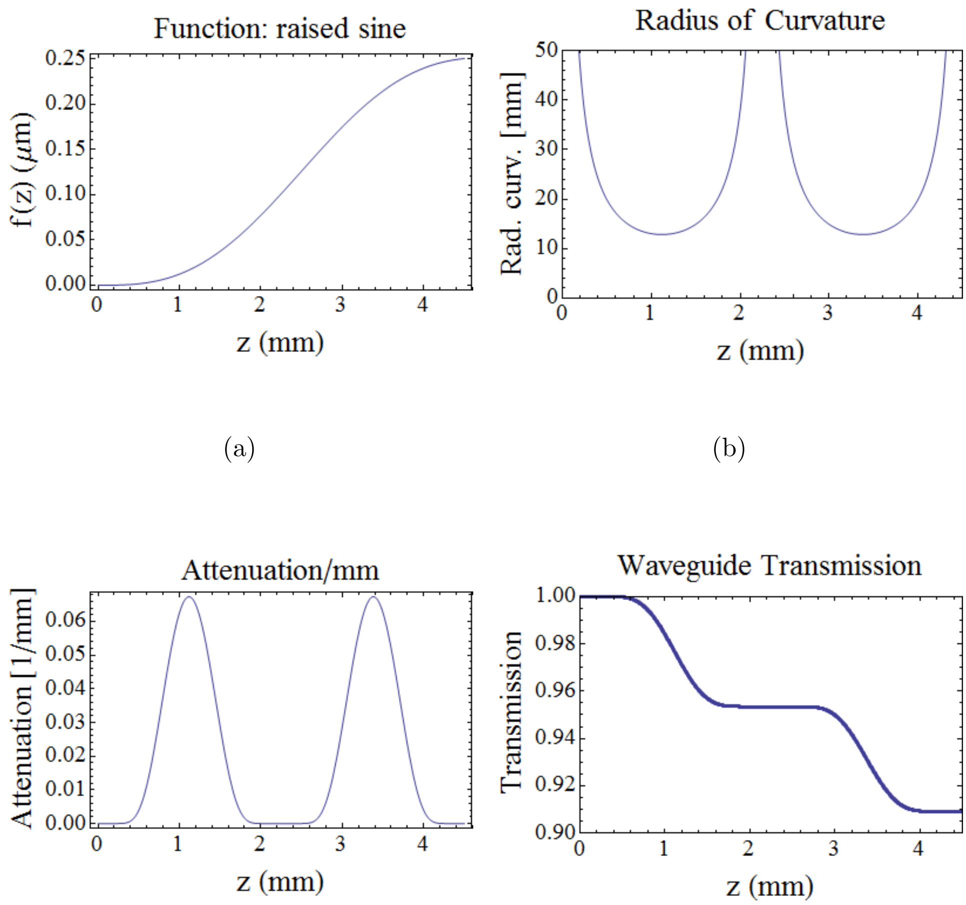

(a) (b)

(c) (d)

FIGURE 3.3: For a fixed waveguide diameter of 2.9 μm and index contrast of 4.5×10^{-3}, (a) shows a raised sine function which describes a transition from a 250 μm spacing over a length of 4.5 mm, (b) the radius of curvature at each point along that function, (c) the attenuation (mm^{-1}) at each point and (d) is the overall transmitted energy, assuming a unit input.

repetition rate system (5 MHz), was better suited for the processing of borosilicate glasses. Fused silica has desirable properties: high purity glass is readily available (such as Lithosil) and offers intrinsically low absorption, limited typically by Rayleigh scattering. By including dopants, such as the OH^- impurity (found in Suprasil), the glass can be made to fluoresce. This is advantageous because it allows the intensity distribution along a waveguide to be directly imaged [85, 183]. Furthermore, as described in chapter 2, demonstrations of waveguide based polarisation control have exploited laser induced self organised periodic nanoformations within waveguides inscribed in fused silica [152–154, 184]. These properties have motivated two studies within this chapter, high speed fabrication of fused silica and the search for a parameter space for the fabrication of birefringent nanoformations in borosilicates. A study of the modification parameters for both fused silica and borosilicate glass, with optimum processing windows for both, is contained in this section.

3.2.1 Fused silica

Due to the complexity of the circuits used in this thesis reproducibility was an important factor. Using the low repetition rate system it was possible to inscribe high throughput waveguides in fused silica. The parameter space permitting waveguides with a mode field diameter below 30 μm, but not displaying damage, is narrow (See Fig. 3.4). The low loss (<10 dB insertion loss) operation range corresponded to this region. The typical translation speeds were in the range of 1-8 mm/min and required multiple overpasses 2-8. This meant a single waveguide of 20 mm in length would require a fabrication time of 4-160 minutes. When performing a parametric study, where a circuit is composed of multiple waveguides and multiple different parameters to iterate, it becomes challenging to ensure that the laser system maintains its stability over several days of fabrication time.

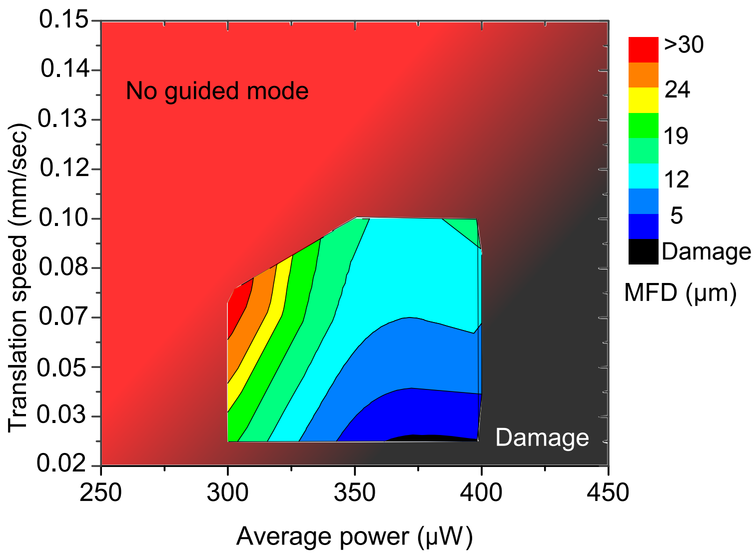

Figure 3.4: Parameter space where single mode waveguides with mode field diameters below 30 μm could be found. The dark region indicates where waveguides with significant damage could be observed with a microscope. Measurements are recorded at intervals of 50 μW and 0.01 mm/sec.

Despite reports of waveguide fabrication in fused silica using >MHz repetition rate lasers it still requires extremely low translation speeds which negate the advantage of using these laser systems over kHz repetition rate lasers [185–187]. Graf *et al.* observed that when fused silica samples are modified using high repetition rate lasers (10 MHz) pearl chaining (a periodic modulation of refractive index which resembles a pearl chain necklace) occurs resulting in high loss (6 dB/cm) waveguide formation [188]. Using

500 kHz pulse trains, high-quality waveguide formation (<1 dB insertion loss) has been observed in fused silica exploiting high energy photons (522 nm). However the translation speed of 0.22 mm/min used in that study results in extended fabrication times [152]. Fused silica shows a high working temperature (defined as the temperature at which a glass may be reshaped) of 1800°C which is 1.4 times greater than borosilicate [109]. Furthermore, it features a bandgap of 9.1 eV which is twice that of borosilicate. Hence, additional pulse energy is required for absorption and a higher temperature must be reached to achieve melting. This is the reason that the parameter space for smooth, low loss refractive index modification in fused silica is so limited. The onset of cumulative heating in fused silica appears to correspond very closely with the onset of breakdown and damage of the material even if very low pulse energies (10 nJ) combined with high repetition rates (26 MHz) are used [189].

Hence a parametric study was performed to isolate a high speed processing window using a 100 kHz repetition rate regime, which is below the cumulative heating threshold (approximately 200 kHz), where low loss waveguides could be formed. This repetition rate was obtained by using a Pockels cell to select only one out of every 50 pulses from the 5 MHz pulse train of the laser oscillator. However, the results in Fig. 3.5 show that there was a limited range of speeds above 100 mm/min where low loss (<10 dB insertion loss) waveguides could be found. Within that region the lowest measured insertion loss was 8 dB. Damaged regions were formed for translation speeds below 300 mm/min and for pulse energies above 110 nJ. For translation speeds above 600 mm/min and pulse energies below 60 nJ no observable index change could be observed. The 100 kHz repetition rate window was below the cumulative heating threshold (of approximately 200 kHz) but still remained two orders of magnitude above the Hurricane 1kHz repetition rate system. Hence it is possible that there exists a processing window between 1-100 kHz where low loss waveguides could be formed at high speeds. However, due to the limited pulse energy (max 500 nJ) available from the laser oscillator a study of this parameter space could not be performed.

3.3 Borosilicates

High repetition rate femtosecond lasers (MHz) are particularly well suited to the rapid prototyping of 3D integrated photonic circuits. Femtosecond laser oscillators have the optimal features required for the modification of borosilicates because only low pulse energies (nJ) are required when high repetition rate pulse trains (>200 kHz) are used [190, 191]. It is possible to use low repetition rate lasers to modify borosilicates [192], but by using high repetition rate systems an order of magnitude increase in waveguide writing speed can be achieved [193]. Indeed, it is possible to inscribe a quantum logic chip in a few minutes using the cumulative heating mechanisms associated with this class of laser. By comparison, the same inscription process, when undertaken with a kHz pulse rate femtosecond laser, can take days. This section will detail the high speed fabrication of waveguides in both Eagle-2000 (Corning) and in AF-45 (Schott)and the fabrication of periodic nano-gratings in Eagle-2000.

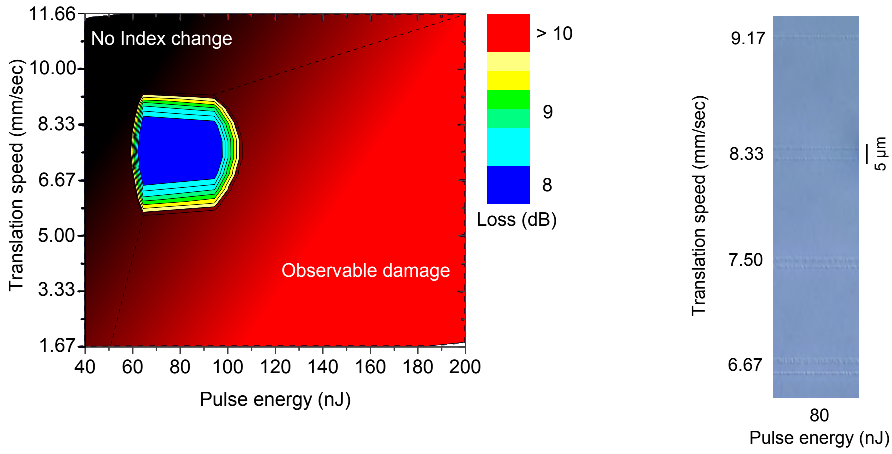

(a) (b)

Figure 3.5: (a) Parameter space where waveguide formation with insertion losses of <10 dB can be found in fused silica (Suprasil) a 100 kHz pulse train. The length of the waveguides in this study was 15.5 mm. Measurements were recorded at intervals of 5 nJ in pulse energy and 0.80 mm/sec in translation speed. (b) Transmission differential interference contrast (TDIC) microscope image showing laser modifications of a fused silica "suprasil" performed using a high repetition rate modification regime.

3.3.1 Borosilicate: high speed waveguide fabrication

Using the 5.1 MHz laser system two glasses were investigated at 800 nm, Schott AF-45 (alkali-free aluminoborosilicate) and Corning Eagle-2000 (alkaline earth boro-aluminosilicate), typically used with MHz pulse rate femtosecond lasers exploiting cumulative heating mechanisms [194]. A large range of writing powers and high translation speeds produce waveguides with insertion losses below 5 dB. The details of these waveguides will form this section.

3.3.2 Waveguide thermal treatment

The 5.1 MHz repetition rate oscillator laser (FEMTOSOURCE XL 500) was used and a 100× oil immersion objective (Zeiss N-Achroplan, numerical aperture = 1.25) focused light inside samples, which were translated using Aerotech air bearing stages. The waveguides were formed in the cumulative heating modification regime [195], in which successive pulses arrive within the thermal diffusion time of the material. The resulting waveguides feature a core region with a refractive index above the bulk glass, a surrounding "depressed" region of lower refractive index to the bulk and a region of positive refractive index (See Fig. 3.6). Following the writing process the samples were then thermally annealed, in order to produce a more symmetric and Gaussian refractive index profile. This has been shown to significantly improve insertion losses [111]. The procedure involves heating the glass above the annealing point of the material before

TABLE 3.1: Thermal characteristics of Schott AF-45 and Corning Eagle-2000 [196, 197].

Material	AF-45	Eagle-2000
Strain point (°C)	627	666
Annealing point (°C)	663	722
Softening point (°C)	883	985

slowly cooling below the strain point in order to avoid inducing any stress fields. The Eagle-2000 sample was heated to a maximum 750°C, while the AF-45 was heated to a maximum 690°C. These temperatures corresponded to a slight excess over the material annealing point (as shown in Tab. 3.1) but below the softening point of the material [196, 197].

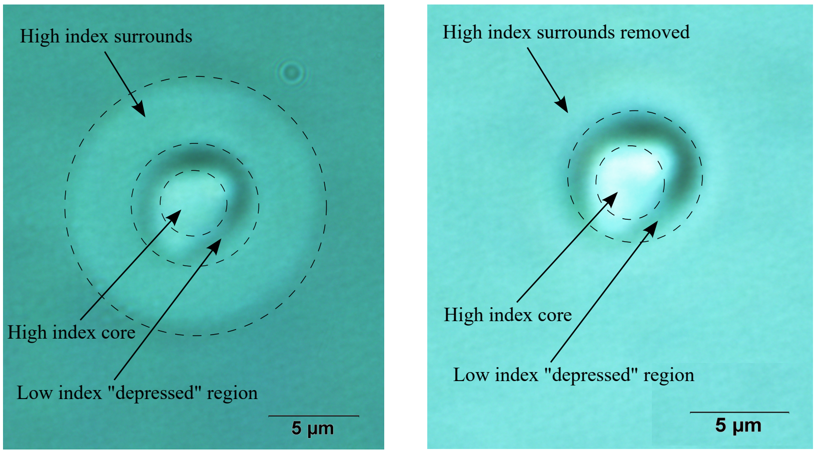

FIGURE 3.6: Microscope image of waveguides before and after annealing.

3.3.3 Mode field diameter measurements

In order to reduce system loss, it is important to isolate contributions to circuit insertion losses. These factors include propagation losses, which encompass absorption, scattering, radiation, and bend losses. However, coupling losses from fibre to waveguides, caused by a mismatch between the waveguide mode and the fibre mode, are a significant contributor to insertion loss. Thus, it is necessary to map out the range of waveguide processing parameters which give a mode field diameter (MFD) w which is well matched to a single mode fibre (SMF). An SM 800 (Fibercore) has a $w = 5.6$ μm mode at 800 nm. MFD measurements were performed by imaging the near field profile of the waveguide onto a CCD array using an objective and performing analysis using Spiricon beam profiling software. The measurements were then calibrated by measuring a 0.01 mm rule in both the horizontal and vertical directions. The second moment widths (or D4σ) are recorded. The graphs shown here all display the D4σ in the horizontal direction for uniformity.

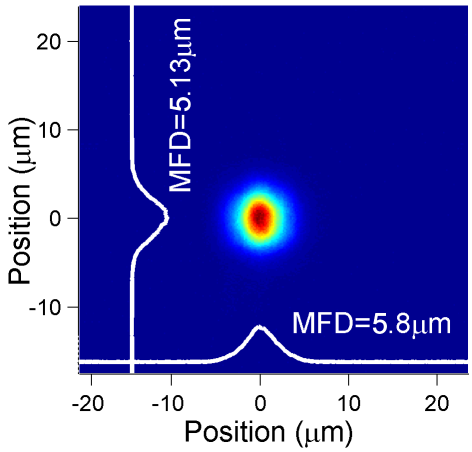

(a)

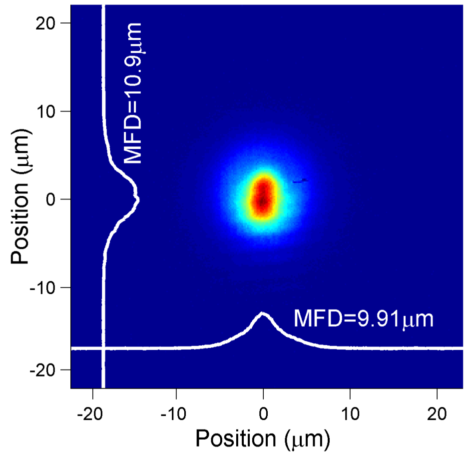

(b)

Figure 3.7: The mode field profile, at 800 nm, of a single mode fibre (left) and a single mode waveguide (right).

Fig. 3.8 shows where MFDs matched to SM 800 of 5.6 μm can be found. This is important for minimizing the coupling losses and therefore reducing the total insertion losses. Waveguides fabricated in Eagle-2000 show a large combination of translation speeds and pulse energies which produce single-mode waveguides (SMWs) with modes well matched to the corresponding SMF. This contrasts with waveguides fabricated in AF-45 (see Fig. 3.9) where a much smaller range of MFDs are obtained. A mode size below 4 μm is observed for translation speeds greater than 13.33 mm/sec, regardless of the pulse energy. Furthermore, the parameter space which yields SMWs with good mode overlap to SMFs is much narrower in AF-45 than in Eagle-2000.

These results can be explained by the two factors which define the MFD of a waveguide, the waveguide diameter and the refractive index contrast, Δn. The contour plot contained in Fig. A.1 shows the MFD of a waveguide for different waveguide diameters and refractive index contrasts. The waveguides produced in AF45 show an MFD of 3 μm for translation speeds from 33.33-10.00 mm/sec over a range of pulse energies. This indicates that the maximum obtainable Δn must be higher in AF45 than Eagle-2000. This can be seen in Fig. A.1 where a $\Delta n > 0.3 \times 10^{-2}$ is required to produce a mode of 3 μm and below. At the threshold of 10.00 mm/sec an increase in MFD occurs and for translation speeds below 5.00 mm/sec(not shown on graph) the waveguides become multimode. This indicates that the translation speeds between 10.00-5.00 mm/sec have a high V number but remain below the single mode cutoff ($V \sim 2.4$). The effect of the waveguide diameter, for fixed values of Δn, on MFD size is significant when V is between $1 - 1.7$. However, after this point the MFD does not respond to an increase in diameter (while V remains below 2.405). Hence, this implies that in the range of speeds 10.00-5.00 mm/sec the refractive index must in fact reduce. This is also accompanied by a corresponding increase in waveguide diameter as confirmed by microscope observations.

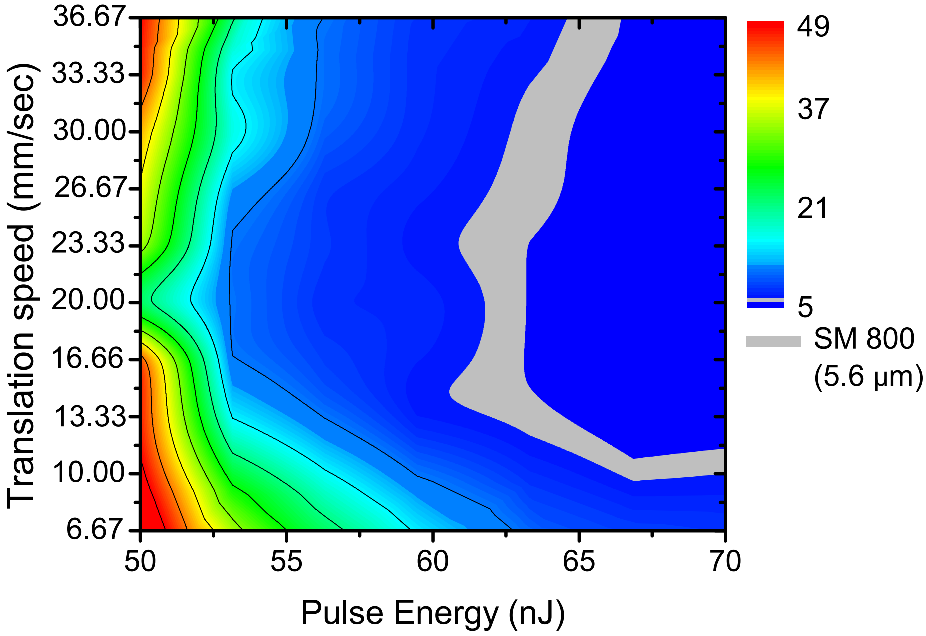

FIGURE 3.8: Eagle-2000, waveguide mode field diameter (MFD), in microns, for a range of writing speeds and pulse energies at 800 nm. Measurements were recorded at intervals of 2 nJ in pulse energy and 3.33 mm/sec in translation speed. The region in grey highlights where an MFD which is well matched to that of a single mode fibre can be found.

3.3.4 Insertion loss

To measure the total insertion loss of a waveguide, a pair of cleaved SMFs are butt-coupled to either facet of the waveguide chip. Refractive index matching oil is applied to each facet to eliminate losses due to Fresnel reflections. This measurement incorporates both coupling and propagation losses.

Figure 3.11 shows the insertion loss for 29.3 mm long 800 nm single-mode waveguide samples written in Eagle-2000 as a function of translation speed and pulse energy. This is consistent with the corresponding relationship in Fig. 3.8 between mode field diameter and writing speed, where excellent overlap between the waveguide and an SM-800 fibre mode is observed for writing speeds above 13.33 mm/sec. The same relationship is observed for waveguides in AF-45 (See Fig. 3.12) where the optimum waveguide throughput corresponds to the range in Fig. 3.9 where the waveguide MFD is most closely matched to the fibre MFD. Although the parameter space of low loss waveguides fabricated in AF-45 is smaller compared to Eagle-2000, they show a significant increase in maximum waveguide throughput. A maximum throughput of $82 \pm 2\%$ is observed in AF-45 compared with $63 \pm 2\%$ in Eagle-2000. Cut-back measurements

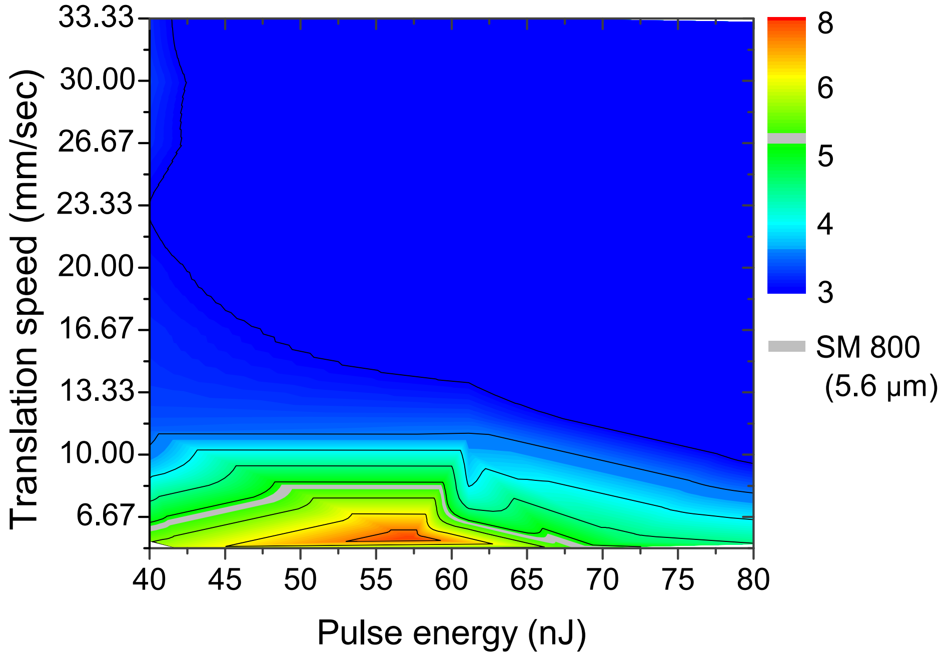

FIGURE 3.9: AF-45, waveguide mode field diameter, in microns, for a range of writing speeds and pulse energies at 800 nm. Measurements were recorded at intervals of 2 nJ in pulse energy and 3.33 mm/sec in translation speed.

were performed on SMWs at 800 nm, fabricated in AF-45, to determine the propagation loss associated with each waveguide. Figure 3.13 shows the transmission values as the AF-45 sample length was reduced from 44 mm to 30 mm and finally 15 mm in length. The total transmission for the waveguides fabricated at pulse energies of 72 and 76 nJ were relatively invariant as a function of length, in those cases corresponding to a propagation loss of 0.1 ± 0.1 dB/cm. The other waveguides, fabricated at pulse energies of 74 and 78 nJ exhibited reduced transmission as a function of length, in these cases corresponding to a propagation loss of 0.4 ± 0.1 dB/cm. Although the loss properties for the full set of waveguides (shown in Fig. 3.13) do not follow a sequential pattern they do indicate a narrow processing window where low propagation loss waveguides can be produced.

3.3.5 Propagation loss and absorption

One of the limiting factors to the transmission of waveguides written in glass substrates is the intrinsic absorption of the glass substrate. Hence understanding intrinsic material absorption places an upper bound on waveguide transmission. In fact, propagation losses in femtosecond laser written waveguides have been mostly attributed to fabrication imperfections causing strongly wavelength dependent Rayleigh scattering at short wavelengths, weakly wavelength dependent Mie scattering [198] and scattering due to

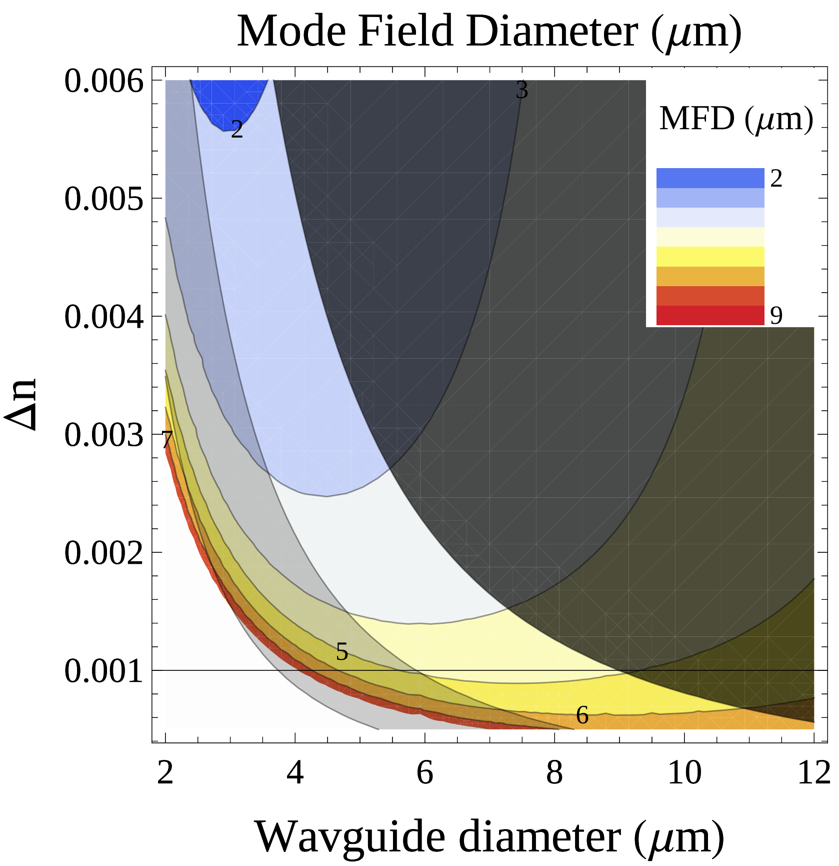

FIGURE 3.10: Reproduced from appendix B, the mode field diameter (MFD) plotted for the range of index contrasts (Δn) and waveguide diameters attainable using the FLDW fabrication method. The top right shaded region shows the single mode cuttoff ($V = 2.405$), while the bottom shaded region ($V < 1.7$) is where the majority of the mode is no longer confined in the waveguide region. Note this simulation was performed at a wavelength of 800 nm.

the finite side wall roughness at the boundaries between the bulk glass and the modified regions [199]. However, bulk absorption losses, apart from the hydroxyl overtone, are often neglected [198]. Technical glasses such as Eagle-2000 and AF-45 are not intended for guided wave applications, hence they do not provide the high purity of fused silica. To shed light on the impurity induced contribution to the waveguide propagation losses, we performed differential bulk absorption measurements with a photon spectrometer, using two glass pieces of different thickness. This avoids measurement errors induced by the uncertainty in Fresnel reflection coefficients when extracting the internal transmission values of the samples (for both glasses the data sheet only provides refractive index values for the visible spectral region [196, 197]). Figure 3.14 shows the absorption coefficient for Schott AF-45 and Corning Eagle-2000. Both glasses show an overtone of the hydroxyl ion OH^- absorption at ~1400 nm. However, a very broad absorption band centred at 1100 nm is evident in the case of Eagle-2000 but absent

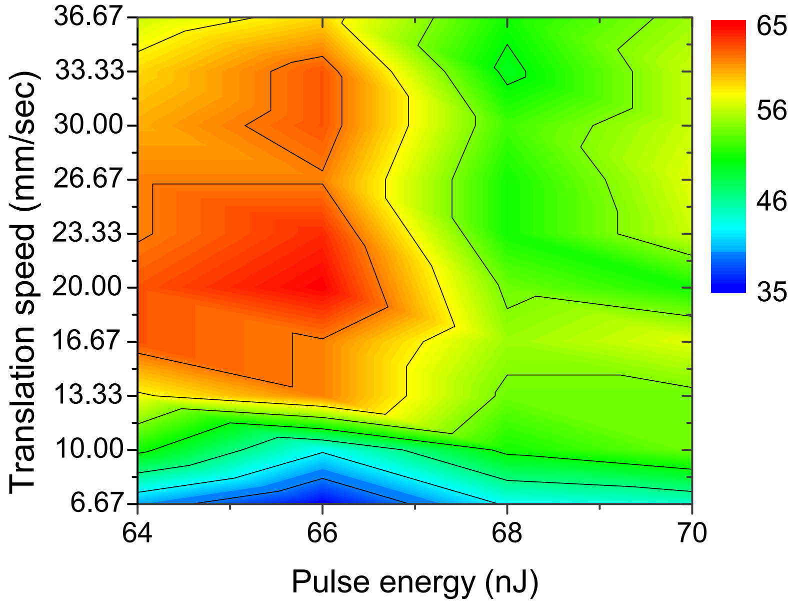

Figure 3.11: Dependence of Eagle-2000, 800 nm waveguide transmission (%) for a range of translation speeds and pulse energies. The sample length is 29.3 mm. Measurements were recorded at intervals of 2 nJ in pulse energy and 3.33 mm/sec in translation speed. The high transmission region is at low pulse energies and high translation speeds.

in AF-45. Broad absorption bands in silicate glasses located in the ultraviolet, visible and near-infrared spectral region often arise from 3d transition metal impurities like titanium, vanadium, chromium, manganese, iron, cobalt, nickel and copper [200, 201]. The broad 1100 nm absorption has been reported by Glebov *et al.* to be a signature of ferrous iron (Fe^{2+}) [202]. Indeed, laser ablation inductively coupled plasma mass spectrometry (LA-ICP-MS) showed a $>$ 3 times larger amount of iron in Eagle-2000 than in AF-45 (see Fig. 3.15). For comparison, N-BK7 showed an iron trace concentration that was 20 times lower than that of Eagle-2000. This results in absorption losses for Eagle-2000 of 0.1 dB/cm at 800 nm and 0.27 dB/cm at 1550 nm. In contrast, in AF-45 the absorption induced losses are well below 0.1 dB/cm for both wavelengths.

The absorption losses in Eagle-2000 are primarily due to Fe^{2+}, which results in a broad absorption band centred at 1100 nm. Although iron can also exist in the glass in its trivalent redox state, Fe^{3+} has weak absorption bands in the visible (below 500 nm) and strong UV absorption [202]. The redox ratio between divalent and trivalent iron depends on the glass composition, in particular its optical basicity, which is influenced by the content of alkali and alkaline-earth oxides [203]. The thermal history of the glass can also affect the redox ratio [204]. Therefore, during waveguide fabrication in the thermal regime (cumulative heating) a transformation from Fe^{2+} to Fe^{3+} (or vice versa) can take place. Furthermore, trace element concentration in glass batches may vary depending on the contamination of the raw materials. In the case of Eagle-2000, three different glass samples, purchased over the course of 5 years, were investigated

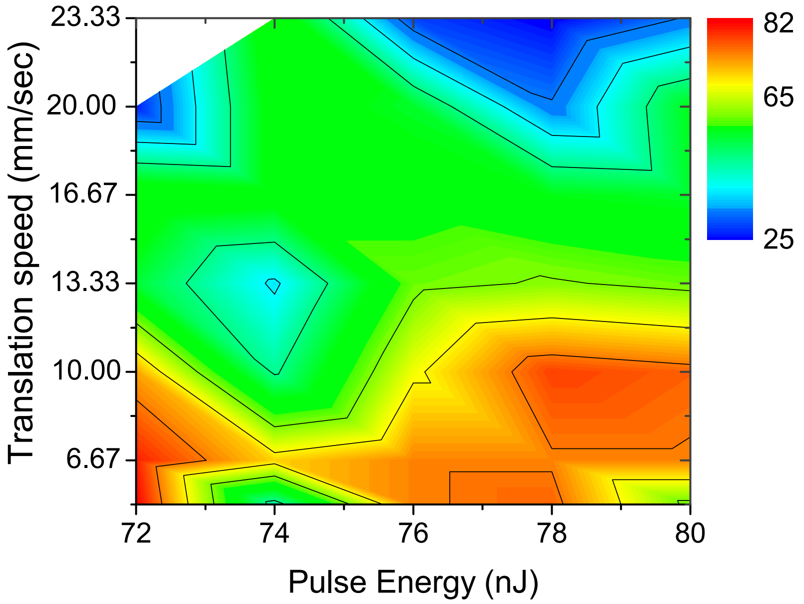

FIGURE 3.12: AF-45, 800 nm waveguide transmission (%) for a range of translation speeds and pulse energies. The sample length was 30.2 mm. Measurements were recorded at intervals of 2 nJ in pulse energy and 3.33 mm/sec in translation speed. The highest transmission waveguides were obtained in a narrow region of low translation speeds which is relatively consistent for different pulse energies.

but no significant differences in the absorption within the measurement error could be found.

Borosilicate: sub-micron structure

Due to the potential application of polarisation control in circuits [70–72], an exploration of the parameter space which can produce highly birefringent structures in Eagle-2000 was undertaken. This is motivated by the recent progress in high repetition rate formation of nanogratings in both fused silica and borosilicate (Borofloat and ULE) glass [205, 206].

To date no observations of self-organised nanograting formations have been reported in Eagle-2000. Richter *et al.* examined the contribution of repetition rate and pulse energy to the formation of nanogratings and has observed a processing window before the onset of cumulative heating where nano structure formation can be observed at high repetition rates [206]. In the 100 kHz regime Richter *et al.* observed nanograting formation in borosilicate glasses [206] for a narrow range of pulse durations (150-250 fs).

Hence, a study of a 100 kHz repetition rate regime in Eagle-2000 was undertaken. The output of the laser oscillator can be adjusted using a prism pair compensator. This was adjusted to produce a pulse duration of 200±50 fs and a Pockels cell was used to give a 100 kHz pulse train which is below the onset of cumulative heating.

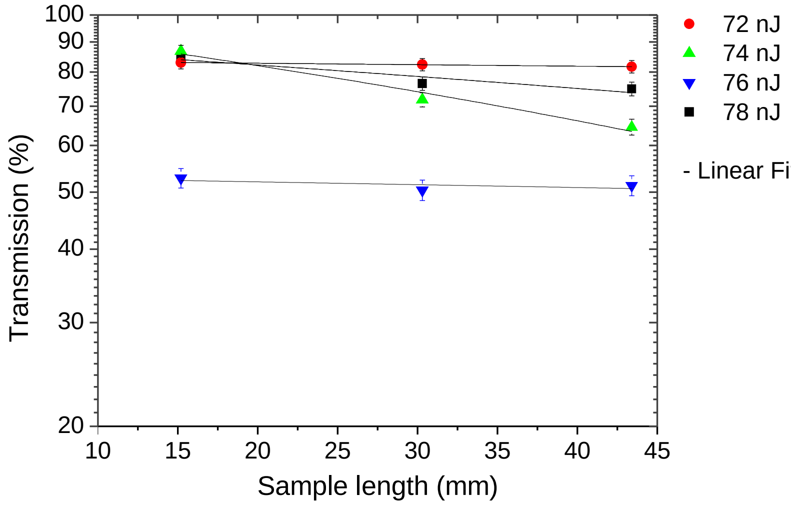

Figure 3.13: AF-45, 800 nm waveguide transmission vs. waveguide length for a range of pulse energies and a fixed translation speed of 5.00 mm/sec. A linear fit is applied to each set of pulse energies. The resulting coupling loss for a pulse energy of 72 nJ is 0.8 ± 0.1 dB and a propagation loss of 0.1 ± 0.1 dB/cm. A minimum coupling loss, of 0.1 ± 0.1 dB, was obtained for a pulse energy of 74 nJ.

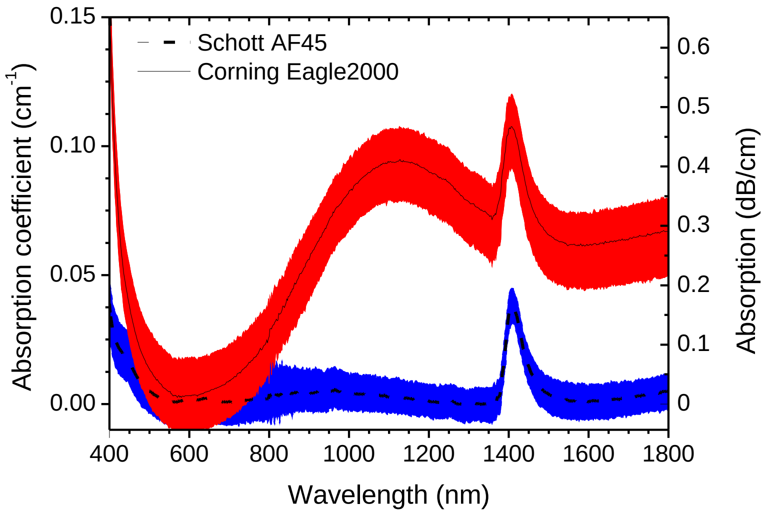

Figure 3.14: Bulk absorption spectra of Schott AF-45 and Corning Eagle-2000, including error bands due to experimental uncertainty. The absorption values were obtained by a differential measurement, comparing two different sample sizes in order to avoid influence from uncertainties in the Fresnel reflection coefficients. The large peak visible in the absorption spectrum of Eagle-2000 is due to trace concentrations of Fe^{3+}. (Image courtesy of Simon Gross) .

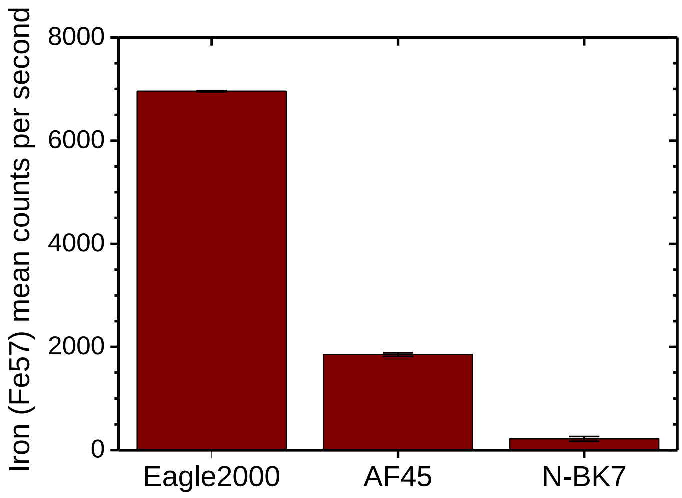

Figure 3.15: Counts per second, of iron, as detected by the mass spectrometer in Eagle2000, AF45 and N-BK7. This illustrates the difference in iron contamination of the three glasses (Image courtesy of Simon Gross).

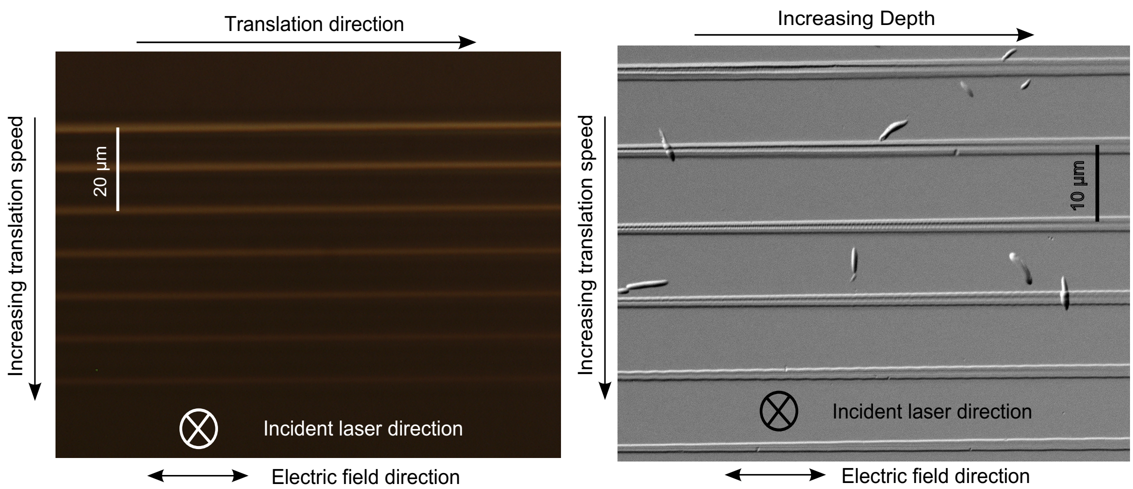

(a) (b)

Figure 3.16: (a)A microscope image of a set of waveguides (bright lines) written with 450 nJ pulse energy. The incident laser direction is into the page and the polarisation direction was parallel to the translation direction. The resulting fast axis of the waveguides was in the same direction as the incident laser polarisation. Measurements were not recorded for orthogonally incident laser beams. (b) A corresponding scanning electron microscope (SEM) image of the waveguides

The waveguides were written using an aspheric lens with a focal length of 4.51 mm (Thorlabs 230 TME-B) in order to produce a large modification of 8 μm in depth. Seven translation speeds (100, 0.83, 0.33, 0.17, 0.08, 0.03 and, 0.02 mm/sec) were used for a range of pulse energies from 100 nJ to 450 nJ. The evidence of birefringent structures can be obtained by examining the waveguide sample between a pair of crossed polarisers. When the fast axis of the birefringent structures is tuned from 0 to 45°, with respect to the first polariser, the structures should change from dark to bright. Hence indicating the presence of a birefringent structure and the location of its fast axis. The brightness of the structures increased with increasing writing energy and with slower writing speeds. A microscope image of the waveguides written at 450 nJ pulse energy and for seven different speeds is shown in Fig. 3.16, the brightest waveguide was written at 0.02 mm/sec corresponding to 8000 incident pulses for each irradiated focal spot of 1.3 μm diameter. These structures are then polished to expose the interior of the waveguide, etched and imaged using an SEM and Fig 3.16 shows the resulting waveguide structure. The evidence of periodic formations only becomes apparent for translations speeds below 0.83 mm/sec and for translation speeds below 0.03 mm/sec it becomes difficult to resolve periodic structure and hence its presence cannot be confirmed for these speeds. The relationship between the number of pulses and the periodic spacing of the resulting structure is consistent with reports in the literature [139, 184, 207]. As the writing speed decreases, corresponding to an increase in the number of pulses deposited, the spacing between nano planes decreases. Figure 3.17 shows an image of waveguides formed with low translation speeds. The graph in Fig 3.19 shows the resulting spacings between modifications as a function of writing velocity and the inset shows the minimum resolved periodic spacing of 250 nm. It has been previously observed that the development of nanograting occurs in stages which correspond to the initial formation, subsequent vacancy and nanoformation and finally the periodic development [205]. The final stage only begins after several hundred pulses and convergence to a minimal value occurs after 3000 pulses (0.04 mm/sec) [205]. This can be seen in the graph in Fig. 3.19 where, between the translation speeds of 0.03-0.08 mm/sec (4000-1600 pulses), a convergence to the minimum resolvable period of 250 nm is observed. This period is above the values reported for fused silica (of 150 nm [139]) but can be explained by the different glass composition of borosilicate compared to fused silica [206]. Furthermore the relationship between depth and period can be seen in the image in Fig. 3.18 where periodicity changes as a function of depth [207]. This is due to the disruption of the formation process of a deeper modification caused by the formation of an initial shallower structure. These structures did not exhibit a guided mode and therefore a measurement of loss could not be completed, nor could an analysis of the spectral response of the grating [208].

These results confirm that there exists a parameter space where birefringent nanostructure formation can be observed in Eagle-2000 borosilicate glass. The results show that the relationship between deposited pulses (of translation speed) and periodicity correlate well to results obtained in fused silica [205]. However, these structures exhibit high loss due to scattering from the imperfect nano-plane formations [152, 153]. Furthermore, due to the low translation speeds required for formation and the narrow processing window the practical application of these structures in waveguide circuit is

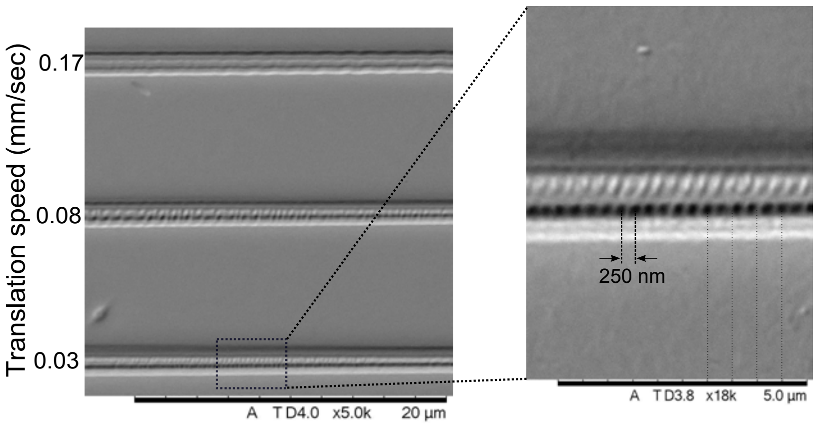

FIGURE 3.17: An SEM image of waveguide nanogratings for three translation speeds. The inset shows an image of the grating period of ~250 nm for 0.03 mm/sec translation speed.

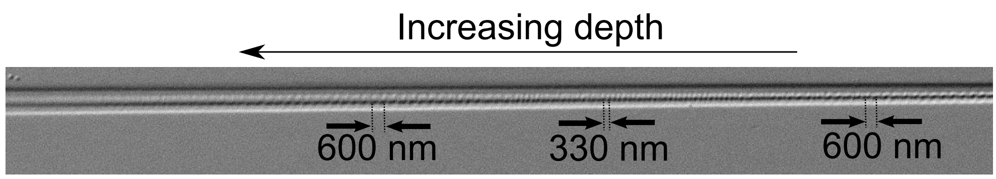

FIGURE 3.18: An SEM image of a nanograting at various positions along it's depth. The different plane spacings can be observed at different depths.

limited and was therefore further studies were not pursued.

3.4 Discussion and outlook

This potential for mode field diameter shaping, shown in both Eagle-2000 and AF-45, could prove useful for optimisation of circuit design by tapering from high coupling efficiency waveguides at the facet of a chip to a waveguide with a lower propagation or bend loss. Furthermore, flexibility in producing different mode field diameters could prove useful for nonlinear process enhancement, exploiting increased confinement. The relationship between the effective mode area, $A_{eff} = \frac{\pi}{4}MFD^2$ and the nonlinear process efficiency is

$$\gamma = \frac{\omega n_2}{cA_{eff}}, \tag{3.2}$$

where n_2 is the nonlinear refractive index, ω is the angular frequency of the light and c is the speed of light in vacuum. Measurements of the nonlinear refractive index in fused silica have found similar values in laser written waveguides of 30-90% of the bulk material of 2.7×10^{-20} m^2/W dependent on the writing velocity [209]. Although it is important to note that these measurements did observe that n_2 was much more strongly effected than the linear refractive index during laser processing. In AF-45 it can be seen

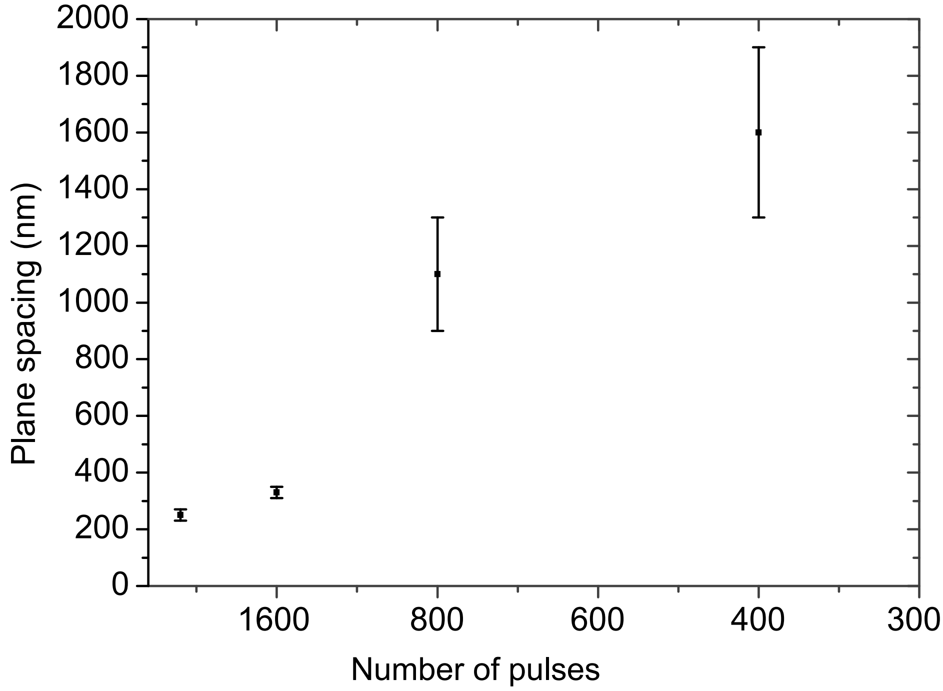

FIGURE 3.19: A graph which shows the change in the plane spacing of the nanogratings as a function of translation speed for a waveguide fabricated at 450 nJ pulse energy and 5.1 MHz repetition rate pulse train. The minimum plane spacing begins converging to $\lambda/4$ at a translation speed of 0.03 mm/sec (4000 pulses). The large error bars are due to the fact that the formations produced at lower translation speeds etch at a faster rate leaving less definition in SEM images.

in Fig. 3.12 that it is possible to produce a mode field diameter significantly smaller than an 800 nm fibre mode (see Fig. 3.9). This could be applied to the production of heralded single photons on-chip and Spring *et al.* have shown that the high extraction efficiency from laser written waveguides compensates for the lower production efficiency compared to other materials [210]. Furthermore the nonlinearity of the amorphous $\chi^{(3)}$ material can be enhanced using thermal poling methods to produce an effective second order nonlinearity from a third order nonlinearity [211, 212]. This process uses a high voltage applied across a sample while it is heated and once it cools to room temperature this electrostatic field is frozen into the material. The resulting $\chi^{(2)}_{eff}$ is related to $\chi^{(3)}$ through, $\chi^{(2)}_{eff} = 3\chi^{(3)}E_{frozen}$, where an electric field, E_{frozen} is frozen within the glass structure. This was initially applied to laser written waveguides by Corbari *et al.* and later an electro-optically tuned Mach Zehnder was produced exploiting this technique [213, 214]. Thermal poling has been applied to laser written waveguides in Eagle-2000 glass and the results do show a higher nonlinearity that that of the bulk glass and of unmodified fused silica [214–216]. The electro-optic and optical nonlinearity could then potentially be exploited in a waveguide circuit composed of Eagle-2000 which has inherently low insertion loss. By using glasses with a higher $\chi^{(3)}$ the effective $\chi^{(2)}_{eff}$ will therefore be higher. Laser written waveguides have been produced in chalcogenide glasses, such as gallium lanthanum sulphide (GLS), with transmission losses as low as 0.65 dB/cm [217]. Directional couplers and even waveguide Bragg gratings (WBG) have been fabricated in GLS showing the potential for quantum integrated circuit applications exploiting this material.

Although the sub micron structure formation in Eagle-2000 exhibited high losses limiting their potential use as polarisation controllers in circuits, they could be exploited for high quality optofluidic inclusions in integrated circuits. It has been shown that when the nanoplanes of these periodic formations are aligned parallel to the waveguide significant increases in selective etch rates can be achieved [138, 218, 219]. Such optofluidic inclusions in glass substrates have a diverse range of applications [148, 220, 221], most relevant of which is the incorporation of microfluidic inclusions with laser written waveguides for sensing [222–224]. By exploiting the increased etch rates of the nanostructured waveguides optofluidic inclusions could be incorporated into Eagle-2000 glass substrates which would further increase their potential range of applications.

3.5 Conclusions

Fabricating waveguides in glass substrates for quantum optics applications means managing waveguide loss is crucial to the advancement of the field. Loss affects both experimental durations and experimental capabilities and hence motivated a study of waveguide loss at the wavelength of 800 nm. In this chapter parametric studies of fused silica and borosilicate glasses were performed using a femtosecond laser direct write (FLDW) method. Only a narrow range of pulse energies and translation speeds could be found which would permit the modification of fused silica and no high speed processing window was discovered. However, in borosilicate glass a regime where submicron self organised structures could be found and a high speed processing window was found. Prior to these studies no periodic self organised structures had been observed in Eagle-2000 glass. However, due to low processing speed and high loss of the sub micron structures in borosilicate the potential application of such structures in borosilicate glass was not pursued.

The high speed processing window in borosilicate glass was analysed for both Corning Eagle-2000 and Schott Af-45 glass substrates. The parameter space for low loss waveguide formation was narrower in AF-45 than in Eagle-2000, but for the narrow processing window in AF-45 the loss was found to be lower. Studies of these two glasses had been performed by Eaton *et al.* at telecommunications wavelengths but this was the first rigorous study to be performed a the wavelength of 800 nm [198]. The contribution of propagation loss and coupling loss to overall insertion loss were discerned for AF-45. Finally a measurement of the intrinsic absorption of the substrate was performed to place an upper bound on the potential throughput achievable in AF-45 compared to Eagle-2000. An increased absorption in Eagle-2000 was found and the origin was found, which was due to trace element absorption. A large Fe^{2+} absorption band resulted in absorption losses of 0.1 dB/cm at 800 nm and 0.27 dB/cm at 1550 nm in Eagle-2000. In contrast, in AF-45 the absorption induced losses are well below

0.1 dB/cm for both wavelengths. This was the first time the origin of absorption loss in both glasses had been isolated to trace element absorption.

The studies performed in this chapter, though not applied to all circuits described in this thesis, act as a critical fundamental building block for device development. The methods used in this chapter highlight the potential to discern the origin of loss in waveguide circuit and, in doing so, to help reduce them. By using AF-45 rather than Eagle-2000 an increase in overall throughput can be obtained and thus to increase the practicality of laser written circuits for integrated quantum optics.

"I come from the land of pigs and bacon. If you think I'll eat your fish and chips, by jaysus you're mistaken"

The Pecker Dunne

4
Multiport beamsplitters

A multiport device separates an input into two or more outputs. In optics this can be visualised as a bulk optical element such as a beamsplitter which separates a light beam into a pair of outputs with the intensity of each given by the splitting ratio, or reflectivity, of the beamsplitter. This can be scaled and a single input can be separated into multiple outputs which is useful for applications in both quantum and classical information science. In classical information such devices are routinely used as splitters which can separate an input signal into a number of output channels. Applications have emerged exploiting fused fibre and integrated optical multiport splitters for use in sensing and optical coherence tomography (OCT) [225–229]. These designs exploit either the multiple output ports of a multiport splitting device to reduce signal-to-noise ratios, or concatenating multiports in interferometer configurations to exploit the more diverse array of phase offsets which can be imparted on individual channels [230–232]. Applications extend to stellar interferometry where multiport interferometers with complex, stable and precise phase relationships are highly desirable devices for use in nulling interferometry [233, 234].

This chapter discusses the fabrication of two distinct multiport splitters, a 3-port and 4-port, which are formed using two different design methods. The 3-port device is a 3 dimensional interaction region which equally distributes light in a single operation, while the 4-port device is comprised of four individual beamsplitters with phases carefully matched to induce a resultant four mode transformation. These devices are characterised classically and this information is used to predict the non-classical operation of the device when using pairs of single photon inputs. The experimental two-photon measurements agree with what is predicted using the classical characterisation. The non-classical characterisation compares well with bulk, fibre and lithographically fabricated examples showing the potential for laser written multiports in quantum information science.

4.1 Multiport splitters: interest and motivation

Optical multiports provide the ability to produce an arbitrary unitary transformation on a set of optical modes [34]. Multiports are therefore an extremely important component in optical quantum information processing (QIP) and state preparation [235]. Producing and manipulating entangled states is a key process required for quantum enabling technologies [236]. Combining unitary transformations with postselection is the foundation of linear optic quantum computing (LOQC). Producing high quality multiport devices is therefore critical to ultimately designing a postselected quantum circuit such as a controlled-NOT gate. Furthermore, it has been recently proposed and experimentally demonstrated that such unitary transformations can be used for a unique computational process, the boson sampling problem. To determine the permanent of a matrix operation is a problem of computational complexity which is referred to as #P-complete and likely to be intractable [237]. By sampling this unitary process, or scattering matrix, using bosons the output distribution can reconstruct the permanent of the matrix in a way that does not scale exponentially as would be the case for a method of computation which only uses classical resources [238]. While determination of the actual computational complexity of this problem is well outside the scope of this thesis it has been asserted to be hard [91].

Reck *et al.* showed that by using combinations of phase shifters and 2-port beamsplitters it is possible to construct any arbitrary unitary operator on any number of optical modes [34]. Proposals to probabilistically generate path entangled states by combinations of N-port splitters combined with a 2-port beamsplitters exist [239]. In this case a maximally entangled NOON state can be produced by postselection. Furthermore, interferometry based on such a scheme seeks to obtain a phase ϕ from $|N,0\rangle + e^{iN\phi}|0,N$ with fringe period which scales as λ/N where N is the input photon number into the multiport. Such a scheme and other similar approaches will be discussed in the application section at the end of the chapter.

The fundamental idealised multiport device is the familiar beamsplitter which implements a desired 2×2 unitary operation. This can be generalised to a multiport operation on N input modes $\hat{a}_N$ into N output modes $\hat{b}_N$ described by the unitary $N \times N$ matrix [240]

$$\begin{bmatrix} \hat{b}_i \\ \hat{b}_j \\ \vdots \\ \hat{b}_N \end{bmatrix} = \begin{bmatrix} U_{1,1} & U_{1,2} & \cdots & U_{1,N} \\ U_{2,1} & U_{2,2} & \cdots & U_{2,N} \\ \vdots & \vdots & \ddots & \vdots \\ U_{N,1} & U_{N,2} & \cdots & U_{N,N} \end{bmatrix} \begin{bmatrix} \hat{a}_i \\ \hat{a}_j \\ \vdots \\ \hat{a}_N \end{bmatrix}. \tag{4.1}$$

The interest in such a unitary for the purpose of state preparation is immediately apparent, a Fock state input of a single photon such as $\Phi_{in} = |1,0,...0\rangle_{1,2,...N}$ is transformed according to $\Phi_{out} = U_{11}|1,0,...0\rangle + U_{21}|0,1,...0\rangle + ... + U_{N1}|0,0,...1\rangle$ which is the so called W state encoded in path [241].

4.2 Multiport implementations

Multiports and their applications in quantum optics were originally explored using bulk optic beamsplitters and phase shifters [240], for which non-classical interference was observed in both 3-port and 4-port splitters. Following from this work a study of a 3-port fiber coupler was undertaken [242]. However neither of these approaches provide the scalability and stability requirements needed for large scale optical quantum circuits [243]. The extreme difficulty of working with large numbers of bulk optical elements and fibre components has limited the development of these devices.

The challenges of scaling and stability in various quantum optical applications have been the main drivers for the recent explosion of interest in integrated quantum devices, such as integrated waveguide circuits [42, 244], waveguide array quantum walks [245–247] and single photon sources [248, 249]. Desirable qualities such as reconfigurability have been demonstrated [250], notably in lithium niobate-based devices which allow for telecommunications wavelength photon manipulation at GHz speeds [63]. Miniaturisation using silicon-on-insulator nanowire based photonic circuits have been shown [251] and there is also great promise to incorporate these platforms with existing on chip detectors [74]. In addition the integration of photon pair sources and circuits have been achieved using a nonlinear waveguide array fabricated in lithium niobate [252]. The advantages of integrated components have been applied to the construction of integrated quantum multiports. Peruzzo *et al.* have demonstrated multiport functionality with an on-chip 4-port multimode interference device [253] in the silica-on-silicon platform.

The majority of these demonstrations have relied on mature planar platforms, but there are limitations associated with the inherently two dimensional (2D) nature of planar quantum circuits. As circuits become more complicated, both the circuit area and the proportion of "neutral" elements, whose only purpose is to provide transparent waveguide crossings, will become significant. Hence techniques which allow the fabrication of structures in three dimensions could offer some specific and unique possibilities.

In this chapter the implementation of a 3-port and 4-port device using a 3D FLDW technique is described. Each device highlights a different advantage of the 3D geometry. The 3-port is implemented as a single coupling region that replaces three 2-port devices [254]. The 4-port is composed of four 2-port directional couplers, but avoids a crossing that would require an additional coupler in 2D. Taken together these kinds of structures could reduce the complexity and sensitivity of higher order concatenated multiport based circuits. This fact is established by the observation of 2 photon interference in both structures. Using the laser inscription process, the compact size and phase stability of an integrated multiport can be combined with the convenience of a 3D interaction region provided by a fused fibre device. This can be used to simplify device designs which, for instance, may be based on overlapping interferometers which exploit these components.

4.3 Fabricating multiports

The integrated photonics analogue of the basic 2-port beamsplitter is the directional coupler, in which two waveguides are brought into close proximity so that their evanescent fields can overlap and exchange energy [42, 255]. The degree of coupling is determined by the waveguide separation and interaction length which can be adjusted to produce directional couplers of any reflectivity. Using the well-known decomposition of the $N \times N$ unitary into a concatenation of beamsplitters and phase shifters [254], it is possible to construct an arbitrary multiport in two dimensions in integrated optics by designing a suitable arrangement of directional couplers and phase delays. However as the number of directional couplers scales with N^2, at large N, such a device is prohibitive to build due to fabrication errors.

Previous investigations have looked at cases of bulk optic beamsplitters [240], fiber optic directional couplers [242], and multimode interference devices [253], to produce multiports. This section describes the methods used to design multiports using the laser inscription technique and the specific cases of a three and four port beamsplitter based on an arrangement of coupled waveguides.

4.3.1 Mode evolution in the three port (tritter)

In three dimensions a 3×3 multiport or tritter can be constructed from a single coupling element involving three waveguides (see Fig. 4.1). This single element can replace up to three directional couplers and phase shifters [254].

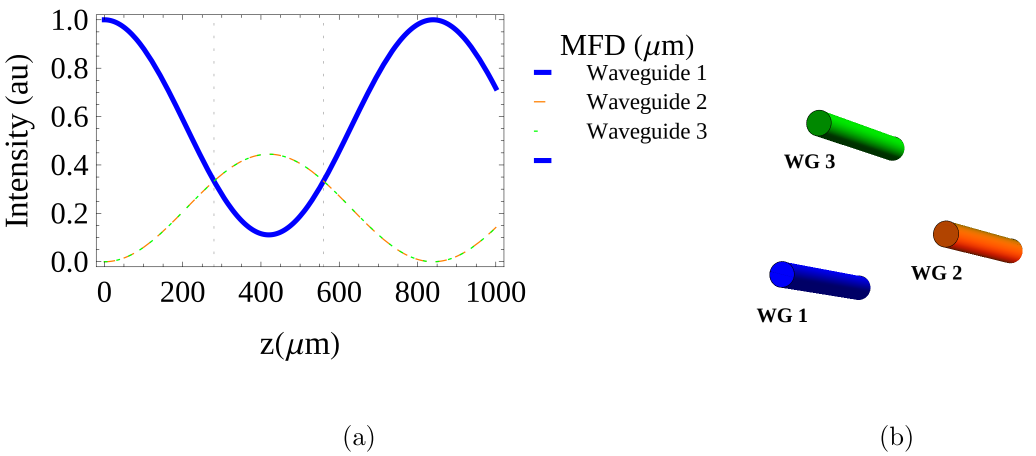

FIGURE 4.1: (a)The intensity along a three waveguide symmetric array as a function of propagation distance, dotted veritcal lines show regions where the intensity in each waveguide is equal at 33/33/33. (b) The layout of a symmetric 3D waveguide array.

Although in an idealised 3-port device the coupling between waveguides is identical in all directions, for the laser inscription process this is not the case. It has been shown that in laser written waveguides, due to an ellipticity of the refractive index modifications, the inter-waveguide coupling is dependent on the orientation of the waveguides with respect to one another [256]. This can be understood by considering that the coupling between waveguides is dependent on the mode overlap. Therefore, a pair of elliptical waveguide, which exhibit elliptical modes, the coupling increases for waveguides separated vertically rather than than horizontally. Hence, to describe the coupling in a realistic model of a 3-port interaction a pair of coupling coefficients are used. Coupling coefficient $G(z)$ describes coupling between waveguides 1 and 2, and $g(z)$ describes the coupling between waveguides 1 and 3 and waveguides 2 and 3. In general, all three of the couplings could have different values, but the 'isosceles' geometry considered here is appropriate as a result of the laser writing process (see Fig. 4.2(a)).

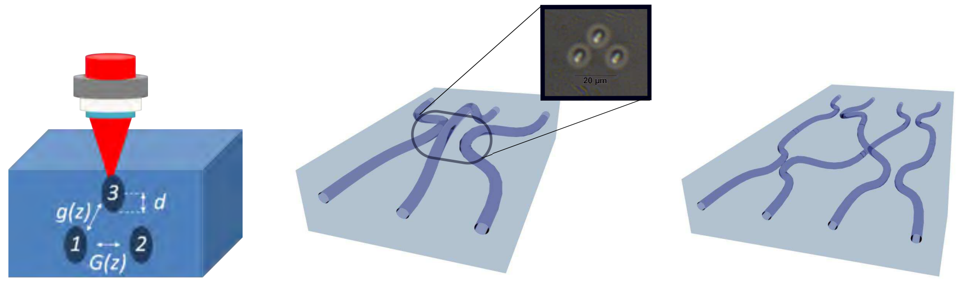

(a) (b) (c)

FIGURE 4.2: (a) Idealised coupling region of a tritter device. Writing considerations induce an effective isosceles geometry with two coupling strengths $g(z)$ and $G(z)$. (b) A schematic of a 3D implementation of a tritter, where three waveguides taper from a planar arrangement to a triangular interaction region, shown in the inset microscope image, and taper back to a planar array. Note that the waveguides used in this study have not been annealed and hence the ring surrounding the central high index core is still present. (c) the layout of the four directional couplers and the waveguide avoided crossing in the 4-port device

Such a structure is described by a Hamiltonian of the form

$$\hat{H} = \hbar v_p \sum_{n,m=1}^{3} C_{n,m} \hat{a}_n^\dagger \hat{a}_m, \tag{4.2}$$

where the coupling matrix is

$$C = \begin{bmatrix} \beta & g & G \\ g & \beta & g \\ G & g & \beta \end{bmatrix}. \tag{4.3}$$

The propagation constant $\beta = \omega/v_p$ of the three waveguide modes is assumed to be common (v_p is the phase velocity and $\omega/2\pi$ the optical frequency). Explicitly including the common phase velocity v_p in $\hat{H}$ means that operator evolution with distance z rather than time t follows naturally.

After propagation through the interaction region, photons have encountered the mode transformation

$$\hat{\mathbf{b}} = U\hat{\mathbf{a}}, \tag{4.4}$$

where the input and output mode vectors are $\hat{\mathbf{a}} = (\hat{a}_1, \hat{a}_2, \hat{a}_3)$ and $\hat{\mathbf{b}} = (\hat{b}_1, \hat{b}_2, \hat{b}_3)$, and the transfer matrix U is the solution of Heisenberg's equation, $d\hat{\mathbf{a}}/dz = -iC(z)\hat{\mathbf{a}}$. The transfer matrix U completely determines the operation of the device, in particular the classical output intensities and quantum interference between photons in the device.

4.3.2 Mode evolution in the four-port

In contrast to the single element tritter the four port (depicted in Fig. 4.2(c)) is made up of four directional couplers. This device used the 3D advantage to cross two waveguides without interaction, reducing the number of required directional couplers by one. As the device is made up of four discrete elements, the device can be modelled as a product of beam splitter operators. Assuming each directional coupler is identical, the operator corresponding to the four port transfer matrix is

$$\hat{U} = \hat{B}_{2,4}(\eta)\hat{B}_{1,3}(\eta)\hat{P}_2(\phi)\hat{P}_3(\phi)\hat{B}_{3,4}(\eta)\hat{B}_{1,2}(\eta), \tag{4.5}$$

where the directional couplers have the beam splitter action,

$$\begin{bmatrix}\hat{b}_i\\ \hat{b}_j\end{bmatrix} = \hat{B}_{i,j}(\eta)\begin{bmatrix}\hat{a}_i\\ \hat{a}_j\end{bmatrix} = \begin{bmatrix}\sqrt{\eta} & -i\sqrt{1-\eta}\\ -i\sqrt{1-\eta} & \sqrt{\eta}\end{bmatrix}\begin{bmatrix}\hat{a}_i\\ \hat{a}_j\end{bmatrix}, \tag{4.6}$$

where η is the reflectivity of the beamsplitter and and $\hat{P}_j(\phi)$ describes the phase difference between the inner crossing arms and the outer "straight-through" arms (See Fig. 1(c)) where $\hat{P}_j(\phi)\hat{a}_j = e^{-i\phi}\hat{a}_j$. Using these relations we find the transfer matrix corresponding to the four port operator (4.5) is

$$U = \begin{pmatrix} \eta & -ie^{i\phi}\sqrt{(1-\eta)\eta} & -i\sqrt{(1-\eta)\eta} & e^{i\phi}(\eta-1)\\ -i\sqrt{(1-\eta)\eta} & e^{i\phi}\eta & \eta-1 & -ie^{i\phi}\sqrt{(1-\eta)\eta}\\ -ie^{i\phi}\sqrt{(1-\eta)\eta} & \eta-1 & e^{i\phi}\eta & -i\sqrt{(1-\eta)\eta}\\ e^{i\phi}(\eta-1) & -i\sqrt{(1-\eta)\eta} & -ie^{i\phi}\sqrt{(1-\eta)\eta} & \eta \end{pmatrix}. \tag{4.7}$$

4.4 Fabrication methods and design

The devices were fabricated inside boro-aluminosilicate (Eagle 2000) using a Femtosource 5.1 MHz laser and a 100× oil immersion objective (Zeiss N-Achroplan, $NA = 1.25$) for focusing inside the sample. The samples were not annealed after processing and hence the ring surrounding the waveguides (see inset in Fig. 4.2(b)) was not removed after processing. The sample translation was completed using Aerotech high precision motion control stages at writing speeds of 2000 mm/min. The waveguides were written using pulse energies of 28 nJ which created waveguides suitable for single mode operation at 800 nm. Individual waveguides displayed an insertion loss of 1.8 dB for a length of 30 mm, which was dominated by mode mismatch between the launch/collection fibre and the waveguide mode. Note that the waveguides used in this study had not been annealed. The refractive index change is ellipsoidal in nature and it has been shown that laser written waveguides display non-isotropic coupling due to waveguide asymmetry [256]. The waveguides have a mode size of 6.9 μm in the semi-major elliptical axis and 6 μm in the semi-minor axis. Since the tritter is a triangular arrangement of modes (as shown in Fig. 4.2(a)) there are two effective coupling ratios, $g(z) \neq G(z)$. To help reduce the impact of this effect the central waveguide in the coupling region was fabricated slightly above the lower waveguides, with a spacing from an equilateral position of d, to try and create a device which operated symmetrically. The waveguides are initially separated, in a planar array, by 127 μm before an s-bend transitioning to an interaction region, where evanescent coupling occurs with typical spacings of 15 μm and subsequently another s-bend transition out to a 127 μm planar array spacing. This is best illustrated in Fig. 4.2(b), which shows the waveguides tapering towards interaction regions and returning to the original spacing at the output of the device. An ideal tritter displays equal splitting between output ports of 33/33/33 and a 4-port has equal splitting between output ports of 25/25/25/25. Hence a range of devices were fabricated with different length interaction regions targeting the ideal coupling ratios. A classical characterization is performed to determine which structure best matched the intended constraints of the correct length coupling region which was the most symmetrical.

4.5 Classical characterization

In order to determine the coupling ratios in the tritter and splitting ratios for the four port a classical characterization was performed. If classical light of intensity M is injected into port j, the output intensity N at port k can be modelled as,

$$N_j^k \quad = \quad \epsilon_j^{in}\epsilon_k^{out}M|U_{j,k}|^2, \tag{4.8}$$

where the input and output losses at port l are characterized by the pre-factors, $0 < \epsilon_l^{in/out} < 1$. By forming the following ratios,

$$F_{j,r}^{k,s} \quad \equiv \quad \frac{N_j^k N_r^s}{N_r^k N_j^s} = \frac{|U_{j,k}|^2|U_{r,s}|^2}{|U_{r,k}|^2|U_{j,s}|^2}, \tag{4.9}$$

it is possible to relate the measured classical intensities directly to the unknown tritter couplings, $g(z)$ and $G(z)$ or four-port splitting ratios and cancel the loss terms.

For the tritter a model is fitted to the classical measurements by assuming uniform coupling over an interaction region of length L, i.e. $g(0 \leq z \leq L)\nu_p/L = \bar{g}$ and $G(0 \leq z \leq L)\nu_p/L = \bar{G}$ with zero coupling elsewhere. Using maximum likelihood estimation [257], $\bar{g}$ and $\bar{G}$ in the transfer matrix U are varied to find the best fit to the three experimentally determined fractions $F_{1,2}^{1,2}$, $F_{1,3}^{1,3}$ and $F_{2,3}^{2,3}$. This involved minimizing the difference between the experimentally measured left hand side and theoretical right hand side of Eq. (4.9) for $F_{1,2}^{1,2}$, $F_{1,3}^{1,3}$ and $F_{2,3}^{2,3}$, weighted by the uncertainties in the fractions (found from the uncertainties of the measured intensities N_j^k) [257]. This fit determined $\bar{g} \approx 0.81\nu_p/L$ and $\bar{G} \approx 0.51\nu_p/L$, indicating that waveguides one and two couple more strongly than waveguides one and three. Using this fit the tritter with the most symmetric operation obtained had the matrix of classical output intensities

$$|U_{tritter}|^2 = \begin{pmatrix} 0.37 & 0.41 & 0.23 \\ 0.41 & 0.19 & 0.41 \\ 0.23 & 0.41 & 0.37 \end{pmatrix}. \tag{4.10}$$

The ideal symmetric tritter has $|U_{i,j}|^2 = 1/3$, therefore this device has a slightly asymmetric power splitting [240]. The device had a waveguide spacing of 7 μm, an interaction length of 1 mm and waveguide 3 was separated from an equilateral position by 0.35 μm. In addition to determining this we can also determine the origin of the asymmetry. For a 3 mode coupling region where the coupling between all modes is different, it can be shown that certain combinations of inputs and outputs are identical to others. This occurs for the off diagonal terms. Hence this assumption was used in the predictions of $|U_{tritter}|^2$. However, this approximation neglects coupling which occurs in the fold in regions outside of the interaction region. Waveguides couple prior to entering the interaction region and result in power transfer between waveguides before the coupling which occurs in the interaction region. Hence, even a small asymmetry in the coupling in this fold in region will lead to a large change in the energy exchange within the interaction region which is extremely difficult to deconvolve from an asymmetric coupling due to the ellipticity of the waveguides.

Similar to the tritter, we can use a maximum likelihood approach to fit η, the beamsplitter reflectivity, from (4.7) using the following six fractions, $F^{1,2}_{1,2}$, $F^{1,3}_{1,3}$, $F^{1,4}_{1,4}$, $F^{2,3}_{2,3}$, $F^{2,4}_{2,4}$, and $F^{3,4}_{3,4}$. This fit determined $\eta = 0.377$. Substituting this fit into Eq. (4.7) we find the matrix of classical output intensities for the four-port

$$|U_{4port}|^2 = \begin{pmatrix} 0.14 & 0.23 & 0.23 & 0.39 \\ 0.23 & 0.14 & 0.39 & 0.23 \\ 0.23 & 0.39 & 0.14 & 0.23 \\ 0.39 & 0.23 & 0.23 & 0.14 \end{pmatrix}. \tag{4.11}$$

The four-port device differs from the ideal symmetric four-port, $|U_{i,j}|^2 = 0.25$ and has a non-uniform power splitting [240]. This is due to the fact that the measured value for $\eta = 0.377$ is not the ideal value of $\eta = 0.5$. However, this measurement also assumes the the four beamplitters are each identical which leads to errors in the non-classical predictions.

4.6 Quantum characterization

A two-photon characterization is performed on the devices using 804 nm photons produced using a type-I spontaneous parametric down conversion (SPDC) source, as described in [68]. The setup used a Toptica 402 nm blue diode laser which was focused into a 1 mm thick BiBO crystal cut to give a 6 ° opening cone angle. Down converted photons were produced at 804 nm in an output cone and then coupled into polarization maintaining single mode fibers. These were then butt-coupled to the device under test using 127 μm spaced V-groove arrays. The outputs were then monitored using silicon avalanche photodiode detectors (SAPD) from Perkin Elmer. The 2-fold coincidences across all the output modes were measured simultaneously (in a 5 ns window) using a 4 channel time tagging unit. The arrival time of the photons into the chips was varied as a means of continuously controlling the degree of indistinguishability between the two photons and thereby moving between classical propagation of light and quantum interference.

Signatures of two-photon interference are detected in the devices through the Hong-Ou-Mandel (HOM) effect [258], whereby the probability of two photon coincidences are reduced (HOM dip) or enhanced (HOM peak) due to quantum interference in the device. The degree of quantum interference is quantified using the visibility, $V_{i,j}^{k,l}$, defined for injecting a single photon into waveguides i, j and detecting in waveguides k, l as,

$$V_{i,j}^{k,l} = \frac{C_{i,j}^{k,l} - Q_{i,j}^{k,l}}{C_{i,j}^{k,l}}, \tag{4.12}$$

where the quantum and classical coincidence probabilities are,

$$Q_{i,j}^{k,l} = \frac{1}{1+\delta_{i,j}}|U_{i,k}U_{j,l} + U_{i,l}U_{j,k}|^2 \tag{4.13}$$

$$C_{i,j}^{k,l} = |U_{i,k}U_{j,l}|^2 + |U_{i,l}U_{j,k}|^2, \tag{4.14}$$

where $\delta_{i,j}$ is the Kronecker delta term satisfying $\delta_{i,j} = 1$ if $i = j$ and zero otherwise. We see that the quantum two photon coincidence probability $Q_{i,j}^{k,l}$ is strongly dependent on the relative phases of the elements of U. When these phases destructively interfere, two photon coincidences are reduced compared to the classical case, leading to a large positive visibility (a HOM dip). Whereas when these phases constructively interfere, two photon coincidences are enhanced compared to the classical case, leading to a large negative visibility (a HOM peak).

4.6.1 Visibilities in tritter

As the visibilities are strongly dependent on the relative phases of the matrix elements of U, the tritter visibilities depend on the length and geometry of the coupling region as defined by the coupling functions $g(z)$ and $G(z)$ in Eq. (4.2). To illustrate the variety of tritter visibilities that can be observed in the 3D device, a plot of the visibilities as a function of effective coupling $\bar{g}L$ is shown in Fig. 4.3 assuming uniform coupling over the interaction region. Figure 4.3(a) shows a symmetric tritter as gL is varied. Only at one coupling (the symmetric 33/33/33 case) do we see equal visibilities of 50%. However Fig. 4.3(b) considers an asymmetric case, which corresponds to the value of $g(z) \neq G(z)$, taken from the classical characterisation in section 4.5. In this case for input 1 and 2, due to the asymmetry, $V_{1,2}^{1,3} \neq V_{1,2}^{2,3}$. The vertical line in Fig. 4.3(b) shows what is expected from the classical characterisation.

Nine HOM dips were measured for the tritter (Fig. 4.4) by injecting two photons into the device at different delays and observing coincidences at the output ports. The

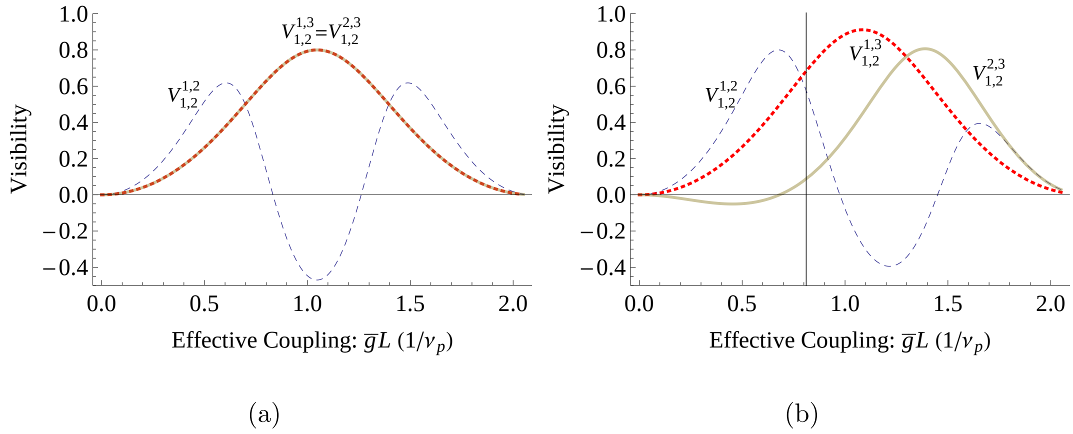

FIGURE 4.3: Tritter visibilities as a function of effective coupling, $\bar{g}L$, assuming uniform coupling over an interaction region of length L, $g(0 \leq z \leq L)L/\nu_p = \bar{g}$ and $G(0 \leq z \leq L)L/\nu_p = \bar{G}$ with zero coupling elsewhere. a) symmetric coupling region ($\bar{G} = \bar{g}$). b) Isosceles coupling region ($\bar{G} = 0.6234\bar{g}$). Vertical line corresponds to the fit to the experimental tritter with $\bar{g}L \approx 0.81\nu_p$.

measured visibilities (Fig. 4.4(d)) were found from the relative depth of each dip. A clear reduction in the visibilities is observed in the cases of $V_{1,2}^{2,3}$, this corresponds to Fig. 4.4(b), we also see reductions in the visibilities for different input ports $V_{1,3}^{1,3}$ and $V_{2,3}^{1,2}$.

In section 4.5 a simple model was used to determine the tritter couplings $g(z)$ and $G(z)$ using only classical intensity measurements of the device. As this fit uniquely determines U the visibilities for this model can be predicted using Eq. (4.12). Therefore, using only classical intensity measurements, the quantum correlations for the device can be predicted. This is a convenient tool, since in order to produce a device with the correct coupling ratios a range of devices must be fabricated around this intended parameter. It is much more convenient to perform a range of intensity measurements prior to any quantum measurements to confirm the device has the desired functioning. The predicted visibilities are compared to the experimental visibilities in Fig. 4.4(d), show there a qualitative match; issues which are causing the minor mismatch between this prediction and the experimentally observed values are the assumptions upon which the intensity dependent measurement is based. The model assumes a constant input intensity which can fluctuate during the course of the measurement and input/output facet losses which may change also. This is the dominant cause of the deviation from the theoretical predictions. Furthermore the model assumes the interaction region is constant in z but input and output tapering regions do contribute to the overall coupling which was not accounted for.

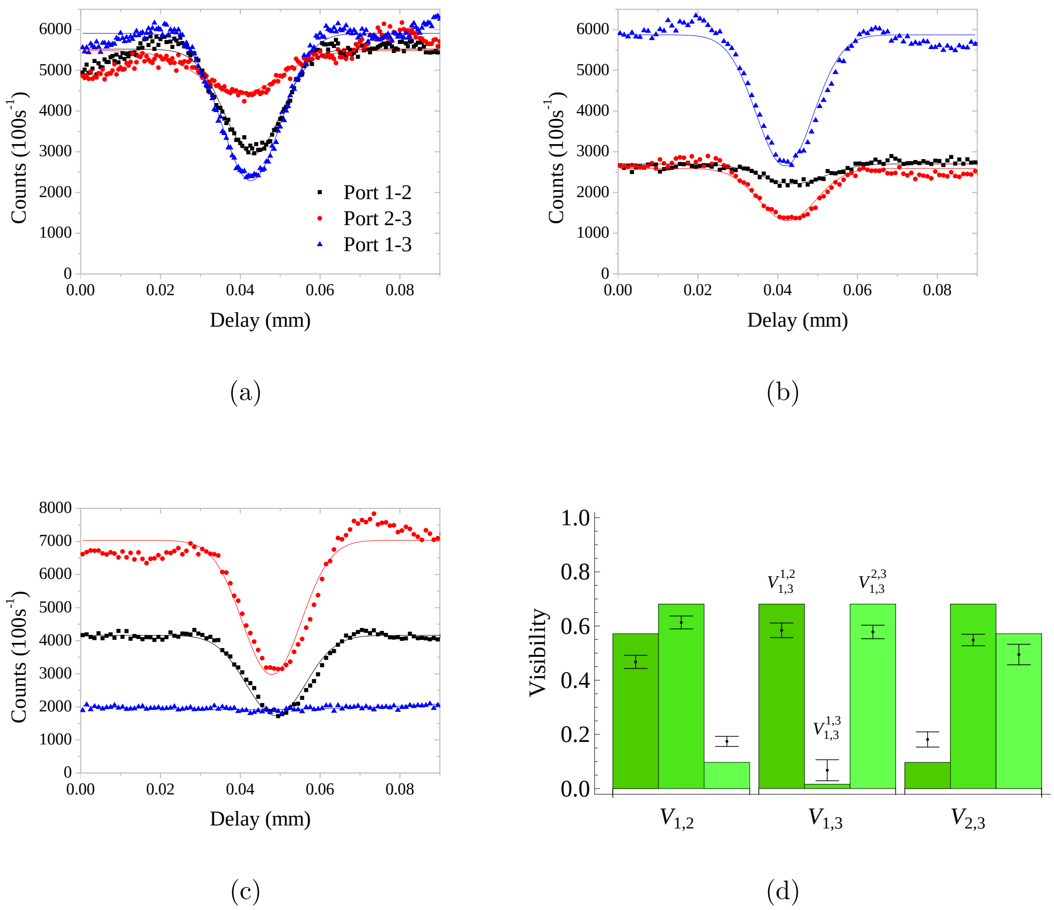

FIGURE 4.4: Tritter HOM dips for (a) input ports 1 and 2, (b) for input ports 2 and 3 (c) for input ports 1 and 3. (d) Comparison of measured tritter visibilities (error bars) and theoretical predictions (columns) from the simple tritter model in section 4.5.

4.6.2 4-port

HOM interference was measured for all input and output combinations in the 4-port device. These measurements are shown in Fig. 4.5). We see a variety of different magnitudes and signs of the visibilities for the various input/output combinations. This is due to the quantum term $Q_{i,j}^{k,l}$ in Eq. (4.12), which exhibits constructive or destructive interference, depending on the relative phases of the elements of U. The fact that all outputs had a visibility greater than 50% (or less than (−50%)) indicates that the output states are strongly non-classical.

The experimental visibilities can be compared to those predicted from the 4-port model in section 4.5. In contrast to the tritter the classical intensity measurements in the 4-port are insufficient to determine the phase ϕ due to the additional path lengths of waveguides two and three. Therefore after fitting $\eta = 0.377$ from the classical intensity measurements, the visibility measurements from a single input are used, namely inputs two and three, to fit ϕ. Using maximum likelihood estimation, ϕ was fitted from the six HOM dips in Fig. 4.5(d). This fit determined $\phi = 0.07\pi$. It is clear that this value, corresponding to the path length differences between the inner and outer arms of the 4-port (see Fig. 4.2(c)), is very close to the intended value of zero. This demonstrates the precision available when fabricating laser written circuits with specific and stable phase relationships. After substituting the determined η and ϕ into the transfer matrix Eq. (4.7) we can use (4.12) to predict the other 30 visibilities in Fig. 4.5. The predicted visibilities are compared to the measured visibilities (see Fig. 4.5(g)) and display a qualitative match, correctly identifying the sign and magnitude of each visibility. Using other input combinations to determine ϕ produced similar predictions. However, due to the assumption that all directional couplers in the circuit had the same reflectivity, the resultant overlap in Fig. 4.5(g) between the predicted visibility and measured visibility is not exact. This assumption simplified numerical calculations and is therefore still a valid method for the rapid characterisation and predictions of non-classical performance.

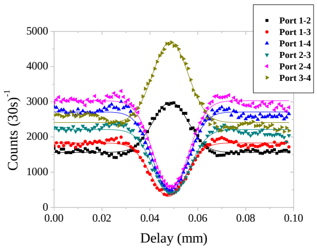

(a)

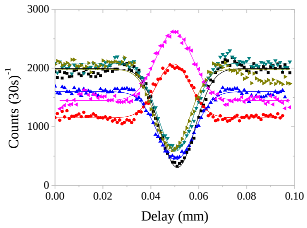

(b)

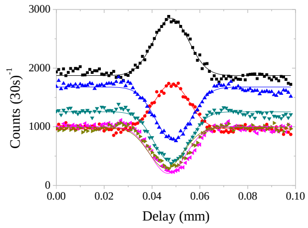

(c)

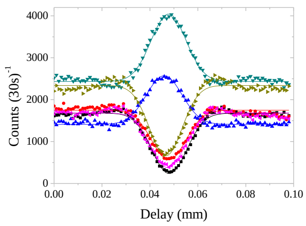

(d)

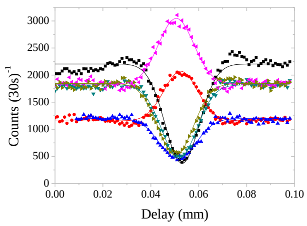

(e)

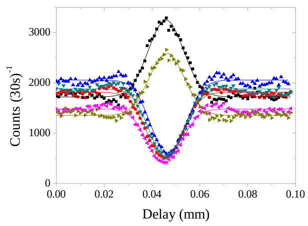

(f)

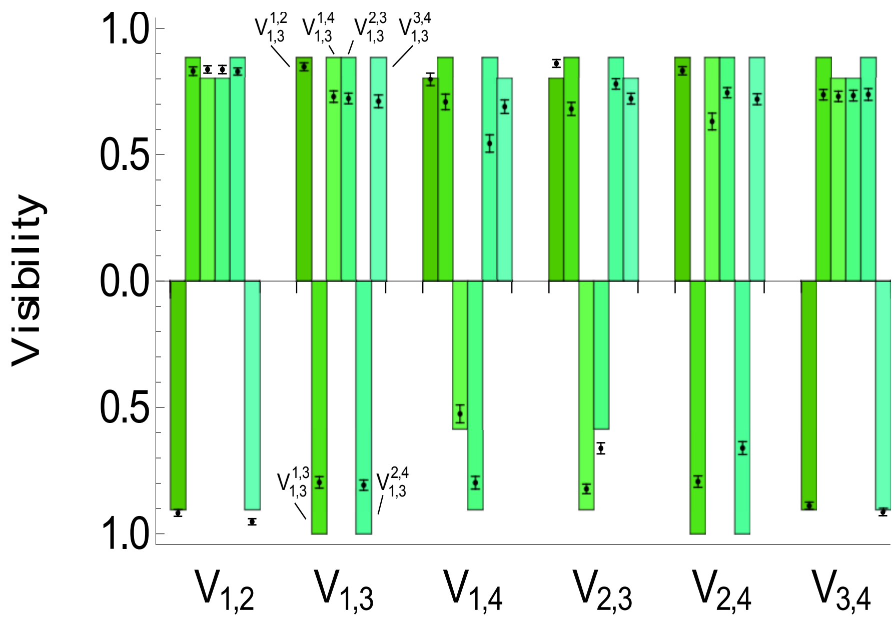

(g)

Figure 4.5: Four-port HOM dips for (a) input ports 1 and 2, (b) for input ports 1 and 3 (c) for input ports 1 and 4 (c) for input ports 2 and 3 (d) for input ports 2 and 4 (e) for input ports 3 and 4. (f) Experimental four-port visibility matrix determined from the HOM dips. (g) Comparison of measured four port visibilities (error bars) and theoretical predictions (columns) from the four-port model. Note the slight offset in the minimum values in each graph is due to photon collection arm realignments required after each measurement resulting from thermal drift.

4.7 Comparison with the existing literature

Two-photon correlation measurements were performed on integrated 3 and 4 port devices. The visibilities observed for our tritter compare extremely well with bulk optic demonstrations where visibilities, for only one pair of input ports, $V^{1,2}_{1,2} \sim 50\%, V^{1,3}_{1,2} \sim 48\%$ and $V^{2,3}_{1,2} \sim 26\%$ are observed [240]. In addition our tritter displays greater symmetry than a fiber optic based example where visibilities, observed only for a single pair of input ports $V^{1,2}_{1,2} \sim 50\%, V^{1,3}_{1,2} \sim 30\%$ and $V^{2,3}_{1,2} \sim 25\%$ [242]. The four port has shown a uniform output very similar to a bulk optic example, where visibilities of $V^{1,2}_{1,2} \sim 75\%, V^{1,3}_{1,2} \sim 66\%, V^{1,4}_{1,2} \sim -66\%, V^{2,3}_{1,2} \sim -80\%, V^{2,4}_{1,2} \sim 75\%$ and $V^{3,4}_{1,2} \sim 66\%$ were observed [240]. Thus the analysis is both more thorough and of a similar quality when compared to these technique, with the significant benefit of being highly compact. Future work could seek to exploit methods of beam shaping to counteract the effect of modification elongation which is otherwise unavoidable due to the Rayleigh range of the objective compared to the focal spot size and the limitations on numerical aperture. By using schemes such as those exploited by Salter *et al.* which use adaptive methods to produce a highly circular spot size at any depth in a glass substrate [165, 170]. This would mean that the coupling between waveguides would be identical in all directions resulting in highly symmetric device operation.

Furthermore our 4-port device out performs a multimode interference device described in [253]. The significant challenge of MMI devices is the extremely narrow bandwidth operation [259]. This is a significant fact since it demonstrates that, as an integrated platform, the laser writing technique offers the potential to produce high fidelity quantum circuit components where a 3D capability is advantageous for circuit size or complexity requirements. Advances have been made since this work was completed and a tunable waveguide array has been produced which was characterised with 3 photons in three separate modes [260]. Furthermore, a laser written three-port has also been fabricated and characterised with three photons showing extremely symmetric operation [78]. The methods used to produce a more symmetric device relied both on the symmetry of the input waveguide s-bend prior to the interaction region combined with offsetting the elliptical waveguides to produce a resultant symmetric supermode.

4.8 Application of multiports

The multiports described in this chapter have a number of key applications, among them the interlinking methods of state preparation and interferometry. Spagnolo *et al.* showed that multiport interferometers, combined with Fock state inputs, can in principle provide means of phase estimation which is more sensitive than that obtained with the equivalent photon number injected into a two mode interferometer. Although this interferometry scheme, which exploits the 3 dimensional geometry of the laser writing technique, was outlined [261], the potential convenience of combining state preparation with this process was overlooked. Pryde *et al.* proposed a simple scheme which combines (we will not use the labelling scheme from that paper but continue with the convention used throughout this chapter) an N-port device with a 2-port device to form a Mach Zehnder interferometer [262]. The basic example, the N=2 port results is a Mach Zehnder where an input of $|1_a, 1_b\rangle$ results in the maximally path entangled state $|2,0\rangle + e^{i2\phi}|0,2\rangle$ and therefore a fringe visibility of $\lambda/2$ is obtained. However, for the N=3,4 port a greater diversity of options are available. For a Fock state input such as $|1_a, 1_b, 1_c\rangle$ in the 3-port or $|1_a, 1_b, 1_c, 1_d\rangle$ in the 4-port it is possible to then post select on the $\lambda/3$ or $\lambda/4$ fringe. Potential simplifications on the photon source requirements are possible by supplementing a Fock state for one or more coherent states. This is extremely desirable and further highlights the application of multiports in interferometry. A further prospect would be the heralded generation of a path entangled NOON state. This would greatly enhance the practicality of multiports as state preparation facilities. Pryde *et al.* showed that injecting the state $|2_a, 2_b, 1_c, 1_d\rangle$ into a 4-port would yield an output of between modes b and d of $|4,0\rangle + e^{i4\phi}|0,4\rangle$ and a single photon at both modes a and c [262]. Thus by detecting photons in modes a and c the creation of the NOON state can be confirmed (with success probability of 3/64) and does not need to be destroyed through postselection. Although, unless the state $|2_a, 2_b, 1_c, 1_d\rangle$ is deterministically prepared then postselection of the output modes b and d is still required to confirm operation. However, alternatively in this instance postselection with quasi-number resolution could be used to observe the $|4,0\rangle+e^{i4\phi}|0,4\rangle$ fringe which is similar to those schemes used in [263–265].

Another interesting question is the entanglement which can be produced using a multiport or indeed an interferometer where a pair of multiports form a multi-arm Mach Zehnder interferometer (as shown in Fig. 4.6). Brougham *et al.* showed that such multiport interferometers can produce a wide range of entangled states and a simple condition can be used to assist in determining the range of states which can be produced using a multiport interferometer [236]. The excitement and manipulation challenges of these states also increases since systems composed of three qubits can be bi-separable (only two of the three qubits are entangled with the third separable) or exhibit tri-partite entanglement [266]. Three qubit states which are bi-separable, such as W states, or tri-partite entangled Greenberger-Horne-Zeilinger (GHZ) states, are exciting as they are (though complex to delineate in practice) maximally entangled [267]. Such entangled states are interesting for fundamental tests of quantum mechanics [268–271]. A W-state can be easily produced using multiports and for a 3-port device a path encoded state is easily produced by injecting a single photon input resulting in the output $W = \frac{1}{\sqrt{3}}(|100\rangle + |100\rangle + |100\rangle)$. Though this state is potentially useful it may be more desirable to produce entanglement of three polarisation encoded qubits using a 3-port. It must be noted however that this would require a polarisation insensitive device since multiple polarisation states would need to be interacted in the structure. This can be achieved (probabilistically with $\frac{1}{9}$ success rate) using three photons two H and one V each injected into separate ports of a 3-port with

$$U = \frac{1}{\sqrt{3}} \begin{pmatrix} 1 & 1 & 1 \\ 1 & e^{\left(i\frac{2\pi}{3}\right)} & e^{\left(i\frac{4\pi}{3}\right)} \\ 1 & e^{\left(i\frac{4\pi}{3}\right)} & e^{\left(i\frac{2\pi}{3}\right)} \end{pmatrix} \tag{4.15}$$

and a postselected output of $\left(e^{\left(i\frac{4\pi}{3}\right)} + e^{\left(i\frac{2\pi}{3}\right)}\right)(|VHH\rangle + |HVH\rangle + |HHV\rangle)$ can be obtained [241]. This process can be combined with different combinations of type-I, type-II SPDC sources and three or four ports to produce three or four photon W states with different probabilities [272]. For instance the state

$$\sqrt{\frac{2}{3}}|VHH\rangle - \frac{1}{\sqrt{6}}|HVH\rangle - \frac{1}{\sqrt{6}}|HHV\rangle \tag{4.16}$$

is used in the telecloning protocol of Bužek *et al.* which seeks to examine the imperfect cloning of quantum encoded data and hence motivates interest for cryptography protocols [272, 273].

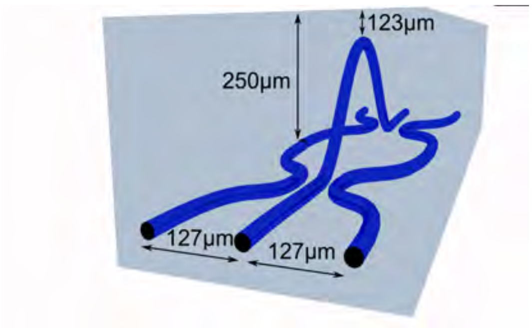

FIGURE 4.6: A rendering of the design of a multiport interferometer where one arm of the interferometer is brought close to the surface of the glass sample. Using this method a resistive heater can be used to tune its relative phase.

Spagnolo *et al.* analysed the output of a 3-port when injecting $|111\rangle$ and observed the resulting output states [261]. By adjusting input state polarisation configuration the W state described above could be produced and incorporated into interferometric measurements. Furthermore, multiport devices offer an interesting means of interacting states encoded in higher-dimensional Hilbert spaces or *qudits* [274]. Such *qudits* are exciting for both enhanced informational security and fundamental tests of nonlocality [275, 276]. There are demonstrations where information is encoded onto a pair of particles with two degrees of freedom have been combined and encoded in four degrees of freedom of a single particle [277–279]. Such a procedure has its classical communication analogue in for instance the amplitude, frequency and spatial mode encoding of data. Proposals to exploit multiple degrees of freedom to encode classical information and multiplex/demultiplex it in 3D integrated photonics exist, for instance using spatial modes of a low mode optical fibre or on-chip devices [280, 281]. These translate directly to the "quantum joining" or "quantum splitting" of n lower dimensional Hilbert spaces of dimension d onto a new n/d Hilbert spaces of dimension nd [275, 279]. Therefore, higher dimensional spaces encoded onto multiple single photons could be interacted in multiport splitter and interferometers and generate highly entangled multidimensional outputs. Controlling such interactions could be advantageous in quantum communication where multiple degrees of freedom encoded on a single particle may be more robust to environmental decoherence. This could form a transmission or data line which require fewer particles on which to encode information. Obtaining multiple single photons is challenging and therefore if more information can be encoded on the same single photon then a reduction in resource size is possible. In a quantum computer, exploiting atoms as the processing qubits, a multiplexer/demultiplexer could form the backbone of a photon based bus or other short range interconnect which exploits a photons reduced decoherence with the environment and multiple degrees of freedom for encoding and act as a processor interface.

4.9 Conclusions

This chapter has outlined the design, fabrication and characterisation of multiport splitters. A laser inscription technique was used to fabricate a 3-port and 4-port device. Both devices exploit the 3D fabrication potential of the laser inscription process. Devices were fabricated and characterised using both classical methods and non-classical photon pair measurements. The non-classical operation was predicted using the classical measurements and the visibilities were found to be a function of errors in producing the ideal reflectivity of the devices. For the 3-port device this was due to the asymmetric coupling of the waveguides in the interaction region and the tapering region. In the four port device, composed of four individual directional couplers, the reflectivity of the individual directional couplers was below the ideal value of 0.5 and there were minor variations in each coupler due to reproducibility constraints of the laser writing process. Despite these inaccuracies the non-classical visibilities compared well with previous implementations of multiports using bulk, fibre and integrated optic components. These devices show potential in state preparation and manipulation.

"If I called 35 degrees hot then what the hell would I call 45?"

Andrew White

5
Quantum circuits

At the end of the last chapter the concept of unitary design, state preparation and post selection were introduced. This chapter builds on these concepts to produce a specific component which enables a conditional state transformation on a qubit in a post selected way. The theory of linear optical quantum computing (LOQC) is built on the concept of sacrificing deterministic nonlinear transformations for the ability to probabilistically perform these transformations on states by using linear optical components.

Despite the rapid adoption of integrated waveguide devices for quantum computing applications, logic gates often operate in a destructive post-selected fashion, thus not allowing for further scaling, of a larger quantum circuit, beyond the depth of a single gate. This chapter describes an on-chip version of a heralded controlled-phase (C-Phase) gate known as the Knill gate. Since the gate is heralded, it is non-destructive and in principle could permit circuit scalability. This gate produces a π phase shift on a target qubit conditional on the state of a control qubit [282], and does so in a heralded way without destroying the control and target qubits. It requires four photons for operation, two of which act as the target and control path-encoded qubits and two ancillary photons which herald a successful operation of the gate.

In this chapter the FLDW fabrication of the Knill gate is outlined. Parametric studies were performed to isolate directional coupler designs required for the fabrication of the Knill gate. The fabrication tolerances and sources of error during fabrication are detailed. A coherent state characterization method [283] was performed to obtain the unitary implemented by the fabricated device. A preliminary study of the potential to reprocess a circuit is discussed. Finally, the remaining challenges which prevent the full characterisation of the circuit operation are discussed. This includes the apparatus required to perform a quantum process tomography measurement and the lack of deterministic photon sources.

5.1 Controlled-phase gate

The C-Phase gate, a two-qubit gate, is ubiquitous in quantum information, because together with single-qubit gates, it forms a universal gate set capable of constructing any unitary operation. In optical implementations the entangling two-qubit gate is the most difficult component to realise since it requires excellent multi-photon indistinguishability. For an arbitrary two qubit input state this gate flips the sign on one term: $\alpha_{00}00 + \alpha_{01}01 + \alpha_{10}10 + \alpha_{11}11 \rightarrow \alpha_{00}00 + \alpha_{01}01 + \alpha_{10}10 - \alpha_{11}11$.

The heralded C-Phase gate, originally proposed by Knill [282], as shown in Fig. 5.1, is implemented using four beamsplitter operations on four modes with two initial π phase shifts on the input target and control arms [282]. The circuit induces an additional π phase shift if there is a photon in both the control and target modes when conditioned on the detection of one photon in each ancilla mode. Bulk optical implementations of C-Phase gates have been realized in the past using polarization and spatial encoding [284]. However, the Knill circuit lends itself well to an on-chip design, with the FLDW technique making circuit crossing convenient, while integration also ensures phase stability.

Since the coupling is symmetric between modes, we can define the beam splitter operation in a similarly symmetric way:

$$U_{BS} = \begin{bmatrix} \cos\theta_n & -i\sin\theta_n \\ -i\sin\theta_n & \cos\theta_n \end{bmatrix}, \tag{5.1}$$

the ideal required values are $\theta_1 = \theta_2 = \cos^{-1}\frac{1}{\sqrt{3}}$, $\theta_3 = -\cos^{-1}\frac{1}{\sqrt{3}}$ and $\theta_4 = \cos^{-1}\sqrt{\frac{1}{2}+\frac{1}{\sqrt{6}}}$, corresponding to beamsplitter reflectivities of $\eta_{1,2}$=33%, η_3= − 33% and η_4=90.8% as shown in Fig. 5.1. This set of operations results in the ideal unitary

$$U_{\text{ideal}} = \begin{bmatrix} -\frac{1}{3} & -\frac{\sqrt{2}}{3} & \frac{\sqrt{2}}{3} & \frac{2}{3} \\ \frac{\sqrt{2}}{3} & -\frac{1}{3} & -\frac{2}{3} & \frac{\sqrt{2}}{3} \\ -\frac{\sqrt{3+\sqrt{6}}}{3} & \frac{\sqrt{3-\sqrt{6}}}{3} & -\frac{\sqrt{3+\sqrt{6}}}{3\sqrt{2}} & \sqrt{\frac{1}{6}-\frac{1}{3\sqrt{6}}} \\ -\frac{\sqrt{3-\sqrt{6}}}{3} & -\frac{\sqrt{3+\sqrt{6}}}{3} & -\sqrt{\frac{1}{6}-\frac{1}{3\sqrt{6}}} & -\frac{\sqrt{3+\sqrt{6}}}{3\sqrt{2}} \end{bmatrix}. \tag{5.2}$$

This unitary represents the action of the gate on linear functions of the mode creation operators $U[\alpha_c a_c^\dagger, \alpha_t a_t^\dagger, \alpha_a a_a^\dagger, \alpha_b a_b^\dagger]^T$ where $a_c^\dagger, a_t^\dagger, a_a^\dagger, a_b^\dagger$ are the bosonic mode creation operators in the control, target and the two ancilla modes respectively. Alternatively it can be thought of as the unitary governing the four-dimensional space of a single photon input and output in the device.

5.2 Device fabrication

The Femtosource 5.1 MHz repetition rate laser and 100× oil immersion objective (Zeiss N-Achroplan, $NA = 1.25$) were used to fabricate the waveguide circuits in boro-aluminosilicate samples (Corning Eagle 2000 glass substrate). The writing speed used

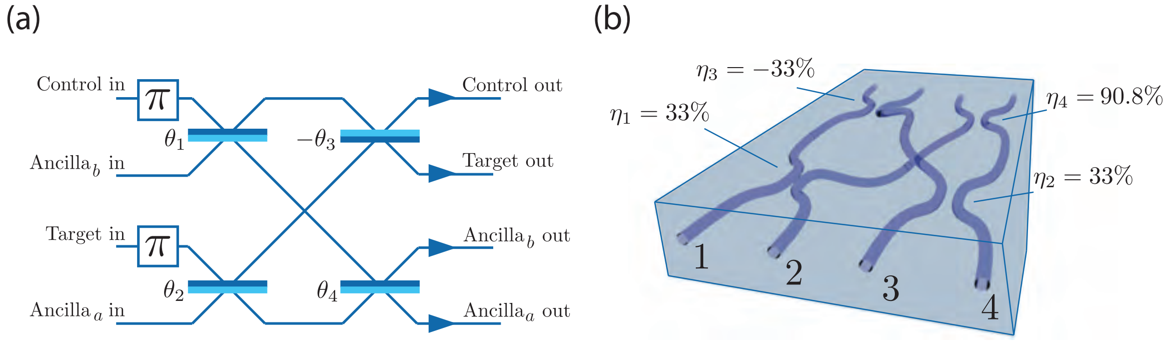

Figure 5.1: (a) A layout of the Knill C-Phase device using linear optic components showing input modes, phases and outputs, (b) A rendering of the same device using 3D waveguides where input 1 corresponds to control in, input 3 corresponds to target in and inputs 2 and 4 correspond to ancillas. The waveguides are initially separated by 127 μm and then taper into the four separate beamsplitter regions and waveguide crossover, before returning to a planar output array.

was 20 mm/sec, the pulse energy was 66 nJ and a 5 to 1 telescope was used to produce a beam sufficient to completely fill the 4.5 mm back aperture of the writing objective. Following the writing process, the sample was subject to annealing, in order to produce a more symmetric refractive index profile [111]. The reader is referred to chapter 3 for more details but briefly the procedure involves heating the glass chip to above the stress point of the material and then returning to room temperature slowly to avoid producing any additional stress. The sample was heated to 750 °C over a 12 hour period and a subsequent cooling stage of 24 hours to room temperature. The resulting refractive index profile is significantly different from that of an un-annealed waveguide. Figure 5.2(a) shows a transmission interference contrast (TDIC) microscope image of a waveguide which supports an 800 nm mode. There is a bright region in the center of the waveguide with a positive refractive index change, a dark region which indicates a negative index change, and an additional outer region of positive index change. After annealing however, the outer region is completely removed while the high index core and a surrounding negative region remains the same. Figure 5.2(b) is a bright field (BF) microscope post-annealing, of a waveguide which is single mode at 800 nm, showing that the outer region of positive refractive index change has been completely removed. This results in a mode field diameter of 5 μm which has excellent overlap with a 800 nm single-mode optical fibre. Using this technique an insertion loss of 1.8 dB was measured for straight waveguides of length 40 mm. To accommodate for variance in the writing conditions, a total of twelve separate Knill circuits were fabricated. This required a detailed study of the evanescent coupling relationship in directional couplers composed of annealed waveguides.

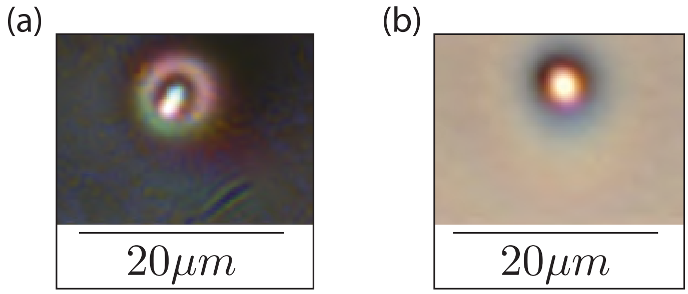

FIGURE 5.2: (a) TDIC microscope image of a laser written waveguide which is single mode at 800 nm prior to annealing. (b) A bright field microscope image of a waveguide after annealing is shown since a TDIC image would not highlight the presence of the depressed, or darker region surrounding the core. It is important to note that these are different waveguides, an annealed waveguide which is single mode at 800 nm is not single mode prior to annealing.

5.2.1 Parametric study of directional coupling

Prior to fabrication of the Knill gate a scan of the evanescent coupling between a pair of waveguides was performed to ascertain the parameters required for obtaining three different reflectivity directional couplers using annealed waveguides. Initially a measurement of the optimal spacing was performed. Figure 5.3 shows the relationship between waveguide spacing, interaction length and the energy transfer between waveguides. A small waveguide spacing results in a large mode overlap and it is difficult to obtain a range of reflectivities with high precision since very small changes in length will result in a change in the coupling between waveguides. The waveguide spacing of 5-6 μm results in a large energy exchange at short interaction lengths. Unfortunately, this is also due to the waveguide s-bend region which means there is coupling prior to the interaction region. Hence, it is desirable select a waveguide spacing which minimises this advanced coupling while still requiring a short interaction length. A waveguide spacing above 7 μm was found to offer the best balance between minimising the coupling prior to the interaction region, yet still requiring a short interaction length. It is also clear from this graph that the length of the directional coupler is the optimal parameter to vary when seeking to tune the reflectivity since this allows much finer control on the reflectivity compared to the waveguide spacing.

The reproducibility of these devices is critical to circuit design. The day to day repeatability of directional coupler reflectivity varies with laser output power and pulse duration, resulting in changes to waveguide parameters like waveguide width and refractive index, these in turn effect the coupling ratio. Therefore a parameter scan must be performed varying the length of the interaction region to isolate the device with the correct reflectivity. However, for this technique to be effective the reproducibility of the devices within a fabrication run must be consistent. Hence an understanding of the effects of minor variations which can occur during the waveguide fabrication process is important.

The laser writing process focuses a high power laser inside a glass substrate and

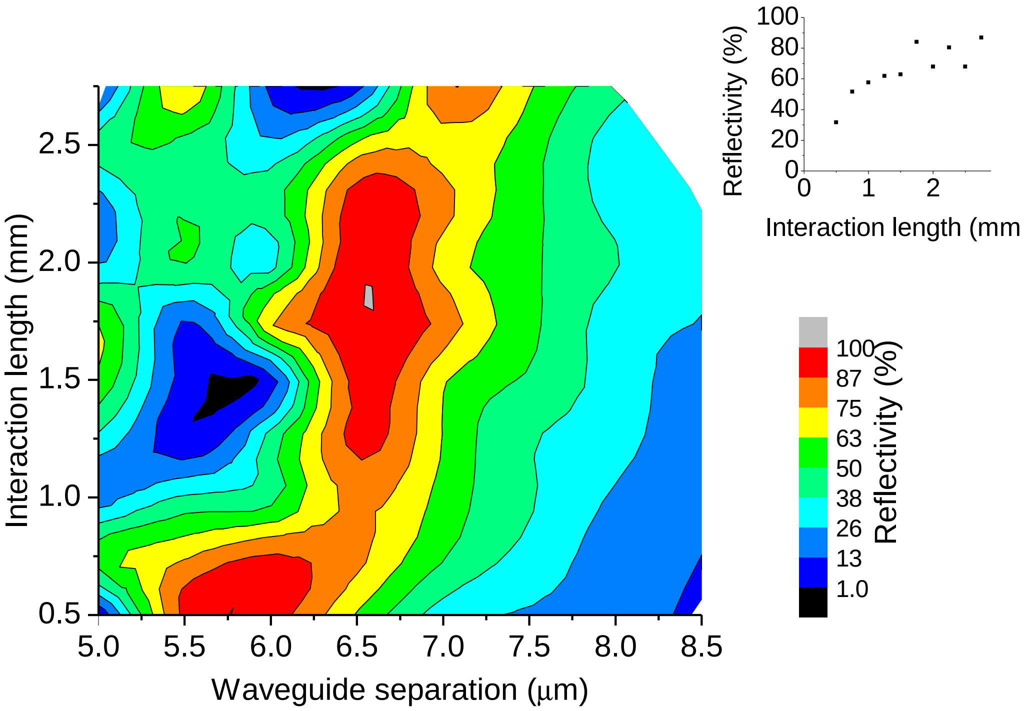

FIGURE 5.3: A plot showing the measured coupling between a pairs of waveguides with different waveguide spacings and interaction lengths. Measurements were performed for waveguide spacing intervals of 0.5 mm and the inset shows the data collected for a 7 μm separation.

then translates the substrate using 3-axis stage system with respect to the laser. The reflectivity of directional couplers will be affected by changes in waveguide spacing, diameter, refractive index and refractive index mismatch. The waveguide spacing could be caused by beam pointing stability issues or translation stage inaccuracy. This is unlikely to be the origin of the reproducibility errors, the stages are specified to provide 10 nm accuracy and has been measured by S. Gross to be be within this range [285]. Furthermore the beam pointing stability is sufficiently stable to eliminate it as a source of error since work by S. Gross in writing waveguide Bragg gratings (WBG), using the same translation stages and laser, has shown resolutions below 100 nm [158, 285]. A waveguide spacing change of $\pm$100 nm can cause an change in waveguide coupling. Therefore, the stages and beam pointing stability, may contribute to a change in reflectivity but are not the main contributors. Waveguide diameter does have a significant effect on waveguide coupling but only when the mode is not tightly confined, for V numbers below 1.5. The refractive index of the waveguides contributes to the coupling between waveguides, in effect an increase or decrease in refractive index (if the refractive index of the two waveguides remains the same) will result in a change in the confining potential and thus affect the tunnelling rate between the waveguides. However, the most significant affect on waveguide coupling ratio is due to the refractive index mismatch between waveguides. This is illustrated in Fig. 5.4, where the relationship between a refractive index mismatch between waveguides is shown. The plots also show the effect of waveguide spacing on the sensitivity of the reflectivity to a refractive index mismatch of 1.5% and below. For larger waveguide spacings of 8 μm the, phase mismatch caused by a refractive index difference of 0.75%, results in a maximum energy exchange of 50%, compared with the normal value of 100%. This is also another motivation for keeping waveguide spacings as small as reasonably possible, since the effect of index mismatch is reduced, as can be seen for the case of a 7 μm spacing. Furthermore, the desired waveguide reflectivity also effects the reproducibility since for splitting ratios requiring a short interaction length the refractive index mismatch has a much smaller effect than for longer devices.

The relationship between interaction length and waveguide reflectivity can also be exploited to produce waveguides with specific phase relationships, by increasing the waveguide interaction length, z to complete an oscillation between waveguides a π phase shift can be induced in the output amplitudes,

$$\begin{aligned} A_1(z) &= A_1(0)\cos(Cz) \\ A_2(z) &= -iA_1(0)\sin(Cz) \end{aligned} \tag{5.3}$$

where C is a coupling coefficient. Extending the waveguide length through an oscillation (meaning a full power transfer between waveguides) gives,

$$A_2(z) = -iA_1(0)\sin(Cz) \rightarrow -iA_1(0)\sin(Cz_1 + \pi) \rightarrow iA_1(0)\sin(Cz_1). \tag{5.4}$$

Thus mapping out the parameter space where this value is observed requires a measurement of a full oscillation of a directional coupler. Figure 5.5 shows a measurement of the coupling between two waveguides with spacings of 7 μm and 8 μm. For the spacing of 7 μm and an interaction length between 5-6 mm a directional coupler with a π phase shift and a reflectivity of 33% is obtained. The directional coupler errors can also be seen, in particular the longer the interaction length the more sensitive the directional coupler is to minor refractive index mismatches. A random, large change can also be seen for the 7 μm spaced waveguides at 3.5 mm interaction length, which corresponds to refractive index mismatch between the two waveguides of 2×10^{-4}, or a 3% difference.

5.3 Knill gate characterization

To characterize the operation of the fabricated Knill circuits we employed a technique demonstrated by Rahimi-Keshari *et al.* [283] which allows for a robust and efficient characterization of multiport optical circuits using only single and two-mode bright coherent states and output intensity measurements.

The technique therefore gives the matrix U_{meas}, which maps the input creation operators $a^\dagger$ to the outputs $b^\dagger$ via the transformation $b_j = \sum_i U_{\text{meas}_{ij}} a_i$. Each element of U_{meas} comprises of a modulus r_{ij} and a phase θ_{ij}, such that $U_{ij} = r_{ij} e^{i\theta_{ij}}$. The moduli are obtained simply by measuring the intensity at every output j given an input intensity at the input i, thus giving 16 individual moduli for the four-by-four mode circuit. The

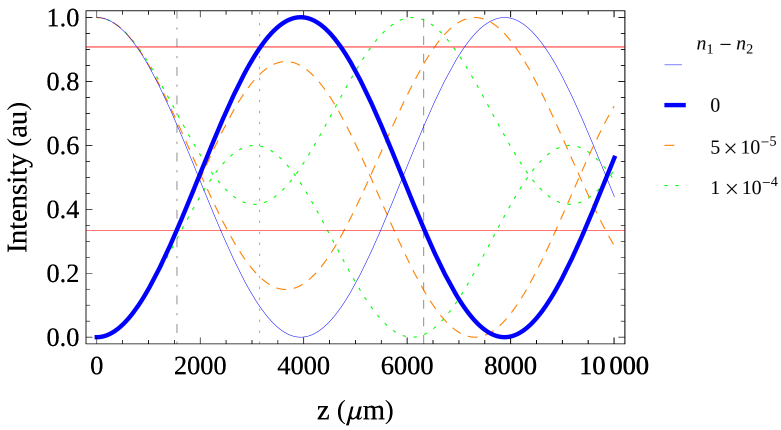

(a)

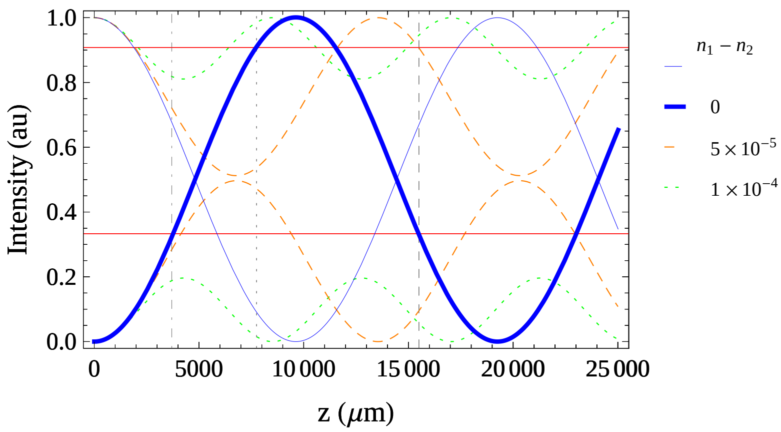

(b)

Figure 5.4: Theoretical plots showing the sinusoidal exchange of energy between a pair of waveguides with $n_1 = 1.54 + 6.5 \times 10^{-3}$ and diameters of 4.5 μm. The differences between the refractive indices of these waveguides are plotted, $n_1 - n_2$ is 0 (blue, solid), 5×10^{-5} (orange, dashed) and 1×10^{-4} (green, dotted). This results in a phase mismatch between waveguides and means full power exchange between waveguides is not possible. The points for the $n_1 - n_2 = 0$ curve, where the power exchange is 0.33 (vertical, dashed-dotted), 0.908 (vertical, dotted) and -0.33 (vertical, dashed), are highlighted with horizontal red lines. (a) shows this for a waveguides separated by 7 μm and (b) 8 μm.

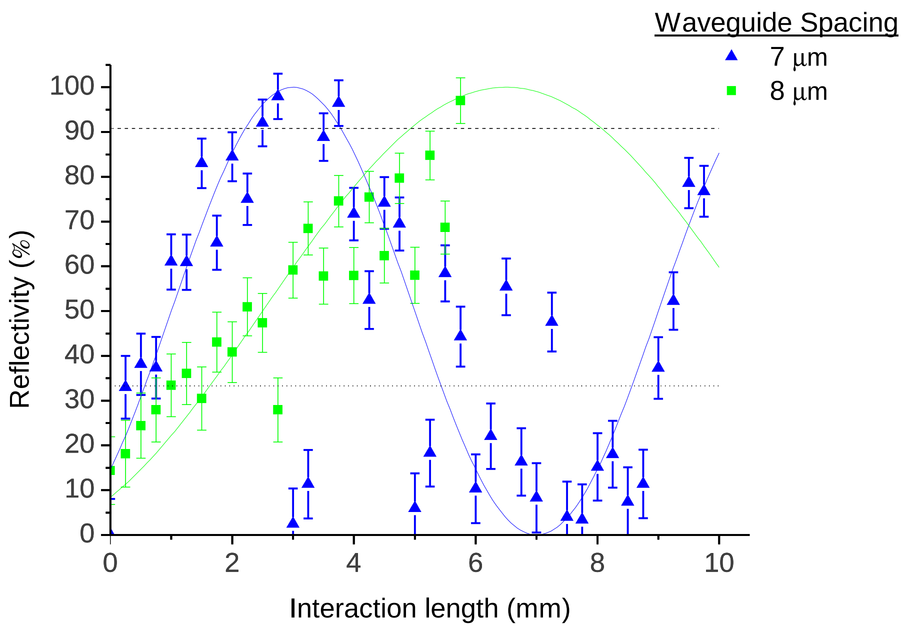

FIGURE 5.5: This graph shows the measured reflectivity between two waveguides which form a directional coupler. The spacing of the two waveguides is 7 μm (blue) and 8 μm (green) with fits given by assuming step index waveguide refractive indices of 1.54+6.5 $\times$ 10^{-3} and diameters of 4.5 μm. Reflectivity values of 33% (dotted) and 90.8% (dashed) are highlighted with horizontal lines.

phases θ_{ij} of each element are obtained via phase sensitive two-mode coherent state inputs. Here the two-mode coherent state is injected into a pair of input ports and a phase offset is induced in one of them. The output interference fringes are monitored using fast photodiodes and an oscilloscope from which the phases θ_{ij} can be directly obtained. Combined with the moduli, the results are used to produce a map of the circuit which is close to unitary, where losses are modelled as virtual beamsplitters which are included in a larger 8 by 8 near-unitary matrix.

Using the experimentally obtained map, the unitary matrix U_{meas}, a measure of the fidelity with the ideal unitary, U_{ideal}, can be defined as

$$F = \frac{|Tr\{U_{\text{ideal}}^{\dagger} U_{\text{meas}}\}|^2}{N^2}, \tag{5.5}$$

where $N = 4$ is the number of modes. Using moduli data and the reconstructed unitary it was possible to isolate beamsplitter reflectivities, and to calculating the fidelity for each device, this was performed for 12 different Knill gates and the results are shown in Fig. 5.6. This shows the reflectivities and relative phase in each device and is ordered in terms of decreasing fidelity. BS 3 was erroneously fabricated with a 60% reflectivity, rather than the intended value of 90.8%. This was due to a coding error which meant that the interaction length of the directional coupler was not iterated like the rest of the directional couplers (also clearly seen in Fig. 5.7). The highest fidelity obtained

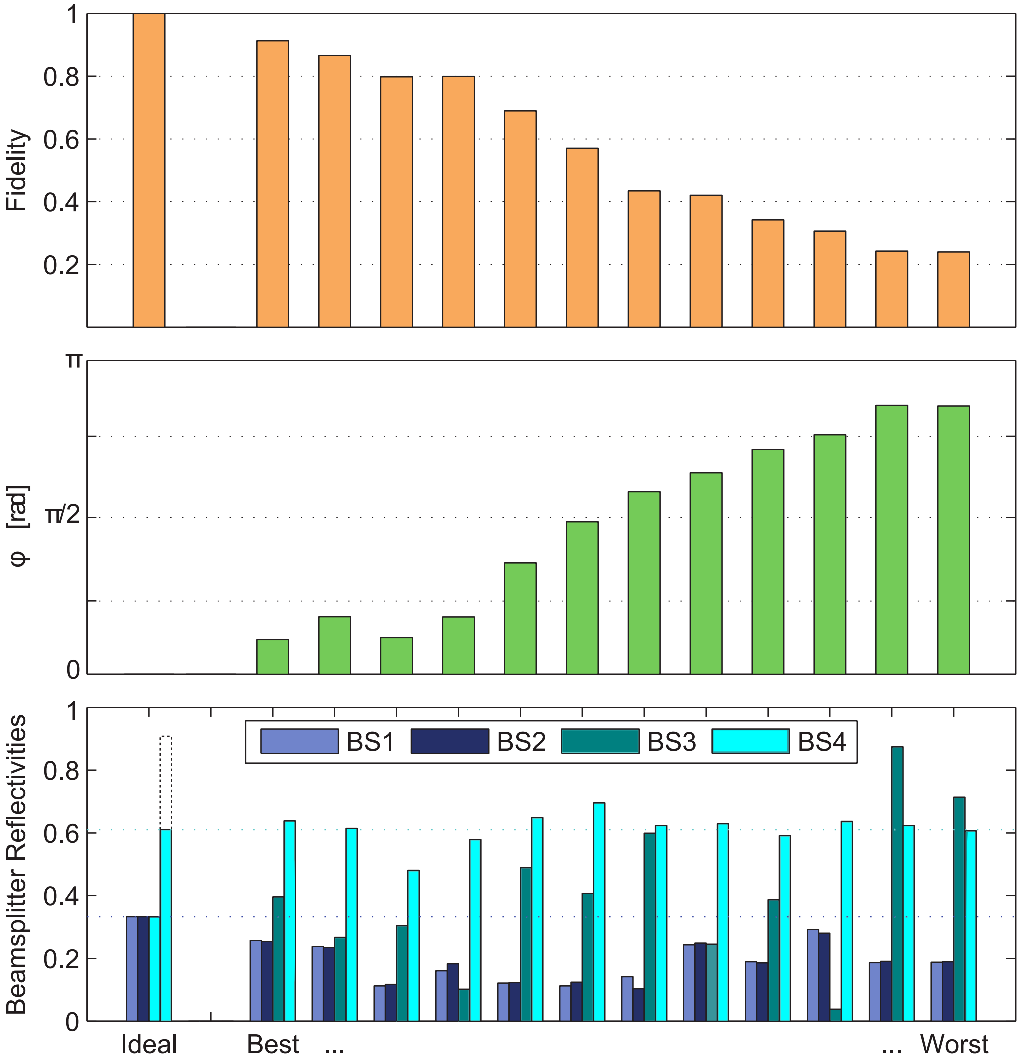

FIGURE 5.6: The calculated fidelity (from Eq. 5.5) is shown for each of the twelve fabricated Knill circuits. The phase offset from π is shown as well as the reflectivity of each beamsplitter in the device. The ideal Knill gate with a fidelity of one is on the left of the figure with the data ordered in terms of decreasing fidelity.

was 89% with respect to the ideal circuit and it demonstrates the proximity of the four directional couplers to both the ideal reflectivities and relative phase relationship. This data is further analysed in Fig. 5.7, which illustrates the relationship between the spread of beamsplitter reflectivities and the length of the directional coupler interaction region, for a fixed separation. Beamsplitter reflectivities, for short devices (0.25-0.75 mm) are reproducible within $\pm 5\%$. This shows the stability of the laser writing process during a fabrication run.

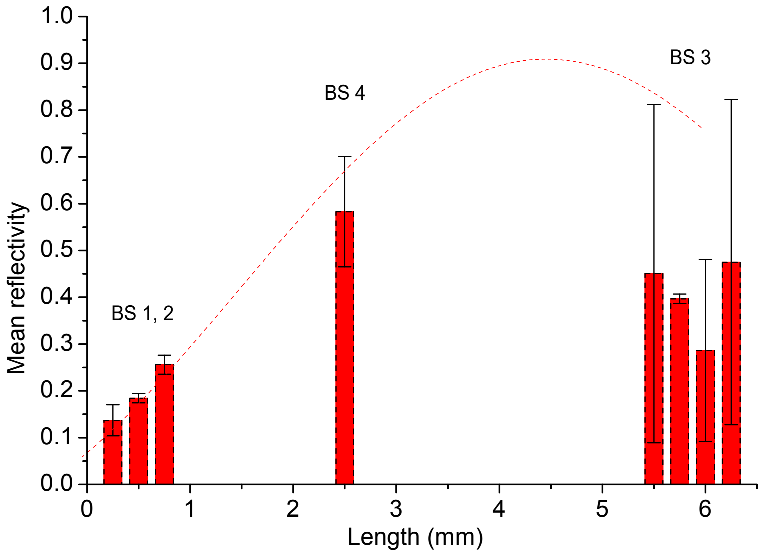

FIGURE 5.7: Showing the same reflectivity data contained in Fig. 5.6 but showing the mean reflectivity of directional couplers, with the error bars showing the standard deviation, for each interaction length. This shows the increase in the spread of reflectivities as the interaction length is increased. The dotted line shows the expected trend with an inflection point illustrating the length at which light begins to return to the initial waveguide.

5.4 Post tuning

The device characterisations have shown that the fidelity is highly sensitive to directional reflectivity. It is therefore desirable to improve the reproducibility of the waveguide circuits, or alternatively correct any errors. In fact the origin of the reproducibility constraints, the extreme sensitivity of a directional coupler to any change in refractive index of either arm, is what also permits adjustment of this structure. Figure. 5.4 shows the energy exchange between two waveguides separated by 7 μm. The refractive index of the two waveguides are $n_1 = 1.54 + 6.5 \times 10^{-3}$ and n_2 and it can be seen that when $|n_1 - n_2| > 0$ full power exchange between the two waveguides is not possible. Furthermore, it can be seen that the effect of a change in refractive index between the two waveguides effects longer devices more than shorter devices. It is clear that a small change in refractive index of below 3% can have a significant effect on the evanescent coupling, changing a 90% coupler to a 60% coupler. By packaging a device, bonding V-groove arrays to input and output facets, the circuit can be reprocessed and actively monitored to select the correct beamsplitter reflectivity. the imaging system of the laser inscription setup allow the imaging of waveguides forming a directional coupler. A screenshot of the image obtained by the laser vision system is shown in Fig. 5.8 which demonstrates the capability of locating and visualising the micron sized refractive index modifications. The location of the laser spot can be seen since it produces a white light emission due to supercontinuum generation at the focus. The laser power used was just high enough to produce a white light emission, of 15 nJ pulse energy, with a writing speed of 1.6 mm/sec. This was below the threshold for thermal accumulation meaning that the modification size was defined by the numerical aperture (NA=1.4) of the objective. This resulted in a very small refractive index modification estimated to be below 1×10^{-4}. A test sample, composed of a 70% directional coupler was modified to ascertain the refractive index response. It was possible to adjust the reflectivity of the device from 70±4% to 50±4% using 8 overpasses on one of the waveguides with respect to another. This resulted in an estimated refractive index shift of 1.5×10^{-4}, producing a phase mismatch which shifted the reflectivity of the coupler. The total loss of the structure (two facets and propagation loss) was not increased, within error, from the original 2.3 dB.

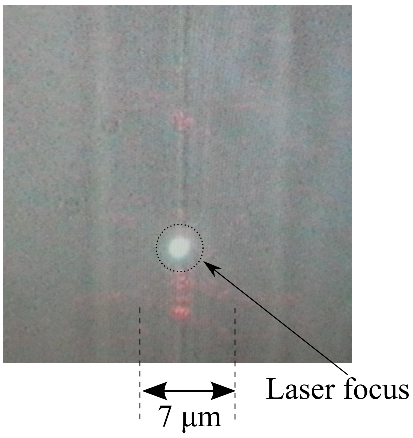

(a)

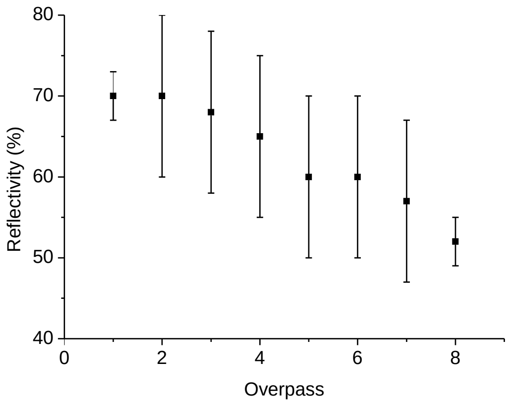

(b)

Figure 5.8: (a)Screenshot of the imaging system during reprocessing of a directional coupler, the laser focus is positioned between two waveguides forming a directional coupler, (b) the result of a postprocessing of a chip. The large error bars between 1 and 7 overpasses is due to the large fluctuations observed during the post processing experiment while the chip remains on the processing stage. V groove arrays are attached to the input and outputs of the chip and small temperature variations and mechanical vibrations cause the measured output power to fluctuate. Points 1 and 8 are taken once the chip has been measured before and after the process and the error bars are significantly reduced since the sample is stationary.

This calibration was used to modify a directional coupler in the Knill gate device. The 60% splitter was modified with the intention of producing a 90% splitter. This required a different approach which is to modify the interstitial region between waveguides, in effect to promote coupling. This technique produced a device with an 80±4% splitting ratio, however the total loss of the device was increased by 20% due to the large scattering loss from the modification located between the two waveguides. This technique could in principle be further improved to remedy the incorrect splitting ratios in circuits.

5.5 Characterisation challenges

Despite progress in forming the circuits required for a heralded and potentially scalable quantum gate, the resources required for a full characterisation are still lacking. Although measurements of two photon interferences yield an insight into the interactions occurring in the device, circuit operation still requires a pair of ancilla photons combined with a target and control qubit. Furthermore, since this circuit only produces a sign shift upon successful operation, it therefore can not be characterised by using, for instance, a truth table as for a CNOT gate. Although this circuit could be combined with Hadamard rotations at the input and output, it would not simplify the characterisation process significantly. This is due to the fact that the Hadamard rotations would require a pair of beamsplitters, forming an interferometer, which will need to be phase stabilised and the circuit embedded within. The most thorough characterisation method would use what is referred to a quantum process tomography (although a variety of other measures have been described) [286]. This would involve preparing a combination of input states, for both the target and qubit in the presence of ancilla photons, which are then injected in the device and the output projected to the corresponding combination of output states. Such a combination is typically composed of combinations of horizontally, vertically, diagonally and left/right circularly encoded states but can in fact be quite simple, such as described by Shabani *et al.* [287]. These states could be prepared in the spatial encoding basis by using a waveplate and a polarising beamsplitter. However, this would require a setup which embeds the waveguide circuit in a phase stabilised interferometer as shown in Fig. 5.9. Furthermore, the preparation of the ancillas and qubits require photon sources which are not currently available, as will be discussed in the next section.

5.5.1 Challenges of SPDC

Sources of identical single photons are required for the preparation of qubits. However, the quantum characterisation of the Knill gate, specifically full quantum process tomography, requires a minimum of four coincident single photons. Despite incredible progress in the production of multiple photon states [288], four-fold coincidences remain a challenging obstacle. The most efficient mean of photon generation remains spontaneous parametric downconversion, where the rate of obtaining a pair of photons from a single crystal per second is

$$C = \mu \eta_I \eta_S R, \tag{5.6}$$

here μ is the probability of obtaining a photon pair per pulse, $\eta_{I,S}$ are the extraction efficiencies for each photon and R is the repetition rate of the incident pump laser. The probability of obtaining four single photons is $\frac{C^2}{R}$. Assuming C is 50 kHz and the laser repetition rate is 100 MHz (typical values for a frequency doubled TiS pumped system), a typical fourfold rate is 25 Hz. However, multi-photon production probability, resulting in a reduced probability of obtaining a single photon in a single mode means this approach is not appropriate for the production of four single photons as will be described below.

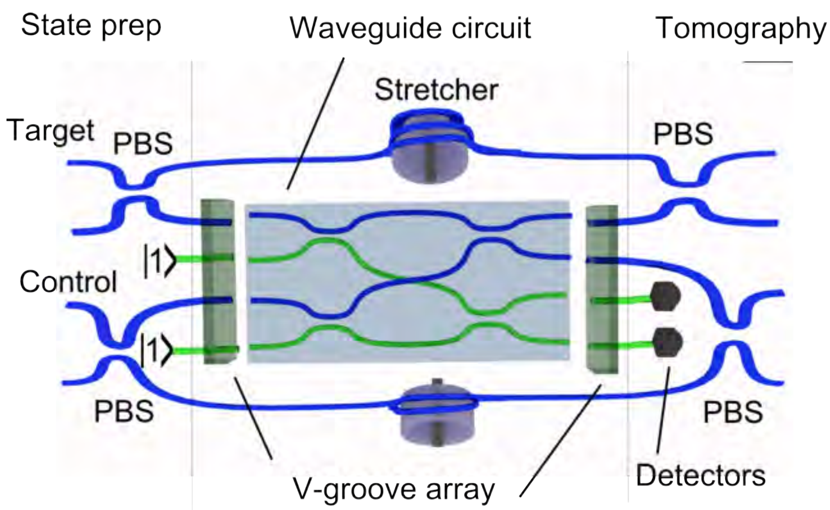

Figure 5.9: A schematic showing the layout of a quantum process tomography measurement of the Knill gate. The circuit must be embedded in a larger circuit comprising the logical 0 modes and furthermore methods for mapping input qubit states to output qubit states are required. The whole system demands phase stability hence necessitating active components shown here as fibre stretchers.

Recall from chapter 2 the pump beam interaction with a nonlinear medium (assuming a single mode approximation) is described by a Hamiltonian [94]

$$\hat{H} = \xi\hbar\left(i\hat{a}_1^\dagger\hat{b}_1^\dagger + H.c.\right), \tag{5.7}$$

Where $\hat{a}_1^\dagger$ and$\hat{b}_1^\dagger$ are photon creation operators in signal and idler modes a_1 and b_1 (H.c. is the Hermitian conjugate). ξ is the production efficiency parameter which contains the information about the nonlinear interaction and is linearly proportional to the pump amplitude. The state produced by a single SPDC source is

$$|\Psi_{SPDC}\rangle = \sqrt{1-|\lambda|^2}\sum_{N=1}^{\infty}\lambda^N|N,N\rangle_{a_1,b_1}, \tag{5.8}$$

where $\lambda = \xi\tau$ and τ is the interaction time in the nonlinear medium. Therefore the probability of generating N photon pairs is

$$P(N) = (1-|\lambda|^2)|\lambda|^{2N}. \tag{5.9}$$

For a pair of sources this becomes

$$P(N_1,N_2) = (1-|\lambda_1|^2)(1-|\lambda_2|^2)|\lambda_1|^{2N_1}|\lambda_2|^{2N_2} \tag{5.10}$$

where, if we assume that the source efficiencies are equal, $\lambda_2 = \lambda_1 = \lambda$, then we see that the case of a single pair of photons, simultaneously generated by each source, is an equally probable event as a pair of pairs generated by one source, i,e,

$$P(N_1,N_2) = P(0,2) = P(2,0) = P(1,1) = (1-|\lambda|^2)^2|\lambda|^4. \tag{5.11}$$

Most single photon avalanche diodes are unable to distinguish between 1 or 2 photons. Multiphoton events result in noise that can only be removed by postselection, or post processing (assuming it is possible) to only monitor events which were due to the $P(1,1)$ photon terms. In practice, when injecting states into a unitary, the goal of which is to learn about the unitary, it becomes extremely challenging to extract events only related to the $P(1,1)$ events. Hence another approach is to herald or trigger detection apparatus based on detection of one photon from one of the downconverted pairs. A method for producing a source of four single photons would be similar to that shown in Fig. 5.10. Using this process the $P(2,0)$ and $P(0,2)$ can be removed but an additional source is now required to obtain four photons. This then means post selection only occurs when a $P(1,1,1)$ event occurs. However, it should be noted that other probabilities such as $P(2,1,1)$, $P(2,2,1)$, $P(2,2,2)$ or other combinations are not eliminated using this approach and result in noise. Furthermore the rate for such a system, requiring 6 fold coincidences is sub-hertz meaning process tomography,which requires the mapping of six input states to six output states for each of the control and target channels, would take weeks or months depending on the overall system loss [287].

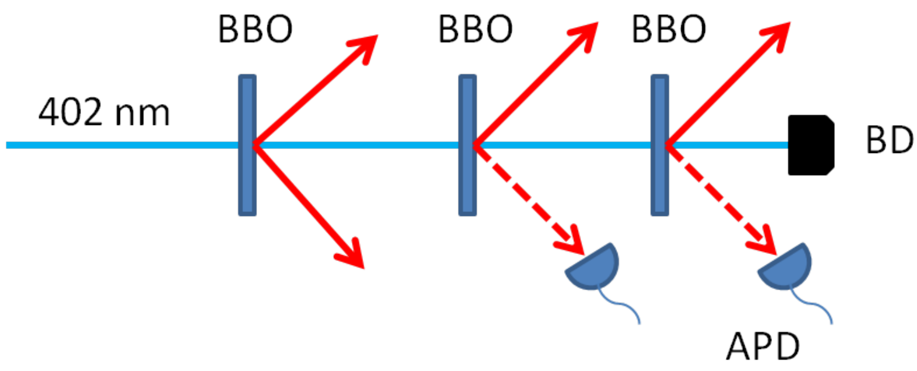

FIGURE 5.10: Typical layout for the production of a single, identical, four-fold photon coincidences

5.6 Conclusions

The application of mode transformations, achievable using the FLDW technique, have been applied to the design of a quantum logic gate. Integrated linear optics C-Phase gates have been fabricated using a 3 dimensional geometry. The design and performance of these gates have been determined and shows that it is possible to produce complex unitary transformations using the FLDW technique. The potential to enhance this further using a post-processing technique is described. However, these devices could not be fully characterised due to a lack of resources, specifically single photon sources. The next chapter will detail the potential to integrate sources with laser written circuits and methods to enhance the intrinsic signal-to-noise ratio available from these on-chip devices.

"We who had given up drink had always a soft spot for Michael's [Collins] use of drink."

Ernie O'Malley

6 Hybrid integration

During this thesis work integrated devices have been fabricated and ultimately characterised using a bulk spontaneous parametric downconversion (SPDC) photon pair source, where light is coupled from free space into optical fibres. Photons are collected and routed into a waveguide circuit to perform a characterisation. However, at the end of the last chapter is became clear that although integrated circuit design using FLDW methods is advancing, the resources necessary to characterise such devices are still unavailable – specifically multiple identical single photon sources. This is a serious impediment to the realisation of complex quantum information protocols since with no means to characterise a circuit, there is no way to completely calibrate performance or even consider the prospect of scalability.

This motivates the work in this chapter. Currently, due to a lack of truly single photon sources the spontaneous production of photon pairs, where one photon triggers the presence of the other, is the most effective means of obtaining single photons. By using an on-chip photon source, which can then be butt coupled to a waveguide circuit, a reduction in overall resource size is obtained and miniaturisation permits both scalability and stability. This is the approach used in this chapter to obtain multiple single photon sources and route them into a waveguide circuit. Using these multiple heralded single photons, it is possible to use a spatial multiplexing technique, to help improve both the determinism of the sources and/or reduce multi-photon pair contributions below what is possible using a single source.

This chapter is arranged to provide the reader with an introduction to single photon sources, clearly outlining the challenge posed by multiphoton terms and the potential to enhance this using a spatial multiplexing scheme. The methods used to obtain a scalable source of photons, namely hybrid integration, are discussed in detail. This includes the fabrication of laser written components and the nonlinear waveguide source of telecommunication band photons. A detailed characterisation of the source's signal-to-noise properties, both in isolation and when included in a multiplexed circuit, is completed. Finally, an outlook section describes ongoing work on a tunable source of photon pairs, where the output state can be tuned between a product state and a path entangled state, using an entirely integrated hybrid chip.

6.1 The search for a single photon source

One of the simplest means of producing a single photon source is to use an attenuated laser beam. If this beam is stable temporally then this process can be described as a coherent source with a Poissonian photon number distribution. The probability of obtaining a single photon in a given time interval, described in terms of the average number of photons, $\bar{n}$, is

$$P_n = e^{-\bar{n}}\frac{\bar{n}^n}{n!}. \tag{6.1}$$

Thus the ratio of $P_1/P_{n>1}$ is high, particularly as the intensity is reduced. However, since there is no means of heralding the presence of a photon the resultant process will always result in a low photon production probability (See Fig. 6.1(a)).

Currently there are a range of structures that in the future promise to produce truly single photons on demand at high rates, in other words a single photon with no higher photon terms and a collection efficiency of unity (See Fig. 6.1(d)). These structures, such as colour centres in diamond and more recently in silicon carbide, have significant advantages. Diamond has a range of desirable qualities, a wide bandgap, a large number of colour centres, bio-compatibility and is transparent from the ultraviolet to the infrared [289]. The nitrogen-vacancy (NV^-) colour centre in diamond can operate at room temperature and MHz photon rates have been achieved [290]. Other colour centres in diamond, including the nickel-based NE8 centre show extremely narrow (1.6 nm FWHM) wavelength emission at 795 nm [291]. Furthermore, as material processing techniques have matured, the extraction efficiencies from bulk diamond [292], nanodiamonds [293], and diamond colour centres embedded in integrated devices have improved [294]. Colour centres in silicon carbide (SiC) offer an even greater potential for interfacing with conventional fabrication technologies and single photon emission from an SiC defect has been demonstrated [295]. However, interacting with multiple colour centres to show multiphoton interference has seen limited progress due to the challenge of isolating and interfacing multiple identical colour centres [296, 297].

Quantum dots (QD) fabricated in semiconductors, such as GaAs, have a key advantage over other single photon emitters since they can be incorporated into cavities which allow enhanced emission and directionality [298]. QDs have been incorporated in photonic crystal waveguides [299], operating at telecommunications wavelengths [300], and improvements in source-circuit interfaces have been achieved [301]. QDs embedded in nano-pillar arrays demonstrated by Santori *et al.* [302], offer extremely high probabilities of producing a single photon per pulse of >80% . However, these structures require cryogenic conditions to operate and producing multiple devices involves precise engineering. Their effectiveness in quantum circuits is currently limited due to reduced interference visibilities, even between photons generated from the same quantum dot [303, 304].

A fundamentally different approach to the generation of single photons involves the heralded generation of a photon. Through a nonlinear process, a pair of photons are created and one photon of the pair can be used to herald the existence of the other. One of these processes, based on a $\chi^{(3)}$ nonlinearity, is spontaneous four wave mixing (SFWM) where a pair of pump photons annihilate to form a higher and lower energy photon. This process can be performed using fibres and on-chip devices [305, 306]. The efficiency of the interaction can be further enhanced through carefully engineering the waveguide dispersion [48], using novel techniques such as slow light propagation [47], or resonant devices [307]. Integrated waveguide circuits have been fabricated in silicon-on-insulator (SOI) and multiphoton interference has been demonstrated [58, 308]. Photons produced by SFWM can even be efficiently extracted from pure fused silica fibres and on-chip waveguides [210, 309]. However, one of the major limiting factors of SFWM sources are Raman scattering and multiphoton absorption which result in noise and limits source brightness [310, 311]. Furthermore, fabricating multiple ($N > 2$) devices remains challenging and has not yet been demonstrated.

Spontaneous parametric downconversion (SPDC), in crystals exhibiting a $\chi^{(2)}$ nonlinearity, remains the workhorse for the quantum optical community for the production of photons. This process relies on the production of two lower energy photons from a single parent photon according to the phase matching condition. It is a flexible technique since photon energy can be chosen such that photons are degenerate and can be used as a source of pairs of identical photons. Photons generated by SPDC have a statistical distribution of photon pairs which is well described by thermal source. The probability of finding n photons in a field is [95]

$$P_n = \frac{\bar{n}^n}{(1+\bar{n})^{n+1}} \tag{6.2}$$

where $\bar{n}$ is the average number of photons. By comparing P_1 to $P_{n>1}$ (and excluding P_0) we see that it is actually more likely to achieve a $P_1/P_{n>1} > 1$ as the $\bar{n}$ is reduced. Setting $\bar{n}$ to 1 yeilds a signal to noise ratio of $P_1/P_{n>1} = 0.25/0.25 = 1$, while $\bar{n} = 0.1$ gives $P_1/P_{n>1} = 0.08/0.008 = 10$. Hence, it is clear that simply increasing $\bar{n}$ by increasing the pump power of a laser is not a means to increasing $P_n/P_{n>1}$. The most probable event is $n = 0$ photons. By heralding P_0 terms are ignored. A comparison of the heralded thermal source and a thermal source which is unheralded is shown in Fig. 6.1. It can be seen that the heralded SPDC source approaches the case of a truly single photon source, however the presence of higher order terms cannot be ignored. These terms also begin to dominate as the average photon number increases, hence limiting the extraction efficiency of the source. The actual probability of obtaining a pair of photons from a single downconversion crystal, per second is

$$C = \mu\eta_I\eta_S R, \tag{6.3}$$

here μ is the pair per pulse rate (or average photon number, $\bar{n}$ to use the previous notation) , $\eta_{I,S}$ are the extraction efficiencies for each photon and R is the repetition rate of the incident pump laser. The probability of obtaining 4 single photons is $\frac{C^2}{R}$. This equation shows that the production rates for simultaneous heralded single photon generation is severely reduced by the stochastic nature of the process. Of course it is clear that reducing loss is essential but due to multi-pair generation, μ is fundamentally limited by the thermal emission statistics of the source. A scheme which could increase μ is thus highly desirable.

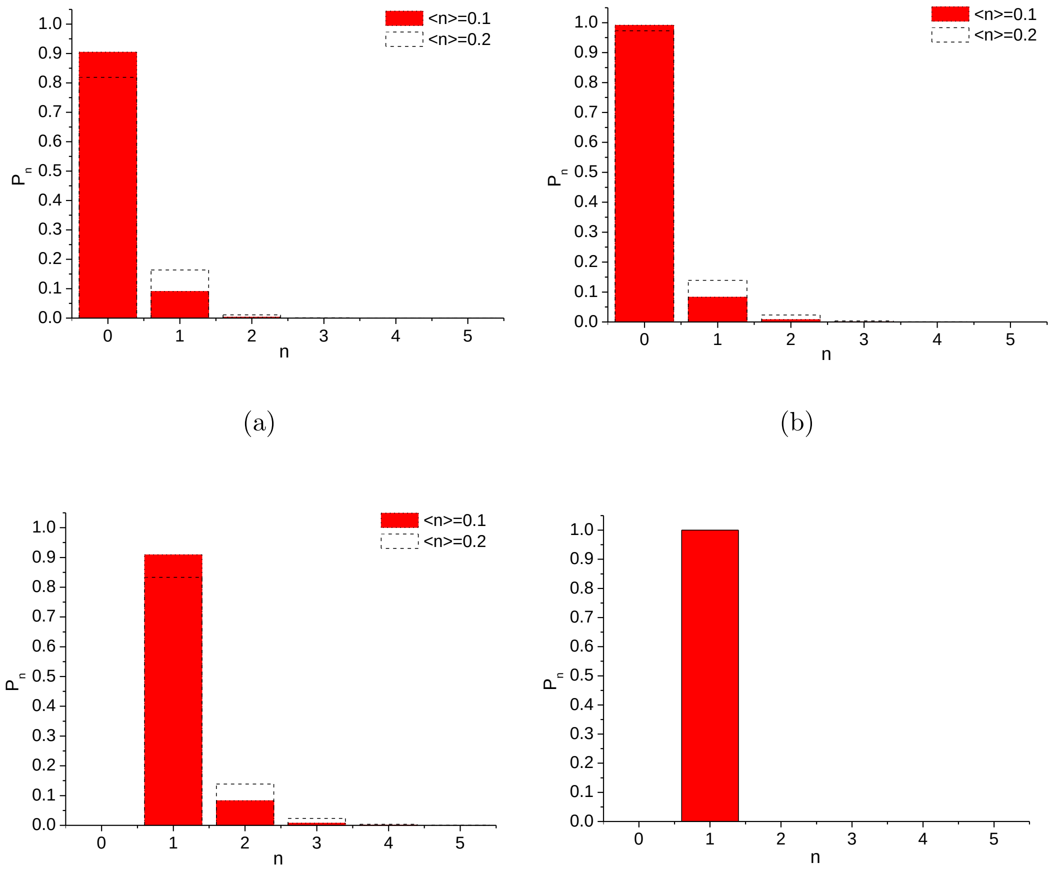

(a) (b) (c) (d)

FIGURE 6.1: Showing the probability for obtaining n photons, (a) from a Poissonian light source, (b) from a thermal source (c) from a heralded thermal source (n=0 terms eliminated) and (d) an ideal single photon emitter, as yet unavailable. Clearly the heralded thermal source is closest to an ideal single photon source.

6.1.1 Enhancing photon rates from SPDC

Clearly an approach for the production of high brightness, low noise, single photons is required. Equation 6.3 shows that to increase coincidences, apart from increasing the laser repetition rate and improving extraction efficiencies, the only means to increasing C is to increase μ, the probability of producing a pair per pulse. However, this cannot simply be increased by increasing laser pump power without sacrificing signal-to-noise ratio.

This signal-to-noise ratio can be improved by passive temporal multiplexing where the power of the pump pulse is halved and the repetition rate is doubled. Performing this successively yeilds a 2^{n-1} reduction in $n > 1$ photon events [312] (although this scheme used degenerate pairs of photons). However, many single photon avalanche detectors, such as commercially available InGaAs models (IDQ 210), have a dead time (1-25 μs) which limits their maximum trigger rate to 100 MHz. Hence, triggering any faster than this will not result in an increased heralding rate.

In contrast, active temporal multiplexing schemes can increase the probability of obtaining a photon pair per pulse [313], however due to implementation challenges there has been to date no experimental demonstration. To address this, Migdall *et al.* proposed a spatial multiplexing scheme to increase photon rates while maintaining the corresponding noise level [314] which is conceptually described as a "photon switch-yard". If a photon pair source fires, then the herald photon triggers a fast switch to route the other photon to an output. Using this approach the effective μ, the probability of producing a pair per pulse, can be increased to one in theory. A bulk optic demonstration of a multiplexed source used a pair of SPDC crystals [315].

Here a spatial multiplexing scheme is used to actively route single photons, from spatially separated sources, to a single output [314]. This approach is ideal for increasing a photon pair sources brightness while maintaining a fixed noise level or maintaining a source brightness and reducing multi-photon pair noise. This approach has the potential to enable the production of multiple, identical, single photon sources with higher brightness and reduced noise to that available otherwise.

6.2 Multiplexed tunable photon source: Hybrid integration

The layout of the on-chip portion of the experiment is shown in Fig. 6.2(a). The pump laser (stretched Coherent Chameleon) provides 1.2 ps-duration, time-bandwidth limited ($\Delta\lambda_p = 0.5$ nm) pulses, at a wavelength of $\lambda_p = 710$ nm and a repetition rate of 76 MHz. The pulses are sent to a polarisation maintaining fiber pigtailed to an FLDW 1-4 waveguide splitter.

In the heralding arm, pairs of photons are collected using optical circulators and apodized point-by-point laser inscribed fibre Bragg gratings (FBG) [316]. These are set to reflect photons at 1312 nm with a bandwidth of 85 GHz. A 100 GHz filter (DiCon MTF-08) is used to transmit energy-matched paired photons at 1548 nm, while the pump bandwidth is 300 GHz. The heralded photons are detected by four ID210 detectors, triggered by the 76 MHz pump laser, with a gate window of 5 ns and a deadtime of 3 μs. Upon detection of a photon the output of these detectors then triggers both the lead lanthanum zirconium titanate (PLZT) switches and an ID201 detector, with an adjustable gate window. The arrangement of these switches is shown in Fig. 6.2(b) where three switches can be used to combine the 1550 nm outputs from each source to the detector. It is also possible to selectively turn switches on and off in order to produce any combination of 4, 3 and 2 output photons. Using in-fibre polarisation controllers and an analyser at the output we ensure photons are identical in polarisation,

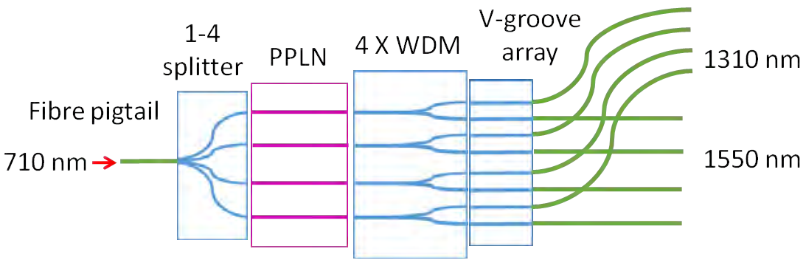

(a)

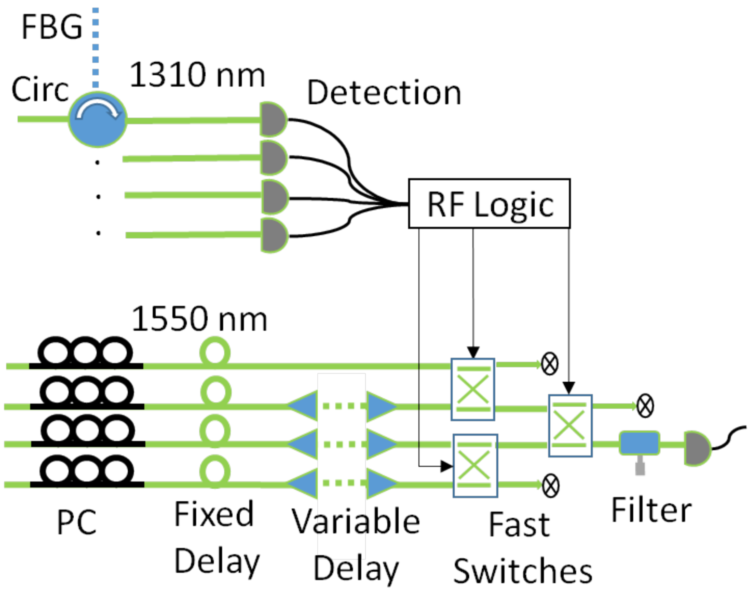

(b)

FIGURE 6.2: (a) A picosecond laser pumped array of 4 identical PPLN waveguides, where a pair of FLDW chips couple light in and out of the device. (b) The output of the laser written WDMs is sent to a multiplexing setup. Four single photon channels at 1300 nm, which are filtered by fibre Bragg gratings (FBG) and circulators (Circ) herald the arrival of 1550 nm photons through radio frequency (RF) electronics. These control fast switches, routing 1550 nm photons appropriately. The polarisation is controlled using polarisation controllers (PC).

while path lengths are controlled using variable delays to ensure maximal temporal indistinguishability of the output photons.

6.2.1 Laser written components

Interfacing between a nonlinear waveguide array and laser written components involved design of both a 1-4 splitter and an array of identical WDMs. The 1-4 splitter uses a 3D interaction geometry to produce equal splitting as described in chapter 4. The WDMs were fabricated in AF-45 (See Fig. 6.3) and relies on the wavelength dependence of the coupled mode equation described in chapter 2. This wavelength dependence can be exploited by increasing the length of a directional coupler interaction region until a length is achieved where in the ideal case there is a 100% coupling for one wavelength and a 0% coupling for the other. This coarse wavelength division process leads to a broadband (>20 nm) wavelength region where the two couplings are different, however the extinction achieved using this technique is not as high as more advanced techniques such as those using arrayed waveguide gratings (AWG). A range of couplers were fabricated and extinctions of 10 dB±1 dB were obtained for an interaction length of 3.35 mm and a waveguide spacing of 7 μm(See Fig. 6.3(b)), comparable to previous demonstrations where a maximum of 18 dB was achieved [198].

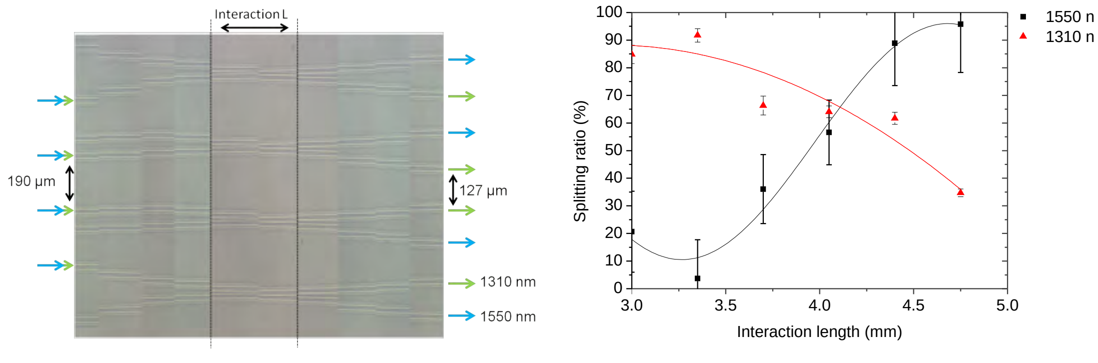

(a) (b)

Figure 6.3: (a) A series of microscope images of the four laser written WDMs. The input of the devices collects photon pairs from the four PPLN waveguide simultaneously and spatially separates the 1310 nm and 1550 nm wavelengths to interface with a 127 μm spaced linear array. (b) The wavelength dependent splitting ratio vs. interaction length. Each point is an average of 2 measurements performed on each of four devices.

6.2.2 PPLN waveguides: Overview

Lithium niobate ($LiNbO_3$) is a crystal which exhibits a $\chi^{(2)}$ nonlinearity. The length over which the nonlinear interaction can efficiently occur can be increased by exploiting phase-matching techniques such as birefringent phase-matching or quasi phase-matching (QPM). Birefringent phase matching relies on the difference between ordinary and extraordinary refractive indices of a crystal. A pump beam is injected along one axis while the downconverted photons travel along the orthogonal polarization. QPM can be induced by using electric field poling, periodically flipping the sign of the $\chi^{(2)}$ nonlinearity. The periodic inversion of the ferroelectric domain is achieved through application of high voltage periodically across a 0.5 mm $LiNbO_3$ wafer [317].

Waveguides can be formed in lithium niobate in order to further increase the length of the nonlinear interaction while maintaining a small mode area. This can be completed using a number of methods, ion implantation and also ion beam etching to form ridge waveguides, metal in-diffusion, lithium out diffusion from the surface and proton exchange methods [318, 319]. In proton exchange, waveguides are formed through a diffusion process, essentially involving a phase mask and immersion in acid, commonly benzoic acid, for varying times at varying temperatures. In annealed proton exchange (APE) samples are subject to repeated stages of annealing in air inside an oven, this tends to be a repeatable process but can affect both the nonlinear coefficient and the domain orientation [320]. Reverse proton exchange (RPE) permits the burial of the waveguide by means of an additional annealing step in a Li rich salt melt to restore the Li^+ content to the surface thus burying the increased index produced by the initial proton exchange step [321, 322]. This results in a more symmetric mode profile.

The waveguides used in this study were formed by soft proton exchange (SPE) [62, 323]. SPE has the advantage of being a one step process utilising a phase mask and a single immersion step in a low concentration benzoic acid and lithium benzoate bath, at ∼300°C, for extended periods, up to 3 or more days [324]. It has virtually no affect on the non-linearity or inversion domains but has the inconvenience of being less reproducible than conventional APE due to the acidity and temperature stability demands. For the samples described here the resulting index profile has a maximum $\Delta n \sim 10^{-2}$ and a diffusion profile with a highly elliptical mode profile (see Fig. 6.4).

Typically the poling period, waveguide dispersion and temperature are used to fine tune the phase matching parameters for the down converted photons. Yielding, ideally, photon pairs at 1310 and 1542 nm for a pump wavelength ∼ 710 nm. For the samples described here, a poling period of 13-14 μm is used for sample lengths varying from ∼0.5-1.5 cm. Waveguide diameters vary between 4-8 μm and temperatures are tuned between 80-120°C.

6.2.3 PPLN waveguides: Characterisation

The four waveguides used in this work had a poling period of 13.8 μm and a diameter of 7 μm. The pump wavelength used was 710 nm, while the chip temperature was maintained at 90°C and downconverted photons were observed at 1310 nm and 1550 nm. It should be noted that the waveguide is multimode at the pump wavelength meaning

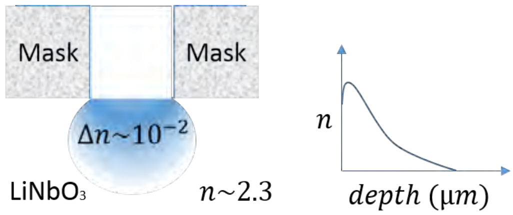

(a)

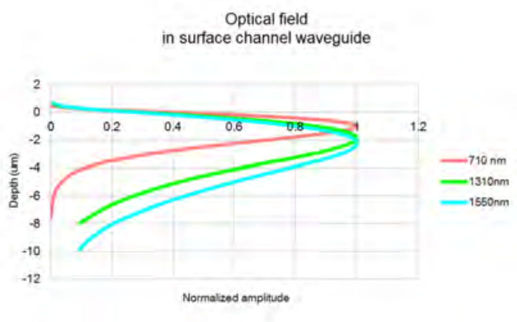

(b)

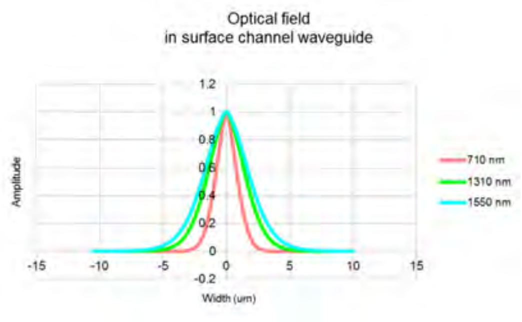

(c)

Figure 6.4: (a) Diffusion profile of surface waveguides in PPLN with a 1D profile showing the refractive index vs. depth, (b) Theoretical calculations of the field profile of a surface diffusion waveguide vs. depth and (c) vs. waveguide width.

that any small alignment variations contribute to substantial coupling to high order modes which will have a different photon production rate. The output spectrum from each source was $\sim$ 20 nm broad when pumped with a bandwidth of 0.5 nm centred at 710 nm. The overlap of the observed downconverted photon spectrum can be seen in Fig. 6.5 where all four sources are centred at 1550 nm. Source output wavelength can also be tuned by adjusting either the pump wavelength or the waveguide chip temperature (see inset Fig. 6.5).

Despite overlap between output photon spectra, the efficiency of each source varies. This is due both to inhomogeneous waveguide diameters as well as minor damage to the surface of the waveguide and the the waveguide facets. Since the waveguides are surface diffused structures and lithium niobate is a relatively soft crystal it is prone to surface and facet damage. In order to measure the intrinsic efficiency of each source, prior to collection using laser written components or multiplexing, a measurement of the source brightness and coincidence vs. accidental ratio (CAR) is performed. The apparatus used for this measurement is shown in Fig. 6.6(a) where the output of each PPLN waveguide is collected using an SMF-28 fibre and wavelength separation is performed using a commercial wavelength de-multiplexer (WDM). The 1310 nm photon is used as a herald and gates the second detector. The detector gate window 200 ns during which time the 12.5 ns delay between successive laser pulses gives accidental coincidences as

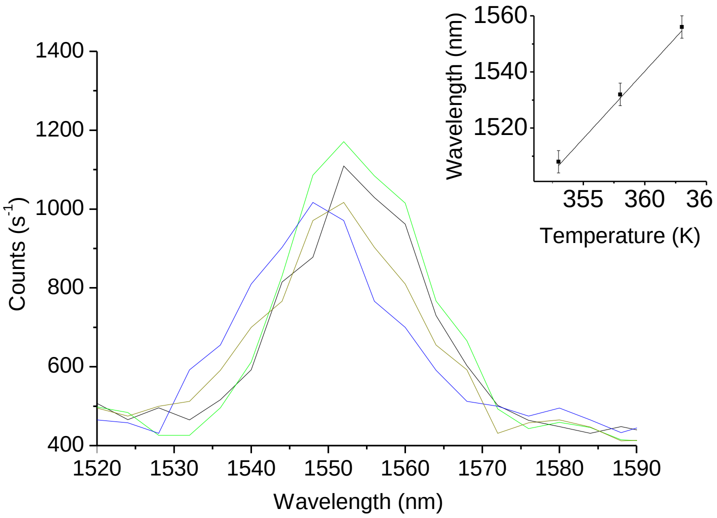

FIGURE 6.5: The output spectra of the individual PPLN waveguide channels. The inset shows the change in central wavelength with temperature (courtesy of Olivier Alibart).

well as true coincidences (see Fig. 6.6(b)). The precise delay between pulses is measured using a time interval analyser and by measuring the ratio of coincidences to accidental coincidences the CAR can be calculated (see fig. 6.6(c)).

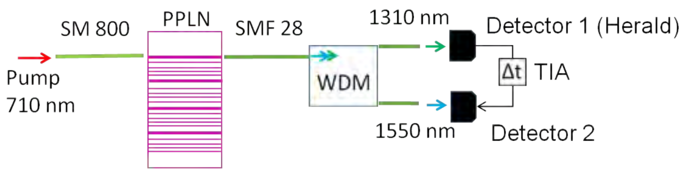

(a)

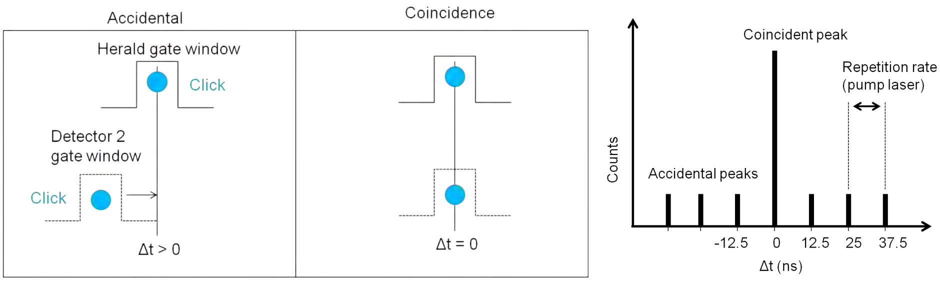

(b) (c)

FIGURE 6.6: (a) Layout of the experiment used to measure source efficiency and the calculate the CAR (b) A conceptual image of accidental coincidences compared to true coincidences (c) A conceptual plot of coincidences vs. relative delay showing a peak centred at $\Delta t = 0$ and accidental coincidence peaks spaced by the laser repetition rate.

6.2.4 Component loss

Individual component loss is a significant contributor to both a reduction in coincidences and a reduction in CAR. The losses for each channel,$\eta_{I,S}$, can be measured (see Table 6.1) The singles rates $N_{I,S}$ and the coincidence rates C then depend on these values. The formulae $N_{I,S} = \mu\eta_{I,S} + d_{I,S}$ and $C = \mu\eta_I\eta_S$, where μ is the photon pair rate per pulse describe the singles rate and coincidence rate as a function of the loss in each channel [325]. However, due to the number of facets being interfaced in the experiment the losses for both the signal and idler channel can vary. This results in a fluctuation in the coincidence count rates(see fig. 6.10(a)) which is the product of the losses. The coincidences can be rescaled by using the following equation $C = (N_S - d_S)\eta_I$ which gives the coincidence rate between the two detectors as a function of the singles rate at the heralding detector (N_S or 1310 nm channel).

The coincidence vs. accidental ratio (CAR) can be obtained experimentally by measuring the ratio of coincidence to accidental rates (per pulse) and can be calculated as the ratio of coincidence rates, $C = \mu\eta_I\eta_S R$, to the accidental rates, $A = N_S N_I = (\mu\eta_I + d_I)(\mu\eta_S + d_S)$:

$$CAR = \frac{\mu\eta_I\eta_S}{(\mu\eta_I + d_I)(\mu\eta_S + d_S)}, \tag{6.4}$$

or

$$CAR = \frac{C}{(\frac{C}{\eta_S} + d_I)(\frac{C}{\eta_I} + d_S)}. \tag{6.5}$$

So using the equations above it is possible to calculate the CAR for a range of recorded coincidence values. The loss values are obtained from table 6.1.

The multiplexing rates can then be calculated as the sum of the coincidence rates. However, since the switches can only transmit a single mode, coincidence events from multiple sources must be removed. The switches have a master source which will be transmitted should multiple photon pairs be emitted simultaneously from separate sources. Hence the coincidence rates are $C_{MUX} = C_1 + C_2(1 - N_{S,1}) + C_3(1 - N_{S,1} - N_{S,2})$ and the accidental rates are $A_{MUX} = A_1 + A_2(1 - N_{S,1}) + A_3(1 - N_{S,1} - N_{S,2})$.

6.2.5 Spectral filtering

Pump suppression is important limiting factor to CARs since it results directly in noise at the detector. This can be seen in Fig. 6.7(a), where in order to reduce pump leakage, additional filters were employed yielding a factor of two increase in the CAR demonstrating that the extinction was doubled. The CAR for each individual source, when using two filters, is shown in Fig. 6.7(b) when only a commercial WDM and single collection fibre are used for collection.

This experiment utilised laser written WDMs with extinctions ranging from 10-18dB. This means that there is up to 10% of the idler photons in the signal channel and vice versa. Once the laser written WDMs are used in the experiment it can be seen that the CAR for channel 1 drops considerably (see Fig. 6.8), this is due the loss of the FLDW component, 3.5 dB average, and the non-optimal extinction ratio due to the

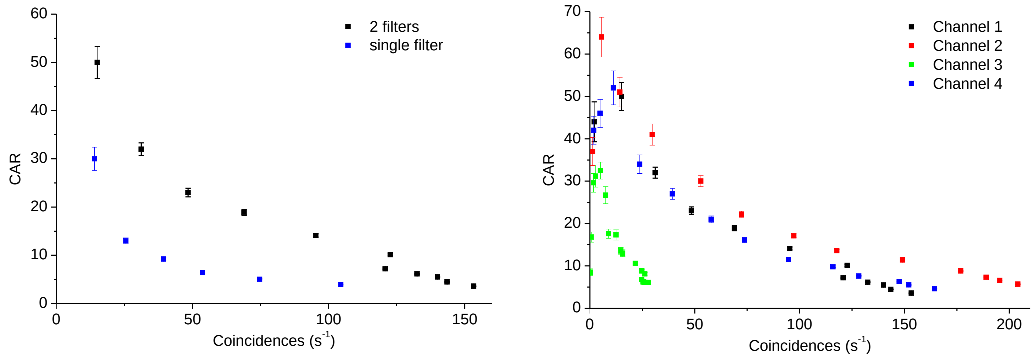

(a) (b)

FIGURE 6.7: (a)Showing the increase in CAR when using two filters for channel 1 and (b) shows the CAR vs. coincidences for all four sources.

filter transmitting 1310 nm photons (see Fig. 6.3). To show this a measurement was performed using only the laser written WDM and another after a 27 dB commercial 1310/1550 WDM was inserted in the 1550 nm channel (see Fig. 6.8). This yielded a factor of two increase in the CAR. A measurement was repeated on the 1310 channel but no improvement in the CAR was observed. This implies that the rejection of the 1310 nm FBGs was sufficient to remove the majority of 1550 nm photons.

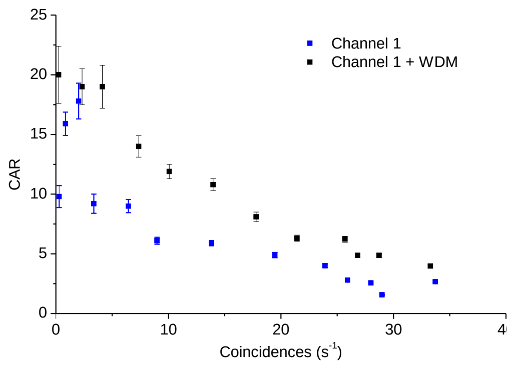

FIGURE 6.8: A comparison of the CAR for channel 1 when using firstly a laser written WDM and then including an additional WDM (27 dB extinction) in the 1550 channel.

Initially a point-by-point laser inscribed fibre Bragg grating (FBG), FWHM$\sim$ 0.4 nm was used in the idler channel and a santec FWHM$\sim$ 0.3 nm was used in the signal arm. Typically a wider filter is used on the idler channel since the photons that arrive there are time gated, i,e, discriminated by the heralding photon, so only a coarse filter is required to suppress pump photons or leaked signal photons. A narrow filter results both in a reduction of the number of heralded photons arriving at the detector but also it results in additional noise since once the herald photon is detected the 1550 nm detector is opened and thus produces additional dark counts. Therefore

Table 6.1: The maximum measured CAR and maximum calculated photon pair production rate, μ, from each PPLN channel, the losses for the idler and signal arms ($\eta_{I,S}$), the efficiency of the heralding detectors (η_{Detector}) and the corresponding dark count rate (d_{Herald}) for the detection arrangement used during multiplexing is shown. The detector loss is a quoted value from the manufacturer and the loss in each channel is calculated from the fits to the experimental data.

Single channel	1	2	3	4
μ ($\times 10^{-3}$)	12.8	23.1	1.9	10.8
Max. CAR	21	15	7	25
η_I (dB incl detector)	19	21	26	20.5
η_S (dB incl detector)	33	33.5	32	33.1
η_{Detector} (%)	17.5	17.5	7.5	12.5
d_{Herald} (KHz)	1.8	1.5	2	1

the filter mismatch was a significant limiting factor to experimental performance. By removing the Santec filter and using a 0.8 nm FWHM DiCon filter the CAR and count rate were improved by a factor of 5 (see Fig. 6.9).

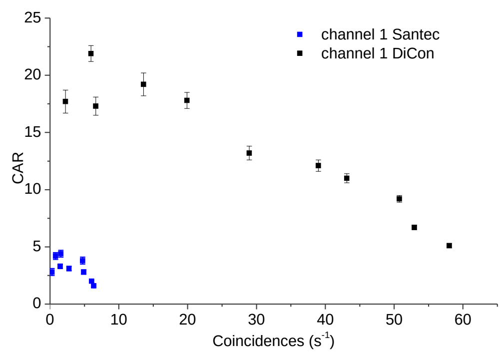

Figure 6.9: A comparison of the CAR for channel 1 when using a laser written WDM and including all variable delays, polarisation controllers and switches. In blue is the CAR for a Santec 0.3 nm FWHM and black shows a DiCon 0.8 nm FWHM.

6.2.6 Results

Figure 6.10(a) shows heralded single photon rates, for individual channels and multiplexed outputs. Single channel 1 (black) and channel 2 (green) have maximum coincidence rates, for pump powers of 4.25 mW, of 27 Hz each. Single channels 4 (blue) and 3 (orange) show rates of 17 Hz and 6 Hz. By actively multiplexing, the source brightness is increased. First channel 1 and 4 (MUX-2-1) are combined using a single switch and then subsequently channels 1, 2 and 4 (MUX-3-1) are routed to a single output (See Fig. 6.10(a)). This results in coincidence rates, for all pump powers, above those obtained from any individual channel. However, when multiplexing 4 channels (MUX-4-1) the coincidence rate is approximately the same as that observed for 3 channels (MUX-3-1). This is due to the lower overall efficiency for channel 3, combined with a

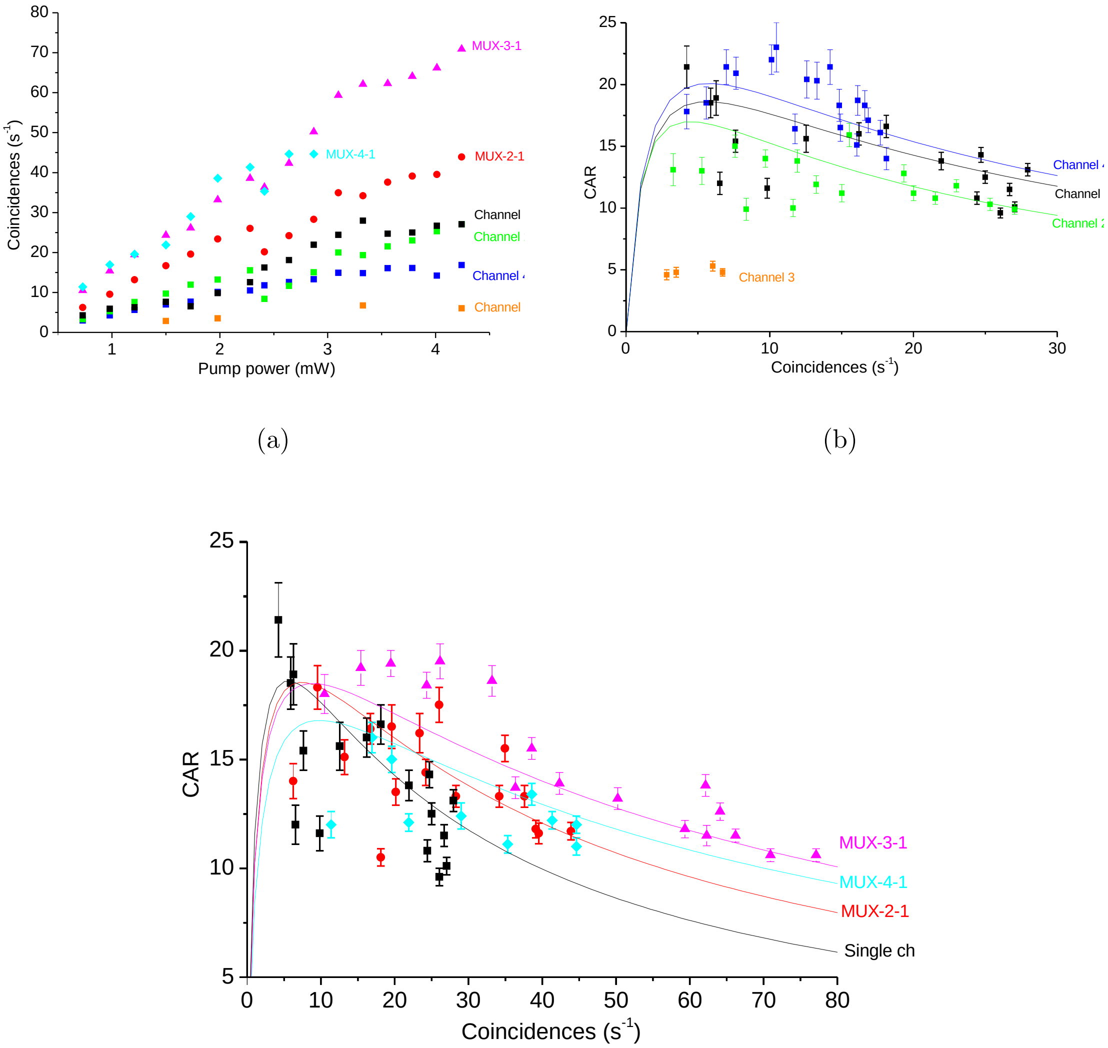

(a) (b)

(c)

FIGURE 6.10: (a) Heralded photon rate vs. pump power for single channels and a 4-1 multiplexing scheme (b) CAR vs. coincidence rate for each single PPLN waveguide channel. (c) CAR vs. coincidences for multiplexing 2, 3 and 4 channels. Single channel 1 is shown for comparison.

heralding detector with a low efficiency and a high dark count rate. Table 6.1 shows the individual photon production efficiency for each individual channel and the detector performance, efficiency (η_d) and dark count rates (d_{Herald}). Detectors which display a lower, more uniform, dark count rate and collection efficiency would improve the uniformity of heralding rates. It can be seen in Fig. 6.10 that in the range of pump powers from 2.2 mW to 3.2 mW, there is a deviation from a linear trend, observed for all channels, in the source brightness. This was caused by a change in the coupling between the fibre pigtail and the 1-4 waveguide splitter. The index matching adhesive used to bind these facets can expand with temperature, due to the high laser intensity resulting in a consistent change in output power from the 1-4 splitter. Furthermore, this adhesive has a damage threshold of approximately 20 mW meaning that individual channels could not be pumped beyond a pump power of 4.5 mW.

It can be seen in Fig. 6.10(b) that the CAR values for a range of coincidences are different for each channel. Table 6.1 shows that this is due to differences in detector performance and intrinsic waveguide performance. Channel 3 has a low photon production efficiency, combined with a low detection efficiency and high dark count rate resulting in a CAR substantially below other channels. The CAR can also be considered to be a measure of the ratio of the multi-photon induced noise rate from a $\chi^{(2)}$ source, since additional nonlinear processes are not as significant as in $\chi^{(3)}$ materials [310]. It can be seen that for a fixed CAR value of >10 that, when multiplexing, the photon rate is increased above the single channel values while the noise remains fixed (see Fig. 6.10(c)). This is the key feature of the spatially multiplexed source as it demonstrates an increase in the heralded single photon rate while maintaining the corresponding signal-to-noise ratio. However, the effect of the dark count rates and low efficiency of single channel 3 reduces the CAR for the MUX-4-1, since the coincidence contribution from single channel 3 is low but its dark counts are added. When multiplexing 3 sources (excluding single channel 3) a clear increase in single photon rates can be seen over a range of CARs from 10-20. We note the CAR values for lower coincidence rates do not show an enhancement due to dark count rates >1 KHz in the single channel heralding detectors (see Table 6.1).

The loss in each channel also varies due to differences in individual component losses required for interfacing and multiplexing: PPLN facet extraction efficiency (3 dB), laser written WDMs (3 dB), circulators and FBGs (3 dB), pump suppression filters (1 dB), polarisation controllers (1 dB), variable delays (1.5 dB), PLZT switch (1 dB) and bandpass filter (3.5 dB). Increasing the uniformity of these individual component losses and reducing them can significantly increase the overall source brightness and CAR. The stability of the system can be improved by using index matching adhesives which have a reduced sensitivity to thermal fluctuations which we observe to be the limiting factor to the temporal stability. Ideally, the 1548 nm filter bandwidth should equate to the sum of the pump and the 1312 nm filter bandwidth, corrected by the phase-matching acceptance of the nonlinear waveguide. Any deviation from this results in a loss and reduction of the overall CAR and this factor has been estimated to be 0.5 in our case. By using a 200 GHz filter for the 1548 nm photons that factor could be improved to one. It is also possible to produce waveguide tapers in the laser written circuits to enhance the collection efficiencies from the highly elliptical PPLN waveguide mode [165]. Furthermore, by increasing photon rates the indistinguishability of the multiplexed outputs could be observed, as it has been previously demonstrated that by using narrow filtering it is possible to achieve extremely high interference visibility [323]. In the future as manufacturing techniques mature it is also possible to further integrate components onto a single chip, components such as edge filters to suppress the pump laser [326].

This experiment has interfaced PPLN waveguide based sources of photons with laser written waveguide circuits to produce four spatially separated heralded photons, tunable across the communications band of 1520-1580 nm. We show the feasibility of actively routing photons to pairs of outputs and a single output using electronically controlled switches. Our output photon rates are an order of magnitude higher than a previous integrated spatial multiplexing demonstration [325] and almost double the rate of a previous demonstration of integrated bidirectional multiplexing [327]. We have interfaced, simultaneously, the largest number of SPDC sources on a single chip which is comparable to bulk optic demonstrations [288]. This shows the practicality of hybrid integration for the preparation of single and multiple photon states. Increasing photon rates, while maintaining a fixed signal-to-noise ratio through multiplexing, demonstrates the scalability of the hybrid multiplexing scheme.

6.2.7 Further measurements

Photons are only useful for quantum information if they are indistinguishable. Showing this would require a Hong-Ou-Mandel interference experiment as has been described in previous chapters. By performing non-classical interference between single channels but also multiplexed channels it will be possible to show that the photons from all separated channels are indistinguishable in every degree of freedom. It is anticipated that since the temporal delay is carefully controllable, the wavelength is defined by the narrow filter bandwidths and well overlapped, the polarisations are identical that the interference visibility will be high. This would demonstrate spatial multiplexing as a truly valuable tool in photon source development for quantum information applications. Finally if the interference between multiple sources could be controlled using the switches in this experiment as variable beamsplitters then it would show this technique as useful not just for the development of single photons but also multi-photon states which are electronically tunable.

6.3 Outlook: Integrated, tunable, NOON state generator.

As numerous research groups continue to push for integrating additional functionality into on-chip devices. It is likely that in the short term the flexibility of the femtosecond laser direct-write (FLDW) technique will prove useful. It is a process which can produce low loss waveguide circuits without the use of a phase mask, meaning low cost prototyping can be performed quickly. Furthermore, since the process can produce three dimensional geometries, not possible using other fabrication methods, it also has the potential to produce unique structures exploiting this capability.

The ideal integrated photonic structure could be based on a similar structure to what is described by Silverstone *et al.* [58]. This is a silicon-on-insulator (SOI) waveguide source of photons produced through $\chi^{(3)}$ spontaneous four wave mixing (SFWM). It operates in the telecommunications band and is potentially compatible with CMOS electronic manufacturing methods (although not using existing foundries [59–61]) making it a very practical for large scale fabrication and integration. Furthermore the high refractive index contrast of the SOI waveguides leads to an extremely well confined mode meaning very tight bends can be produced enabling optical delay lines and circuit compactness. However, due to the low photon production and extraction efficiency the resulting count rates are low, this is despite the use of high efficiency superconducting detectors. Furthermore, the wavelength separation must be performed off chip due to the narrow wavelength separation between signal and idler pairs. Recently a source, which is almost identical to the source described by Silverstone *et al.* [58], has been demonstrated by Jin *et al.* using a lithium niobate monolithic integrated circuit [64]. However, neither of these technique provide heralded pairs which, as described section 6.1 of this chapter, are crucial for approaching an effective deterministic photon source.

This is an area where, in the short term, the FLDW technique has some distinct advantages. The Interfacing of PPLN with FLDW waveguides means that a very high efficiency nonlinear source can be used for the production of photon pairs, while a low loss linear circuit can separate and manipulate those photons (see Fig. 6.11). This could prove an extremely efficient means of on-chip photon state preparation. Enhancements could also be made to this setup by providing a dielectric coating on the facets of the PPLN chip to reduce Fresnel reflections [328]. Laser written waveguides could use a tapered region to increase the collection efficiency from the PPLN chip. Another useful application of the wavelength separation would be to include long pass filters in the circuit to reject the 710 nm pump [326]. The wavelength splitting could also be narrowed by exploiting techniques used by Ng *et al.* in fabricating high extinction WDMs [329]. Their technique exploits a series of cascaded unbalanced Mach Zehnders and achieves a channel spacing of 3 nm across 30 nm with 15 dB extinction. It would be possible to modify this arrangement to separate narrow wavelengths from a broad photon spectrum on-chip.

In this section a description of a preliminary result which uses photon pairs that are produced in PPLN waveguides and collected by a laser written waveguide chip (See fig. 6.11). The 1550/1310 photons are separated by a pair of laser written WDMs. The 1310 nm photons travel to the end of the waveguide chip and are collected by heralding detectors while the 1550 nm photons enter a Mach Zehnder interferometer with a tunable phase on one arm. The Mach Zehnder interferometer thus acts as a tunable beamsplitter. Phase tuning is achieved using a thin film resistive heater, deposited on the surface of the waveguide chip, which heats one arm of the interferometer inducing a change in refractive index. The design is similar to the Si based source used by Silverstone *et al.* [58]. However, it is anticipated that the rates will be much higher and crucially the wavelength separation will be completed on chip.

6.3.1 Chip design and operation

In order to produce the desired device operation, a Mach Zehnder (MZ) interferometer is used as a tunable beamsplitter. The arms are separated vertically permitting phase tuning by producing a temperature gradient between the top and bottom surface of the waveguide chip (See Fig. 6.11(b)). In order to produce this temperature gradient a thin film resistive heater is deposited on the surface of the chip. This is the first time to the authors knowledge that such a technique has been applied to a laser written

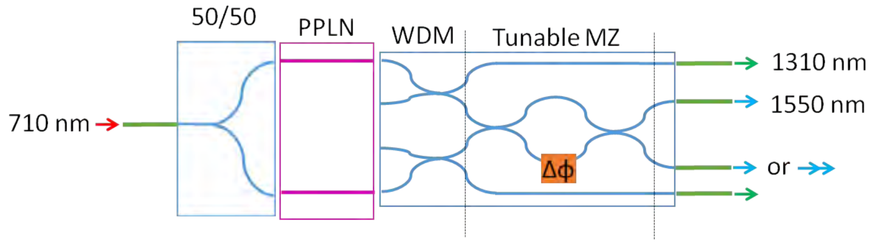

(a)

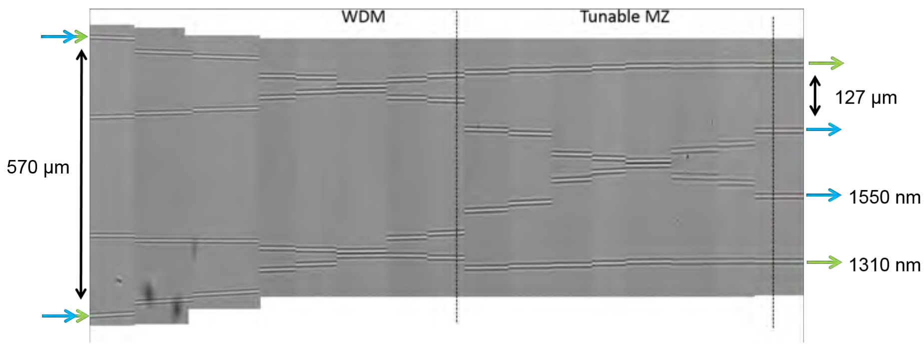

(b)

FIGURE 6.11: (a) The layout of a hybrid tunable fully integrated NOON state generator. (b) A stitched image of a series of microscope images of a hybrid tunable fully integrated NOON state generator. The Mach Zehnder interferometer arms are separated vertically (into the page) and hence cannot be seen in this image.

circuit. A nichrome (NiCr 80/20) alloy was chosen due to its high resistivity and good adhesion to glass. This was first deposited on the surface of the glass in a 10 mm wide strip above the MZ interferometer arms (see Fig. 6.12(a)). Once this was applied it permitted a characterisation of the MZ interference visibilities. Once a device was chosen which had a good overlap between WDM operation and interferometer operation a patterning step was applied to the metal layer to increase the resistivity and localise the heat dissipation.

6.3.2 Interferometer design

The change in refractive index (n) per unit shit of temperature (T), $\frac{dn}{dT} = 1.2 \times 10^{-5}/°\mathrm{C}$, for fused silica. This means, for a π phase shift, an optical path length difference in one of the waveguides in the interferometer arm of $\lambda/2 = 7.5 \times 10^{-7}$ m is required. Thus for the interferometer arms in this experiment of length $l = 5$ mm, the $\frac{dn}{dT} l = (0.5 \times 10^{-2})(1.2 \times 10^{-5}) = 0.6 \times 10^{-7}$ m/°C, hence a temperature differential of $\Delta T = 12.5°\mathrm{C}$ is required to produce a π phase shift. A steady state 1D heat flow model describes

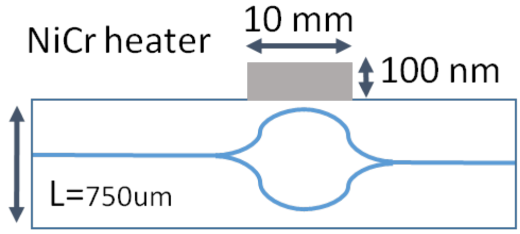

(a)

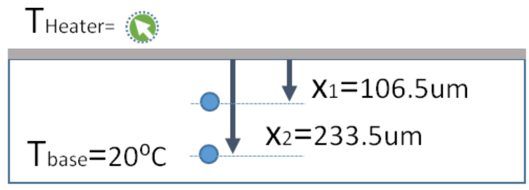

(b)

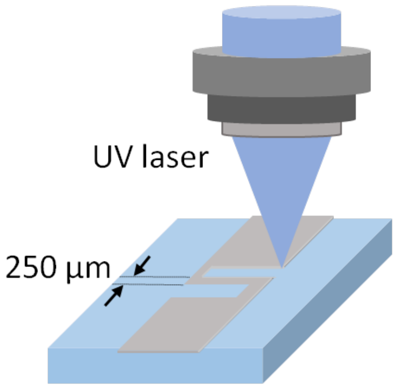

(c)

Figure 6.12: (a) A side view of the laser written chip with a surface deposited resistive heater shown on top of a Mach Zhender whose arms are displaced vertically. A temperature gradient allows for thermally tuning. (b) Position of waveguides in Mach Zehnder interferometer arm with respect to the surface of the sample. (c) UV laser patterning of a surface resister.

the variation of temperature as a function of depth in the sample of thickness L,

$$T(x) = T_{Heater} + (T_{Base} - T_{Heater})\frac{x}{L}, \tag{6.6}$$

where T_{Heater} is the temperature of the heating element, T_{Base} is the temperature of a water cooled base plate (we assume this is fixed), L is the thickness of the glass sample and x is the distance from the surface. The position of the waveguides in the glass is shown in Fig. 6.12(b). Since we are interested in knowing what T_{Heater} is required achieve a $\Delta T = T(x_1 - x_2) = 12.5°\text{C}$ between x_1 and x_2, we can rearrange equation 6.7 to

$$T_{Heater} = \frac{T_{Base}(x_1 - x_2) - \Delta T L}{(x_1 - x_2)}, \tag{6.7}$$

and if we insert values from Fig. 6.12(b) we obtain a heater temperature of $T_{Heater} = 89°\text{C}$.

6.3.3 Resistive heater design

In order to produce a NiCr strip across the surface of the chip Kapton tape was applied to the sample as a simple mask. Using a vacuum deposition system a sample of NiCr is heated to a high vapour pressure by resistive heating. The deposited film is 100 nm. The resistance can be calculated from $R = \rho\frac{s}{A}$, where ρ is the resistivity of the material ($1 - 1.5 \times 10^{-6}$ Ωm), s is the length of the resister and A is the cross sectional area. For a surface area of 3×10^{-4} m^2 a resistance, $R = 10$ Ω was obtained which required a voltage, $V = 14$ V to obtain a temperature of 90°C. T the current, I, is calculated from $V = IR$, giving $I = 1.4$ A and a power dissipation $P = 19.6$ W. This is a large amount of dissipated heat and means the baseplate must be actively cooled. To do so a laser chiller was used to chill a copper baseplate. The sample was then placed on the surface of this baseplate with a layer of thermally conductive paste to maintain thermal contact. A thermistor placed on the surface of the metal monitored the NiCr layer temperature (see Fig. 6.13(a)).

This method was sufficient to characterise a large number of interferometers before an optimal device was found. To produce a heater which can give a temperature of 88 degrees without dissipating excessive heat a reduction in the surface area was performed. This was done by UV picosecond laser patterning the NiCr layer. The ablation threshold for NiCr is below that of glass and the short pulse duration produces a localised energy deposition. This results in removal of the metal surface with a limited affect to the glass surface. The UV laser removed material in 5 μm raster periods and "S" bend was produced with a narrow central strip of 250 μm and 8 mm in length (see Fig. 6.12(c)). This strip is centred above the interferometer arm. This has a twofold advantage: an increase in resistance by a factor of 10 and a reduction of surface area by a factor of 600 meaning low voltage operation can now be achieved. A voltage of 1.8 V is sufficient to produce a localised 90°C temperature shift. Although in fact the voltage required for a π phase shift was 12 V due to the fact that the simply 1D heat flow model did not account for the substantial amount of heat conduction occurring in all areas surrounding the resistor.

6.3.4 Optical characterisation

As previously outlined the chip features both WDMs, which separate 1310/1550 nm light, and MZ interferometers which act as tunable beamsplitters. Since ultimately the interference visibility both classical and non classical depends on the quality of the MZs, the characterisation centred on these. The device which had the best overlap between WDM extiction ratio and MZ interference visibility. The WDM splitting ratio (how much light is transmitted from on waveguide to another) 1310:0.5 dB 1550 7dB and the corresponding MZ had an interference visibility of 90% (See Fig. 6.13(b)). The loss (including non-optimal extinction) for the 1550 nm channel was 5 dB and 3.5 dB on the 1310 nm channel.

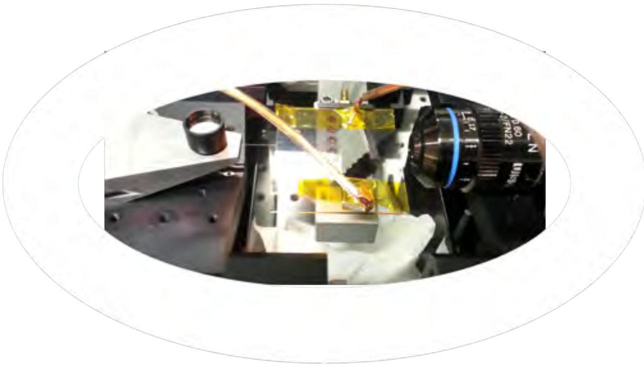

(a)

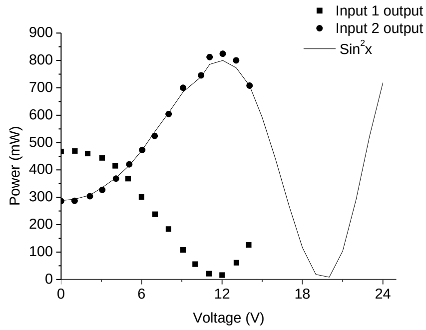

(b)

Figure 6.13: (a) A layout of the characterisation procedure. The waveguide chip is placed in a baseplate and an optical fibre (left) couples light into the circuits and the outputs are collected using an objective and monitored by a power meter. The surface of the chip is heated by applying a voltage across the resistive heater which has been patterned across it. (b) The result of the tuning of the MZI once the resistive heater has been patterned on the surface.

6.4 Conclusion

By interfacing laser written components with PPLN waveguides it has been possible to demonstrate device operation which is challenging or impossible using other integrated architectures. In doing so a demonstration of more sources produced simultaneously using a single chip has been achieved. These sources have been combined to produce a single, multiplexed output which can produce photon statistics unobtainable using any other means. Furthermore the interfacing of nonlinear waveguides with more advanced circuits has been completed and is an important step toward all integrated circuits. This work is important for the development of one of the key ingredients in optical quantum information science, a source of optically encoded qubits. This could be combined with two qubit gates, such as the controlled-phase gate described in chapter 5, to enable on-chip scalable quantum computing.

"My existence led by confusion ships, mutiny from stern to bow, ah but I was so much older then, I'm younger than that now."

Bob Dylan

7 Conclusion

This thesis outlined the fabrication of integrated optic circuits for use in quantum information science experiments. The fabrication of circuits was achieved using a laser inscription technique, the femtosecond laser direct-write (FLDW) technique. This method has evolved as an alternative, fabrication process, in contrast to other "bottom-up" processes, such as self assembly, or "top-down" fabrication schemes ,such as photo-lithography. It could reasonably be called an "inside-out" process and this makes the FLDW technique unique. It requires no complex preparation procedure or clean room environment. It has the potential to produce waveguides at multiple depths inside a material, something which no other platform is designed to do. The technique is flexible, it requires no photo-mask, but merely a code to direct a sample through a laser focus. This means a code can be adjusted and changed rapidly. In fact, this author has often tested fabrication code and writing parameters by simply fabricating multiple test structures in a microscope slide or a sacrificial glass substrate, analysing under a microscope and then modifying the codes and parameters accordingly. Furthermore, waveguides are not the only device which can be fabricated using this technique. microfluidic circuits have been produced in glass samples, along with self organised sub micro structures. It is these unique features, flexibility and simplicity, that have motivated the commercialisation of the laser inscription technique. However, the fabrication process is by no means perfect and that has meant that the bulk of this thesis was focused on the fabrication of reproducible optical elements, waveguides and beam-splitters.

Chapter 3 detailed the methods used for the production of low loss waveguides, which were single mode at 800 nm, in various glass substrates. Both fused silica (Suprasil) and borosilicate glass (Corning Eagle-2000 and Schott AF-45) were used as substrates. These glasses were modified using two laser systems whose main difference was their repetition rate. This defined waveguide writing parameters such as translation speed, laser intensity and focusing. It was found that only a small parameter regime produced low loss waveguides in fused silica, using the low (1 kHz) laser. The high repetition rate laser could successfully modify borosilicate and produce waveguides more than 100 times faster than the low repetition rate laser. In addition high throughput waveguides, with transmission above 70% were found in both Eagle-2000 and AF-45 which were ideally suited to integrated quantum optics applications. It was found that waveguides fabricated in AF-45 exibited substantially lower propagation loss than those in Eagle-2000. This was found to be due to trace impurities notably Fe^{3+} and substantially limits the lower bound of transmission loss in Eagle-2000 due to absorption. Prior to this study a detailed loss characterisation for waveguides single mode at 800 nm had not been reported. Finally, a study of the formation of nano-gratings, periodic self-assembled sub micron structures in borosilicate glass was performed. Nano-gratings were observed for the first time in Eagle-2000 opening up possibilities for high birefringence optical elements. However, this work was not pursued due to the high loss of the structures.

Chapter 4 studied the application of waveguides as 3D circuit elements. Waveguides were used to form mode transformations on three and four modes. The three mode device was a 3D interaction region which simplified the implementation of the three mode transformation to a single component. Such a structure is only possible using the 3 dimensional fabrication capability afforded by the laser inscription technique. The four mode device used four individual directional couplers which then attested to the reproducibility of the procedure during an individual run since these four beamsplitters were close to their target range. Both devices were characterised using photon pairs from a spontaneous downconversion source. This was the first time that a non-classical measurement had been performed on a laser inscribed multiport. The devices operated as well as fibre based structures [242] and showed more consistent visibilities that on-chip devices using multimode interference devices (MMI) [330]. These results show that laser written circuits do have the potential to act as circuit elements and motivate the further studies of quantum circuits in a subsequent chapter.

Chapter 5 detailed the development of a quantum circuit, the controlled-phase gate, or Knill gate. It is circuit which applies a phase shift to a target qubit conditional on the state of a control qubit and is heralded by two photons in a pair of ancilla modes. This circuit is inherently non-destructive, in principle could be scalable and combined with single qubit rotations could be used for universal quantum computing. For these reasons is an exciting device design and the challenge of experimentally producing the individual components of the circuit was achieved. Three different beamsplitter reflectivities were required necessitating a rigorous study of the evanescent coupling between waveguides. Furthermore, the potential to reprocess a circuit, correcting beamsplitter reflectivities which were erroneous was explored. This is the first time such a circuit had been fabricated and its design was enabled by the high precision of the laser inscription technique both in the individual beamsplitter reflectivities and in the relative phases between these beamsplitters. The full characterisation of this circuit using four single photons could not be completed since the resources required for characterisation were not available. This lack of single photon sources motivated the studies contained in the final chapter.

Chapter 6 seeks to address the shortcomings of chapter 5 by exploring the integration of on-chip sources of heralded single photons at telecommunications wavelengths, with laser inscribed circuits. This led to the interfacing of four nonlinear waveguide sources with laser written multiport splitting elements and wavelength de-multiplexers. Prior to this no hybrid source circuit element had been demonstrated and this was the most heralded sources simultaneously pumped on a single chip ever demonstrated. These sources were then used to create a multiplexed single photon source, where fast switches combine individual channels in an effort to produce a higher brightness, lower noise source than would be otherwise achievable. Finally the outlook section of this chapter describes ongoing work in the design, fabrication and characterisation of an entirely integrated photon source generator and manipulator.

7.1 outlook

The final section of each chapter individually addresses the possible routes for advancement of the studies contained in that chapter and here a brief summary of those will be discussed in a broader context. The overall goal of this work was to advance the study of quantum information science by using uniquely 3D waveguide chips. The efficiency of light transmission through a chip plays a crucial role in determining the feasibility of quantum experiments and hence any methods which can improve this are crucial to advancing the field. Many of the methods for adapting beam profiles to reduce spherical aberration as described for instance by De la Cruz *et al.* [177], or Salter *et al.* [165, 165, 170]could be used to produce waveguide tapers. These tapers could be used to more efficiently collect light from a nonlinear waveguide chip when forming a hybrid circuit as described in chapter 6. Furthermore, such adaptive schemes would be extremely well suited to forming circuits within nonlinear substrates themselves, such as chalcogenide [217]. Additionally a second order nonlinearity could be produced in waveguide circuits by using a thermal poling technique [215, 216]. These methods would begin to reduce circuit size by incorporating additional functionalities into devices and in doing so eliminates loss that occurs in transmission between devices.

Building on the work contained in chapter 4 a waveguide circuit comprising of concatenated three port devices could be used to produce a three port interferometer which could not easily be reproduced using a lithographic approach. Furthermore provided the polarisation independence of circuits could be maintained it would be desirable to scale up the number of modes in the interaction region to produce compact multimode transformations. Furthermore, an alternative encoding schemes for qubits which uses the transverse spatial mode of a single photon is also a method for exploiting the 3D capability of the fabrication technique to allow greater circuit density in a similar chip area. Components such as photonic lanterns allow one to transition from a multimode to an equivalent number of single mode components with high efficiency [331].

An exciting goal in the development of on chip quantum circuits is the potential to produce a monolithic circuit containing photon sources, a routing capability and detectors. Sources of single photons from laser written waveguides have already been demonstrated by Spring *et al.* [210], who have shown that the high extraction efficiency of laser written waveguides in silica is sufficient to balance the substantially lower intrinsic nonlinearity of the material. Furthermore the same group has demonstrated waveguide based detectors using laser written waveguides [74]. This makes the FLDW technique one of the few fabrications methods to have shown the individual components on a monolithic circuit. In the future combining all of these individual elements should be a goal of the community.

A
Appendix I: Waveguide theory

A brief overview of the background theory of optical waveguides is contained here. However this is by no means an exhaustive review as a detailed background in optical waveguide theory can be found in the two source textbooks [332, 333].

A conventional optical waveguide guides light by total internal reflection and has only a few free parameters: the refractive index of the higher index core n_{co}, the refractive index of the cladding n_{cl}, the radius a of the n_{co} region and the wavelength of light, λ which is propagating. Using this information the properties of the waveguide such as the number of modes it supports and the size of those modes can be calculated. The properties of a waveguide can be found, starting with the harmonic time form of the scalar wave equation,

$$\nabla^2 E + k_0^2 \epsilon(\vec{x}, k_0) E = 0, \tag{A.1}$$

where the free space wavenumber is $k_0 = \frac{2\pi}{\lambda}$ and the dielectric constant is $\epsilon(\vec{x}, k_0)$. A solution for the electric field $E(x)$ of the form,

$$\vec{E}(x) = \frac{1}{2}\left(a\hat{x}e^{i\beta z} f(x,y) + c.c.\right) \tag{A.2}$$

can be inserted leading to the eigenvalue equation,

$$\left[\nabla_t^2 + k_0^2 \epsilon(x,y)\right] f = \beta^2 f. \tag{A.3}$$

Here, $\nabla_t^2 = \frac{\partial^2 f}{\partial x^2} + \frac{\partial^2 f}{\partial y^2}$ is the transverse Laplacian, $f(x,y)$ the transverse mode profile and β is the eigenvalue which is referred to as the propagation constant. This is an important parameter which we can now use to define a dimensionless parameter called the effective index $n_{eff} = \frac{\beta}{k}$, which is convenient to use when discussing waveguide properties. By rewriting Eq. A.3 in terms of n_{eff} we can see the convenience of this definition:

$$\nabla_t^2 f = k_0^2 (n_{eff}^2 - \epsilon(x_t)) f, \tag{A.4}$$

results in modes with an exponentially decaying relationship if $n_{eff}^2 - \epsilon(x,y) > 0$ (with normalisation $\langle f|f\rangle = 1$) and localised within the waveguide core (provided $n_{eff} > n_{cl}$). These are referred to as bound modes and propagate within the waveguide. Other solutions for which $n_{eff} < n_{cl}$ are oscillatory and are referred to as radiation modes. The wave equation can be solved for a circularly symmetric step index fibre by using symmetry arguments to simplify complex equations composed of Bessel and Hankel functions. The scalar wave equation can be written in cylindrical coordinates (with radius ρ, azimuthal angle ϕ and propagation direction z):

$$\frac{\partial^2 E_z}{\partial \rho^2} + \frac{1}{\rho}\frac{\partial E_z}{\partial \rho} + \frac{1}{\rho^2}\frac{\partial^2 E_z}{\partial \phi^2} + k_0^2(\epsilon(\rho,\phi) - n_{eff}^2)E_z = 0. \tag{A.5}$$

A solution for E_z is given by

$$E_z = \begin{cases} AJ_0(\kappa\rho) & 0 \leq \rho \leq a \\ BK_0(\sigma\rho) & \rho > a \end{cases}, \tag{A.6}$$

where J_0 and K_0 are zeroth order bessel functions with constants A and B, while $\kappa = k_0\sqrt{n_{co}^2 - n_{eff}^2}$ and $\sigma = k_0\sqrt{n_{eff}^2 - n_{cl}^2}$. By applying a separation of variables and requiring the fields to vanish at an infinite radius and be continuous at the core-cladding interface while the scalar approximation imposes the weakly guiding approximation $n_{co}/n_{cl} \cong 1$, the dispersion relation for the linear polarised (LP) modes can be written as:

$$\frac{J_m^{'(\kappa a)}}{\kappa a J_m(\kappa a)} + \frac{K_m^{'(\sigma a)}}{\sigma a K_m(\sigma a)} = \pm m\left(\frac{1}{(\kappa a)^2} + \frac{1}{(\sigma a)^2}\right). \tag{A.7}$$

We can define the refractive index contrast which is the relative index difference,

$$\Delta = \frac{n_{co}^2 - n_{cl}^2}{2n_{co}^2} \tag{A.8}$$

and we can use this and Eq. A.7 to define the normalised frequency $V \equiv \sqrt{(\kappa a + \sigma a)} = k_0 a\sqrt{2\Delta}$. These equations can be used to determine the properties of a waveguide, such as the single mode cutoff which occurs for $V = 2.405$ in a step index waveguide. The resultant optical intensity distribution of the mode, or mode field diameter (MFD), can be calculated using the Gaussian approximation (valid to within 90% for $V > 1$) [180],

$$MFD = 2a\left(.65 + \frac{1.619}{V^{\frac{3}{2}}} + \frac{2.879}{V^6}\right) \tag{A.9}$$

as shown in Fig. A.1. This figure shows the MFD for the typical range of refractive index contrasts and waveguide diameters obtained using the laser inscription technique.

Waveguides brought in close proximity can exchange energy through the evanescent coupling which occurs from the exponential decaying portion of the field outside the waveguide. The field can be expressed as a linear combination of the normal modes of the system,

$$\tilde{E} = \sum_m A_m(z)E_m(x,y)e^{(i(\beta_m z))} + c.c., \tag{A.10}$$

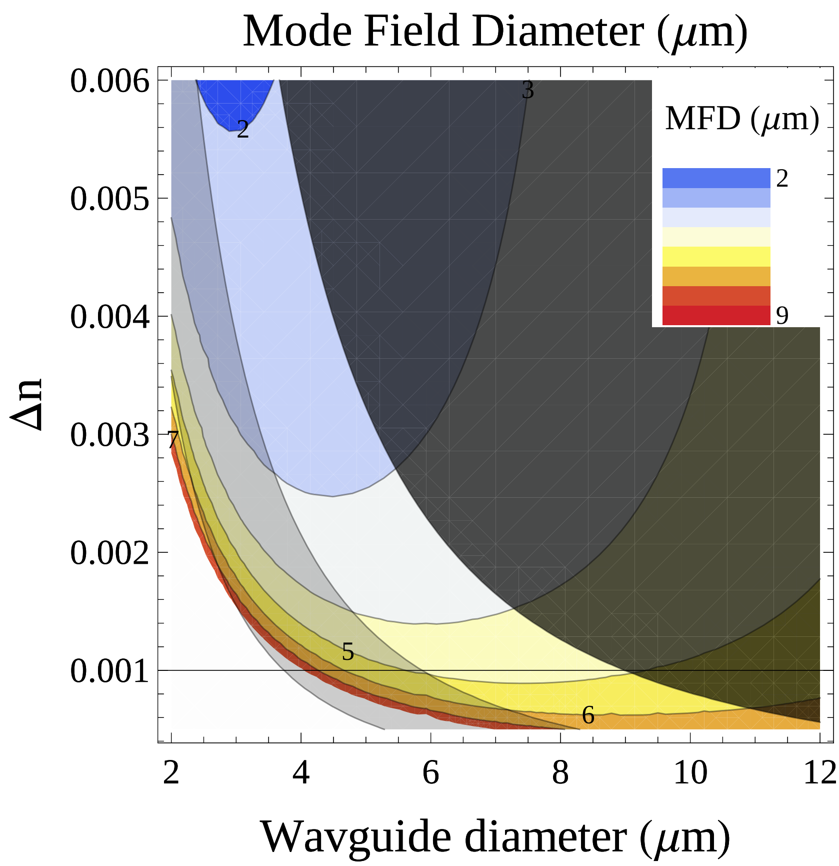

Figure A.1: Mode field diameter (MFD) plotted for the range of index contrasts (Δn) and waveguide diameters attainable using the FLDW fabrication method (using Eq.3.14). The top right shaded region shows the single mode cutoff, while the bottom shaded region is where the majority of the mode is no longer confined in the waveguide region.

where the amplitude coefficients are defined by A_m. This equation is inserted into Eq. A.3. For a pair of waveguides in the case of co-directional coupling ($\beta_1 > 0$,$\beta_2 > 0$), coupled mode equations can be formed:

$$\begin{aligned} \frac{dA_1}{dz} + iCA_2e^{i(\beta_1-\beta_2)z} = 0 \\ \frac{dA_2}{dz} + iCA_1e^{i(\beta_2-\beta_1)z} = 0 \end{aligned} \tag{A.11}$$

where the coupling coefficient,

$$C = \frac{k_0}{2n_{eff}}(n_{co}^2 - n_{cl}^2)\int_2 E_1(x,y)E_2(x,y)dxdy. \tag{A.12}$$

A solution of Eq. A.11 is:

$$\begin{aligned} A_1(z) = A_1(0)cos(Cz) \\ A_2(z) = -iA_1(0)sin(Cz) \end{aligned} \tag{A.13}$$

when light is launched in waveguide 1. The light oscillates sinusoidally between waveguides and the propagation length required for a full oscillation is called the beat length $l_B = \pi/C$. It is also important to note that the coupling coefficient contains a wavelength dependence and therefore the beat length is also a function of wavelength. This fact is exploited in chapter 6 to form a coarse wavelength division multiplexer (WDM).

"The Light of Death [in reference to a laser]: get some people to devote entirely to this. Feed them and don't let them do anything else."

Mao Tse Tung

B
Experimental methods

In this appendix the methods used to produce waveguides and waveguide circuits in glass substrates will be outlined. Throughout this thesis an iterative approach as shown in Fig. B.1 has been used. Devices are fabricated and ultimately characterised to measure and calibrate their performance. At each step new methods or approaches unique to that specific device are often applied necessitating many trips through the iterative cycle to produce a desired performance. One of the true advantages of the FLDW technique is the flexibility to adjust the fabrication process quickly and to apply new methods or test procedures between production cycles. Hence, there is no simple fabrication recipe but rather an approach. Furthermore, many of the techniques described here have only been applied to a device which was designed and fabricated for a single experiment.

B.1 Waveguide fabrication

Recall from chapter 2 that two modification regimes were identified. These relate to the repetition rate of the laser and result in thermally induced modifications or an athermal response. These material responses are explored using two laser systems, a repetition rate and low repetition rate system.

B.1.1 Low repetition rate laser: Hurricane

The Hurricane laser system is a regeneratively amplified Ti:sapphire with a 1 kHz pulse train, up to μJ range pulse energy and 120 fs pulse duration. The system is composed of four interlinking sections: an oscillator, a regenerative amplifier, a pump laser and a pulse stretcher/compressor (arrangement shown in Fig. B.2). An oscillator (Mai-Tai), composed of a Ti:Sapphire crystal which is pumped by a frequency doubled

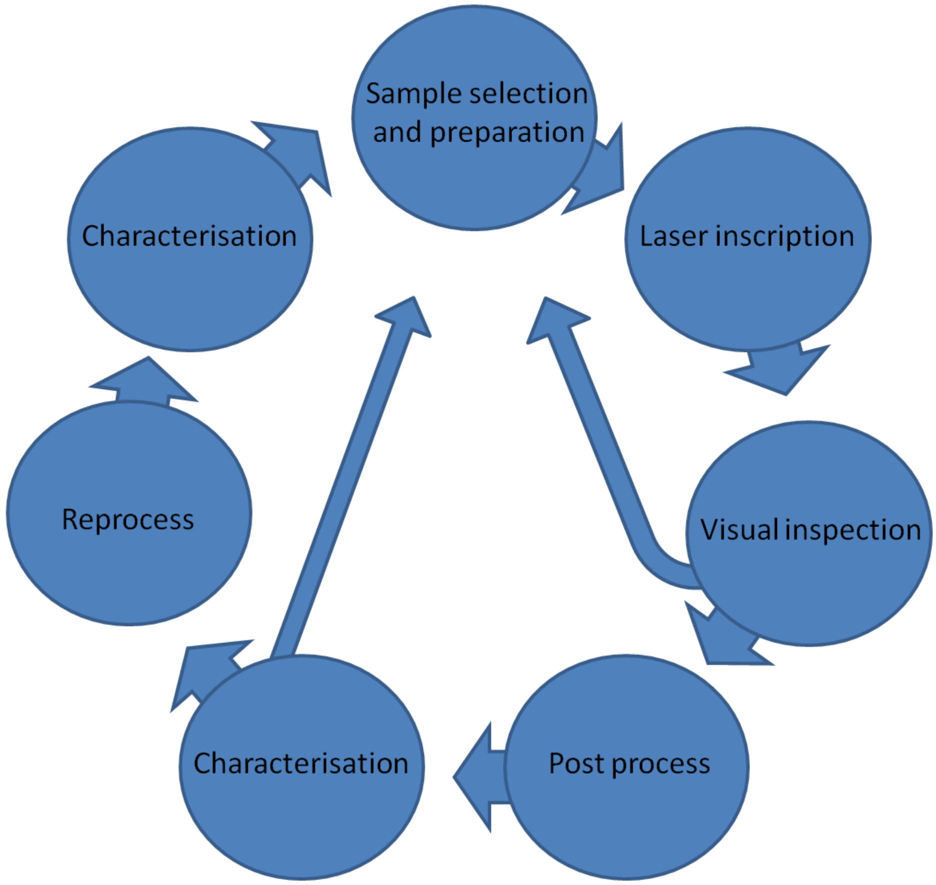

FIGURE B.1: Schematic of the device prototyping cycle. This cycle can take from 1 day to several months depending on device requirements and resource availability.

Nd:YVO_4, provides a seed pulse of 120 fs with a repetition rate of 80 MHz to an amplifier. A regenerative amplifier (RA), using chirped pulse amplification (CPA), is used to increase the pulse energy. The RA is composed of a cavity with a Ti:sapphire crystal, pumped using a 5 W 532 nm frequency doubled Nd:YAG, with the output coupling achieved using a Pockels cell. A pair of diffraction gratings are used to stretch the pulse before entering the RA to allow amplification of the pulse to occur without resulting in excessively high peak powers which would damage the gain medium. After the seed pulse has been stretched and amplified in the RA it is switched out using a Pockels cell which is triggered at 1 kHz. These pulses are then recompressed using a second pair of diffraction gratings and exit the laser.

The output power of the laser system is controlled externally using a polarising beamsplitter (PBS) and halfwave (HW) plate (800 nm zero-order). The HW plate is mounted on a motorized stage (Aerotech ADR75 direct drive rotary stage) which is then computer controlled (U-axis). The beam then passes through an optional set of increasing optical density filters to provide an additional control over the output intensity. Laser polarisation is controlled using a Berek compensator (New Focus model 5540). Finally the beam passes through a slit which produces an elliptical beam cross section in order to increase the symmetry of the waveguides [169]. The beam passes through an objective and onto the sample which is mounted on a vacuum chuck fixed to a three axis translation stage (Aerotech).

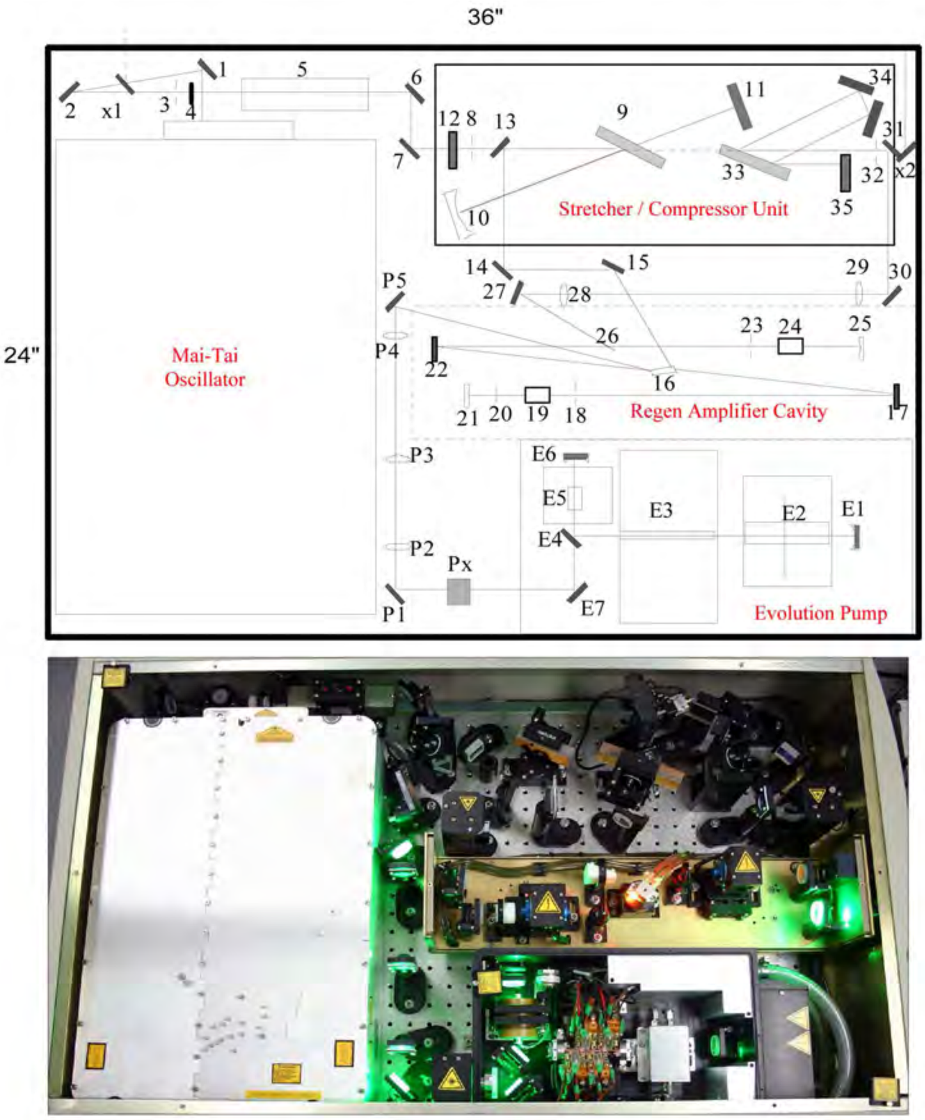

Figure B.2: Schematic of the Hurricane laser internal components (above) and an image which shows the actual layout of the corresponding components in the laser (below)(images courtesy of Spectra physics).

B.1.2 High repetition rate laser: Femtosource XL

This laser system was the main laser used during this thesis. The laser (Femtosource XL 500, Femtolasers) is a Ti:Sapphire chirped pulse oscillator with no additional amplification stage. The key advantage of this system is that it provides a balance between high pulse energy and moderately high repetition rates. The advantage when compared to Ti:Sapphire amplifiers (kHz repetition rate and mJ pulse energy) is that it permits operation in the cumulative heating regime, where multiple pulses arrive successively before the characteristic thermal diffusion time of the material. However, it provides a higher per-pulse energy than conventional mode locked amplifiers (<100 MHz and several nJ pulse energy), meaning that higher bandgap materials can be successfully modified.

The laser system layout is shown in Fig. B.3. A cavity length of 30 m, which includes a multipass Heriott cell [334], defines the repetition rate of the laser of 5.1 MHz. This long cavity length enables pulse energy scaling but requires careful intracavity dispersion management [335, 336]. The intracavity dispersion is controlled using dispersive optics providing a positive group delay dispersion (GDD) meaning a long pulse circulates in the cavity experiencing gain but avoiding excessive peak power which would destroy optical components [337]. A semiconductor saturable absorber mirror (SESAM) provides an intensity dependent loss in the cavity assisting in stabilized mode locked operation [338]. The Ti:sapphire crystal is cooled to 240 K in a dry flow air chamber and pumped with a continuous wave, frequency doubled (1064-532 nm) $Nd:YVO_4$ laser (Millennia XV, Spectra Physics). After the output coupler the pulses are compressed using a tunable prism pair compressor providing a negative GDD and the resulting compressed pulses are <50 fs duration. The pulse energy is up to 550 nJ giving an average power of 2.7 W at a central wavelength of 800 nm.

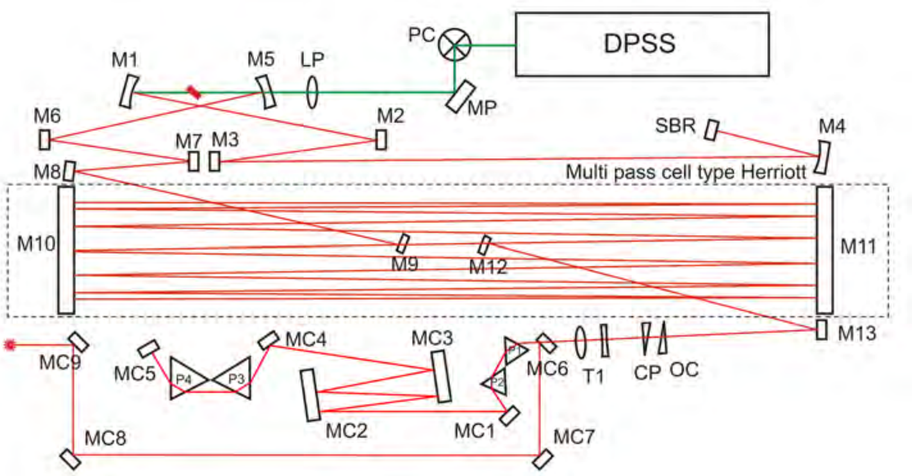

FIGURE B.3: Schematic of the Femtosource XL cavity layout (images courtesy of Spectra Physics).

As in the low repetition rate system, the output power of the laser system is controlled externally using a polarising beamsplitter (PBS) and halfwave (HW) plate. The beam is expanded and passes through a Pockels cell which can be used to adjust the repetition rate of the laser. It then passes through a HW plate and PBS which can be tuned manually. This step allows the selection of maximum transmission when using the 5.1 MHz pulse train or can be operated for maximum extinction. In the case where the HW plate and PBS are aligned for maximum extinction, the Pockels cell applies a halfwave rotation when triggered which means only the pulses selected by the Pockels cell can be transmitted. The beam is then directed through a final quarter wave (QW) plate. When aligned at 45° to the incoming linear polarisation, the QW produces a circularly polarised beam or at 0° produces no change to the input polarisation. The beam is then directed vertically, using a periscope, and directed toward the translation stages used for translating samples with respect to the beam. A transparent vacuum chuck, with LED illumination from below, is mounted on top of the translation stages (Aerotech) to hold samples in place during fabrication. A vision system is mounted above the translation stage, permitting alignment and active monitoring of the sample fabrication. The vision system is a combination of a lens (Raptar, Wollensak) and CCTV camera (DH745 colour, Sony).

B.1.3 Translation stages

Waveguides in this thesis were all fabricated by translating glass samples with respect to a laser focus. To effectively, efficiently and reproducibly perform this process a set of three-axis Aerotech linear translation stages were used. The stages used for each axis are chosen according to their function. The Z axis which moves a sample parallel to the laser focus is an Aerotech WaferMax Z lift stage with 5 mm of travel and a maximum translation speed of 240 mm/min. The Y axis uses an ABL1000 linear motor air bearing stage as this is the stage that moves in the direction of the waveguides. The final stage, at the base of the setup, is an ABL2000 which moves the stage laterally perpendicular to the direction of the waveguide writing direction. Both the X and Y stages feature a maximum of 3000 mm/min translation speed and 100 mm of travel.

B.1.4 Glass selection and preparation

Glass selection must be appropriate both to the device being designed but also the laser parameters being used, since the two laser systems used are so different it meant that glass selection was driven by this feature. The low repetition rate system can offer short pulse duration (< 200 fs), high pulse energy (> 1 μJ) but a low repetition rate (max 1 kHz). This is sufficient to initiate nonlinear absorption in most materials including fused silica. Fused silica such as Lithosil is extremely pure and ideal for low loss structures for telecommunications applications. Furthermore, Suprasil, contains an OH^- impurity, which fluoresces at 650 nm, allowing waveguide circuits to be imaged from the surface and intensity distributions in waveguide arrays to be monitored [339]. However, the low repetition rate system, which operates almost exclusively in the athermal modification regime [109], has the limitation of requiring extremely low sample translation speeds of 1-10 mm/min and multiple overpasses (2-8) to produce a practical index change. This means a typical circuit, consisting of four waveguides each 30 mm in length would take between 0.5-16 hrs. Since typically multiple circuits must be fabricated, varying parameters such as laser power, translation speed and circuit designs, it can take several days to produce a single sample. During this period temperature fluctuations in the surrounding environment become a significant contributor to the uniformity of structures and ultimately limits the flexibility of design.

The high repetition rate laser has a short pulse duration ($\sim$ 50 fs), a low pulse energy ($<$ 600 nJ) and a high repetition rate of 5.1 MHz. The low pulse energy and high repetition rate originate from the 30 m long cavity (Herriot cell) used in the laser oscillator which is subsequently unamplified. The high repetition rate is advantageous for producing devices rapidly and translation speeds of 500-2000 mm/min are sufficient to produce waveguides. Furthermore, a Pockels cell in the beam path allows the repetition rate to be changed. This is advantageous for instance if there is a need to switch rapidly between a thermal or athermal modification regime. However, due to the low pulse energy it is not possible to efficiently modify fused silica to produce low loss waveguides. It has been observed that high repetition rate modifications in fused silica lead to a pearl chaining (repeated chains of refractive index chains resembling a pearl chain necklace) effect due to its high bandgap. Hence, borosilicates including Schott AF-45 and Corning Eagle 2000 were the optimal candidates for producing smooth, thermally induced refractive index change.

Preparing glass samples which come as unprocessed ingots requires a substantial investment in time and energy. This process involves dicing an ingot using a diamond blade and polishing the two faces of the sample to achieve a high quality optical surface for producing a laser focus in the material. This was not required since the author purchased samples (or used already prepared samples from S. Gross, M. Ams and G. D. Marshall) for laser inscription experiments. Typically the only procedure required was to take a polished glass sample and cut to the appropriate size using a diamond blade CNC dicing saw (SYJ-400, MTI Corp.).

B.2 Postprocessing methods

B.2.1 Thermal treatment

Eaton *et al.* first thermally annealed laser written waveguide structures in glass, showing that refractive index modifications can be altered [110]. Arriola *et al.* have shown that by thermally annealing waveguides, written using a high repetition rate laser in the thermal regime, it is possible to modify the induced refractive index change of a waveguide and increase coupling efficiency and reduce bend losses [111]. This has enabled the fabrication of advanced photonic circuitry, low loss waveguides and waveguiding structures in borosilicate and doped borosilicate glasses [111, 340–342]. Thermal annealing has also been applied to other glasses including chalcogenide glass [343]. The procedure involves heating the glass above the annealing point of the material before slowly cooling below the strain point in order to avoid inducing any stress fields. Figure B.4 shows the refractive index distribution of a laser written waveguide both before and after thermal annealing. In this image, before annealing, a core region of high refractive index with a surrounding region of low refractive index and another ring of high refractive index can be seen. After the thermal treatment the refractive index distribution has been altered and the outer region of high refractive index has been removed.

The origin of the laser induced refractive index distribution (for high repetition

Table B.1: Thermal characteristics of Schott AF-45 and Corning Eagle-2000 [196, 197].

Material	AF-45	Eagle-2000
Strain point	627°C	666°C
Annealing point	663°C	722°C
Softening point	883°C	985°C

rates >100 kHz) change is suggested to be due to ion exchange occurring in the focal region and electron probe microanalyzer (EPMA) measurements of materials before and after laser irradiation support this hypothesis [344, 345]. Furthermore, studies of the temperature changes occurring during laser processing further elucidate the required temperatures for elemental migration to occur [346]. This helps to shed light on why, after the thermal annealing of laser written waveguides, the outer positive refractive index region is removed while the core is preserved. Elemental migration requires temperatures above those which occur in annealing and it is postulated that molar refractive index change is the origin of this outer refractive index region and can therefore be eliminated by thermal annealing [111, 126].

In order to reproducibly modify a refractive index distribution of a laser written structure, some knowledge of the material properties is essential. The thermal properties of the two borosilicate glasses used in this thesis, Eagle-2000 and Schott AF45, are summarised in Table B.1. In annealing experiments, Eagle-2000 sample was heated to a maximum 750°C, while the AF-45 was heated to a maximum 690°C. The heating and cooling profile involved two steps each. The heating cycle involved heating quickly (10 minutes) to the stress point of the material and subsequently heating very slowly to the maximum temperature (2 hours). The cooling cycle involved a very slow cooling time (10 hours) from the maximum temperature to the stress point and subsequently a faster cooling speed (5 hours). The maximum temperatures correspond to a slight excess over the material annealing point (as shown in Tab. 3.1) but below the softening point of the material [196, 197]. To avoid inducing any addition stress in the material, a consistent and slow temperature profile was used. This was achieved using a commercial heat treatment furnace composed of a ceramic chamber surrounded by heating elements and thermally isolated from the environment using thermal insulation materials. This system is capable of reaching temperatures of 1100°C. A temperature profile can be programmed by using the integrated Shimaden FP21 (*Shimaden Co. Ltd.*) controller which permits multiple (up to 9) temperature settings in a single profile. Care is taken to minimise large temperature fluctuations when approaching temperatures close to or above the stress point of the material.

B.2.2 Grinding, polishing and etching

Once waveguide structures have been formed in glass samples they then need to be exposed to facilitate characterisation. For the majority of devices in this thesis the

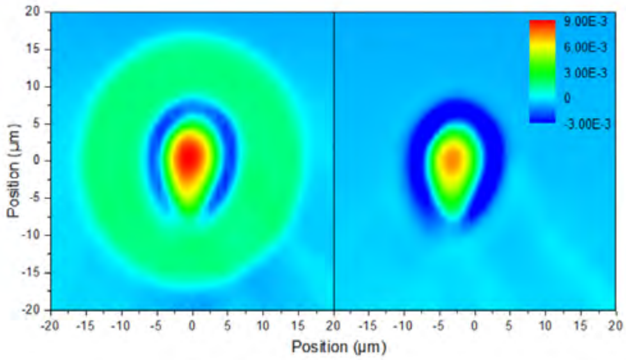

FIGURE B.4: A measurement of the refractive index profile of a laser written waveguide before thermal annealing (left) and after (right) [111].

edges of a sample must be ground and polished. This is for two reasons. Firstly, when a laser reaches the edge of a glass sample waveguide tapering occurs over a distance of approximately 200 μm, which must then be removed to improve coupling to an optical fibre. Secondly, polishing the waveguide facets of a sample reduces scattering losses when coupling to an optical fibre and also allows free space coupling as seen in Fig. B.13.

Grinding and polishing of sample facets is achieved using a Logitech PM4 and PM5. The grinding process uses a large cast iron plate which is then coated continuously in a slurry containing suspended grit (Al_2O_3) of maximum sizes of 25 μm, 5 μm and 1 μm (Micro Abrasives Corporation, MA). The plate is then dressed in order to ensure uniform coating and surface flatness. Then a sample is placed on the plate using a PP5 jig, which uses a custom made adaptor (the *star* designed by Simon Gross) to suspend samples perpendicular to the grinding wheel. Samples can be attached to the star using UV curing adhesive (Norland Blocking adhesive). The PP5 jig permits angular adjustment to ensure the sample is perpendicular to the grinding wheel and an adjustable, spring loaded, mount to fix the pressure between the sample and the grinding wheel. This is chosen to be sufficient to remove material quickly while avoiding excessive pressure which would cause cracks and damage to the sample. The conceptual approach of the lapping procedure is to remove material gradually ($\sim 5\times$ grit size) and at each stage decrease the grit size. The amount of material removed from the sample is monitored using a micrometer attached to the PP5. Material is removed from the sample at a rate determined by the hardness of the sample, the size of the particle size in the lapping compound and the sample pressure on the lapping wheel. Once the sample has been ground and a visual inspection confirms no chips or scratches are present, the polishing process can begin. This procedure uses a polyurethane foam surface wheel and an aqueous slurry of colloidal silica (80 nm mean particle size) suspended in an alkaline solution to prevent aggregation (Ultra-sol^{TM} 500S, Eminess Technologies Inc., AZ). To prevent this solution from drying and solidifying a low alkalinity (pH$\sim$ 9) NaOH solution is also applied to the polishing wheel during processing. Once this procedure is complete the star holder and sample are removed from the PP5 jig, immersed in a beaker of acetone to remove the bonding adhesive and the process is hastened by placing the acetone in an ultrasonic bath.

In addition to polishing glass samples to reveal waveguide facets, it is also desirable to polish the surface of glass chips to expose waveguides for additional characterisation procedures such as scanning electron microscopy (SEM). This can be competed using the PP5 jig and Logitech polisher. Subsequently, in order to study sub-micron structures within the waveguides, a selective etching procedure was required to increase the contrast necessary for imaging using SEM. This was completed using a hydroflouric (HF) acid etch. A glass sample, with an exposed waveguide, was submerged in a HF acid bath of varying concentrations and durations. The etching procedure used identical samples with immersion durations of 60 and 90 seconds in a HF concentration of 5% (5%=15 mL H_2O and 1.5 mL of 50% HF acid). The results of the etching process are displayed in Fig. B.5 and further information is contained in chapter 3. It was revealed by SEM analysis that the optimum etch duration was not reached and even the 60 second etch was too long resulting in significant degradation of the contrast of sub micron structures in the waveguide.

Alternatively, etching can be performed using focused ion-beam mills (Leica EM TIC 3X triple ion-beam cutter). This has the advantage of removing very small quantities of material very slowly leading to a very smooth cut with feature roughness below 100 nm. Furthermore, this could be maintained over depths of several mm (see Fig. B.6).

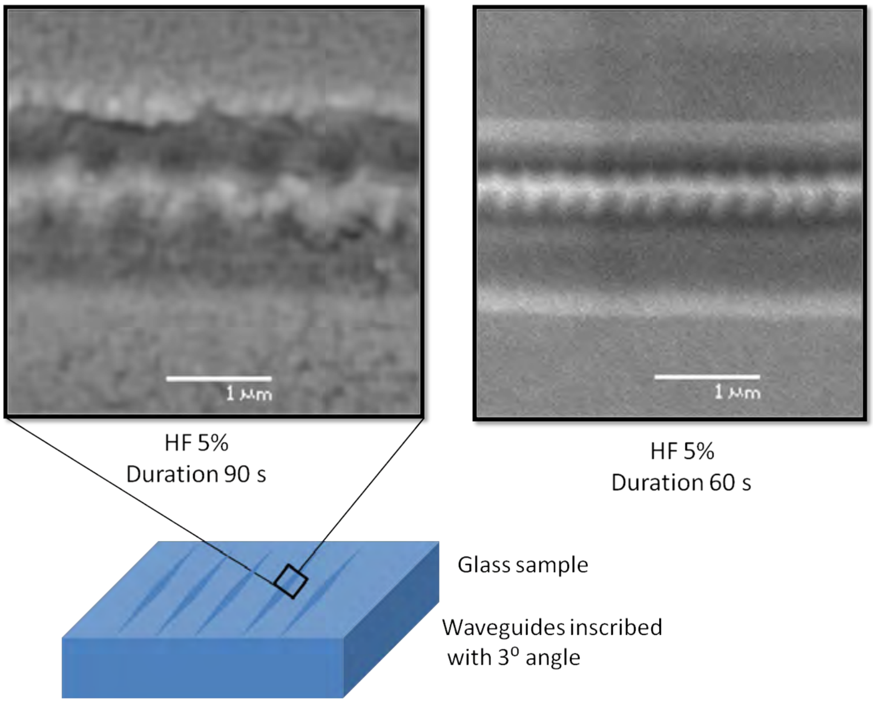

Figure B.5: A waveguide from a top down view shows the result of HF etching durations on the contrast available in SEM images. An identical sample has been exposed to 90 s of etching in the left SEM image and 60 s in the right image.

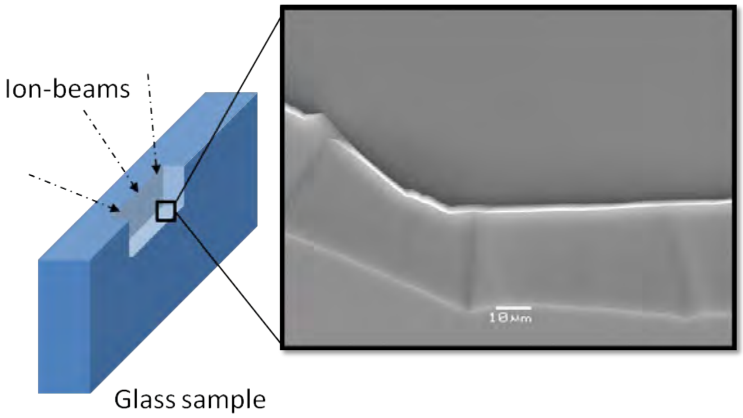

FIGURE B.6: Showing the result of the triple beam Leica cutter. The inset shows the SEM image of the edge of a waveguide chip after irradiation for 3 hours.

B.2.3 Deposition techniques

Deposition of materials on the surface of glass samples is important for two processes, firstly a conductive coating must be applied when imaging using an SEM to prevent charge buildup. Secondly, it is desirable for post-processing and tuning applications to use a metallic surface deposited layer as a resistive element.

The deposition system used was thermal evaporator (Leybold) which was modified in house to include a turbo molecular pump enabling pumping to high vacuum ($< 10^{-7}$ mbar) quickly. A sample is placed in a vacuum chamber and an electrical current is passed through a tungsten boat containing a metal (See Fig. B.7). This causes the metal to heat and vaporise thus coating the sample. The thickness of the coating on the surface of the metal can be monitored using a quartz piezo crystal thickness monitor (STM 100, Sycom) capable of monitoring average film thickness down to Angstrom resolution. The metal in the boat is heated by a current which is gradually increased to achieve a deposition rate of 2.5 $\mathring{A}$/s, this gives a balance between efficient deposition and uniform thickness across the sample. This was especially crucial in the case of the deposition of a nickel-chromium alloy (NiCr concentration: Ni-80%, Cr-20%) which, at the vaporisation temperature of 1100 °C and a vacuum of 10^{-7} mbar, has a tendency to form an alloy with tungsten and therefore destroy the evaporation boat if operated for long durations. A film thickness of 100±1 nm was achieved for the NiCr metallic film. To produce a 10 mm wide strip across the sample a simple mask of Kapton tape was used since it does not out-gas in high vacuum.

The NiCr alloy showed excellent adhesion to the glass surface and was not removed by the application of mechanical pressure or from immersion in solvents such as ethanol or acetone. This makes it a robust material for the production of metallic thin films on glass surfaces and its high resistivity makes it useful for the production of resistive heaters. However, conventional solder does not adhere well to NiCr making it difficult to bond wires to the surface of a sample. Hence a layer of gold was chosen to produce an additional intermediate layer between the solder and NiCr to form contacts. Once the NiCr coating was removed from the vacuum chamber it began to oxidise and the gold adhesion was poor. Unfortunately gold does not adhere well to oxidised samples meaning when coating either glass or oxidised chromium, it is easily removed by very minor mechanical force and immersion in liquids. However, it was later found that the best means of attaching a wire to the NiCr surface was using a conductive adhesive.

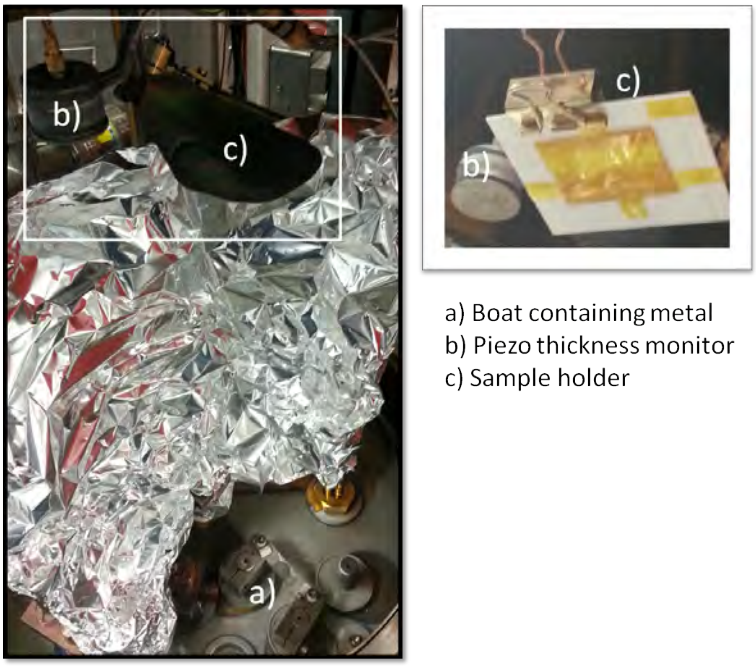

Figure B.7: An image showing the the thermal deposition system, the inset shows the bottom of the sample holder (c) and piezo crystal monitor (b) which is directly facing the boat containing the metal to be deposited (a). The Kapton tape (yellow coating) which acts as a crude mask can be seen on the surface, bases and facets of the sample (Schott AF45 30 mm×30 mm) to be coated.

B.2.4 Laser reprocessing and post-processing

Modifying a photonic chip, after it has been fabricated, is a highly desirable technique due to challenges in improving the reproducibility of the laser processing technique. This can be achieved by either reprocessing a circuit, where the parameters of a circuit are changed after it has been fabricated by tuning it permanently, or by post-processing, where an additional functionality can be employed such as a tunable circuit element. In this thesis both approaches were employed to improve the operation of circuits.

A reprocessing step was employed to adjust the splitting ratio of directional couplers used in a laser written circuit and its application is discussed in detail in chapter 5. A laser written chip was fabricated, characterised and subsequently packaged (see section B.3.3). The chip was then placed on the vacuum chuck fixed to the motion control stages of the Femtosource XL laser. Light from a diode laser was coupled into the input of the device and the intensity at both output ports monitored using two power meters. Using the vision system the laser focus can be aligned to the waveguide splitter which is to be modified. This means that the chip can now be tuned by writing over one arm of a directional coupler with respect to another until the correct beamsplitter ratio is reached. Using this process the beamsplitter reflectivity could be tuned to within ±5% which could be improved by modifying the structures using an athermal processing regime. This method, although effective, was extremely inefficient since minor misalignment can also cause large amounts of scattering loss as can be seen in Fig. B.8.

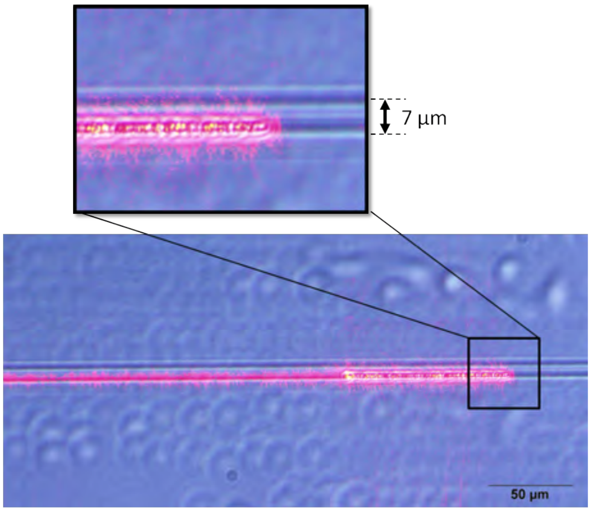

FIGURE B.8: A microscope image of a highly lossy modification located between two waveguides forming a directional coupler. The scattering from a 635 helium-neon laser is visible and resulted in a loss of 12 dB.

Post-processing was used to produce a low voltage operation resistive heater on the surface of a waveguide chip (See chapter 6). This permits the temperature tuning of one arm of a Mach Zehnder interferometer to create a tunable beamsplitter. This was achieved by ablating a NiCr surface deposited thin film forming a narrow strip which acted as a localised heater (See Fig. B.9). A UV laser can ablate NiCr films enabling the removal of NiCr from the surface of a chip with very little effect to the glass surface. This process took a 10 mm wide strip of NiCr with an initial resistance of 10 Ω and by producing a 250 μm wide strip in the NiCr layer the resistance was increased to 200 Ω.

B.3 Characterisation processes

B.3.1 Microscopy

One of the primary characterisation processes used for analysing waveguide structures is microscopy. Both longitudinal and cross sectional images of buried structures in transparent substrates can be collected by using a transmission differential interference contrast (TDIC) microscope. This instrument is capable of imaging structures which display a minor variation in refractive index and hence is ideal for imaging buried waveguides in glass.

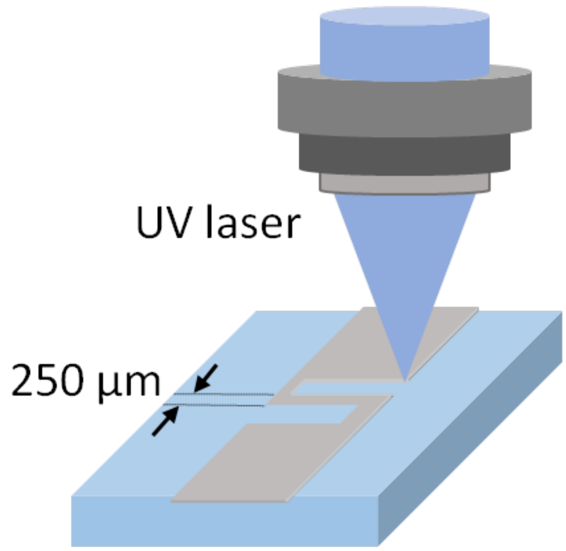

Figure B.9: Schematic of the surface patterning applied to a laser written chip to fabricate a low voltage operation resistive heating element.

The TDIC microscope (Olympus IX81) is an interferometric beam-shearing technique. This method increases the contrast of minor path length variations caused by small variations in refractive index. This allows the imaging of waveguides, buried in glass substrates, with small variation of refractive index ($\Delta n < 10^{-2}$) compared to the surrounding bulk. The beam-shearing method uses a pair of birefringent components (Wollaston prism) which separates the light, polarised at 45° to the optical axis, into spatially separated orthogonal components. These are transmitted through the sample by the condenser, collected by the objective and the second Wollaston prism and pass through an analyser (See Fig. B.10). Upon passing through the sample the orthogonal polarisations may experience a different optical path if they pass through regions of different refractive indices and this results in a phase difference which, upon passing through an analyser, is translated into an intensity change. Thus the TDIC method increases the contrast available from minor refractive index change. This is a suitable, non-destructive, method for viewing the shape and cross section of waveguides at micron resolution. However to image sub-micron formations within the waveguides an SEM is required.

(a)

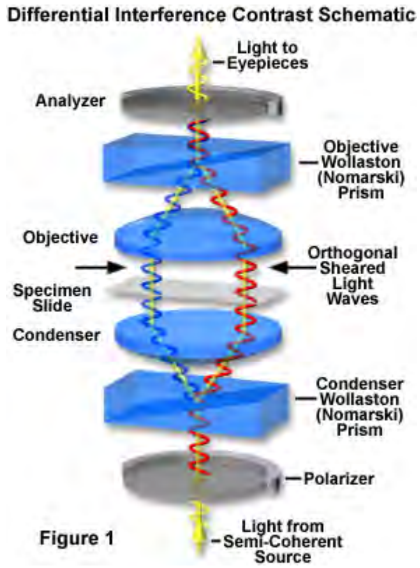

(b)

FIGURE B.10: (a) The Olympus IX81 microscope and (b) the operational principle of the differential interference contrast imaging technique (Images courtesy of Olympus America).

Scanning electron microscopy (SEM) is an imaging technique which uses a beam of focused electrons for imaging structures at a scale of nanometres. Electrons can be produced by the thermionic emission from a material and an accelerating voltage can be used to direct and translate the beam across a sample. The accelerating voltage can be from 0-40 keV and when electrons strike a sample they can then scatter elastically, inelastically or emit electromagnetic radiation which can be detected. The SEM used for imaging waveguides in this thesis (JOEL 6480LV) incorporated detection methods for backscattered electrons (BSE), secondary electron imaging (SEI)and energy dispersive spectroscopy (EDS) to image structures. A sample is mounted on a carbon stubbed post, coated in gold if not conductive and then inserted into the SEM vacuum chamber. Once the system is evacuated samples can be imaged. Accelerating voltage has the most significant effect on image quality. At low accelerating voltages the BSE can be imaged however it is essential to use high accelerating voltage to image secondary electron emission.

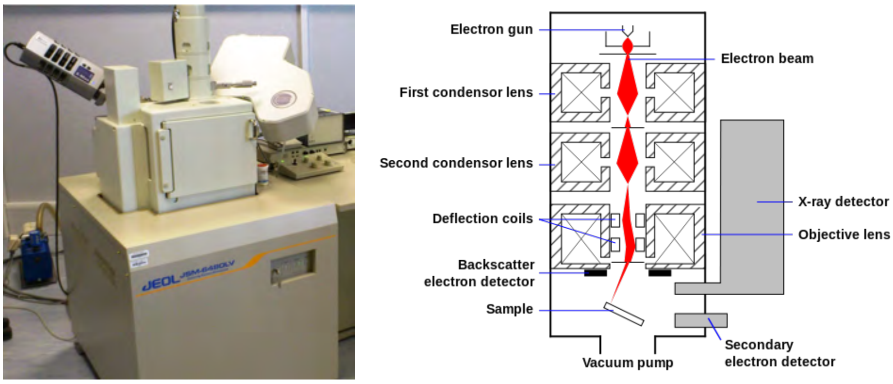

(a) (b) (c)

FIGURE B.11: (a) The JOEL 6480LV and (b) the operational principle of scanning electron beam microscopy (Images courtesy of JOEL and Debra Birch), (c) gold coated sample mounted on carbon tipped post.

B.3.2 Waveguide characterisation

Assessment of the operation of waveguides and circuits centres on the guidance properties of a device. Light is coupled into and out of waveguide circuits using optical fibres or arrays of optical fibres (V-groove arrays). These are typically mounted onto a holder and fixed to 6-axis flexure stages (Thorlabs NanoMax600 series). Two stages (right and left handed) are located on either side of a vacuum chuck which holds the device-under-test (DUT) (see layout in Fig. B.12). The vacuum chuck is placed on a 3-axis (Newport XYZ) stage to allow coarse alignment of the DUT. The 6-axis stages are fitted with piezo-controllers and drivers for fine alignment control. The sample and fibres could be imaged and roughly aligned using a vision system consisting of an adjustable lens tube (Navatar) and CCTV camera (SH745, Samsung). The imaging system was mounted directly above the DUT on a 3-axis translation stage along with a fibre optic illumination system (Navatar) coupled to the base of the lens tube.

A variety of fibre coupled laser diodes were used for characterisation of devices. Typically a 658 diode was used for coarse alignment as it is easily seen by eye. However, 808 nm, 1310 nm and 1550 nm diodes (4-channel diode, Thorlabs) were used for characterisation of device propagation properties at specific wavelengths. In addition a fibre coupling setup was also used to couple light from a tunable (700-1100 nm) femtosecond ($\sim$100 fs) laser (Chameleon, Coherent Inc.) into waveguide devices.

Fibres can be interfaced with either side of a waveguide device but it is also practical to couple light into one port of a waveguide device and image the near field output of the other. This allows one to perform characterisations of the shape of the mode of a waveguide. The output of a multiport device is shown in Fig. B.13 where a single fibre couples red light (658 nm) into the input of a waveguide chip while an objective captures the output distribution which can be seen on the white screen behind. More details on the methods used to characterise near field waveguide profiles is contained in chapter 3.

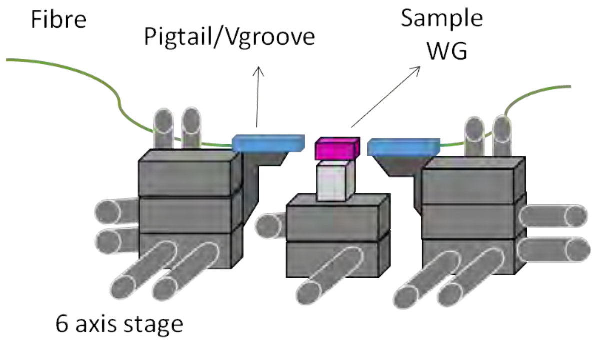

FIGURE B.12: Schematic of the characterisation setup for coupling light in and out of waveguide samples.

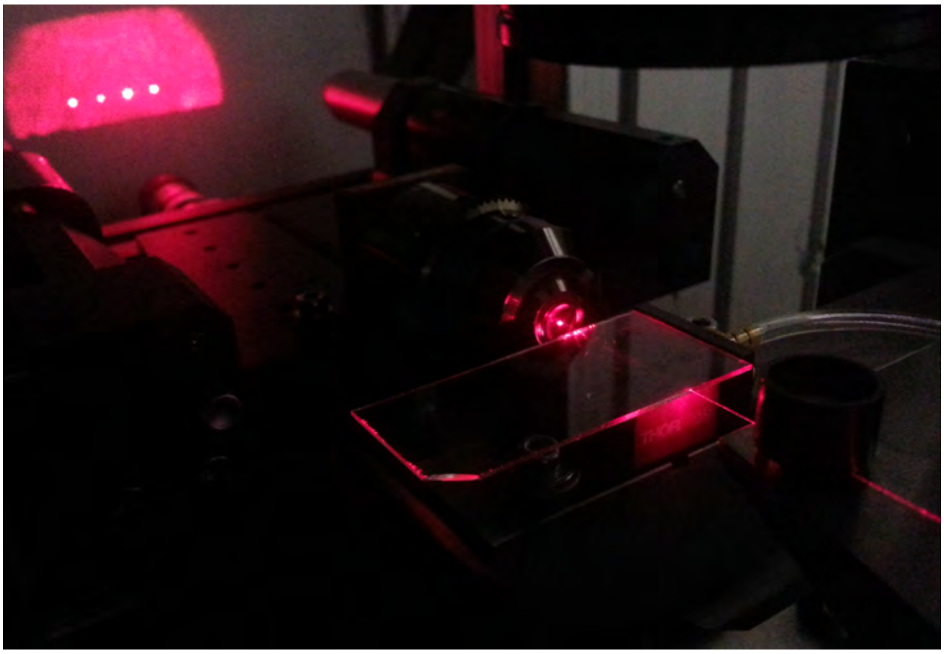

FIGURE B.13: Image taken of the characterisation procedure used to determine the splitting ratio of a four-port waveguide splitter. Here light is taken from a single input fibre coupled into the circuit and collected at the output by an objective and four illuminated ouputs can be seen at 700 nm. Here a power meter was replaced with a white background screen for demonstration purposes.

B.3.3 Photonic chip packaging

As manufacturing processes advance the efficient interfacing of multiple optical components with other photonic circuitry becomes crucial. A range of structures and fabrication procedures exist which can produce photonic interconnects [347, 348]. Much of this has been driven by the advances in silicon-on-insulator waveguide technologies where mode sizes are substantially smaller than those of a single mode fibre such as SMF-28. Advanced approaches currently exploit mode tapers or grating couplers [349, 350]. In this thesis the mode field diameters of the waveguides closely match those of a standard single mode fibre so novel techniques are not essential. Most commonly a V-groove array is used which is a planar array of waveguides equally spaced by 125/127/250 μm. These are commercially available and offer fibre arrays from 2 to 64 channels. The spacings are defined by the etch rate of the crystalline silicon substrate, although custom spacings are obtainable.

Typically when performing extended characterisation procedures, using chips in an environment where multiple 6 axis stages are not available or for active monitoring of reprocessing it is desirable to package chips using UV curing adhesive and V-groove arrays. This requires aligning the V-groove facets with the waveguide chip and optimising input and output coupling using a multiaxis alignment system (see Fig. B.12). Once the coupling has been optimised a UV curing adhesive (initially a viscous liquid) is applied to the location requiring bonding. Then a low intensity UV torch is used to cure and polymerise the adhesive, during this time minor adjustments to coupling are performed to compensate for the expansion/contraction of the adhesive during curing. Finally a high intensity UV dosage is applied, ideally for a long period of time, to the bonding area. Figure B.14 shows a packaged chip which displays the bonding regions and V-groove facets.

The UV curing adhesives used for the experiments described in this thesis are from Norland and adhesives 61, 65 and blocking adhesives were used and no significant difference in performance noted. The disadvantage of the UV curing adhesives is their susceptibility to temperature fluctuations and damage thresholds. The UV adhesives experienced fluctuations in bond position due to heating from input laser intensity, from the fibre, and surrounding environmental temperature changes (>10 K). A threshold of ∼20 mW average power was observed to damage the adhesive resulting in coupling changes and ultimately irreversible photo-darkening. Alternatives to UV curing do exist and novel approaches such as silicone rubber bonding show excellent adhesion and temperature stability [351]. Furthermore companies routinely use UV curing adhesives for high power applications and therefore it is possible a more effective means of photonic chip bonding is available.

B.3.4 Temperature stabilisation

In chapter 6, a periodically poled lithium niobate (PPLN) chip is used to produce correlated photon pairs. To fine tune the phase-matching wavelengths of downconverted photon pairs and prevent photorefractive effects the PPLN chip must be heated [320, 324]. The temperature must be tunable and also be maintained stable since the phase-matching condition is temperature sensitive. A 1 K temperature shift results in a 4 nm central wavelength shift of downconverted photons. To produce photons at 1310/1550 nm a temperature of 363.0 K is required and this is maintained to within 0.1 K. The layout of the control system for maintaining the oven temperature is shown in Fig. B.15(a) and the layout of the actual oven in the experiment is

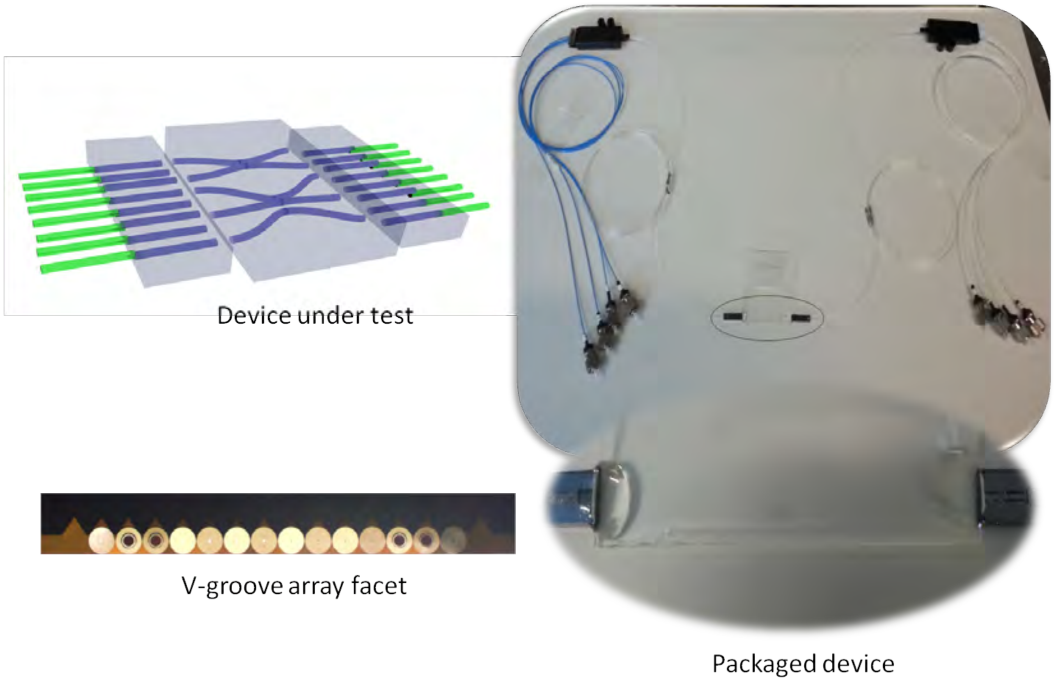

FIGURE B.14: Layout of the V-grooves bonded to the facets of a waveguide chip. Inset shows the facet of a V-groove array where waveguides are spaced equally in an etched silicon substrate. Image of a packaged chip with blue fibres, polarisation maintaining (PM) single mode (SM) fibres at the input to the chip and SM at the output. The inset shows a close up image of the V-groove arrays bonded to the input and output facets of the waveguide chip.

shown in Fig. B.15(b). By using a feedback from the baseplate to monitor the temperature change a thermoelectric cooler (TEC) controller was capable of providing a driving voltage to a resistive heater to stabilise the temperature of the baseplate to a selected value. An external power supply was used to provide the voltage required to coarsely set the temperature at a particular value meaning the TEC was only required to provide very small current changes.

B.4 Photon pair source

B.4.1 Spontaneous parametric downconversion

One of the crucial components required to perform a non-classical characterisation of a waveguide circuit is a source of multiple, indistinguisable, single photons. Unfortunately, an on-demand source of single photons has yet to be demonstrated. Currently the best available means of producing identical photons is to use spontaneous parametric downconversion (SPDC) [352]. This process uses a material which exhibits a $\chi^{(2)}$ nonlinearity to produce a pair of lower energy photons from a single parent photon. Non-centrosymmetric materials, anisotropic crystalline structures with no center of inversion, exhibit a $\chi^{(2)}$ nonlinearity [168, 353]. Many crystals have been used for SPDC

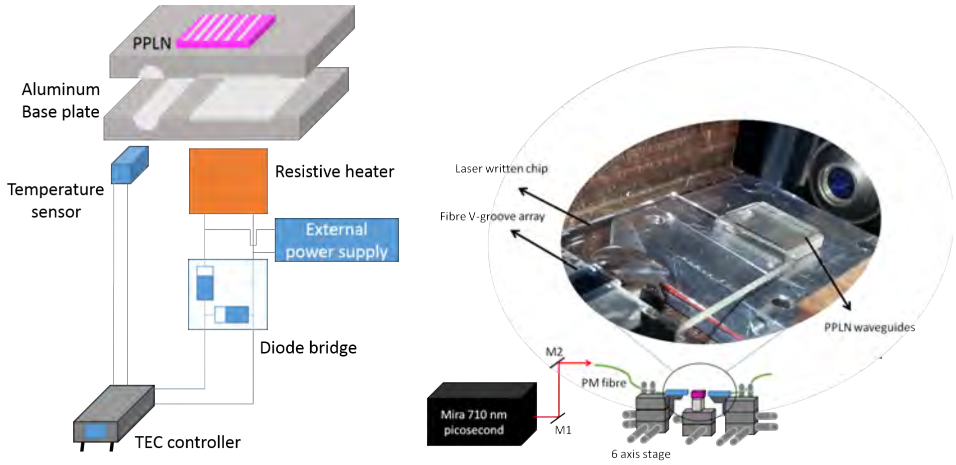

(a) (b)

Figure B.15: Design of oven for heating and temperature stabilized operation of a PPLN chip. In the image to the left the PPLN is not bonded to the waveguide chip but is brought into close contact.

such as uniaxial crystals Beta-Barium Borate, BaB_2O_4 (BBO) [354], and Lithium niobate, $LiNbO_3$ (LN) [355], or biaxial crystals Potassium Titanyl Phosphate, $KTiOPO_4$ (KTP) [356], and Bismuth Borate BiB_3O_6 (BiBO) [68].

Energy and momentum are conserved in the downconversion process and the downconverted pairs, are referred to as signal and idler. For both uniaxial and biaxial crystals the geometry of the optical axes(s) with respect to the incoming and outgoing photons must be selected carefully to produce the desired combination of pump, signal and idler wavelength and propagation directions [8, 357].

B.4.2 Photon pair source design

A bulk SPDC source was used to produce photon pairs and consisted of a nonlinear crystal (a BiBO biaxial crystal) cut to achieve degenerate ($\omega_s = \omega_i = \frac{\omega_p}{2}$) downconverted photons in a non-collinear arrangement with an opening angle of 6 degrees (See Fig. B.16). The input pump wavelength was 402 nm and the output pairs were generated at 804 nm. The BiBO crystal (Newlight Photonics) was 5×5 mm^2 in area and 2 mm thick. The input and outputs were antireflection coated for the wavelengths of 402 nm and 804 nm.

The laser, a blue 402 nm CW laser diode at an output power of 100 mW (iBeam smart, Toptica), was focused inside the crystal using a 1 inch uncoated lens with a focal length of 175 mm and waist of 100±5 μm. The blue laser showed excellent beam quality, with an M^2 of 1.1 (see Fig. B.17) This was selected to give a slightly smaller beam waist than the pair of aspheric lenses used for the collection of the down converted photons (anitreflection coated at 800 nm).

The down converted photons were filtered using 3 nm FWHM interference filters

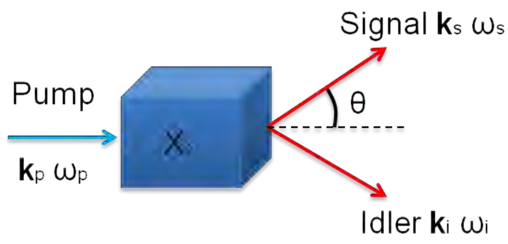

FIGURE B.16: Spontaneous parametric downconversion (SPDC) produces a pair of lower energy photons from a single parent photon.

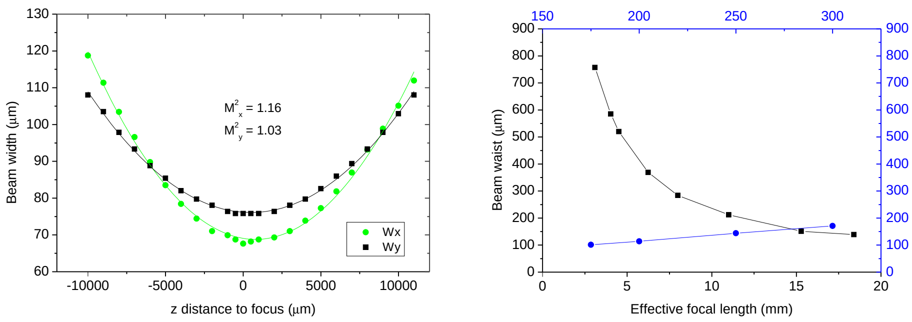

(a) (b)

FIGURE B.17: (a) An M^2 measurement to assess the beam quality of the laser diode and (b) a measurement of the beam waist produced by both aspheric (black) and 1 inch lenses (blue).

(Semrock) before being coupled into fibres using the aspheric lenses. A characterisation of the interference visibility when two photons are directed to different ports of a beamsplitter gives an assessment of the indistinguishability of the photons and resulted in an interference visibility of 96 % (see Fig. B.18.

B.4.3 Detection

Measuring photons is an essential component of any optical experiment. However, in quantum optics, where photon numbers are low, specialised detection equipment must be used. One common apparatus for photon detection is the photomultiplier tube (PMT). PMTs exploit vacuum tubes where a photon, upon impinging on a photocathode material, produces an electron which through a series of high voltage electrodes then produces and accelerates secondary electrons which are then detected as a pulse at the anode. These devices are still actively used in a number of fields including quantum optics. However, since the advent and advances of semiconductor technologies, the use of solid state avalanche photo diodes (APD) is widespread. APDs replace the PMT with a small diode (p-n junction) which upon absorbing a photon releases an electron.

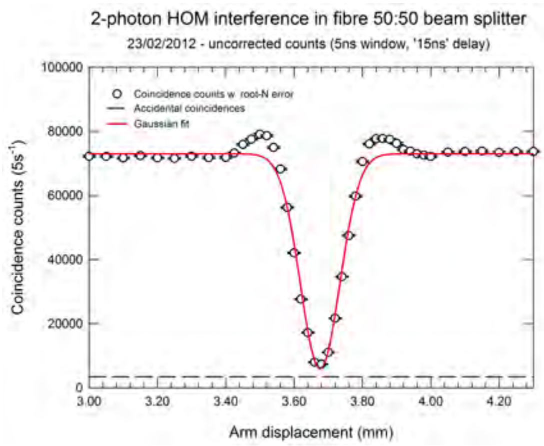

Figure B.18: Hong Ou mandel dip performed in a bulk optic, fused fibre beamsplitter showing a visibility of 96 % (when corrected for accidental coincidences).

Similar to the PMT, electrons in the APD are accelerated by a large bias voltage, V_{Bias}, and create secondary electrons forming an avalanche of electrons which can then be detected as a current. This V_{Bias} is crucial to the operation of the device as a single photon detector (geiger-mode) since when APDs are used for quantum optics the V_{Bias} is high enough to allow a single photo-generated electron to produce a self sustaining avalanche. The complexity of detector design then begins when attempting to build a circuit which can detect the current, quench the avalanche and return the APD to its initial state. This is also complicated by the challenges of detector noise which occurs from thermal photons produced as a result of the high bias current. Detectors also require a semiconductor with an appropriate response to the wavelength of light which is to be detected. Silicon is absorbing for wavelengths of light from 600-900 nm with typical efficiencies of 60-80 %. For experiments which were conducted at 800 nm, corresponding to the wavelength of the downconversion source describe in the previous section, a four channel array of fibre coupled detectors were used (Excelitas). InGaAs has a spectral response from 1100-1800 nm but also has the additional challenge of requiring thermal cooling to reduce the much larger dark count rates which occur in the detectors. Hence InGaAs detectors have a lower efficiency of 10-25 %, to reduce the noise associated with spontaneous recombination events. The InGaAs detectors used were IDQ201 and IDQ210 gated photon detectors (ID Quantique).

Bibliography

[1] T. Lawrence and R. Fisk, *Seven Pillars of Wisdom*, Vintage classics (Random House, 2010).

[2] P. Kavanagh, *Collected Poems* (Penguin Books Limited, 2005).

[3] J. M. Keynes, "The great slump of 1930," London: The Nation and Athenaeum (1930).

[4] P. W. Shor, "Polynomial-time algorithms for prime factorization and discrete logarithms on a quantum computer," SIAM J. Comput. **26**, 1484–1509 (1997).

[5] C. K. Hong, Z. Y. Ou, and L. Mandel, "Measurement of subpicosecond time intervals between two photons by interference," Phys. Rev. Lett. **59**, 2044–2046 (1987).

[6] D. C. Burnham and D. L. Weinberg, "Observation of simultaneity in parametric production of optical photon pairs," Phys. Rev. Lett. **25**, 84–87 (1970).

[7] I. Abram, R. K. Raj, J. L. Oudar, and G. Dolique, "Direct observation of the second-order coherence of parametrically generated light," Phys. Rev. Lett. **57**, 2516–2519 (1986).

[8] N. Boeuf, D. Branning, I. Chaperot, E. Dauler, S. Guerin, G. Jaeger, A. Muller, and A. Migdall, "Calculating characteristics of noncollinear phase matching in uniaxial and biaxial crystals," Opt. Eng. **39**, 1016–1024 (2000).

[9] A. Zeilinger, "General properties of lossless beam splitters in interferometry," American Journal of Physics **49**, 882 (1981).

[10] H. Fearn and R. Loudon, "Theory of two-photon interference," JOSA B **6**, 917–927 (1989).

[11] Z. Y. Ou, "Quantum theory of fourth-order interference," Physical Review A **37**, 1607–1619 (1988).

[12] T. Pittman, D. Strekalov, a. Migdall, M. Rubin, A. Sergienko, and Y. Shih, "Can Two-Photon Interference be Considered the Interference of Two Photons?" Physical review letters **77**, 1917–1920 (1996).

[13] W. Wootters and W. Zurek, “A single quantum cannot be cloned,” Nature **299**, 802–803 (1982).

[14] T. Metodi and F. Chong, “Quantum computing for computer architects,” Synthesis Lectures on Computer Architecture 13 (2006).

[15] D. DiVincenzo, “Two-bit gates are universal for quantum computation.” Physical review. A **51**, 1015–1022 (1995).

[16] C. Bennett, G. Brassard, C. Crépeau, R. Jozsa, a. Peres, and W. Wootters, “Teleporting an unknown quantum state via dual classical and Einstein-Podolsky-Rosen channels.” Physical review letters **70**, 1895–1899 (1993).

[17] D. Gottesman and I. Chuang, “Demonstrating the viability of universal quantum computation using teleportation and single-qubit operations,” Nature **402**, 390–393 (1999).

[18] D. P. DiVincenzo, “The Physical Implementation of Quantum Computation,” Fortschritte der Physik **48**, 771–783 (2000).

[19] P. C. Humphreys, B. J. Metcalf, J. B. Spring, M. Moore, X.-M. Jin, M. Barbieri, W. S. Kolthammer, and I. A. Walmsley, “Linear Optical Quantum Computing in a Single Spatial Mode,” Physical Review Letters **111**, 150501 (2013).

[20] S. Ramelow, L. Ratschbacher, A. Fedrizzi, N. K. Langford, and A. Zeilinger, “Discrete Tunable Color Entanglement,” Physical Review Letters **103**, 253601 (2009).

[21] G. Calvo and A. Picón, “Manipulation of single-photon states encoded in transverse spatial modes: Possible and impossible tasks,” Physical Review A **77**, 012302 (2008).

[22] J. Carpenter, B. Eggleton, and J. Schröder, “110x110 optical mode transfer matrix inversion,” Optics Express **22**, 96–101 (2014).

[23] J. Carpenter, C. Xiong, M. J. Collins, J. Li, T. F. Krauss, B. J. Eggleton, A. S. Clark, and J. Schröder, “Mode multiplexed single-photon and classical channels in a few-mode fiber,” Optics Express **21**, 28794 (2013).

[24] S. K. Goyal and T. Konrad, “Teleporting photonic qudits using multimode quantum scissors.” Scientific reports **3**, 3548 (2013).

[25] F. Kaiser, A. Issautier, L. a. Ngah, O. Alibart, A. Martin, and S. Tanzilli, “A versatile source of polarization entangled photons for quantum network applications,” Laser Physics Letters **10**, 045202 (2013).

[26] A. Martin, F. Kaiser, A. Vernier, A. Beveratos, V. Scarani, and S. Tanzilli, “Cross time-bin photonic entanglement for quantum key distribution,” Physical Review A **87**, 020301 (2013).

[27] J. Carpenter, B. J. Eggleton, and J. Schröder, "Reconfigurable spatially-diverse optical vector network analyzer," Optics Express **22**, 2706 (2014).

[28] G. Milburn, "Quantum optical Fredkin gate," Physical Review Letters **62**, 2124–2127 (1989).

[29] E. Fredkin and T. Toffoli, "Conservative logic," International Journal of Theoretical Physics **21**, 219–253 (1982). 10.1007/BF01857727.

[30] N. Cerf, C. Adami, and P. Kwiat, "Optical simulation of quantum logic," Physical Review A **57**, R1477–R1480 (1998).

[31] J. Howell and J. Yeazell, "Reducing the complexity of linear optics quantum circuits," Physical Review A **61**, 1–5 (2000).

[32] P. Kwiat and J. Mitchell, "Grover's search algorithm: an optical approach," Journal of Modern Optics **47**, 257–266 (2000).

[33] E. Knill, R. Laflamme, and G. Milburn, "A scheme for efficient quantum computation with linear optics," nature **409**, 46–52 (2001).

[34] M. Reck, A. Zeilinger, H. Bernstein, and P. Bertani, "Experimental realization of any discrete unitary operator," Physical Review Letters **73**, 58–61 (1994).

[35] T. Ralph, A. White, W. Munro, and G. Milburn, "Simple scheme for efficient linear optics quantum gates," Physical Review A **65**, 012314 (2001).

[36] E. Knill, "Quantum gates using linear optics and postselection," Physical Review A **66**, 052306 (2002).

[37] T. Ralph, N. Langford, T. Bell, and A. White, "Linear optical controlled-NOT gate in the coincidence basis," Physical Review A **65**, 062324 (2002).

[38] A. Lund, T. Bell, and T. Ralph, "Comparison of linear optics quantum-computation control-sign gates with ancilla inefficiency and an improvement to functionality under these conditions," Physical Review A **68**, 022313 (2003).

[39] T. Pittman, M. Fitch, B. Jacobs, and J. Franson, "Experimental controlled-NOT logic gate for single photons in the coincidence basis," Physical Review A **68**, 032316 (2003).

[40] J. O'Brien, G. Pryde, A. White, T. Ralph, and D. Branning, "Demonstration of an all-optical quantum controlled-NOT gate," Nature **426**, 264–267 (2003).

[41] N. Langford, T. Weinhold, R. Prevedel, K. Resch, A. Gilchrist, J. O'Brien, G. Pryde, and A. White, "Demonstration of a Simple Entangling Optical Gate and Its Use in Bell-State Analysis," Physical Review Letters **95**, 210504 (2005).

[42] A. Politi, M. J. Cryan, J. G. Rarity, S. Yu, and J. L. O'Brien, "Silica-on-silicon waveguide quantum circuits," Science **320**, 646–649 (2008).

[43] T. C. Ralph, N. K. Langford, T. B. Bell, and A. G. White, "Linear optical controlled-not gate in the coincidence basis," Phys. Rev. A **65**, 062324 (2002).

[44] A. G. W. T. C. R. J. L. O'Brien, G. J. Pryde and D. Branning, "Demonstration of an all-optical quantum controlled-not gate," Nature **426**, 264–267 (2003).

[45] P. West, S. Ishii, G. Naik, N. Emani, V. Shalaev, and A. Boltasseva, "Searching for better plasmonic materials," Laser & Photonics Reviews **4**, 795–808 (2010).

[46] J. S. Fakonas, H. Lee, Y. A. Kelaita, and H. A. Atwater, "Two-plasmon quantum interference," Nature Photonics **8**, 317–320 (2014).

[47] C. Xiong, C. Monat, A. S. Clark, C. Grillet, G. D. Marshall, M. J. Steel, J. Li, L. O'Faolain, T. F. Krauss, J. G. Rarity, and Others, "Slow-light enhanced correlated photon pair generation in a silicon photonic crystal waveguide," Optics Letters **36**, 3413–3415 (2011).

[48] A. S. Clark, C. Husko, M. J. Collins, G. Lehoucq, S. Xavier, A. De Rossi, S. Combrié, C. Xiong, and B. J. Eggleton, "Heralded single-photon source in a III-V photonic crystal." Optics letters **38**, 649–51 (2013).

[49] Y. Zhang, L. McKnight, E. Engin, I. M. Watson, M. J. Cryan, E. Gu, M. G. Thompson, S. Calvez, J. L. O'Brien, and M. D. Dawson, "GaN directional couplers for integrated quantum photonics," Applied Physics Letters **99**, 161119 (2011).

[50] J. Wang, A. Santamato, P. Jiang, D. Bonneau, E. Engin, J. W. Silverstone, M. Lermer, J. Beetz, M. Kamp, S. Höfling, M. G. Tanner, C. M. Natarajan, R. H. Hadfield, S. N. Dorenbos, V. Zwiller, J. L. O'Brien, and M. G. Thompson, "Gallium arsenide (GaAs) quantum photonic waveguide circuits," arXiv:1403.2635v2 (2014).

[51] A. Politi, J. C. F. Matthews, and J. L. O'Brien, "Shor's quantum factoring algorithm on a photonic chip." Science (New York, N.Y.) **325**, 1221 (2009).

[52] A. Peruzzo, J. Mcclean, P. Shadbolt, M.-h. Yung, X.-q. Zhou, P. J. Love, and J. L. O. Brien, "A variational eigenvalue solver on a quantum processor," arXiv:1304.3061v1 (2013).

[53] A. Peruzzo, M. Lobino, J. C. F. Matthews, N. Matsuda, A. Politi, K. Poulios, X.-Q. Zhou, Y. Lahini, N. Ismail, K. Wörhoff, Y. Bromberg, Y. Silberberg, M. G. Thompson, and J. L. OBrien, "Quantum walks of correlated photons." Science (New York, N.Y.) **329**, 1500–3 (2010).

[54] J. C. F. Matthews, A. Politi, D. Bonneau, and J. L. O'Brien, "Heralding Two-Photon and Four-Photon Path Entanglement on a Chip," Physical Review Letters **107**, 163602 (2011).

[55] J. Matthews, A. Politi, A. Stefanov, and J. O'Brien, "Manipulation of multiphoton entanglement in waveguide quantum circuits," Nature Photonics **3** (2009).

[56] P. J. Shadbolt, M. R. Verde, A. Peruzzo, A. Politi, A. Laing, M. Lobino, J. C. F. Matthews, M. G. Thompson, and J. L. O'Brien, "Generating, manipulating and measuring entanglement and mixture with a reconfigurable photonic circuit," Nature Photonics **6**, 45–49 (2011).

[57] H. W. Li, S. Przeslak, a. O. Niskanen, J. C. F. Matthews, a. Politi, P. Shadbolt, a. Laing, M. Lobino, M. G. Thompson, and J. L. O'Brien, "Reconfigurable controlled two-qubit operation on a quantum photonic chip," New Journal of Physics **13**, 115009 (2011).

[58] J. W. Silverstone, D. Bonneau, K. Ohira, N. Suzuki, H. Yoshida, N. Iizuka, M. Ezaki, C. M. Natarajan, M. G. Tanner, R. H. Hadfield, V. Zwiller, G. D. Marshall, J. G. Rarity, J. L. O'Brien, and M. G. Thompson, "On-chip quantum interference between silicon photon-pair sources," Nature Photonics **8**, 104–108 (2013).

[59] J. S. Orcutt, B. Moss, C. Sun, J. Leu, M. Georgas, J. Shainline, E. Zgraggen, H. Li, J. Sun, M. Weaver, S. Urošević, M. Popović, R. J. Ram, and V. Stojanović, "Open foundry platform for high-performance electronic-photonic integration." Optics express **20**, 12222–32 (2012).

[60] J. S. Orcutt, A. Khilo, C. W. Holzwarth, M. a. Popović, H. Li, J. Sun, T. Bonifield, R. Hollingsworth, F. X. Kärtner, H. I. Smith, V. Stojanović, and R. J. Ram, "Nanophotonic integration in state-of-the-art CMOS foundries." Optics express **19**, 2335–46 (2011).

[61] Y. Lee, M. Thompson, and M. Lipson, "Deposited low temperature silicon GHz modulator," Optics express **21**, 26688–26692 (2013).

[62] O. Alibart, D. B. Ostrowsky, P. Baldi, and S. Tanzilli, "High-performance guided-wave asynchronous heralded single-photon source," Optics Letters **30**, 1539 (2005).

[63] D. Bonneau, M. Lobino, P. Jiang, C. M. Natarajan, M. G. Tanner, R. H. Hadfield, S. N. Dorenbos, V. Zwiller, M. G. Thompson, and J. L. O'Brien, "Fast path and polarization manipulation of telecom wavelength single photons in lithium niobate waveguide devices," Phys. Rev. Lett. **108**, 053601 (2012).

[64] H. Jin, F. M. Liu, P. Xu, J. L. Xia, M. L. Zhong, Y. Yuan, and Y. X. Gong, "Reconfigurable on-chip entangled sources based on lithium-niobate waveguide circuits," arXiv:1404.0274 (2014).

[65] J. P. Sprengers, A. Gaggero, D. Sahin, S. Jahanmirinejad, G. Frucci, F. Mattioli, R. Leoni, J. Beetz, M. Lermer, M. Kamp, S. Hofling, R. Sanjines, and A. Fiore, "Waveguide superconducting single-photon detectors for integrated quantum photonic circuits," Applied Physics Letters **99**, 181110 (2011).

[66] D. Sahin, A. Gaggero, Z. Zhou, S. Jahanmirinejad, F. Mattioli, R. Leoni, J. Beetz, M. Lermer, M. Kamp, S. Hofling, and A. Fiore, "Waveguide photon-number-resolving detectors for quantum photonic integrated circuits," Applied Physics Letters **103**, 111116 (2013).

[67] M. G. Tanner, L. S. E. Alvarez, W. Jiang, R. J. Warburton, Z. H. Barber, and R. H. Hadfield, "A superconducting nanowire single photon detector on lithium niobate." Nanotechnology **23**, 505201 (2012).

[68] G. D. Marshall, A. Politi, J. C. F. Matthews, P. Dekker, M. Ams, M. J. Withford, and J. L. O'Brien, "Laser written waveguide photonic quantum circuits," Opt. Express **17**, 12546–12554 (2009).

[69] L. Sansoni, F. Sciarrino, G. Vallone, P. Mataloni, A. Crespi, R. Ramponi, and R. Osellame, "Polarization Entangled State Measurement on a Chip," Physical Review Letters **105**, 200503 (2010).

[70] A. Crespi, R. R. andRoberto Osellame, L. Sansoni, I. Bongioanni, F. Sciarrino, G. Vallone, and P. Mataloni, "Integrated photonic quantum gates for polarization qubits," Nature Communications **2** (2011).

[71] G. Corrielli, A. Crespi, R. Osellame, R. Geremia, R. Ramponi, L. Sansoni, A. Santinelli, P. Mataloni, and F. Sciarrino, "Integrated optical waveplates for arbitrary operations on polarization-encoded single-qubits," arXiv:1307.7541v1 (2013).

[72] R. Heilmann, M. Gräfe, S. Nolte, and A. Szameit, "Arbitrary photonic wave plate operations on chip: Realizing Hadamard, Pauli-X, and rotation gates for polarisation qubits." Scientific reports **4**, 4118 (2014).

[73] B. J. Smith, D. Kundys, N. Thomas-Peter, P. G. R. Smith, and I. A. Walmsley, "Phase-controlled integrated photonic quantum circuits," Opt. Express **17**, 13516–13525 (2009).

[74] T. Gerrits, N. Thomas-Peter, J. C. Gates, A. E. Lita, B. J. Metcalf, B. Calkins, N. A. Tomlin, A. E. Fox, A. L. Linares, J. B. Spring, N. K. Langford, R. P. Mirin, P. G. R. Smith, I. A. Walmsley, and S. W. Nam, "On-chip, photon-number-resolving, telecommunication-band detectors for scalable photonic information processing," Phys. Rev. A **84**, 060301 (2011).

[75] B. Calkins, P. Mennea, and A. Lita, "High quantum-efficiency photon-number-resolving detector for photonic on-chip information processing," Opt. Express **21**, 22657–22670 (2013).

[76] T. Meany, M. Delanty, S. Gross, G. D. Marshall, M. J. Steel, and M. J. Withford, "Non-classical interference in integrated 3D multiports," Opt. Express **20**, 26895–26905 (2012).

[77] J. O. Owens, M. a. Broome, D. N. Biggerstaff, M. E. Goggin, a. Fedrizzi, T. Linjordet, M. Ams, G. D. Marshall, J. Twamley, M. J. Withford, and a. G. White, “Two-photon quantum walks in an elliptical direct-write waveguide array,” New Journal of Physics **13**, 075003 (2011).

[78] N. Spagnolo, C. Vitelli, L. Aparo, P. Mataloni, F. Sciarrino, A. Crespi, R. Ramponi, and R. Osellame, “Three-photon bosonic coalescence in an integrated tritter.” Nature communications **4**, 1606 (2013).

[79] M. Gräfe, a. S. Solntsev, R. Keil, a. a. Sukhorukov, M. Heinrich, A. Tünnermann, S. Nolte, A. Szameit, and Y. S. Kivshar, “Biphoton generation in quadratic waveguide arrays: a classical optical simulation.” Scientific reports **2**, 1–5 (2012).

[80] M. C. Rechtsman, J. M. Zeuner, Y. Plotnik, Y. Lumer, D. Podolsky, F. Dreisow, S. Nolte, M. Segev, and A. Szameit, “Photonic Floquet topological insulators,” Nature **496**, 196–200 (2013).

[81] A. Crespi, G. Corrielli, G. D. Valle, R. Osellame, and S. Longhi, “Dynamic band collapse in photonic graphene,” New Journal of Physics **15**, 013012 (2013).

[82] M. C. Rechtsman, J. M. Zeuner, A. Tünnermann, S. Nolte, M. Segev, and A. Szameit, “Strain-induced pseudomagnetic field and photonic Landau levels in dielectric structures,” Nature Photonics **7**, 153–158 (2012).

[83] R. Keil, A. Szameit, F. Dreisow, M. Heinrich, S. Nolte, and A. Tünnermann, “Photon correlations in two-dimensional waveguide arrays and their classical estimate,” Phys. Rev. A **81**, 023834 (2010).

[84] K. Poulios, R. Keil, and D. Fry, “Quantum walks of correlated photon pairs in two-dimensional waveguide arrays,” arXiv:1308.2554v1 (2013).

[85] F. Dreisow, A. Szameit, T. Pertsch, S. Nolte, and A. Tuennermann, “Visualization of light propagation in fs laser written waveguide arrays,” in “Proc. of SPIE Vol. 6460,” , vol. 6460, J. Neev, S. Nolte, A. Heisterkamp, and C. B. Schaffer, eds. (2007), vol. 6460.

[86] G. Di Giuseppe, L. Martin, A. Perez-Leija, R. Keil, F. Dreisow, S. Nolte, A. Szameit, A. Abouraddy, D. Christodoulides, and B. Saleh, “Einstein-Podolsky-Rosen Spatial Entanglement in Ordered and Anderson Photonic Lattices,” Physical Review Letters **110**, 150503 (2013).

[87] R. Keil, A. Perez-Leija, F. Dreisow, M. Heinrich, H. Moya-Cessa, S. Nolte, D. N. Christodoulides, and A. Szameit, “Classical Analogue of Displaced Fock States and Quantum Correlations in Glauber-Fock Photonic Lattices,” Physical Review Letters **107**, 103601 (2011).

[88] L. Sansoni, F. Sciarrino, G. Vallone, P. Mataloni, A. Crespi, R. Ramponi, and R. Osellame, “Two-particle bosonic-fermionic quantum walk via integrated photonics,” Phys. Rev. Lett. **108**, 010502 (2012).

[89] A. Crespi, R. Osellame, R. Ramponi, V. Giovannetti, R. Fazio, L. Sansoni, F. De Nicola, F. Sciarrino, and P. Mataloni, “Anderson localization of entangled photons in an integrated quantum walk,” Nature Photonics **7**, 322–328 (2013).

[90] G. Corrielli, A. Crespi, G. Della Valle, S. Longhi, and R. Osellame, “Fractional Bloch oscillations in photonic lattices.” Nature communications **4**, 1555 (2013).

[91] N. Spagnolo, C. Vitelli, L. Sansoni, E. Maiorino, P. Mataloni, F. Sciarrino, D. J. Brod, E. F. Galvão, A. Crespi, R. Ramponi, and R. Osellame, “General Rules for Bosonic Bunching in Multimode Interferometers,” Physical Review Letters **111**, 130503 (2013).

[92] A. Crespi, R. Osellame, R. Ramponi, D. J. Brod, E. F. Galvão, N. Spagnolo, C. Vitelli, E. Maiorino, P. Mataloni, and F. Sciarrino, “Integrated multimode interferometers with arbitrary designs for photonic boson sampling,” Nature Photonics **7**, 545–549 (2013).

[93] M. Tillmann, B. Dakić, R. Heilmann, S. Nolte, A. Szameit, and P. Walther, “Experimental boson sampling,” Nature Photonics **7**, 540–544 (2013).

[94] Zhe-Yu Jeff Ou, *Multi-photon quantum interference* (springer, 2007), 1st ed.

[95] C. C. Gerry and P. L. Knight, *Introductory quantum optics* (Cambridge University Press, 2005).

[96] K. M. Davis, K. Miura, N. Sugimoto, and K. Hirao, “Writing waveguides in glass with a femtosecond laser.” Optics letters **21**, 1729–31 (1996).

[97] N. Anscombe, “Direct laser writing,” Nature Photonics **4**, 22–23 (2010).

[98] Y. Bellouard, A. Champion, B. Lenssen, M. Matteucci, A. Schaap, M. Beresna, C. Corbari, M. Gecevičius, P. Kazansky, O. Chappuis, M. Kral, R. Clavel, F. Barrot, J.-M. Breguet, Y. Mabillard, S. Bottinelli, M. Hopper, C. Hoenninger, E. Mottay, and J. Lopez, “The Femtoprint Project,” Journal of Laser Micro/Nanoengineering **7**, 1–10 (2012).

[99] Optoscribe Ltd., “3D MMux Photonic Lantern,” Tech. rep., Kirkton Campus, Livingston, West Lothian (2014).

[100] T. Miya, “Silica-based planar lightwave circuits: Passive and thermally active devices,” IEEE Journal of Selected Topics in Quantum Electronics **6**, 38–45 (2000).

[101] H. Misawa and S. Juodkazis, eds., *3D Laser Microfabrication: Principles and Applications* (Wiley-VCH Verlag GmbH & Co. KGaA, Weinheim, FRG., 2006), 1st ed.

[102] R. Osellame, G. Cerullo, and R. Ramponi, eds., *Femtosecond Laser Micromachining photonic and microfluidic devices in transparent materials* (Springer-Verlag, 2012).

[103] J. E. Shelby, *Introduction to Glass Science and Technology* (Royal Society of Chemistry, 2005).

[104] R. W. Douglas and S. Frank, *A History of Glass Making* (Foulis, 1972).

[105] R. Brückner, "Properties and structure of vitreous silicA. I," Journal of non-crystalline Solids **5** (1970).

[106] A. Q. Tool, "RELATION BETWEEN INELASTIC DEFORMABILITY AND THERMAL EXPANSION OF GLASS IN ITS ANNEALING RANGE," Journal of the American Ceramic Society **29**, 240–253 (1946).

[107] E. B. Shand, *Glass engineering handbook* (McGraw-Hill, 1958).

[108] C. Schaffer, J. García, and E. Mazur, "Bulk heating of transparent materials using a high-repetition-rate femtosecond laser," Applied Physics A: Materials Science & Processing **76**, 351–354 (2003).

[109] S. M. Eaton, H. Zhang, P. R. Herman, F. Yoshino, L. Shah, J. Bovatsek, and A. Y. Arai, "Heat accumulation effects in femtosecond laser-written waveguides with variable repetition rate," Optics Express **13**, 4708 (2005).

[110] S. M. Eaton, H. Zhang, M. L. Ng, J. Li, W.-J. Chen, S. Ho, and P. R. Herman, "Transition from thermal diffusion to heat accumulation in high repetition rate femtosecond laser writing of buried optical waveguides," Opt. Express **16**, 9443–9458 (2008).

[111] A. Arriola, S. Gross, N. Jovanovic, N. Charles, P. G. Tuthill, S. M. Olaizola, A. Fuerbach, and M. J. Withford, "Low bend loss waveguides enable compact, efficient 3D photonic chips," Opt. Express **21**, 2978–2986 (2013).

[112] J. W. Chan, T. R. Huser, S. H. Risbud, J. S. Hayden, and D. M. Krol, "Waveguide fabrication in phosphate glasses using femtosecond laser pulses," Applied Physics Letters **82**, 2371 (2003).

[113] C. W. Ponader, J. F. Schroeder, and A. M. Streltsov, "Origin of the refractive-index increase in laser-written waveguides in glasses," Journal of Applied Physics **103**, 063516 (2008).

[114] B. N. Chichkov, C. Momma, S. Nolte, F. Alvensleben, and A. Tünnermann, "Femtosecond, picosecond and nanosecond laser ablation of solids," Applied Physics A Materials Science & Processing **63**, 109–115 (1996).

[115] R. R. Gattass and E. Mazur, "Femtosecond laser micromachining in transparent materials," Nature Photonics **2**, 219–225 (2008).

[116] G. Della Valle, R. Osellame, and P. Laporta, "Micromachining of photonic devices by femtosecond laser pulses," Journal of Optics A: Pure and Applied Optics **11**, 013001 (2009).

[117] L. Keldysh, "Ionization in the field of a strong electromagnetic wave," Soviet Physics JETP (Translated from: Zh. Eksp. Teor. Fiz. 47 1945) **20**, 1307–1314 (1965).

[118] C. B. Schaffer, A. Brodeur, and E. Mazur, "Laser-induced breakdown and damage in bulk transparent materials induced by tightly focused femtosecond laser pulses," Measurement Science and Technology **12**, 1784–1794 (2001).

[119] V. Temnov, K. Sokolowski-Tinten, P. Zhou, A. El-Khamhawy, and D. von der Linde, "Multiphoton Ionization in Dielectrics: Comparison of Circular and Linear Polarization," Physical Review Letters **97**, 237403 (2006).

[120] C. DeMichelis, "Laser induced gas breakdown: A bibliographical review," IEEE Journal of Quantum Electronics **5**, 188–202 (1969).

[121] S. Juodkazis, H. Misawa, and I. Maksimov, "Thermal accumulation effect in three-dimensional recording by picosecond pulses," Applied Physics Letters **85**, 5239 (2004).

[122] S. Juodkazis, K. Nishimura, S. Tanaka, H. Misawa, E. Gamaly, B. Luther-Davies, L. Hallo, P. Nicolai, and V. Tikhonchuk, "Laser-Induced Microexplosion Confined in the Bulk of a Sapphire Crystal: Evidence of Multimegabar Pressures," Physical Review Letters **96**, 166101 (2006).

[123] D. J. Little, M. Ams, P. Dekker, G. D. Marshall, J. M. Dawes, and M. J. Withford, "Femtosecond laser modification of fused silica: the effect of writing polarization on Si-O ring structure." Optics express **16**, 20029–37 (2008).

[124] J. W. Chan, T. Huser, J. S. Hayden, S. H. Risbud, and D. M. Krol, "Fluorescence Spectroscopy of Color Centers Generated in Phosphate Glasses after Exposure to Femtosecond Laser Pulses," J. Am. Ceram. Soc. **85**, 1037–1040 (2002).

[125] D. J. Little, M. Ams, P. Dekker, G. D. Marshall, and M. J. Withford, "Mechanism of femtosecond-laser induced refractive index change in phosphate glass under a low repetition-rate regime," Journal of Applied Physics **108**, 033110 (2010).

[126] D. J. Little, M. Ams, S. Gross, P. Dekker, C. T. Miese, A. Fuerbach, and M. J. Withford, "Structural changes in BK7 glass upon exposure to femtosecond laser pulses," Journal of Raman Spectroscopy **42**, 715–718 (2011).

[127] A. M. Streltsov and N. F. Borrelli, "Study of femtosecond-laser-written waveguides in glasses," Journal of the Optical Society of America B **19**, 2496 (2002).

[128] P. Dekker, M. Ams, G. D. Marshall, D. J. Little, and M. J. Withford, "Annealing dynamics of waveguide Bragg gratings: evidence of femtosecond laser induced colour centres," Optics Express **18**, 3274 (2010).

[129] J. W. Chan, T. Huser, S. Risbud, and D. M. Krol, “Structural changes in fused silica after exposure to focused femtosecond laser pulses.” Optics letters **26**, 1726–8 (2001).

[130] J. Chan, T. Huser, S. Risbud, and D. Krol, “Modification of the fused silica glass network associated with waveguide fabrication using femtosecond laser pulses,” Applied Physics A: Materials Science & Processing **76**, 367–372 (2003).

[131] K. Itoh, W. Watanabe, S. Nolte, and C. Schaffer, “Ultrafast processes for bulk modification of transparent materials,” MRS bulletin **31**, 620–625 (2006).

[132] E. N. Glezer and E. Mazur, “Ultrafast-laser driven micro-explosions in transparent materials,” Applied Physics Letters **71**, 882 (1997).

[133] Y. Bellouard and M.-O. Hongler, “Femtosecond-laser generation of self-organized bubble patterns in fused silicA.” Optics express **19**, 6807–21 (2011).

[134] E. N. Glezer, M. Milosavljevic, L. Huang, R. J. Finlay, T. H. Her, J. P. Callan, and E. Mazur, “Three-dimensional optical storage inside transparent materials,” Optics letters **22**, 422 (1997).

[135] L. Sudrie, M. Franco, B. Prade, and A. Mysyrowicz, “Writing of permanent birefringent microlayers in bulk fused silica with femtosecond laser pulses,” Optics Communications **171**, 279–284 (1999).

[136] E. Bricchi, J. D. Mills, P. G. Kazansky, B. G. Klappauf, and J. J. Baumberg, “Birefringent Fresnel zone plates in silica fabricated by femtosecond laser machining.” Optics letters **27**, 2200–2 (2002).

[137] Y. Shimotsuma, P. Kazansky, J. Qiu, and K. Hirao, “Self-Organized Nanogratings in Glass Irradiated by Ultrashort Light Pulses,” Physical Review Letters **91**, 247405 (2003).

[138] C. Hnatovsky, R. Taylor, E. Simova, P. Rajeev, D. Rayner, V. Bhardwaj, and P. Corkum, “Fabrication of microchannels in glass using focused femtosecond laser radiation and selective chemical etching,” Applied Physics A **84**, 47–61 (2006).

[139] S. Richter, M. Heinrich, S. Doring, A. Tunnermann, S. Nolte, and U. Peschel, “Nanogratings in fused silica: Formation, control, and applications,” Journal of Laser Applications **24**, 042008 (2012).

[140] C. Hnatovsky, V. G. Shvedov, and W. Krolikowski, “The role of light-induced nanostructures in femtosecond laser micromachining with vector and scalar pulses,” Optics express **21**, 12651–12656 (2013).

[141] R. S. Taylor, E. Simova, and C. Hnatovsky, “Creation of chiral structures inside fused silica glass.” Optics letters **33**, 1312–4 (2008).

[142] P. G. Kazansky, W. Yang, E. Bricchi, J. Bovatsek, A. Arai, Y. Shimotsuma, K. Miura, and K. Hirao, "“Quill” writing with ultrashort light pulses in transparent materials," Applied Physics Letters **90**, 151120 (2007).

[143] M. Lancry, B. Poumellec, J. Canning, K. Cook, J.-C. Poulin, and F. Brisset, "Ultrafast nanoporous silica formation driven by femtosecond laser irradiation," Laser & Photonics Reviews **7**, 953–962 (2013).

[144] A. Champion, M. Beresna, P. Kazansky, and Y. Bellouard, "Stress distribution around femtosecond laser affected zones: effect of nanogratings orientation," Optics express **21**, 21490–21497 (2013).

[145] S. Richter, S. Döring, F. Burmeister, A. Tünnermann, and S. Nolte, "Formation of periodic disruptions induced by heat accumulation of femtosecond laser pulses," Optics express **21**, 15452–15463 (2013).

[146] S. Richter, F. Jia, M. Heinrich, S. Döring, U. Peschel, A. Tünnermann, and S. Nolte, "The role of self-trapped excitons and defects in the formation of nanogratings in fused silicA." Optics letters **37**, 482–4 (2012).

[147] P. G. Kazansky and Y. Shimotsuma, "Self-assembled sub-wavelength structures and form birefringence created by femtosecond laser writing in glass: properties and applications," Journal of the Ceramic Society of Japan **116**, 1052–1062 (2008).

[148] R. Taylor, C. Hnatovsky, and E. Simova, "Applications of femtosecond laser induced self-organized planar nanocracks inside fused silica glass," Laser & Photonics Review **2**, 26–46 (2008).

[149] Y. Shimotsuma, M. Sakakura, P. G. Kazansky, M. Beresna, J. Qiu, J. Qiu, K. Miura, and K. Hirao, "Ultrafast manipulation of self-assembled form birefringence in glass." Advanced materials (Deerfield Beach, FlA.) **22**, 4039–43 (2010).

[150] J. Zhang, M. Gecevičius, M. Beresna, and P. G. Kazansky, "Seemingly Unlimited Lifetime Data Storage in Nanostructured Glass," Physical Review Letters **112**, 033901 (2014).

[151] E. Bricchi, B. G. Klappauf, and P. G. Kazansky, "Form birefringence and negative index change created by femtosecond direct writing in transparent materials." Optics letters **29**, 119–21 (2004).

[152] L. a. Fernandes, J. R. Grenier, P. R. Herman, J. S. Aitchison, and P. V. S. Marques, "Femtosecond laser writing of waveguide retarders in fused silica for polarization control in optical circuits." Optics express **19**, 18294–301 (2011).

[153] L. A. Fernandes, J. R. Grenier, P. R. Herman, J. S. Aitchison, and P. V. S. Marques, "Femtosecond laser fabrication of birefringent directional couplers as polarization beam splitters in fused silica," Optics Express **19**, 11992 (2011).

[154] Y. Dai, G. Wu, X. Lin, G. Ma, and J. Qiu, "Femtosecond laser induced rotated 3D self-organized nanograting in fused silicA." Optics express **20**, 18072–8 (2012).

[155] S. Gross, D. G. Lancaster, H. Ebendorff-Heidepriem, T. M. Monro, A. Fuerbach, and M. J. Withford, "Femtosecond laser induced structural changes in fluorozirconate glass," Optical Materials Express **3**, 574 (2013).

[156] D. G. Lancaster, S. Gross, A. Fuerbach, M. J. Withford, and T. M. Monro, "2.1 μm waveguide laser fabricatedby femtosecond laser direct-writing in Ho 3 , Tm 3 : ZBLAN glass," Optics Letters **37**, 996–998 (2012).

[157] D. G. Lancaster, S. Gross, a. Fuerbach, H. E. Heidepriem, T. M. Monro, and M. J. Withford, "Versatile large-mode-area femtosecond laser-written Tm:ZBLAN glass chip lasers." Optics express **20**, 27503–9 (2012).

[158] S. Gross, M. Ams, D. G. Lancaster, T. M. Monro, A. Fuerbach, and M. J. Withford, "Femtosecond direct-write Überstructure waveguide Bragg gratings in ZBLAN," Opt. Lett. **37**, 3999–4001 (2012).

[159] G. Palmer, S. Gross, A. Fuerbach, D. G. Lancaster, and M. J. Withford, "High slope efficiency and high refractive index change in direct-written Yb-doped waveguide lasers with depressed claddings," Optics express **12**, 17413–17420 (2013).

[160] D. G. Lancaster, S. Gross, H. Ebendorff-heidepriem, M. J. Withford, T. M. Monro, and S. D. Jackson, "Efficient 2.9 μm fluorozirconate glass waveguide chip laser," Optics express **38**, 2588–2591 (2013).

[161] M.-m. Dong, C.-w. Wang, Z.-x. Wu, Y. Zhang, H.-h. Pan, and Q.-z. Zhao, "Waveguides fabricated by femtosecond laser exploiting both depressed cladding and stress- induced guiding core," Optics express **21**, 15522–15529 (2013).

[162] A. Mermillod-Blondin, I. Burakov, Y. Meshcheryakov, N. Bulgakova, E. Audouard, A. Rosenfeld, A. Husakou, I. Hertel, and R. Stoian, "Flipping the sign of refractive index changes in ultrafast and temporally shaped laser-irradiated borosilicate crown optical glass at high repetition rates," Physical Review B **77**, 104205 (2008).

[163] G. Lin, F. Luo, F. He, Q. Chen, D. Chen, and Y. Cheng, "Different refractive index change behavior in borosilicate glasses induced by 1 kHz and 250 kHz femtosecond lasers [Invited]," Optical Materials Express **1**, 724–731 (2011).

[164] A. Jesacher, G. D. Marshall, T. Wilson, and M. J. Booth, "Adaptive optics for direct laser writing with plasma emission aberration sensing." Optics express **18**, 656–61 (2010).

[165] P. S. Salter and M. J. Booth, "Focussing over the edge: adaptive subsurface laser fabrication up to the sample face." Optics express **20**, 19978–89 (2012).

[166] B. Cumming and S. Debbarma, "Simultaneous compensation for aberration and axial elongation in three-dimensional laser nanofabrication by a high numerical-aperture objective," Optics express **21**, 19135–19141 (2013).

[167] A. Jesacher, P. S. Salter, and M. J. Booth, "Refractive index profiling of direct laser written waveguides: tomographic phase imaging," Optical Materials Express **3**, 1223 (2013).

[168] P. Franken, A. Hill, W. Peters, and G. Weinreich, "Generation of optical harmonics," Physical Review Letters **7**, 118–120 (1961).

[169] M. Ams, G. Marshall, D. Spence, and M. Withford, "Slit beam shaping method for femtosecond laser direct-write fabrication of symmetric waveguides in bulk glasses." Optics express **13**, 5676–81 (2005).

[170] P. S. Salter, a. Jesacher, J. B. Spring, B. J. Metcalf, N. Thomas-Peter, R. D. Simmonds, N. K. Langford, I. a. Walmsley, and M. J. Booth, "Adaptive slit beam shaping for direct laser written waveguides." Optics letters **37**, 470–2 (2012).

[171] G. Cerullo, R. Osellame, S. Taccheo, M. Marangoni, D. Polli, R. Ramponi, P. Laporta, and S. De Silvestri, "Femtosecond micromachining of symmetric waveguides at 1.5 microm by astigmatic beam focusing." Optics letters **27**, 1938–40 (2002).

[172] R. Osellame, S. Taccheo, M. Marangoni, R. Ramponi, P. Laporta, D. Polli, S. De Silvestri, and G. Cerullo, "Femtosecond writing of active optical waveguides with astigmatically shaped beams," Journal of the Optical Society of America B **20**, 1559 (2003).

[173] Y. Nasu, M. Kohtoku, and Y. Hibino, "Low-loss waveguides written with a femtosecond laser for flexible interconnection in a planar light-wave circuit." Optics letters **30**, 723–5 (2005).

[174] P. Bado, M. Dugan, A. Said, and T. Sosnowski, "Waveguide fabrication methods and devices," US Patent 7294454 **B1** (2003).

[175] A. Ródenas, G. Martin, B. Arezki, N. Psaila, G. Jose, A. Jha, L. Labadie, P. Kern, A. Kar, and R. Thomson, "Three-dimensional mid-infrared photonic circuits in chalcogenide glass." Optics letters **37**, 392–4 (2012).

[176] R. R. Thomson, a. S. Bockelt, E. Ramsay, S. Beecher, a. H. Greenaway, a. K. Kar, and D. T. Reid, "Shaping ultrafast laser inscribed optical waveguides using a deformable mirror." Optics express **16**, 12786–93 (2008).

[177] a. Ruiz de la Cruz, a. Ferrer, W. Gawelda, D. Puerto, M. G. Sosa, J. Siegel, and J. Solis, "Independent control of beam astigmatism and ellipticity using a SLM for fs-laser waveguide writing." Optics express **17**, 20853–9 (2009).

[178] F. He, H. Xu, Y. Cheng, J. Ni, and H. Xiong, "Fabrication of microfluidic channels with a circular cross section using spatiotemporally focused femtosecond laser pulses," Optics Letters **35**, 1106–1108 (2010).

[179] D. Vitek, E. Block, and Y. Bellouard, "Spatio-temporally focused femtosecond laser pulses for nonreciprocal writing in optically transparent materials," Optics Express **18**, 24673–24678 (2010).

[180] D. Marcuse, "Curvature loss formula for optical fibers," Journal of the Optical Society of America **66**, 216 (1976).

[181] M. Heilblum and J. P. Harris, "Analysis of Curved Optical Waveguides by conformal mapping," IEEE Journal of Quantum Electronics **QE-11**, 75–83 (1974).

[182] R. T. Schermer and J. H. Cole, "Improved Bend Loss Formula Verified for Optical Fiber by Simulation and Experiment," IEEE Journal of Quantum Electronics **43**, 899–909 (2007).

[183] A. Szameit and S. Nolte, "Discrete optics in femtosecond-laser-written photonic structures," Journal of Physics B: Atomic, Molecular and Optical Physics **43**, 163001 (2010).

[184] L. P. R. Ramirez, M. Heinrich, S. Richter, F. Dreisow, R. Keil, A. V. Korovin, U. Peschel, S. Nolte, and A. Tünnermann, "Tuning the structural properties of femtosecond-laser-induced nanogratings," Applied Physics A **100**, 1–6 (2010).

[185] L. Shah, A. Y. Arai, S. M. Eaton, and P. R. Herman, "Waveguide writing in fused silica with a femtosecond fiber laser at 522 nm and 1 MHz repetition rate," Optics Express **13**, 1999 (2005).

[186] W. J. Reichman, D. M. Krol, L. Shah, F. Yoshino, A. Arai, S. M. Eaton, and P. R. Herman, "A spectroscopic comparison of femtosecond-laser-modified fused silica using kilohertz and megahertz laser systems," Journal of Applied Physics **99**, 123112 (2006).

[187] S. M. Eaton, M. L. Ng, R. Osellame, and P. R. Herman, "High refractive index contrast in fused silica waveguides by tightly focused, high-repetition rate femtosecond laser," Journal of Non-Crystalline Solids **357**, 2387–2391 (2011).

[188] R. Graf, A. Fernandez, M. Dubov, H. Brueckner, B. Chichkov, and A. Apolonski, "Pearl-chain waveguides written at megahertz repetition rate," Applied Physics B **87**, 21–27 (2006).

[189] R. Osellame, N. Chiodo, V. Maselli, A. Yin, M. Zavelani-Rossi, G. Cerullo, P. Laporta, L. Aiello, S. De Nicola, P. Ferraro, A. Finizio, and G. Pierattini, "Optical properties of waveguides written by a 26 MHz stretched cavity Ti:sapphire femtosecond oscillator." Optics express **13**, 612–20 (2005).

[190] C. B. Schaffer, a. Brodeur, J. F. García, and E. Mazur, "Micromachining bulk glass by use of femtosecond laser pulses with nanojoule energy." Optics letters **26**, 93–5 (2001).

[191] T. Allsop, M. Dubov, V. Mezentsev, and I. Bennion, "Inscription and characterization of waveguides written into borosilicate glass by a high-repetition-rate femtosecond laser at 800 nm." Applied optics **49**, 1938–50 (2010).

[192] J. Dharmadhikari, A. Dharmadhikari, A. Bhatnagar, A. Mallik, P. C. Singh, R. K. Dhaman, K. Chalapathi, and D. Mathur, "Writing low-loss waveguides in borosilicate (BK7) glass with a low-repetition-rate femtosecond laser," Optics Communications **284**, 630–634 (2011).

[193] S. M. Eaton, M. L. Ng, J. Bonse, A. Mermillod-Blondin, H. Zhang, A. Rosenfeld, and P. R. Herman, "Low-loss waveguides fabricated in BK7 glass by high repetition rate femtosecond fiber laser." Applied optics **47**, 2098–102 (2008).

[194] S. Nolte, M. Will, J. Burghoff, and A. Tünnermann, "Ultrafast laser processing: New options for three-dimensional photonic structures," Journal of Modern Optics **51**, 2533–2542 (2004).

[195] S. Eaton, H. Zhang, P. Herman, F. Yoshino, L. Shah, J. Bovatsek, and A. Arai, "Heat accumulation effects in femtosecond laser-written waveguides with variable repetition rate," Opt. Express **13**, 4708–4716 (2005).

[196] S. Ag, "Schott AF-45 material profile," Tech. rep. (2008).

[197] A. G. Substrates, "Corning Eagle-2000 material information," Tech. Rep. April (2005).

[198] S. M. Eaton, W.-J. Chen, H. Zhang, R. Iyer, J. Li, M. Ng, S. Ho, J. Aitchison, and P. R. Herman, "Spectral Loss Characterization of Femtosecond Laser Written Waveguides in Glass With Application to Demultiplexing of 1300 and 1550 nm Wavelengths," Journal of Lightwave Technology **27**, 1079–1085 (2009).

[199] L. Tong, R. R. Gattass, I. Maxwell, J. B. Ashcom, and E. Mazur, "Optical loss measurements in femtosecond laser written waveguides in glass," Optics Communications **259**, 626–630 (2006).

[200] P. C. Schultz, "Optical Absorption of the Transition Elements in Vitreous Silica," Journal of the American Ceramic Society **57**, 309–313 (1974).

[201] K. J. Beales, C. R. Day, W. J. Duncan, J. E. Midwinter, and G. Newns, "Preparation of sodium borosilicate glass fibre for optical communication," PROC. IEE **123**, 591–596 (1976).

[202] L. Glebov and E. Boulos, "Absorption of iron and water in the Na 2 O–CaO–MgO–SiO 2 glasses. II. Selection of intrinsic, ferric, and ferrous spectra in the visible and," Journal of non-crystalline solids **242**, 49–62 (1998).

[203] J. Duffy, "A review of optical basicity and its applications to oxidic systems," Geochimica et Cosmochimica Acta **57**, 3961–3970 (1993).

[204] T. Yamashita and Y. Ohishi, "Cooperative energy transfer between and ions co-doped in borosilicate glass," Journal of Non-Crystalline Solids **354**, 1883–1890 (2008).

[205] S. Richter, M. Heinrich, S. Döring, A. Tünnermann, and S. Nolte, "Formation of femtosecond laser-induced nanogratings at high repetition rates," Applied Physics A **104**, 503–507 (2011).

[206] S. Richter, C. Miese, S. Döring, F. Zimmermann, M. J. Withford, A. Tünnermann, and S. Nolte, "Laser induced nanogratings beyond fused silica - periodic nanostructures in borosilicate glasses and ULE^{TM}," Optical Materials Express **3**, 1161 (2013).

[207] L. P. R. Ramirez, M. Heinrich, S. Richter, F. Dreisow, R. Keil, A. V. Korovin, U. Peschel, S. Nolte, and A. Tünnermann, "Birefringent elements based on femtosecond laser-induced nanogratings," in "Proc. of SPIE Vol. 7589 758919," , vol. 7589, A. Heisterkamp, J. Neev, S. Nolte, and R. P. Trebino, eds. (2010), vol. 7589, pp. 1–8.

[208] J. Li, S. Ho, M. Haque, and P. R. Herman, "Nanograting Bragg responses of femtosecond laser written optical waveguides in fused silica glass," Optical Materials Express **2**, 1562 (2012).

[209] D. Blömer, A. Szameit, F. Dreisow, T. Schreiber, S. Nolte, and A. Tünnermann, "Nonlinear refractive index of fs-laser-written waveguides in fused silicA." Optics express **14**, 2151–7 (2006).

[210] J. Spring, P. S. Salter, B. J. Metcalf, P. C. Humphreys, M. Moore, N. Thomas-Peter, M. Barbieri, X.-M. Jin, N. Langford, M. J. Booth, and I. A. Walmsley, "On-chip low loss heralded source of pure single photons," Optics Express **21**, 5932–5935 (2013).

[211] M. Dussauze, T. Cremoux, F. Adamietz, V. Rodriguez, E. Fargin, G. Yang, and T. Cardinal, "Thermal Poling of Optical Glasses: Mechanisms and Second-Order Optical Properties," International Journal of Applied Glass Science **3**, 309–320 (2012).

[212] G. Li, K. a. Winick, A. a. Said, M. Dugan, and P. Bado, "Quasi-phase matched second-harmonic generation through thermal poling in femtosecond laser-written glass waveguides." Optics express **17**, 9442–53 (2009).

[213] C. Corbari, J. D. Mills, O. Deparis, B. G. Klappauf, and P. G. Kazansky, "Thermal poling of glass modified by femtosecond laser irradiation," Applied Physics Letters **81**, 1585 (2002).

[214] G. Li, K. Winick, A. Said, M. Dugan, and P. Bado, "Waveguide electro-optic modulator in fused silica fabricated by femtosecond laser direct writing and thermal poling," Optics letters **31**, 739–741 (2006).

[215] H. An, S. Fleming, B. W. McMillen, K. P. Chen, and D. Snoke, "Thermal poling induced second-order nonlinearity in femtosecond- laser-modified fused silica," Applied Physics Letters **93**, 061115 (2008).

[216] H.-L. An, A. Arriola, S. Gross, A. Fuerbach, M. J. Withford, and S. Fleming, "Creating large second-order optical nonlinearity in optical waveguides written by femtosecond laser pulses in boro-aluminosilicate glass," Applied Physics Letters **104**, 021113 (2014).

[217] B. McMillen, B. Zhang, K. P. Chen, A. Benayas, and D. Jaque, "Ultrafast laser fabrication of low-loss waveguides in chalcogenide glass with 0.65 dB/cm loss." Optics letters **37**, 1418–20 (2012).

[218] Y. Bellouard, A. Said, M. Dugan, and P. Bado, "Fabrication of high-aspect ratio, micro-fluidic channels and tunnels using femtosecond laser pulses and chemical etching." Optics express **12**, 2120–9 (2004).

[219] S. Rajesh and Y. Bellouard, "Towards fast femtosecond laser micromachining of fused silica: The effect of deposited energy." Optics express **18**, 21490–7 (2010).

[220] Y. Bellouard, A. Said, and P. Bado, "Integrating optics and micro-mechanics in a single substrate: a step toward monolithic integration in fused silicA." Optics express **13**, 6635–44 (2005).

[221] R. Osellame, H. Hoekstra, G. Cerullo, and M. Pollnau, "Femtosecond laser microstructuring: an enabling tool for optofluidic lab-on-chips," Laser & Photonics Reviews **5**, 442–463 (2011).

[222] A. Crespi, Y. Gu, B. Ngamsom, H. J. W. M. Hoekstra, C. Dongre, M. Pollnau, R. Ramponi, H. H. van den Vlekkert, P. Watts, G. Cerullo, and R. Osellame, "Three-dimensional Mach-Zehnder interferometer in a microfluidic chip for spatially-resolved label-free detection." Lab on a chip **10**, 1167–73 (2010).

[223] A. Crespi, M. Lobino, J. C. F. Matthews, A. Politi, C. R. Neal, R. Ramponi, R. Osellame, and J. L. O'Brien, "Measuring protein concentration with entangled photons," Applied Physics Letters **100**, 233704 (2012).

[224] M. Haque, N. S. Zacharia, S. Ho, and P. R. Herman, "Laser-written photonic crystal optofluidics for electrochromatography and spectroscopy on a chip." Biomedical optics express **4**, 1472–85 (2013).

[225] P. Hua, B. Jonathan Luff, G. R. Quigley, J. S. Wilkinson, and K. Kawaguchi, "Integrated optical dual Mach–Zehnder interferometer sensor," Sensors and Actuators B: Chemical **87**, 250–257 (2002).

[226] R. Bernini and A. Cusano, “Generalized Mach–Zehnder interferometers for sensing applications,” Sensors and Actuators B: Chemical **100**, 72–74 (2004).

[227] S.-C. Her and C.-M. Yang, “Dynamic strain measured by Mach-Zehnder interferometric optical fiber sensors.” Sensors **12**, 3314–26 (2012).

[228] Y. Mao, S. Sherif, C. Flueraru, and S. Chang, “3x3 Mach-Zehnder interferometer with unbalanced differential detection for full-range swept-source optical coherence tomography.” Applied optics **47**, 2004–10 (2008).

[229] M. Sarunic, M. a. Choma, C. Yang, and J. a. Izatt, “Instantaneous complex conjugate resolved spectral domain and swept-source OCT using 3x3 fiber couplers.” Optics express **13**, 957–67 (2005).

[230] Y. Ja, “Phase Sensitivities of Optical Fibre Ring and Loop Resonators Using a Non-planar or Planar 3 3,” Journal of Modern Optics **42**, 117–130 (1995).

[231] H.-W. Lu, Y.-E. Zhang, and G.-W. Luo, “Study of all-fiber flat-top passband interleaver based on 22 and 33 fiber couplers,” Optics Communications **276**, 116–121 (2007).

[232] E.-E. Ren, H.-W. Lu, B.-G. Zhang, and G.-W. Luo, “Optimization design of all-fiber 33 multiplexer based on an asymmetrical Mach–Zehnder interferometer,” Optics Communications **282**, 2818–2822 (2009).

[233] S. Lacour, P. Tuthill, J. D. Monnier, T. Kotani, L. Gauchet, and P. Labeye, “A new interferometer architecture combining nulling with phase closure measurements,” Monthly Notices of the Royal Astronomical Society **439**, 4018–4029 (2014).

[234] P. R. Labeye, J.-P. Berger, M. Salhi, P. Demolon, K. Rousselet-Perraut, F. Malbet, and P. Y. Kern, “Integrated Optics Components in Silica on Silicon Technology for Stellar Interferometry,” in “Proceedings of SPIE Vol. 5491 New Frontiers in Stellar Interferometry,” , vol. 5491, W. A. Traub, ed. (2004), vol. 5491, pp. 667–676.

[235] A. White, D. James, P. Eberhard, and P. Kwiat, “Nonmaximally entangled states: Production, characterization, and utilization,” Physical Review Letters **83**, 3103–3107 (1999).

[236] T. Brougham, V. Košták, I. Jex, E. Andersson, and T. Kiss, “Entanglement preparation using symmetric multiports,” The European Physical Journal D **61**, 231–236 (2010).

[237] S. Aaronson and A. Arkhipov, “The computational complexity of linear optics,” Proceedings of the 43rd annual ACM symposium on Theory of computing - STOC ’11 p. 333 (2011).

[238] M. a. Broome, A. Fedrizzi, S. Rahimi-Keshari, J. Dove, S. Aaronson, T. C. Ralph, and A. G. White, "Photonic boson sampling in a tunable circuit." Science (New York, N.Y.) **339**, 794–8 (2013).

[239] G. Pryde and A. White, "Creation of maximally entangled photon-number states using optical fiber multiports," Physical Review A **68**, 052315 (2003).

[240] K. Mattle, M. Michler, H. Weinfurter, A. Zeilinger, and M. Żukowski, "Non-classical statistics at multiport beam-splitters," Applied Physics B , Lasers and Optics **60**, 111–117 (1995).

[241] B. Shi and A. Tomita, "Schemes for generating W state of paths and W state of polarization photons," arXivph/0208170 (2002).

[242] G. Weihs, M. Reck, H. Weinfurter, and A. Zeilinger, "Two-photon interference in optical fiber multiports," Phys. Rev. A **54**, 893–897 (1996).

[243] M. Suda, C. Pacher, M. Peev, M. Dušek, and F. Hipp, "Quantum interference of photons in simple networks," Quantum Information Processing **12**, 1915–1945 (2012).

[244] Y. Zhang, L. McKnight, E. Engin, I. M. Watson, M. J. Cryan, E. Gu, M. G. Thompson, S. Calvez, J. L. O'Brien, and M. D. Dawson, "GaN directional couplers for integrated quantum photonics," Applied Physics Letters **99**, 161119 (2011).

[245] H. B. Perets, Y. Lahini, F. Pozzi, M. Sorel, R. Morandotti, and Y. Silberberg, "Realization of quantum walks with negligible decoherence in waveguide lattices," Phys. Rev. Lett. **100**, 170506 (2008).

[246] Y. Bromberg, Y. Lahini, R. Morandotti, and Y. Silberberg, "Quantum and classical correlations in waveguide lattices," Phys. Rev. Lett. **102**, 253904 (2009).

[247] A. Peruzzo, M. Lobino, J. C. F. Matthews, N. Matsuda, A. Politi, K. Poulios, X.-Q. Zhou, Y. Lahini, N. Ismail, K. Wörhoff, Y. Bromberg, Y. Silberberg, M. G. Thompson, and J. L. OBrien, "Quantum walks of correlated photons," Science **329**, 1500–1503 (2010).

[248] A. Martin, A. Issautier, H. Herrmann, W. Sohler, D. B. Ostrowsky, O. Alibart, and S. Tanzilli, "A polarization entangled photon-pair source based on a type-ii ppln waveguide emitting at a telecom wavelength," New Journal of Physics **12**, 103005 (2010).

[249] S. Tanzilli, A. Martin, F. Kaiser, M. De Micheli, O. Alibart, and D. Ostrowsky, "On the genesis and evolution of integrated quantum optics," Laser and Photonics Reviews **6**, 115–143 (2012).

[250] P. J. Shadbolt, M. R. Verde, A. Peruzzo, A. Politi, A. Laing, M. Lobino, J. C. F. Matthews, M. G. Thompson, and J. L. O'Brien, "Generating, manipulating and measuring entanglement and mixture with a reconfigurable photonic circuit," Nature Photonics **6**, 45–49 (2012).

[251] D. Bonneau, E. Engin, K. Ohira, N. Suzuki, H. Yoshida, N. Iizuka, M. Ezaki, C. M. Natarajan, M. G. Tanner, R. H. Hadfield, S. N. Dorenbos, V. Zwiller, J. L. O'Brien, and M. G. Thompson, "Quantum interference and manipulation of entanglement in silicon wire waveguide quantum circuits," New Journal of Physics **14**, 045003 (2012).

[252] A. S. Solntsev, A. A. Sukhorukov, D. N. Neshev, and Y. S. Kivshar, "Spontaneous parametric down-conversion and quantum walks in arrays of quadratic nonlinear waveguides," Phys. Rev. Lett. **108**, 023601 (2012).

[253] A. Peruzzo, A. Laing, A. Politi, T. Rudolph, and J. L. O'Brien, "Multimode quantum interference of photons in multiport integrated devices," Nature Communications **2**, 224 (2011).

[254] M. Reck, A. Zeilinger, H. J. Bernstein, and P. Bertani, "Experimental realization of any discrete unitary operator," Phys. Rev. Lett. **73**, 58–61 (1994).

[255] A. W. Snyder, "Coupled-mode theory for optical fibers," J. Opt. Soc. Am. **62**, 1267–1277 (1972).

[256] A. Szameit, F. Dreisow, T. Pertsch, S. Nolte, and A. Tünnermann, "Control of directional evanescent coupling in fs laser written waveguides," Opt. Express **15**, 1579–1587 (2007).

[257] I. J. Myung, "Tutorial on maximum likelihood estimation," Journal of Mathematical Psychology **47**, 90–100 (2003).

[258] C. K. Hong, Z. Y. Ou, and L. Mandel, "Measurement of subpicosecond time intervals between two photons by interference," Phys. Rev. Lett. **59**, 2044–2046 (1987).

[259] K. Poulios, D. Fry, A. Politi, and N. Ismail, "Two-photon quantum interference in integrated multi-mode interference devices," Optics Express **21**, 23401–23409 (2013).

[260] B. J. Metcalf, N. Thomas-Peter, J. B. Spring, D. Kundys, M. a. Broome, P. C. Humphreys, X.-M. Jin, M. Barbieri, W. S. Kolthammer, J. C. Gates, B. J. Smith, N. K. Langford, P. G. R. Smith, and I. a. Walmsley, "Multiphoton quantum interference in a multiport integrated photonic device." Nature communications **4**, 1356 (2013).

[261] N. Spagnolo, L. Aparo, C. Vitelli, A. Crespi, R. Ramponi, R. Osellame, P. Mataloni, and F. Sciarrino, "Quantum interferometry with three-dimensional geometry." Scientific reports **2**, 862 (2012).

[262] G. J. Pryde and A. G. White, "Creation of maximally entangled photon-number states using optical fiber multiports," Phys. Rev. A **68**, 052315 (2003).

[263] G. Xiang, B. Higgins, D. Berry, H. M. Wiseman, and G. J. Pryde, "Entanglement-enhanced measurement of a completely unknown optical phase," Nature . . . **5**, 43–47 (2010).

[264] G. Y. Xiang, H. F. Hofmann, and G. J. Pryde, "Optimal multi-photon phase sensing with a single interference fringe." Scientific reports **3**, 2684 (2013).

[265] J. C. F. Matthews, X.-q. Zhou, H. Cable, P. J. Shadbolt, D. J. Saunders, G. A. Durkin, G. J. Pryde, and J. L. O. Brien, "Practical quantum metrology," pp. 1–8 (2013).

[266] C. Sabín and G. García-Alcaine, "A classification of entanglement in three-qubit systems," The European Physical Journal D **48**, 435–442 (2008).

[267] W. Dür, G. Vidal, and J. I. Cirac, "Three qubits can be entangled in two inequivalent ways," Physical Review A **62**, 062314 (2000).

[268] D. M. Greenberger, M. Horne, and A. Zeilinger, "Similarities and Differences Between Two-Particle and Three-Particle Interference," Fortschritte der Physik **48**, 243–252 (2000).

[269] M. Zukowski and D. Kaszlikowski, "Greenberger-Horne-Zeilinger paradoxes with symmetric multiport beam splitters," Phys. Rev. A **59**, 3200–3203 (1999).

[270] N. Mermin, "Quantum mysteries revisited," Am. J. Phys **58**, 731–734 (1990).

[271] J. Lee and S. Lee, "Optical test on greenberger-horne-zeilinger paradox of quantum nonlocality," Journal of the Korean Physical Society **46**, 181–186 (2005).

[272] H. Mikami, Y. Li, and T. Kobayashi, "Generation of the four-photon W state and other multiphoton entangled states using parametric down-conversion," Physical Review A **70**, 052308 (2004).

[273] V. Buzek and M. Hillery, "Quantum copying: Beyond the no-cloning theorem." Physical review. A **54**, 1844–1852 (1996).

[274] A. Rossi, G. Vallone, A. Chiuri, F. De Martini, and P. Mataloni, "Multipath Entanglement of Two Photons," Physical Review Letters **102**, 153902 (2009).

[275] N. Langford, R. Dalton, M. Harvey, J. O'Brien, G. Pryde, A. Gilchrist, S. Bartlett, and A. White, "Measuring Entangled Qutrits and Their Use for Quantum Bit Commitment," Physical Review Letters **93**, 053601 (2004).

[276] J. Ahrens, E. Amselem, A. Cabello, and M. Bourennane, "Two fundamental experimental tests of nonclassicality with qutrits." Scientific reports **3**, 2170 (2013).

[277] L. Bartůšková, A. Černoch, and R. Filip, "Encoding two qubits into a single qutrit: An experiment," Acta Phys. Hung. B **26**, 269–276 (2006).

[278] L. Bartůšková, A. Černoch, R. Filip, J. Fiurášek, J. Soubusta, and M. Dušek, "Optical implementation of the encoding of two qubits to a single qutrit," Physical Review A **74**, 022325 (2006).

[279] C. Vitelli, N. Spagnolo, L. Aparo, F. Sciarrino, E. Santamato, and L. Marrucci, "Joining the quantum state of two photons into one," Nature Photonics **7**, 521–526 (2013).

[280] B. Guan, R. Scott, C. Qin, and N. Fontaine, "Free-space coherent optical communication with orbital angular, momentum multiplexing/demultiplexing using a hybrid 3D photonic integrated circuit," Optics Express **22**, 145–156 (2014).

[281] S. Leon-Saval and N. Fontaine, "Mode-selective photonic lanterns for space-division multiplexing," Optics Express **22**, 1–9 (2014).

[282] E. Knill, "Quantum gates using linear optics and postselection," Phys. Rev. A **66**, 52306 (2012).

[283] S. Rahimi-Keshari, M. A. Broome, R. Fickler, A. Fedrizzi, T. C. Ralph, and A. G. White, "Efficient characterisation of any linear photonic device," arXiv:1210.6463v2 (2002).

[284] N. K. Langford, T. J. Weinhold, R. Prevedel, K. J. Resch, A. Gilchrist, J. L. O'Brien, G. J. Pryde, and A. G. White, "Demonstration of a Simple Entangling Optical Gate and Its Use in Bell-State Analysis," Phys. Rev. Lett. **95**, 210504 (2005).

[285] S. Gross, "Direct-write mid-IR waveguide lasers," Phd thesis, Macquarie University (2012).

[286] J. O'Brien, G. Pryde, A. Gilchrist, D. James, N. Langford, T. Ralph, and A. White, "Quantum Process Tomography of a Controlled-NOT Gate," Physical Review Letters **93**, 080502 (2004).

[287] A. Shabani, R. L. Kosut, M. Mohseni, H. Rabitz, M. A. Broome, M. P. Almeida, A. Fedrizzi, and A. G. White, "Efficient Measurement of Quantum Dynamics via Compressive Sensing," Physical Review Letters **106**, 100401 (2011).

[288] X.-C. Yao, T.-X. Wang, P. Xu, H. Lu, G.-S. Pan, X.-H. Bao, C.-Z. Peng, C.-Y. Lu, Y.-A. Chen, and J.-W. Pan, "Observation of eight-photon entanglement," Nature Photonics **6**, 225–228 (2012).

[289] I. Aharonovich, A. D. Greentree, and S. Prawer, "Diamond photonics," Nature Photonics **5**, 397–405 (2011).

[290] I. Aharonovich, S. Castelletto, D. a. Simpson, A. Stacey, J. McCallum, A. D. Greentree, and S. Prawer, "Two-level ultrabright single photon emission from diamond nanocrystals." Nano letters **9**, 3191–5 (2009).

[291] G. D. Marshall, T. Gaebel, J. C. F. Matthews, J. Enderlein, J. L. O'Brien, and J. R. Rabeau, "Coherence properties of a single dipole emitter in diamond," New Journal of Physics **13**, 055016 (2011).

[292] J. P. Hadden, J. P. Harrison, A. C. Stanley-Clarke, L. Marseglia, Y.-L. D. Ho, B. R. Patton, J. L. O'Brien, and J. G. Rarity, "Strongly enhanced photon collection from diamond defect centers under microfabricated integrated solid immersion lenses," Applied Physics Letters **97**, 241901 (2010).

[293] T. Schröder, M. Fujiwara, T. Noda, H.-Q. Zhao, O. Benson, and S. Takeuchi, "A nanodiamond-tapered fiber system with high single-mode coupling efficiency." Optics express **20**, 10490–7 (2012).

[294] A. W. Schell, J. Kaschke, J. Fischer, R. Henze, J. Wolters, M. Wegener, and O. Benson, "Three-dimensional quantum photonic elements based on single nitrogen vacancy-centres in laser-written microstructures." Scientific reports **3**, 1577 (2013).

[295] S. Castelletto, B. C. Johnson, V. Ivády, N. Stavrias, T. Umeda, A. Gali, and T. Ohshima, "A silicon carbide room-temperature single-photon source," Nature materials **12**, 1–6 (2013).

[296] A. Sipahigil, M. L. Goldman, E. Togan, Y. Chu, M. Markham, D. J. Twitchen, A. S. Zibrov, A. Kubanek, and M. D. Lukin, "Quantum Interference of Single Photons from Remote Nitrogen-Vacancy Centers in Diamond," Physical Review Letters **108**, 143601 (2012).

[297] H. Bernien, L. Childress, L. Robledo, M. Markham, D. Twitchen, and R. Hanson, "Two-Photon Quantum Interference from Separate Nitrogen Vacancy Centers in Diamond," Physical Review Letters **108**, 043604 (2012).

[298] A. Shields, "Semiconductor quantum light sources," Nature photonics **1**, 215–223 (2007).

[299] T. Ba Hoang, J. Beetz, L. Midolo, M. Skacel, M. Lermer, M. Kamp, S. Hofling, L. Balet, N. Chauvin, and A. Fiore, "Enhanced spontaneous emission from quantum dots in short photonic crystal waveguides," Applied Physics Letters **100**, 061122 (2012).

[300] T. B. Hoang, J. Beetz, M. Lermer, L. Midolo, M. Kamp, S. Höfling, and A. Fiore, "Widely tunable, efficient on-chip single photon sources at telecommunication wavelengths." Optics express **20**, 21758–65 (2012).

[301] S. Fattah poor, T. B. Hoang, L. Midolo, C. P. Dietrich, L. H. Li, E. H. Linfield, J. F. P. Schouwenberg, T. Xia, F. M. Pagliano, F. W. M. van Otten, and A. Fiore, "Efficient coupling of single photons to ridge-waveguide photonic integrated circuits," Applied Physics Letters **102**, 131105 (2013).

[302] C. Santori, D. Fattal, J. Vučković, G. S. Solomon, and Y. Yamamoto, "Indistinguishable photons from a single-photon device," Nature **419**, 594–597 (2002).

[303] M. A. Pooley, D. J. P. Ellis, R. B. Patel, A. J. Bennett, K. H. A. Chan, I. Farrer, D. A. Ritchie, and A. J. Shields, "Controlled-NOT gate operating with single photons," Applied Physics Letters **100**, 211103 (2012).

[304] O. Gazzano, M. P. Almeida, A. K. Nowak, S. L. Portalupi, A. Lemaître, I. Sagnes, A. G. White, and P. Senellart, "Entangling Quantum-Logic Gate Operated with an Ultrabright Semiconductor Single-Photon Source," Physical Review Letters **110**, 250501 (2013).

[305] C. Xiong, G. D. Marshall, A. Peruzzo, M. Lobino, A. S. Clark, D. Y. Choi, S. J. Madden, C. M. Natarajan, M. G. Tanner, R. H. Hadfield, and Others, "Generation of correlated photon pairs in a chalcogenide As2S3 waveguide," Applied Physics Letters **98**, 51101 (2011).

[306] M. J. Collins, A. S. Clark, J. He, D.-Y. Choi, R. J. Williams, A. C. Judge, S. J. Madden, M. J. Withford, M. J. Steel, B. Luther-Davies, C. Xiong, and B. J. Eggleton, "Low Raman-noise correlated photon-pair generation in a dispersion-engineered chalcogenide As2S3 planar waveguide." Optics letters **37**, 3393–5 (2012).

[307] S. Azzini, D. Grassani, M. J. Strain, M. Sorel, L. G. Helt, J. E. Sipe, M. Liscidini, M. Galli, and D. Bajoni, "Ultra-low power generation of twin photons in a compact silicon ring resonator." Optics express **20**, 23100–7 (2012).

[308] D. Bonneau, E. Engin, K. Ohira, N. Suzuki, H. Yoshida, N. Iizuka, M. Ezaki, C. M. Natarajan, M. G. Tanner, R. H. Hadfield, S. N. Dorenbos, V. Zwiller, J. L. O'Brien, and M. G. Thompson, "Quantum interference and manipulation of entanglement in silicon wire waveguide quantum circuits," New Journal of Physics **14**, 045003 (2012).

[309] E. Meyer-Scott, V. Roy, J.-P. Bourgoin, B. L. Higgins, L. K. Shalm, and T. Jennewein, "Generating polarization-entangled photon pairs using cross-spliced birefringent fibers." Optics express **21**, 6205–12 (2013).

[310] C. a. Husko, A. S. Clark, M. J. Collins, A. De Rossi, S. Combrié, G. Lehoucq, I. H. Rey, T. F. Krauss, C. Xiong, and B. J. Eggleton, "Multi-photon absorption limits to heralded single photon sources." Scientific reports **3**, 3087 (2013).

[311] A. S. Clark, M. J. Collins, A. C. Judge, E. C. Mägi, C. Xiong, and B. J. Eggleton, "Raman scattering effects on correlated photon-pair generation in chalcogenide," Optics Express **20**, 16807 (2012).

[312] M. A. Broome, M. P. Almeida, A. Fedrizzi, and A. G. White, “Reducing multiphoton rates in pulsed down-conversion by temporal multiplexing,” Opt. Express **19**, 22698–22708 (2011).

[313] J. Mower and D. Englund, “Efficient generation of single and entangled photons on a silicon photonic integrated chip,” Physical Review A **84**, 052326 (2011).

[314] A. Migdall, D. Branning, and S. Castelletto, “Tailoring single-photon and multiphoton probabilities of a single-photon on-demand source,” Physical Review A **66**, 053805 (2002).

[315] X.-s. Ma, S. Zotter, J. Kofler, T. Jennewein, and A. Zeilinger, “Experimental generation of single photons via active multiplexing,” Physical Review A **83**, 043814 (2011).

[316] R. J. Williams, C. Voigtländer, G. D. Marshall, A. Tünnermann, S. Nolte, M. J. Steel, and M. J. Withford, “Point-by-point inscription of apodized fiber Bragg gratings.” Optics letters **36**, 2988–90 (2011).

[317] J. Armstrong, N. Bloembergen, J. Ducuing, and P. Pershan, “Interactions between Light Waves in a Nonlinear Dielectric,” Physical Review **127**, 1918–1939 (1962).

[318] M. N. Armenise, “Fabrication techniques of lithium niobate waveguides,” Optoelectronics, IEE Proceedings J **135**, 85–91 (1988).

[319] J.-H. Zhao, X.-H. Liu, Q. Huang, P. Liu, and X.-L. Wang, “Lithium Niobate Ridge Waveguides Fabricated by Ion Implantation Followed by Ion Beam Etching,” Journal of Lightwave Technology **28**, 1913–1916 (2010).

[320] P. Baldi, S. Nouh, K. E. Hadi, M. de Micheli, D. B. Ostrowsky, D. Delacourt, and M. Papuchon, “Quasi-phase-matched parametric fluorescence in room-temperature lithium tantalate waveguides,” Optics Letters **20**, 1471 (1995).

[321] J. L. Jackel and J. J. Johnson, “Reverse exchange method for burying proton exchanged waveguides,” Electronics Letters **27**, 1360–1361 (1991).

[322] Y. N. Korkishko, V. A. Fedorov, T. M. Morozova, F. Caccavale, F. Gonella, and F. Segato, “Reverse proton exchange for buried waveguides in LiNbO3,” Journal of the Optical Society of America A **15**, 1838 (1998).

[323] P. Aboussouan, O. Alibart, D. B. Ostrowsky, P. Baldi, and S. Tanzilli, “High-visibility two-photon interference at a telecom wavelength using picosecond-regime separated sources,” Physical Review A **81**, 021801 (2010).

[324] L. Chanvillard, P. Aschieri, P. Baldi, D. B. Ostrowsky, M. de Micheli, L. Huang, and D. J. Bamford, “Soft proton exchange on periodically poled LiNbO[sub 3]: A simple waveguide fabrication process for highly efficient nonlinear interactions,” Applied Physics Letters **76**, 1089 (2000).

[325] M. J. Collins, C. Xiong, I. H. Rey, T. D. Vo, J. He, S. Shahnia, C. Reardon, T. F. Krauss, M. J. Steel, a. S. Clark, and B. J. Eggleton, "Integrated spatial multiplexing of heralded single-photon sources." Nature communications **4**, 2582 (2013).

[326] J. R. Grenier, L. A. Fernandes, and P. R. Herman, "Femtosecond laser writing of optical edge filters in fused silica optical waveguides," Optics Express **21**, 4493 (2013).

[327] C. Xiong, T. D. Vo, M. J. Collins, J. Li, T. F. Krauss, M. J. Steel, A. S. Clark, and B. J. Eggleton, "Bidirectional multiplexing of heralded single photons from a silicon chip." Optics letters **38**, 5176–9 (2013).

[328] S. Krapick, H. Herrmann, V. Quiring, B. Brecht, H. Suche, and C. Silberhorn, "An efficient integrated two-color source for heralded single photons," New Journal of Physics **15**, 033010 (2013).

[329] J. C. Ng, C. Li, P. R. Herman, and L. Qian, "Femtosecond laser writing of a flat-top interleaver via cascaded Mach-Zehnder interferometers." Optics express **20**, 17894–903 (2012).

[330] A. Peruzzo, A. Laing, A. Politi, T. Rudolph, and J. L. O'Brien, "Multimode quantum interference of photons in multiport integrated devices." Nature communications **2**, 224 (2011).

[331] I. Spaleniak, N. Jovanovic, S. Gross, M. J. Ireland, J. S. Lawrence, and M. J. Withford, "Integrated photonic building blocks for next- generation astronomical instrumentation II : the multimode to single mode transition," **21**, 27197–27208 (2013).

[332] A. Snyder and J. Love, *Optical Waveguide Theory*, vol. 1983 (Springer, 1983).

[333] K. Okamoto, *Fundamentals of optical waveguides* (Academic Press, 2006), 2nd ed.

[334] D. Herriott, H. Kogelnik, and R. Kompfner, "Off-Axis Paths in Spherical Mirror Interferometers," Applied Optics **3**, 523 (1964).

[335] S. H. Cho, B. E. Bouma, E. P. Ippen, and J. G. Fujimoto, "Low-repetition-rate high-peak-power Kerr-lens mode-locked TiAl_2O_3 laser with a multiple-pass cavity," Optics Letters **24**, 417 (1999).

[336] S. H. Cho, F. X. Kärtner, U. Morgner, E. P. Ippen, J. G. Fujimoto, J. Cunningham, and W. H. Knox, "Generation of 90-nJ pulses with a 4-MHz repetition-rate Kerr-lens mode-locked Ti:Al_2O_3 laser operating with net positive and negative intracavity dispersion," Optics Letters **26**, 560 (2001).

[337] A. Fernandez, T. Fuji, A. Poppe, A. Frbach, F. Krausz, and A. Apolonski, “Chirped-pulse oscillators: a route to high-power femtosecond pulses without external amplification,” Optics Letters **29**, 1366 (2004).

[338] S. Tsuda, W. H. Knox, E. A. de Souza, W. Y. Jan, and J. E. Cunningham, “Low-loss intracavity AlAs/AlGaAs saturable Bragg reflector for femtosecond mode locking in solid-state lasers,” Optics Letters **20**, 1406 (1995).

[339] A. Szameit, F. Dreisow, H. Hartung, S. Nolte, A. Tunnermann, and F. Lederer, “Quasi-incoherent propagation in waveguide arrays,” Applied Physics Letters **90**, 241113 (2007).

[340] T. Meany, S. Gross, N. Jovanovic, A. Arriola, M. J. Steel, and M. J. Withford, “Towards low-loss lightwave circuits for non-classical optics at 800 and 1,550 nm,” Applied Physics A **114**, 113–118 (2013).

[341] S. Gross, M. Alberich, A. Arriola, M. J. Withford, and A. Fuerbach, “Fabrication of fully integrated antiresonant reflecting optical waveguides using the femtosecond laser direct-write technique,” Optics Letters **38**, 1872 (2013).

[342] Q. Liu, B. F. Johnston, S. Gross, M. J. Withford, and M. J. Steel, “A parametric study of laser induced-effects in terbium-doped borosilicate glasses: prospects for compact magneto-optic devices,” Optical Materials Express **3**, 2096 (2013).

[343] M. Li, S. Huang, Q. Wang, H. Petek, and K. P. Chen, “Nonlinear lightwave circuits in chalcogenide glasses fabricated by ultrafast laser.” Optics letters **39**, 693–6 (2014).

[344] S. Kanehira, K. Miura, and K. Hirao, “Ion exchange in glass using femtosecond laser irradiation,” Applied Physics Letters **93**, 023112 (2008).

[345] M. Sakakura, T. Kurita, M. Shimizu, K. Yoshimura, Y. Shimotsuma, N. Fukuda, K. Hirao, and K. Miura, “Shape control of elemental distributions inside a glass by simultaneous femtosecond laser irradiation at multiple spots.” Optics letters **38**, 4939–42 (2013).

[346] M. Shimizu, M. Sakakura, M. Ohnishi, M. Yamaji, Y. Shimotsuma, K. Hirao, and K. Miura, “Three-dimensional temperature distribution and modification mechanism in glass during ultrafast laser irradiation at high repetition rates.” Optics express **20**, 934–40 (2012).

[347] J. Mireles, M. Gomez, and M. Garcia, “Packaging Investigation and Study for Optical Interfacing of Micro Components with Optical Fibers, part I,” Revista Superficies y Vacío **20**, 21–33 (2007).

[348] N. Lindenmann, G. Balthasar, D. Hillerkuss, R. Schmogrow, M. Jordan, J. Leuthold, W. Freude, and C. Koos, “Photonic wire bonding: a novel concept for chip-scale interconnects.” Optics express **20**, 17667–77 (2012).

[349] J. van Zantvoort and G.-D. Khoe, "Fiber array-to-photonic-chip fixation and fine tuning using laser support adjustment," IEEE Journal of Selected Topics in Quantum Electronics **8**, 1331–1340 (2002).

[350] H. Sun, A. Chen, A. Szep, and L. R. Dalton, "Efficient fiber coupler for vertical silicon slot waveguides." Optics express **17**, 22571–7 (2009).

[351] M. Okoshi, J. Li, P. R. Herman, and N. Inoue, "Photochemical welding of silica optical components to silicone rubber by F 2 laser," Journal of Physics: Conference Series **59**, 712–715 (2007).

[352] P. G. Kwiat, E. Waks, A. G. White, I. Appelbaum, and P. H. Eberhard, "Ultrabright source of polarization-entangled photons," Physical Review A **60**, R773–R776 (1999).

[353] R. Sutherland, *Handbook of nonlinear optics* (Marcel Dekker, Inc, 2003), 2nd ed.

[354] E. Jeffrey, N. a. Peters, and P. G. Kwiat, "Towards a periodic deterministic source of arbitrary single-photon states," New Journal of Physics **6**, 1–14 (2004).

[355] S. Fasel, O. Alibart, S. Tanzilli, P. Baldi, A. Beveratos, N. Gisin, and H. Zbinden, "High-quality asynchronous heralded single-photon source at telecom wavelength," New Journal of Physics **6**, 1–11 (2004).

[356] M. Fiorentino, S. M. Spillane, R. G. Beausoleil, T. D. Roberts, P. Battle, and M. W. Munro, "Spontaneous parametric down-conversion in periodically poled KTP waveguides and bulk crystals," Optics Express **15**, 7479 (2007).

[357] D. Stepanov, V. Shigorin, and G. Shipulo, "Phase matching directions in optical mixing in biaxial crystals having quadratic susceptibility," Sov. J. Quantum Electron. **14**, 1315–1320 (1984).